Geophysical investigation of Vesta, Ceres and the Moon using gravity and topography data.

by

Anton Ermakov

Engineering Degree in Space Geodesy, Moscow State University of Geodesy and Cartography (2010)

Submitted to the Department of Earth, Atmospheric and Planetary Sciences
in partial fulfillment of the requirements for the degree of

Doctor of Philosophy in Planetary Science

at the

MASSACHUSETTS INSTITUTE OF TECHNOLOGY

February 2017

Signature redacted

Author .....
Department of Earth, Atmospheric and Planetary Sciences
October 31, 2016

Certified by... Signature redacted .....
Maria T. Zuber
E. A. Griswold Professor of Geophysics
Thesis Supervisor

Accepted by . Signature redacted .....
Robert D. van der Hilst
Schlumberger Professor of Earth and Planetary Sciences
Head, Department of Earth, Atmospheric and Planetary Sciences

Geophysical investigation of Vesta, Ceres and the Moon using gravity and topography data.

by

Anton Ermakov

Submitted to the Department of Earth, Atmospheric and Planetary Sciences on October 31st, 2016, in partial fulfillment of the requirements for the degree of Doctor of Philosophy in Planetary Science

Abstract

The shape and gravity field are fundamental properties of a planetary body. Combining gravity and topography data sets is, arguably, the most powerful tool to study planetary interiors from orbit. However, even when gravity and topography data are in hand, typically, a wide range of possible geophysical structures is possible. The reader will find that this problem of non-unique solutions permeates all chapters of this thesis. The general strategy to reduce non-uniqueness is to find ways to use additional observations that are sensitive to the interior structure but are not degenerate with gravity and/or topography.

In this work, we study three Solar System bodies: asteroid Vesta, dwarf planet Ceres and the Earth's Moon. Using the data from the Dawn spacecraft, we find that once hot and hydrostatic, Vesta is no longer either. It was despun by two giant collisions. We use the Dawn gravity/topography data along with meteoritic data to provide constraints on Vesta's internal structure. Unlike Vesta, Ceres is close to hydrostatic equilibrium. Based on Ceres' topographic spectrum, we conclude that it has experienced limited viscous relaxation. Contrary to the pre-Dawn expectations, we find that the cerean crust is mechanically rock-like. We provide constraints on Ceres' rheology and density structure by combining gravity/topography data with finite-element modeling of lithospheric relaxation. Additionally, we find that Ceres' obliquity undergoes large oscillations, which has important implications for volatile transport. The GRAIL mission has produced gravity models of the Moon with an unprecedented accuracy. We study the spectral content of gravity models and characterize their effective resolution to provide users of these models with the information necessary to understand the model limitations.

Thesis Supervisor: Maria T. Zuber
Title: E. A. Griswold Professor of Geophysics

Геофизический анализ Весты, Цереры и Луны с использованием данных гравитационного поля и топографии

Антон Ермаков

Диссертация передана в департамент земных, атмосферных и планетарных наук 31-го октября, 2016 года на соискание степени Доктор Философии по Планетологии

Абстракт

Фигура и гравитационное поле являются фундаментальными характеристиками небесного тела. Совместное использование данных о фигуре и гравитационном поле является мощным инструментом для изучения внутренней структуры планет с орбиты. Однако, даже если фигура и гравитационное поле небесного тела известны, неизбежна неоднозначность в определении внутренней структуры тела. Читатель обнаружит, что данная проблема неуникальных решений присутствует во всех главах этой диссертации. Общая стратегия решения этой проблемы лежит в использовании дополнительных данных, которые чувствительны к внутренней структуре, а также независимы по отношению к гравитационному полю и фигуре.

В этой работе мы изучаем три тела солнечной системы: астероид Весту, карликовую планету Цереру и спутник Земли Луну. Используя данные с миссии Dawn, мы пришли к выводу, что Веста была гидростатична, находясь в расплавленном состоянии на ранних этапах эволюции. В настоящий момент, после охлаждения, Веста не находится в состоянии гидростатического равновесия. Скорость ее вращения была уменьшена в результате двух импактных событий. Комбинирование данных гравитационного поле и топографии с метеоритными данными позволяет улучшить модель внутренней структуры Весты. В отличие от Весты, Церера близка к состоянию гидростатического равновесия. Исходя из спектра дисперсии топографии, поверхность Цереры частично вязкостно релаксирована. Вразрез с представлениями до миссии Dawn, мы заключили, что кора Цереры механически подобна каменистой породе. Применение метода конечных элементов в сочетании с данными о гравитационном поле и топографии позволило улучшить модель реологии и распределения плотности Цереры. Также мы обнаружили, что наклон оси вращения Цереры претерпевает большие изменения, что имеет важные последствия для переноса летучих веществ. Миссия GRAIL произвела определение гравитационного поля Луны с беспрецедентной точностью. Мы изучили спектральный контент моделей гравитационного поля Луны и охарактеризовали эффективное разрешение, что позволяет лучше понять их ограничения и недостатки.

Научный руководитель: Мария Т. Зубер
Должность: Е. А. Грисволд профессор геофизики

(Russian)

التحقيق الجيوفيزيائي لفيستا وسيريس والقمر باستخدام البيانات الطبوغرافية والجاذبية

ل أنتون إرماكوف

مقدم إلى قسم علوم الأرض، الغلاف الجوي والنظام الكوكبي في 31 أكتوبر 2016 من أجل الأستيفاء الجزئي لمتطلبات رسالة الدكتوراة في علوم النظام الكوكبي

ملخص

مجال الشكل والجاذبية هما الخصائص الأساسية لجسم الكوكب. يعتبر دمج البيانات الطبوغرافية وبيانات الجاذبية من أقوى الأدوات لدراسة الشكل الداخلي للكوكب عن طريق المدار. ولكن، حتي بمعرفة البيانات الطبوغرافية وبيانات الجاذبية، امكانية ايجاد هياكل جيوفيزيائية متاح. يجد القارىء أن مشكلة عدم وجود حل أو نتيجة وحيدة تتغلغل خلال فصول هذه الرسالة. الخطة العامة لتقليص هذه المشكلة هي ايجاد طرق لاستخدام ملاحظات اضافية تكون متعلقة بالهيكل الداخلي وليست مترتبة على الطبوغرافيا والجاذبية.

في هذا العمل، ندرس ثلاثة أجسام نظام شمسي وهم كويكب فيستا، كوكب قزم سيريس وقمر الكرة الأرضية. باستخدام بيانات المركبة الفضائية "داون"، وجدنا أن عندما فيستا تكون نتيجة انفجارين هائلين وبعدئذ لم يعد ساخن ومتوازن هيدروستاتيكيا. لقد استخدمنا بيانات الجاذبية والطبوغرافية الخاصة ب "داون" بالإضافة إلى البيانات النيزكية لوضع حدود للهيكل الداخلي لفيستا. بعكس فيستا، سيريس أقرب للتوازن الهيدروستاتيكي. استنادا على الطيف الطبوغرافي لسيريس، استنتجنا أنه مر ببعض المرونة اللزوجية. بعكس توقعات "داون"، وجدنا أن سيريس له قشرة صخرية ميكانيكيا. ونعطي أيضا قيود للكثافة وخصائص الجريان "الريولوجية" لسيريس بدمج البيانات الطبوغرافية وبيانات الجاذبية مع نموذج العناصر المنتهية لمرونة الغلاف الصخري. إضافة إلى ذلك، وجدنا أن الميل المحوري لسيريس مر بذبذبات كبيرة والتي لها دور في النقل البخري. مهمة جريل أخرجت نماذج خاصة بجاذبية القمر بدقة ليس لها مثيل. نقوم بدراسة وتصنيف المحتوى الطيفي لنماذج الجاذبية لإمداد مستخدميها بالمعلومات التي تسهل لهم فهم قصورهذه النماذج.

مشرف الرسالة: ماريا زوبر (أستاذ الجيوفيزيا)
مترجم: محمد حسن شحاته

(Arab)

Վեստայի, Սերեսի և Լունայի երկրաֆիզիկական վերլուծությունը գրավիտացիոն դաշտի և տոպոգրաֆիայի /տեղագրություն/ տվյալների կիրառմամբ

ԱՆՏՈՆ ԵՐՄԱԿՈՎ

Դիսերտացիան/ Թեզիս/ Հանձնվել է երկրային, մթնոլորտային և մոլորակային գիտությունների բաժանմունք/դեպարտամենտ/ 2016 թ.-ի Հոկտեմբերի 31-ին Մոլորակագիտության փիլիսոփայության դոկտորի գիտական աստիճանի Համար:

ԱԲՍՏՐԱԿՏ

Ֆիգուրը/պատկերը/ և գրավիտացիոն դաշտը Հանդիսանում են երկնային մարմնի հիմնական բնութագրերը: Պատկերի և գրավիտացիոն դաշտի մասին տվյալների համատեղ կիրառումը Հանդիսանում է հզոր գործիք մոլորակների ներքին կառուցվածքների ուսումնասիրման Համար ուղեծրից: Սակայն, նույնիսկ եթե հայտնի են երկնային մարմնի պատկերը և գրավիտացիոն դաշտը, անխուսափելի է անմարժեքությունը մարմնի ներքին կառուցվածքի որոշման մեջ: Ընթերցողը կհայտնաբերի, որ ոչ եզակի լուծումների տվյալ խնդիրը ներկա է այս թեզիսի բոլոր գլուխներում: Այս խնդրի լուծումների ընդհանուր ռազմավարությունն ընկած է լրացուցիչ տվյալների օգտագործման մեջ, որոնք զգայուն են ներքին կառուցվածքի Հանդեպ, ինչպես նաև անկախ են գրավիտացիոն դաշտի և պատկերի նկատմամբ:

Այս աշխատությունում մենք ուսումնասիրում ենք արեգակնային Համակարգի երեք մարմիններ. Վեստա աստերոիդը, Սերես թզուկ մոլորակը և Երկրի ուղեծիր Լուսինը: Մենք օգտագործելով տվյալները Dawn-*ի միսիայի Հետ, եկանք այն եզրակացության, որ Վեստան էվոլյուցիայի վաղ փուլում գտնվելով Հալված վիճակում հիդրոստատիկ է եղել: Ներկա պահին սառեցումից Հետո Վեստան չի գտնվում հիդրոստատիկ Հավասարակշռության վիճակում: Նրա պատյտի արագությունը կրճատվել է երկու ազդեցիկ իրադարձությունների արդյունքում: Գրավիտացիոն դաշտի և տոպոգրաֆիայի տվյալների Համակցումը երկնաքարային տվյալների Հետ թույլ է տալիս բարելավել Վեստայի ներքին կառուցվածքի մոդելը: Ի տարբերություն Վեստայի, Սերեսը մոտ է հիդրոստատիկ Հավասարակշռության վիճակին: Ելնելով տոպոգրաֆիայի դիսպերսիայի /ցրում,ցրունակություն/ սպեկտրից Սերեսի մակերևույթը մասամբ մածուցիկ թուլացած է: Մինչև* Dawn-*ի միսիան Հակառակ պատկերացումներով մենք եզրակացրեցինք, որ Սերեսի կեղևը մեխանիկորեն նման է քարային ապարի: Վերջավոր էլեմենտների մեթոդի կիրառումը գրավիտացիոն դաշտի և տոպոգրաֆիայի տվյալների զուգակցմամբ թույլ տվեց բարելավել ռեոլոգիայի /Հոսքաբանություն/ մոդելը և Սերեսի խտության բաշխումը: Ինչպես նաև մենք Հայտնաբերեցինք, որ Սերեսի պատյտի առանցքի թեքությունը կրում է մեծ փոփոխություններ, որն ունի կարևոր Հետևանքներ ցնդող նյութերի տարածման Համար:* GRAIL-*ի միսիան կատարեց Լունայի գրավիտացիոն դաշտի որոշումն աննախատեսի ճշգրտությամբ: Մենք ուսումնասիրեցինք Լունայի գրավիտացիոն դաշտի մոդելների սպեկտրալ պարունակությունը և բնութագրեցինք էֆեկտիվ լուծումը, որը թույլ է տալիս ավելի լավ Հասկանալ դրանց սահմանափակումներն ու թերությունները:*

Գիտական ղեկավար՝ Մարիա Տ.Զուբեր
Պաշտոնը՝ Ե.Ա. Գրիսվոլդ երկրաֆիզիկայի պրոֆեսոր
Թարգմանիչ՝ Մխիթարյան Մխիթար

(Armenian)

Vesta, Serera və Ayın Cazibə Qüvvəsi və Topoqrafik Məlumatlar Əsasında Geofiziki Təhlili

Müəllif: Anton Yermakov

Yer, Atmosfer və Planet Elmləri Departamentinə 31 Oktyabr 2016-cı ildə Planet Elmləri üzrə Elmlər Doktoru dərəcəsinin tələblərinin bir qisminin yerinə yetirilməsi çərçivəsində təqdim olunmuşdur.

Xülasə

Quruluş və cazibə qüvvəsi planet cismlərinin fundamental xüsusiyyətlərini təşkil edir. Cazibə qüvvəsi və topoqrafik məlumatlar silsiləsinin birləşdirilməsi, planetlərin daxili quruluşlarının orbitdən öyrənilməsinin ən güclü üsulu hesab olunur. Ancaq, hətta cazibə qüvvəsi və topoqrafik məlumatlar əsasında belə, geofizik strukturların çox geniş spektrumda mövcud olması mümkündür. Oxucu bu qeyri-unikal problem həllərinin bu dissertasiya işinin bütün fəsillərində istifadə edildiyini görəcəklər. Qeyri-unikal yanaşmanı azaltmanın ən ümumi strategiyası əlavə müşahidələrin istifadə edilməsinin yeni yollarının tapılmasından asılıdır ki, bunlarda daxili struktura çox həssasdırlar, ancaq bununla belə cazibə qüvvəsi və / vəya topoqrafik təsirdən müstəqildirlər.

Bu işdə biz Günəş Sisteminin üç üzvünü təhlil edirik: Vesta asteroidi, cırtdan planet Serera və Yerin sputniki olan Ayı. Dawn missiyasının məlumatlarını tədqiq edərək bu nəticəyə gəlirik ki, bir zamanlar hidrostatik tarazılıq və qızmar maye halında olan Vesta asteroidi, artıq bu xüsusiyyətlərini itirmişdir. İki nəhəng toqquşma vəya təsir nəticəsində onun öz ətrafında fırlanmasının sürəti azalmışdır. Cazibə sahəsi və topoqrafik məlumatları meteoritik məlumatlarla birləşdirilməsi, Vesta asteroidinin daxili strukturunun modelinin yaxşılaşdırılmasına nail olunmasına imkan verir. Vestadan fərqli olar Serera hidrostatik tarazılıq halındadır. Sereranın topoqrafik spektrumuna əsaslanaraq belə nəticəyə gəlirik ki, o çox məhdud viskos genişlənməyə məruz qalıb. Dawn missiyasından öncəki təsəvvürlərin əksinə olaraq biz belə qənaətə gəlirik ki, Sereranın üst qabığı mexaniki olaraq daş-qaya halındadır. Cazibə sahəsi / topoqrafik məlumatları litosferik relaksasiyanın finit-element modelləşdirilməsi ilə birləşdirməklə Sererarnın reologiyasının və sıxlıq sturukturunun paylanmasının yaxşılaşdırılmasına nail olunmuşdur. Eyni zamanda müəyyən etdik ki, Sereranın öz oxu ətrafında fırlanmasının bucağı böyük dəyişikliklərə məruz qalır ki, buda uçan aparatların transportu üçün mühüm təsirə malikdir. GRAIL missiyası Ayın cazibə modellərinin ən dəqiq hesablanması üçün misilsiz imkan yaratmışdır. Biz Ayın cazibə modellərinin spektral tərkibini təhlil etmiş və onların effektiv həllərini xarakterizə etmişik ki, buda bu modellərin istifadəçilərinə modelin məhdudiyyətlərini anlamaq üçün lazım olan məlumatları təqdim edir.

Dissertasiya işinin rəhbəri: Maria T. Zuber
Elmi titulu: E.A. Griswold adına Geofizika Professoru
Tərcümə edən: Ramil Maharramov

(Azerbaijani)

Гравитация ҡыры һәм өҫкө төҙөлөштәре тураһындағы мәғлүмәттәрҙе файҙаланып Вестаны, Цереараны һәм Айҙы геофизик тикшереү

Антон Ермаков

Планеталар буйынса Философия докторы дәрәжәһенә дәғүә итеү өсөн дисертация ер, һауа һәм планеталар фәндәре департаментына 2016 йылдың 31 октябрендә тапшырылды.

Абстракт

Фигура һәм гравитация ҡыры һауалағы есемдең фундаменталь характеристикаһы булып тора. Фигура һәм гравитация ҡыры тураһындағы мәғлүмәттәрҙе бергә ҡулланыу планеталарҙың эске структураларын орбитанан өйрәнеү өсөн ҡеүәтле инструмент булып тора. Шулай ҙа фигура һәм күктәге есемдең гравитацион ҡыры билдәле булһа ла, есемдең эске структураһын билдәләүҙә билдәһеҙлек мәғлүм булып тора. Сиселеше уникаль булмаған был проблема ошо дисертацияның һәр бер бүлегендә сағылыуы уҡыусының ихтибарын йәлеп итер. Был проблеманы сисеүҙең дөйөм стратегияһы эске структураһына һиҙемле, ә гравитация ҡырына һәм фигураға ҡарата үҙаллы булған өҫтәлмә мәғлүмәттәрҙе ҡулланыуҙа ята.

Был эштә беҙ өс есемде тикшерәбеҙ: астероид Веста, карлик планета Церера һәм Ерҙең юлдашы Ай. Dawn миссияһының мәғлүмәттәрен ҡулланып беҙ ошондай һығымтаға килдек: эволюцияның иртә этаптарында Веста иретелгән хәлдә булараҡ гидростатик үҙсәнлеккә эйә булған. Әлеге ваҡытта, һыуынғандан һуң, Веста гидростатик тигеҙлек хәлендә түгел. Уның әйләнеү тиҙлеге ике импакт ваҡиға һөҙөмтәһендә кәмей. Гравитация яланы тураһындағы мәғлүмәттәрҙе һәм метеорит мәғлүмәттәрҙең топографияһын берләштереү Вестаның эске структураһының моделен яҡшыртырға мөмкинлек бирә. Вестанан айырмалы рәүештә Церера гидростатик тигеҙлек хәленә яҡын. Планетаның өҫкө төҙөлөшө спектрының тарҡалыуына ҡараһаң Цереараның йөҙө өлөшләтә үҙлелекле хәлһеҙләнгән. Dawn миссияһына тиклем булған күҙаллауҙарға ҡаршы сығып беҙ Цереараның ҡайыры механик рәүештә ташлы породаға оҡшаған тигән ҡарарға киләбеҙ. Һуңғы элементтарҙың методын, гравитация ҡыры һәм планетаның өҫкө төҙөлөшө тураһындағы мәғлүмәттәре менән берлектә ҡулланыу, Цереараның тығыҙлығы бүленеше һәм ағыусанлыҡ моделен яҡшыртырға мөмкинлек бирҙе. Шулай уҡ беҙ Цереараның әйләнеш күсәре ҙур үҙгәреш кисереүен асыҡланыҡ, был осоусан мәтдәләрҙе күсереүҙә мөһим эҙемтәгә эйә. GRAIL миссияһы Айҙың гравитация ҡырын бығаса булмаған теүәллек менән билдәләне. Беҙ Айҙың гравитация ҡырының моделдәренең спектраль контентын өйрәндек һәм эффектив рөхсәтенә характеристика бирҙек, был уның сикләнеүҙәрен һәм кәмселектәрен яҡшыраҡ аңларға мөмкинселек бирә.

Ғилми етәксе: Мария Т. Зубер
Вазифа: геофизик профессоры Грисволд Е.А.
Тәржемәсе: Флюрә Аскарова (Bashkir)

ভেস্তা,সেরেস এবং চাঁদের জিওফিজিকাল তদন্ত মাধ্যাকর্ষণ এবং ভূসংস্থান তথ্য ব্যবহার করে.

আন্তন এরমাকভ

প্ল্যানেটারি সায়েন্স ডক্টরাল ডিগ্রী জন্য প্রয়োজনীয়তা আংশিক পরিপূর্ণতায় অক্টোবর ৩১ ,২০১৬পৃথিবীর, বায়ুমণ্ডলীয় এবং প্ল্যানেটারি সায়েন্স বিভাগের নিকট পেশ

সারাংশ

ভৌত অবস্থিত ও মহাকর্ষ/অভিকর্ষ ক্ষেত্র হচ্ছে গ্রহনক্ষত্রের মৌলিক বৈশিষ্ট্য। কক্ষপত্র থেকে একটি গ্রহকে আভ্যন্তরীন পর্যবেক্ষনের জন্য ঐ গ্রহের অভিকষ ও স্থানিক উপাত্তেত্তর সমন্বয় খূবই কার্যকরী পন্থা। এমনকি যখন কোন গ্রহের অভিকর্ষ ও স্থানিক উপাত্ত আমাদের হাতে থাকে, তখন উক্ত গ্রহের ভৌত ভৌগলিক আকৃতি সম্পর্কে কাছাকাছি ধারনা করা সম্ভব। এই থিসিস তেকে একজন পাঠক (এই লাইনটা ক্লিয়ার না)। নন-ইউনিকনেস সমস্যা সহজীকরনের মূল কারণ হচ্ছে অভ্যন্তরীন ভৌতগঠন সম্পর্কে জানার জন্য অভিকর্ষ ও স্থানিক উপাত্তের পাশাপাশি অতিরিক্ত পর্যবেক্ষণের সাহায্য নেওয়া।

এই গবেষনায়, আমরা নিতটি সৌরবস্তু নিয়ে পর্যবেক্ষণ করেছি: গ্রহানু ভেস্তা, বামন গ্রহ সেরেস এবং পৃথিবীর চাঁদ। 'ডন' মহাকাশযান তেকে প্রাপ্ত ডাটা থেকে আমরা পাই। এক সময়ের উত্তপত্ত ও হাইড্রোস্ট্যাটিক ভেস্তা এখন অতটা নয়। দুটো বড় সংঘর্ষের ফলে এর গতি/ঘুর্নন হ্রাস পেয়েছে। ভেস্তার আভ্যন্তরিন বৌতিগঠনের সংকোচন সম্পর্কে জানতে আমরা অভিকর্ষ ও টপোলজি উপাত্তের পাশাপশি উলকা থেকে প্রাপ্ত উপাত্ত ও ব্যবহার করেছি। সেরেস হাই ড্রোস্ট্যাটিক ভারসাম্যের কাছাকাছি পর্যায়ে মানে ভেস্তার মত নয়। সেরেসের টপোগ্রাফিক বর্ণালীর উপর ভিত্তি করে বলতে পারি, এতে সমপ্রতি সামান্য ভিসকাস রিলাক্সেশন ঘটেছে এবং আমরা দেখতে পাই সেরেসের উপরিস্তর কঠিন শিলাকৃত (ডনের ক্ষেত্রে এমন উল্টোটি ঘটেছিল)। সেরেসের ভৌত আকৃতির গঠন ও ঘনত্ব জানতে আমরা অভিকর্ষ/স্থানিকবিদ্যা ও ফাইনিট এলিমেন্ট মডেল পদ্ধতি ব্যবহার করেছি। এছাড়া সেরেসের বর্তমান কৌনিক অবস্থান প্রচুর পর্যায়ক্রমিক গতির কারনে হয়েছে। যা থেকে আমরা ভাসমান যানের গতি ও চলাচলের ধারনা পেতে পারি। চাঁদের অভিকর্ষ মডেল ধারনা প্রতিষ্ঠার গ্রেইল মিশনের বোঝার জন্য আমরা উক্ত মডেলের বর্ণালী নিয়ে পর্যবেক্ষন করেছি এবং মডেলের স্বীকার্যগুলোর সীমাবদ্ধতাগুলো বিশ্লেষন করেছি। যা এই মডেলের ব্যবহারকারীদের জন্য বুঝতে সহায়ক হবে.

থিসিস সুপারভাইজার: মারিয়া টি জুবের
ভূপদার্থবিদ্যা অধ্যাপক
অনুবাদিত: মোঃ মাহবুবুর রহমান

(Bengali)

Geofizička ispitivanja Veste, Ceresa i Meseca korišćenjem gravitacionih i topografskih podataka

Anton Ermakov

Predato Departmanu za zemaljske, atmosferske i planetarne nauke, 31. oktobra 2016. godine, kao deo uslova za sticanje diplome doktora nauka za planetarne nauke

Apstrakt

Oblik i gravitaciono polje su fundametalne osobine nebeskih tela. Kombinovanje gravitacionih i topografskih podataka je verovatno najmoćniji vid ispitivanja unutrašnjosti planeta iz orbite. Međutim, čak i kada su nam podaci o gravitaciji i topografiji na raspolaganju, često se ne može sa sigurnošću odrediti o kom tipu geofizičke strukture je reč. Čitalac će zapaziti da je ovaj problem nejedinstvenog rešenja prožet kroz sva poglavlja ovog rada. Generalna strategija za redukovanje nejedinstvenosti, je pronalaženje načina za primenu dodatnih osmatranja osetljivih na unutrašnju strukturu, ali koja su ne degenerisana gravitacijom i/ili topografijom.

Mi u ovom radu izučavamo tri nebeska tela Sunčevog sistema: asteroid Vestu, patuljastu planetu Ceres i Zemljin satelit Mesec. Korišćenjem podataka iz svemirske letelice Don (Dawn – Zora, prim. prev.), nalazimo da, nekadašnji usijani i hidrostatični asteroid Vesta, nije više ni usijan ni hidrostatičan. Njemu se zaustavila rotacija prilikom dva velika sudara. Mi koristimo gravitacione i topografske podatke sa Dona, zajedno sa meteorskim podacima, kako bi ograničili na internu strukturu Veste. Za razliku od Veste, Ceres je bliži hidrostatičnoj ravnoteži. Zasnovano na sopstvenom topografskom spektrumu, mi zaključujemo da je Ceres pretrpeo manju viskoznu relaksaciju. Nasuprot očekivanjima koja smo imali pre upotrebe podataka sa Dona, nalazimo da Ceresova kora ima mehanička svojstva stene. Mi smo prikazali ograničenja Ceresove reologije i strukture rasporeda gustine, kombinovanjem gravitacionih i topografskih podataka sa modeliranjem relaksacije litosfere metodom konačnih elemenata. Pored toga, otkrili smo da Ceresov osni nagib tj, ukošenost, prolazi kroz značajne oscilacije, što nam pruža važne implikacije za volatilni transport. Misija „GRAIL“ (Gravity Recovery and Interior Laboratory), tj, „LIGI“ (Laboratorija za izučavanje gravitacije i interijera), je proizvela gravitacione modele Meseca sa do sada nezabeleženom preciznošću. Mi izučavamo spektralni sastav gravitacionih modela i vršimo karakterizaciju njihove efektivne rezolucije, kako bi obezbedili korisnike ovih modela sa informacijama neophodnim za razumevanje ograničenja ovih modela.

Supervizor teze: Marija T. Zuber
Titula: E. A. Grizvold, profesor geofizike
Preveo: Strahinja Marković

(Bosnian)

Геофизичен анализ на Веста, Церера и Луната въз основа на данни за гравитационното поле и топографията

Антон Ермаков

Дисертация, предадена в Департамента по земни, атмосферни и планетарни науки на 31-ви октомври, 2016-та година в изпълнение на изискванията за придобиване на степента "Доктор на философските науки по планетология"

Абстракт

Формата и гравитационното поле представляват фундаментални характеристики на небесните тела. Смята се, че съвместното използване на данни за формата и гравитационното поле е най-мощната методика за изучаване на вътрешната структура от орбита. Въпреки това, дори когато са на разположение данни за гравитацията и топографията на дадено небесно тяло, те не дават еднозначна предства за вътрешния строеж, а могат да съответстват на различни възможни геофизични структури. Читателят ще обърне внимание, че въпросът за тези неднозначни математически решения е засегнат във всяка глава на дисертацията. Главната стратегия за разрешаване на този проблем се състои в използването на допълнителни данни, които са чувствителни към вътрешната структура, но не се влияят от гравитационното поле и формата на небесното тяло.

В настоящия научен труд изучаваме три тела от Слънчевата система: астероида Веста, планетата-джудже Церера и земния спътник – Луната. Използвайки данните от космическия апарат Dawn („Зора"), достигаме до извода, че Веста е била гореща и в състояние на хидростатично равновесие на по-ранен етап от своята еволюция. Скоростта на въртене на планетата-джудже е била забавена от два големи сблъсъка с космически тела. Към настоящия момент, след своето охлаждане, Веста вече не се намира в състояние на хидростатично равновесие. Комбинирането на данни за гравитационното поле и топографията съвместно с метеоритни данни дава възможност да бъде подобрен моделът на вътрешната структура на Веста. За разлика от Веста, Церера е близо до състояние на хидростатично равновесие. Въз основа на спектралната дисперсия на топографията съдим, че повърхността на Церера е претърпяла частична вискозна релаксация. Обратно на очакванията, след мисията Dawn („Зора") разкриваме, че кората на Церера има механични свойства, съответстващи на каменист характер. Прилагайки метода на крайните елементи в съчетание с данни за гравитационното поле и топографията, ние подобряваме модела на планетарната реология и разпределението на плътността на Церера. Също така достигаме до извода, че наклонът на оста на Церера претърпява големи изменения, а от своя страна, това има важни последствия за преноса на летливи вещества. Мисията GRAIL дава възможност да бъде определено гравитационното поле на Луната с безпрецедентна точност. Ние изучаваме спектралния състав на различни модели на лунното гравитационно поле и описваме тяхната ефективна резолюция, като по този начин изясняваме ограниченията и недостатъците на отделните модели.

Научен ръководител: Мария Т. Зубър
Титла: Професор по геофизика „Е. А. Грисуолд"
Превод: Явор Костов

(Bulgarian)

利用重力和地形数据对灶神星，谷神星和月球的地球物理的研究

作者：
Anton Ermakov (安东·俄曼科夫)

于 2016 年 10 月 31 日 提交给地球，大气与行星科学系，
行星科学哲学博士论文

摘要

形状和重力场是一个行星体的基本性质。可以说，结合其重力和地形数据是目前研究行星内部最有力的工具。然而，即使同时使用重力和地形数据，通常，地球物理结构的非唯一性依然不可避免。读者会发现，非唯一性这个问题贯穿本论文的所有章节。减少非唯一性一般的策略是提供更多的能反映内部结构而又独立于已有观测的其它观测。

在这篇论文中，我们研究了三个太阳系天体：小行星灶神星，矮行星谷神星和地球的卫星月球。使用黎明号太空船的数据，我们发现，灶神星是不再处于炎热和处于流体静力平衡状态。两个巨大的碰撞迫使它停止了自旋。我们使用黎明号的重力／地形数据，并结合陨石数据，约束了灶神星的内部结构。与灶神星不同，谷神星已经接近流体静力平衡。基于谷神星的地形，我们发现它经历了有限的粘性松弛。与使用黎明号的数据之前的理解不同，我们发现谷神星的地壳的力学性质与岩石类似。我们使用重力/地形数据，并结合岩石圈松弛的有限元模型，约束了谷神星的流变性质和密度结构。此外，我们发现，谷神星的倾角的振幅非常大，这对挥发性物质的迁移具有重要意义。GRAIL“圣杯”任务极大的提高了月球的引力模型的精度。我们研究了这个引力模型的频谱和有效分辨率，为用户提供了关于该模型的局限性的必要信息。

论文导师：Maria T. Zuber（玛丽亚· T· 朱伯）
头衔：地球物理 E· A· 格里斯沃尔德教授
翻译：丁忞

(Chinese)

Geofysisch onderzoek van Vesta, Ceres en de maan door middel van zwaartekracht en topografie.

door
Anton Ermakov

Submitted to the Department of Earth, Atmospheric and Planetary Sciences on October 31st, 2016, in partial fulfillment of the requirements for the degree of Doctor of Philosophy in Planetary Science

Abstract

De vorm en het zwaartekrachtsveld zijn fundamentele eigenschappen van een planetair lichaam. De combinatie van deze eigenschappen is mogelijk de meest krachtige manier om het binnenste van een planetair lichaam te bestuderen vanuit een baan eromheen. Zelfs als deze zwaartekracht en topografie data beschikbaar zijn zullen er meerdere mogelijke geofysische structuren zijn die overeen komen met deze data. Dat er geen unieke oplossing is komt terug in alle hoofdstukken van deze scriptie. De gebruikelijke manier om het gebrek aan uniekheid te verminderen is door meer observaties te gebruiken die niet rechtstreeks van zwaartekracht en topografie afgeleid zijn.

In deze scriptie bestuderen we drie hemellichamen in het zonnestelsel: asteroïde Vesta, dwergplaneet Ceres en de maan van de Aarde. Door data van het Dawn ruimtevaartuig te gebruiken ontdekken we dat Vesta eens heet en hydrostatisch was, maar nu geen van beide. Eens was de asteroïde geraakt door twee enorme botsingen. We gebruiken zwaartekracht en topografie data van Dawn in combinatie met meteoritische informatie om Vesta's interne structuur te begrenzen. In tegenstelling tot Vesta is Ceres bijna hydrostatische balans. Gebaseerd op het topografische spectrum van Ceres kunnen we concluderen dat er een gelimiteerde hoeveelheid visceuze relaxatie plaatsgevonden heeft. In tegenstelling tot de verwachtingen voor Dawn ontdekken we dat de korst van Ceres vanuit mechanisch oogpunt op gesteente lijkt. We geven beperkingen voor de rheologie en dichtheidsstructuren door zwaartekracht/topografie data te combineren met finite-element modellen voor de relaxatie van de lithosfeer. We komen ook tot de conclusie dat de obliquiteit onderhevig is aan grote oscillaties wat belangrijke implicaties heeft voor het transport van vluchtige stoffen. De GRAIL missie heeft een zwaartekrachtsmodel van de maan gegeven met ongekende precisie. We bestuderen het zwaartekrachtsspectrum van de maan en karakteriseren de effectieve resolutie, zodat de gebruikers van het model de benodigde informatie hebben om de limitaties te begrijpen.

Thesis Supervisor: Maria T. Zuber
Title: E. A. Griswold Professor of Geophysics
Translated by: Bram Willemsen

(Dutch)

Étude géophysique de Vesta, Cérès, et la Lune à partir de données gravitationnelles et topographiques

par
Anton Ermakov

Soumis au Département de Sciences Terrestres, Atmosphériques et Planétaires
le 31 Octobre 2016, comme exigence partielle du
Doctorat en Planétologie

Résumé

La forme et le champ gravitationnel sont deux caractéristiques fondamentales d'un corps céleste. Combiner des mesures gravitationnelles et topographiques est certainement une des meilleures méthodes pour déterminer la structure interne d'un corps à partir de données accumulées en orbite. Mais même avec ces données gravitationnelles et topographiques prisent en compte ensemble, un grand nombre de structures géophysiques est toujours mathématiquement possible. Le lecteur trouvera que ce problème de non-unicité est récurrent à travers tous les chapitres de cette thèse. La stratégie générale pour réduire cette non-unicité est d'inclure des observations supplémentaires qui sont sensibles à la structure interne sans être corrélées avec la gravité et/ou la topographie.

Dans cette thèse, nous étudions trois corps célestes du système solaire : l'astéroïde Vesta, la planète naine Cérès, et la Lune. À partir de données de la sonde spatiale Dawn, nous mettons en évidence que Vesta n'est ni chaude ni hydrostatique, alors qu'elle l'était auparavant. Sa rotation fut ralentie à cause de deux collisions. Nous utilisons les mesures gravitationnelles et topographiques de Dawn en plus de données météoriques pour calculer des contraintes sur le modèle intérieur de Vesta. À l'inverse de Vesta, Cérès est proche d'un équilibre hydrostatique. À partir du spectre topographique de Cérès, nous concluons que la planète naine n'a connu qu'une relaxation visqueuse limitée. Contrairement aux attentes avant les observations de Dawn, nous constatons que la croute de Cérès de nature mécanique rocheuse. Nous ajoutons des contraintes sur la rhéologie de Cérès et sa structure interne en combinant les mesures gravitationnelles et topographiques avec une modélisation de la méthode des éléments finis de sa relaxation lithosphérique. De plus, nous concluons que son obliquité a connu de larges oscillations, ce qui a eu d'importantes implications pour le transport volatile. La mission spatiale GRAIL a produit des champs gravitationnels lunaires d'une précision sans précédent. Nous étudions le contenu spectral de ces champs gravitationnels et caractérisons leur résolution pour permettre aux utilisateurs de mieux comprendre les limites des modèles.

Sous la direction de : Maria T. Zuber
Titre : E. A. Griswold Professor of Geophysics
Traduit par: Matthieu Talpe

(French)

მიზიდულობის და ტოპოლოგიური მონაცემების გამოყენებით გეოფიზიკური გამოძიება ვესტის, ცერერისა და მთვარის

ანტონ ემარკოვისგან

წარდგენილია დედამიწის, ატმოსფერული და პლანეტარიული მეცნიერებების დეპარტამენტთან, 2016 წლის 31 ოქტომბერს, როგორც ნაწილი დოქტორატურის ხარისხის დასაკმაყოფილებლად ფილოსოფიაში და პლანეტარულ მეცნიერებაში

ანოტაცია

ფიგურა და გრავიტაციული ველი არის ფუნდამენტალური თვისებები პლანეტარიული სხეულების. გრავიტაციული და ტოპოლოგიური მონაცემების სიმრავლეების შერწყმით, შესაძლოა ეს ყველაზე მძლავრი ხელსაწყო იყოს პლანეტარიული ინტერიერის შესასწავლად ორბიტიდან. მაგრამ, იმისდა მიუხედავად რომ გაგვაჩნია გრავიტაციული და ტოპოლოგიური მონაცემები, ტიპიურად, გეოფიზიკური სტრუქტურების დიდი დიაპაზონია. მკითხველია აღმოაჩენს რომ ამ პრობლემის არა-უნიკალური ამონახსი აღწევს ამ დესერტაციის ყოველ თავში. ზოგადი სტრატეგია არა-უნიკალურობის შესამცირებლად არის დამატებითი დაკვირვებების გამოყენებით, რომელიც არის მგრძნობიარე შიდა სტრუქტურის მაგრამ არ არის დეგენირირებული მიზიდულობით და/ან ტოპოგრაფიით.

ამ ნამუშევარში, ჩვენ შევისწავლით სამ მზის სისტემის სხეულებს: ასტეროიდ ვესტის, ჯუჯა პლანეტა ცერერის და დედამიწის მთვარის. კოსმოსური ზონდი "დონი"-დან მიღებული მონაცემების გამოყენებით, ჩვენ აღმოვაჩენთ რომ როგორც კი ცხელი და ჰიდროსტატიკური, ვესტა ც აღარ არის. ორი გიგანტური შეჯახების შედეგად დესპუნ. ჩვენ ვიყენებთ დონის გრავიტაციულ/ტოპოლოგიურ მონაცემებს, მეტეოროლოგიური მონაცემების თანდართვით რომ დავადგინოთ ზღვარები ვესტის შიდა სტრუქტურის. ვესტისგან განსხვავებით, ცერერა არის ახლოს ჰიდროსტატიკური წონასწორობასთან. ცერერის ტოპოგრაფიული სპექტრუმის დაყრდნობით, ჩვენ შეგვიძლია დასკვანა გამოვიტანოთ რომ გაცდილი აქვს შეზღუდული მწებვარე/ბლანტი შესუსტება. დონი -მდელი მოლოდინის საწინააღმდეგოდ, ჩვენ აღმოვაჩინეთ რომ ცერერის ქერქი არის მექანიკურად ქვისსებრი. ჩვენ გამოვიყვანეთ შეზღუდვები ცერერის რეოლოგიური და სტრუქტურული სიმჭიდროვის, გრავიტაციულ/ტოპოლოგიური მონაცემების მეშვეობით, სასრული-ელემენტარული ლითოსფერული შესუსტების მოდელირების დახმარებით. აგრეთვე, ჩვენ აღმოვაჩინეთ რომ ცერერის ირიბი მიმართულება განიცდის დიდ რხევებს, რომელსაც გააჩნია მნიშვნელოვანი შედეგები მჭროლავი ტრანსპორტირებისთვის. "GRAIL"-ის მისიამ შესაძლებლობა მოგვცა დაგვემზადებინა მიზიდულობის მოდელები მთვარისთვის უპრეცენდენტო სისწორით. ჩვენ შევისწავლით გრავიტაციული მოდელების შემცველობას და ვახასიათებთ მათ ეფექტურ რეზოლუციას რომ მივაწოდოთ მომხმარებლებს ეს მოდელები რათა უკეთესად აღიქვან ამ მოდელების შეზღუდულობა.

დისერტაციის ზედამხედველი: მარია ტ. ზუბერი
თანამდებობა: დედამიწის, ატმოსფეროს
თარგმანი: ლუკა ირემაძე

(Georgian)

והירח קרס ,וסטה הגיאופיסי חקירת
.וטופוגרפיה כובד נתוני באמצעות

ידי על נכתב
ירמקוב אנטון

של חלקי מילוי ,2016 ,לאוקטובר 31- ב פלנטריים ומדעים האטמוספירה ,הארץ כדור המחלקה הוגש
.פלנטריים במדעי לפילוסופיה דוקטור התואר לקבלת הדרישות

תקציר

ללא ,הוא סטים שילוב וטופוגרפית כובד נתוני .פלנטרי גוף של בסיסיות תכונות הן הכביד והשדה הצורה ,ביד וטופוגרפיה הכבידו נתונים כאשר גם ,זאת עם .מהמסלול פלנטרית פן ללמוד ביותר החזק הכלי ,ספק מחלחלת סייחודיי שאינם פתרונות של זו בעיה כי ימצא הקורא .רחב מגוון אפשרי גיאופיזי מבנים ,כלל בדרך דרכים למצוא היא הלא הייחוד תופעת את לצמצם כדי הכללית האסטרטגיה .הזו תזה של הפרקים כל .הטופוגרפיה או / ו הכבידה כוח עם להתנוון אינם אך הפנים למבנה רגישים אשר ,נוספות תצפיות להשתמש

קרס ,וסטה האסטרואיד :השמש במערכת גופים שלושה לומדים אנו ,זו בעבודה
חם כי מוצאים אנו ,Dawn מחלליים הנתונים באמצעות .הארץ כדור של הירח ואת הננסי הלכת כוכב משתמשים אנו .ענקיות התנגשויות שתי בידי יציב היה זה .והידרוסטטי חם לא כבר וסטה ,ההידרוסטטי .וסטה של הפנימי המבנה על אילוצים לספק כדי המטאוריט נתוני עם יחד טופוגרפיה / הכביד השחר בנתוני אנו ,קרס של טופוגרפיה ספקטרום על בהתבסס .הידרוסטטי משקל לשיווי קרוב הוא קרס ,וסטה בניגוד הוא קרסי קרום כי מוצאים אנו ,שחר-טרם לציפיות בניגוד .מוגבלת צמיגה הרפיה חווה שזה למסקנה מגיעים נתוני / הכביד שילוב ידי על בקרס יפותוצפ ראולוגיה מבנה על אילוצים מספקים אנו .לסלע דומה מכאני עובר הקרס אלכסוניים כי מוצאים אנו ,בנוסף .הליתוספריים הרפיה של אלמנט ,סופי דוגמנות עם טופוגרפיה הכבידה דגמים ייצרה GRAIL המשימה .נדיפים תחבורת עבור חשובות השלכות לה שיש ,גדולות תנודות הרזולוציה ולאפיין הכבידה מודלים של רפאים תוכן את מדימלו אנחנו .תקדים חסר דיוק עם הירח של .המודל מגבלות את להבין כדי הדרוש המידע את אלה דגמים של למשתמשים לספק כדי שלהם האפקטיבית

.זובר .ט מריה :תזה מפקח
.לגיאופיזיקה פרופסור גריסוולד .א .א :כותרת
תורגם על ידי: אדוארד פוקס.

(Hebrew)

Studio geofisico di Vesta, Cerere e la Luna utilizzando dati delle gravità e topografia

Anton Ermakov

Presentato al Dipartimento di Scienze della Terra, Atmosferiche e Planetarie il 31 ottobre 2016 per adempimento parziale dei requisiti per il grado di Dottore di Ricerca in Planetologia.

Abstract

La forma ed il campo gravitazionale sono proprietà fondamentali di un corpo planetario. Combinare gravità e dati topografici rimane probabilmente uno dei modi più efficaci per studiare l'interno dei corpi planetari dall'orbita. Ciononostante, anche nel caso in cui si abbiano a disposizione dati sulla gravità e la topografia in molti casi molte strutture geofisiche rimangono possibili. Il lettore troverà che tale problema di non-unicità delle soluzioni verrà riproposto in tutti i capitoli di questa tesi. La strategia generalmente adottata per ridurre la non-unicità risiede nell'utilizzare osservazioni aggiuntive che contengano informazioni riguardo la struttura interna, senza essere direttamente riconducibili alla gravità e/o alla topografia.

In questa tesi verranno studiati tre corpi del Sistema Solare: l'asteroide Vesta, il pianeta nano Cerere e la Luna. Utilizzando i dati raccolti dal veicolo spaziale Dawn, si può notare che Vesta fu calda e idrostatica in passato, ma ora non lo è più. La sua rotazione si decelerò a causa di due enormi impatti. Sono stati usati dati gravitazionali e topografici catturati dal veicolo spaziale Dawn e dati meteoritici per limitare le soluzioni riguardanti la struttura interna di Vesta. A differenza di Vesta, Cerere è vicino all'equilibrio idrostatico. Sulla base dello spettro topografico, si può concludere che rilassamento viscoso è successo parzialmente alla superficie di Cerere. Contrariamente a quanto si pensava prima dei dati raccolti da Dawn, si può ora determinare che la crosta di Cerere è rocciosa. In questo studio sono stati trovati vincoli alla reologia e alla densità di Cerere attraverso l'utilizzo combinato di dati gravitazionali/topografici con modellazione con il metodo degli elementi finiti del rilassamento della litosfera. In aggiunta, l'obliquità di Cerere è affetta da notevoli oscillazioni, il che comporta importanti implicazioni per il trasporto delle volatili. La missione GRAIL ha prodotto modelli gravitazionali della Luna con precisione finora ineguagliata. In questa tesi si studia il contenuto dello spettro di modelli gravitazionali e si caratterizza la loro risoluzione effettiva al fine di garantire a coloro i quali usufruiranno di tali modelli le informazioni necessarie per comprenderne le limitazioni.

Relatore di tesi: Maria T. Zuber
Titolo: E. A. Griswold Professore di Geofisica
Tradotto da: Gianmarco de Simone

(Italian)

重力および地形データを用いた Vesta, Ceres, および月の地球物理学的研究

Anton Ermakov 著

Department of Earth, Atmospheric, and Planetary Sciences へ惑星科学の博士号取得条件を部分的に満たすために 2016 年 10 月 31 日提出

要旨

形状および重力場は惑星体の主な特性である．これら形状および重力場を同時に用いることは，惑星軌道から惑星の内部を推測するもっとも重要な方法であるといっても過言ではない．しかし，これら重力および地形をもちいたとしても，たいてい幅広い惑星物理学的構造の可能性が残されてしまう．読者の方々は，単一解が得られないという問題を，本博士論文の至る所で確認していただけるであろう．この問題に対する一般的な対処法としては，より多くの惑星内部の構造に高感度で，かつ重力や地形に対して独立でない観測を行うことである．

本博士論文においては，太陽系内の 3 つの天体：小惑星 Vesta，準惑星，Ceres，および地球の月に焦点を当てて研究を行う．Dawn spacecraft からのデータを用いることによって，かつては Vesta は熱く，静水であると思われていたが，実際はそのどちらでもないということが明らかになった．Vesta は 2 度の大きな衝突によって回転速度が低下したのだ．我々は明け方の重力および地形データ，および隕石のデータを用いることによって Vesta の内部構造を絞り込んだ．Ceres の地形スペクトルに基づくと，Ceres は粘性緩和をほとんど経ていないという結論に至った．明け方前の予測とは反対に，Ceres の地殻は力学的に岩に似ているということを発見した．本論文では重力および地形学データと岩石圏の緩和の有限要素モデルを用いて，Ceres のレオロジーおよび密度構造を提供する．それに加え，Ceres の傾斜が大きな振動を経ていることを発見した．このことは揮発性輸送の重要な指標である．GRAIL ミッションは月の重力モデルをこれまでにない精度で提供した．本博士論文では重力モデルのスペクトル成分を研究し，モデルの適正な解像度を絞り込むことで，これらのモデルの利用者にモデルの限界を理解するのに必要な情報を提供する．

博士論文指導教官: Maria T. Zuber
役職名: E. A. Griswold Professor of Geophysics
日本語訳: 井之村　啓介

(Japanese)

중력과 지형 데이터를 사용하여, 베스타, 케레스와 달의 지구 물리 조사.

Anton Ermakov

안톤 엘마 코프에 의해 쓰임 행성 과학의 철학 박사 학위를 위한 요건의 부분적인 이행으로 10 월 31 일 2016 위 지구 대기 행성 과학 전공에 제출함. 관념적으로

개요

형상이나 중력장은 행성체의 기본적인 성질입니다. 중력과 지형 데이터 세트를 조합함으로써 거의 틀림없이 가장 강력한 도구가 궤도로부터 행성 내부를 연구할 것입니다. 그러나 중력과 지형 데이터를 들고 있는 경우에도 전형적으로는 가능한 지구 물리학적 구조의 넓은 범위가 가능합니다. 독자는 비 특이한 솔루션을 이 문제는 이 논문의 모든 장에 침투하는 것으로 나타납니다. 비 일의성을 저감하는 일반적인 전략은 내부 구조에 민감하지만 중력 및/또는 토포그라피-에서 변성되지 않은 부가적인 관찰을 이용하는 방법을 찾는 것입니다. 소행성 베스타, 왜 행성 세레스와 지구의 달:본 연구에서는 3 태양계 단체를 연구하고 있습니다. 새벽 우주선의 데이터를 사용하여 우리는 핫으로 정수압 1 은 베스 타는 것이 더 이상은 아닐 수 있습니다. 이는 2 거대 충돌로 회전 속도를 떨어뜨려졌습니다. 우리는 베스 타의 내부 구조상의 제약을 제공하기 위해서, 운석의 데이터와 함께 새벽의 중력/지형 데이터를 사용합니다. 베스 타와는 달리 셀레스는 정수압 평형에 가깝습니다. 세레스'지형 스펙트럼에 근거하여 우리는 그것이 제한된 점성 완화를 경험하고 있다고 결론짓고 있습니다. 새벽 전의 예상을 깨고 우리는 곡물의 지각은 기계적으로 바위 같고 나타납니다. 우리는 암권 완화의 유한 요소 모델링과 중력/지형 데이터를 조합함으로써 세레스"레올로지 및 밀도 구조상의 제약을 제공합니다. 이어 당사는 셀레스"경사가 휘발성의 수송 때문에 중요한 의미를 가지고 있는 큰 진동을 받는 것으로 나타납니다. GRAIL 미션은 전례 없는 정도로 달의 중력 모델을 생산하고 있습니다. 우리는 중력 모형의 스펙트럼의 내용을 검토하고 모델의 한계를 이해하는데 필요한 정보와 이들 모델의 사용자에게 제공하기 위해서 그들의 유효 분해능을 특징 짓습니다.

논문의 슈퍼 바이저 : 마리아 T. 주베르
제목 : 지구 물리학의 E. A. 그리스워드 교수
번역 : 박지용

(Korean)

Гравитациялық өріс және топография мәліметтер негізіндегі Вестаның, Цереаның және Айдың геофизикалық талдау

Антон Ермаков

Планетология мамандығы бойынша Философия Докторы дәрежесін алу үшін диссертация 2016 жылғы 31-ші қазанда Жер, Атмосфера және Планетарлық ғылымдар департаментіне тапсырылған

Абстракт

Пішін және гравитациялық өріс аспан денелердің негізгі сипаттамалары болып табылады. Пішін және гравитациялық өріс мәліметтерін бірлесіп пайдалану әдісі планеталардың ішкі құрылымын орбитадан зерттеудің қуатты құралы болып табылады. Бірақ, пішін және гравитациялық өріс белгілі болған жағдайда да, аспан денесінің ішкі құрылымын анықтауында белгісіздіктің орын алуы сөзсіз. Оқырман осы диссертацияның барлық тарауларында бірегей емес шешімдер табылу мәселесі бар болғанын анықтай алады. Осы мәселенің жалпы шешім стратегиясы ішкі құрылымға сезімтал, бірақ пішін және гравитациялық өріске тәуелсіз болып келетін қосымша деректерді пайдалануда жатыр.

Бұл жұмыста біз күн жүйесінің келесі үш денесін зерттейміз: Веста астероиді, Церера кіші ғаламшары, және Ай жердің серігі. Dawn миссияның мәліметтерін пайдалана отырып, біз Вестаның ерте эволюция кезеңдерінде ерітілген және гидростатика күйде болғанын туралы шешімге келдік. Қазіргі уақытта, салқындағаннан кейін, Веста гидростатикалық тепе-теңдік күйде емес екені анық. Екі әсер оқиғалардан кейін оның айналу жылдамдығы азайтылған болатын. Гравитация өрісі мен топография мәліметтерді метеорит мәліметтермен құрамдастыру Вестаның ішкі құрылының моделін жақсартуға мүмкіндік береді. Вестаға қарағанда, Церера гидростатикалық тепе-теңдік жағдайға жақын. Топография шашырауының шоғырлары негізінде, Цереаның беті жартылай тұтқырлы релаксация күйінде екені анықталған. Dawn миссиясына дейін түсініктерге қарама қайшы, Цереаның қабығы механикалық тұрғыда тастақ жынысқа жақын болғаны туралы тұжырымға келдік. Гравитациялық өріс және топография мәліметтер мен шекті элементтер әдісін қолдануы Цереаның тығыздылық үлестірімінің және реология моделін жақсартуға мүмкіндік берді. Сондай-ақ, біз бұл Цереаның көлбеу айналу осьтерін ұшырауда үлкен өзгерістер барын анықтап, ұшпа заттарға көшірудің маңызды екенін таптық. GRAIL миссиясы Айдың гравитациялық өрісін бұрын-соңды болмаған нақтылықта анықтады. Біз жасаған Айдың гравитациялық өріс модельдерінің спектрлік контент зерттеулер және олардың тиімді ажыратымдылық сипаттаулар, олардың шектеулер және кемшіліктерін жақсы түсінуге мүмкіндік береді.

Ғылыми жетекші: Мария Т. Зубер
Лауазымы: Е. А. Грисволд геофизика профессоры
Аударған: Жандос Оразалин

(Kazakh)

Таталцлын талбай, топографи мэдээллийг ашиглан Веста, Церера болон сарны геофизикийн шинжилгээ

Антон Ермаков

Дипломын ажил планетологи ухааны доктор зэрэгтэй нь 2016 аравдугаар сарын 31-нд дэлхий, агаар мандлын болон гаригийн шинжлэх ухааны хэлтэст ирүүлсэн

Товч агуулга

Биеийн галбир болон таталцлын талбай нь селестиел биеийн үндсэн шинж чанар юм. Биеийн галбир болон таталцлын талбайд тухай мэдээллийг хуваалцах нь тойрог зам нь дэлхийн дотоод бүтцийг судлах нь хүчирхэг хэрэгсэл юм. Гэсэн хэдий ч, тэр ч байтугай биеийн галбир, биеийн дотоод бүтцийг тодорхойлоход зайлшгүй тодорхойгүй мэдэх нь селестиел биеийн таталцлын талбайд бол уншигч ойлгон. Энэхүү диссертацийн бүх бүлгүүдэд өнөөгийн төрийн бус өвөрмөц шийдэл болохыг олж мэдэх болно. Энэ асуудлыг шийдвэрлэх ерөнхий зорилго нь нэмэлт мэдээлэл, таталцлын талбайд хувьд, мөн инжрийн дотоод бүтэц эмзэг, хараат бус байх ашиглах оршино.

Бид энэ ажилд нарный системын гурван биеийг суудална: бага гариг (астероид) Веста, одой гариг Цереру, дэлхийн дагуул гариг Сар. Dawn зорилго мэдээллийг ашиглан, бид түүний эхний шатанд нь хайлсан байдалд байхад Веста гидростатик байсан гэсэн дүгнэлтэнд хүрсэн. Одоогийн байдлаар, хөргөлт дараа Веста үгүй биш гидростатик тэнцвэрийн байдалд байна. Эргэлтийн хурд нь хоёр үйл явдлын үр нөлөөний үр дүнд буурсан байна. Солирын мэдээлэл загвар таталцлын талбай болон газрын гадаргын талаарх мэдээллийг нэгтгэн Vesta дотоод бүтцийг сайжруулж болно. Вестагийн ялгаатай нь, Церера гидростатик тэнцвэрийн байдалд ойрхон байна. Церера гадаргуугийн спектр тархалтын зуурамтгай чанар хэсэгчлэн суларч нь газрын гадаргад үндэслэн. Dawn зорилго нь үзэл бодлыг эсрэгээр, бид Церера нь холтос нь чулуурхаг үүсэх механик төстэй юм гэж дүгнэлээ. Таталцлын талбайд болон газрын гадаргын мэдээг хослуулан хязгаарлагдмал элементийн аргыг хэрэглэх загвар реологийн ба Церера нягтрал хуваарилалтыг боловсронгуй болгох нь тусалсан юм. Мөн бид Церера нь эргэлтийн тэнхлэгийн налуу том өөрчлөлт, дэгдэмхий бодисын тээвэрлэх чухал үр дагаврыг нь хийлгэж байна гэж тогтоолоо. GRAIL зорилго урьд өмнө байгаагүй нарийвчлалтайгаар сарны таталцлын талбайд тодорхойлолтын үр дүнд өглөө. Бид сар загвар таталцлын талбайд спектрийн агуулгыг судалж, та илүү сайн өөрсдийн хязгаар, сул талуудыг ойлгох боломжийг олгодог үр дүнтэй шийдлийг тодорхойлоо.

Эрдэмийн ахлагч: Maria T. Zuber
Албан тушаал: геофизикийн профессор E. A. Griswold
Орчуулга: Анжела Хайрат

(Mongolian)

Badania geofizyczne Westy, Ceres i Księżyca z użyciem danych grawitacyjnych i topograficznych

Anton Ermakov

Praca Doktorska w dziedzinie planetologii wykonana w Zakładzie Nauk o Ziemi, Atmosferze i Planetologii 31-ego października 2016 jako jedno z wymagań do uzyskania stopnia naukowego doktora w dziedzinie planetologii.

Streszczenie:

Kształt i pole grawitacyjne to jedne z najważniejszych cech obiektów planetarnych. Możliwość połączenia danych grawitacyjnych i topograficznych jest bezsprzecznie jedną z najbardziej użytecznych metod badania wnętrza obiektów planetarnych z orbity. Jednakże nawet przy dostępności zarówno danych grawitacyjnych jak i topograficznych uzyskuje się często wiele możliwych (równocennych) rozwiązań dotyczących struktur geofizycznych obiektów planetarnych. Czytelnik z pewnością dostrzeże ten problem wielu rozdziałach tej pracy. Podstawowym podejściem ograniczającym ilość możliwych rozwiązań jest wykorzystanie dodatkowych metod obserwacyjnych, które mają wystarczającą czułość umożliwiającą badanie wnętrz obiektów planetarnych i jednocześnie będących niezależnymi od metod grawitacyjnych i topograficznych.

Tematem tej pracy są geofizyczne badania trzech ciał w Układzie Słonecznym: asteroidy Westy, planety karłowatej Ceres i Księżyca. Przy użyciu danych zebranych przez sondę kosmiczną „Dawn" ustaliliśmy, że wnętrze asteroidy Westa nie jest już gorące, sama Westa nie jest w stanie równowagi hydrostatycznej a jej obrót został spowolniony przez dwie kolizje z innymi dużymi obiektami. Połączenie wyników pochodzących z analizy danych grawitacyjnych/topograficznych uzyskanych przez sondę „Dawn" z wynikami uzyskanymi z próbek meteorytowych umożliwiło nam dalszy wgląd w wewnętrzną strukturę Westy. W przeciwieństwie do Westy, Ceres znajduje się blisko stanu równowagi hydrostatycznej. W oparciu o spektrum topograficzne ustaliliśmy również, że Ceres uległa w przeszłości niewielkiej lepkościowej relaksacji naprężeń. Ustaliliśmy też, że z punktu widzenia mechaniki skał skorupa Ceres jest skalista (w przeciwieństwie do wcześniejszych sugestii z przed misji „Dawn"). Dzięki połączeniu danych grawitacyjnych/topograficznych z modelowaniem relaksacji (odprężania) litosferycznego metodą elementów skończonych mogliśmy uzyskać wgląd w dokładna reologię i rozkład gęstości Ceres. Dodatkowo ustaliliśmy, że nachylenie osi Ceres podlega znacznym oscylacjom co ma poważne implikacje dla dystrybucji bardziej lotnych substancji. Wyjątkowo dokładne modele pola grawitacyjnego Księżyca uzyskane dzięki misji GRAIL umożliwiły nam zbadanie spektralnych aspektów modeli pola grawitacyjnego, charakteryzację ich docelowej rozdzielczości i zapewnienie użytkownikom wiarygodnych informacji na temat ograniczeń modeli pola grawitacyjnego.

Praca wykonana pod kierunkiem prof. Marii T. Zuber
Tytuł: Profesor geofizyki im. E. A. Griswolda
Tłumaczenie: Janusz J. Pętkowski

(Polish)

Investigação geofísica de Vesta, Ceres e da Lua usando dados de gravidade e topografia.

Anton Ermakov

Submetido ao Departamento de Terra, Atmosfera e Ciências Planetárias em 31 de outubro de 2016 como cumprimento parcial dos requisitos para obtenção do título de Doutor em Filosofia e Ciências Planetárias.

Resumo:

A forma e o campo de gravidade são propriedades fundamentais de um corpo planetário. Combinando conjuntos de dados sobre gravidade e topografia é, sem dúvida, a ferramenta mais poderosa para estudar interiores planetários em órbita. No entanto, mesmo quando os dados de gravidade e topografia são fornecidos, normalmente, uma ampla gama de possíveis estruturas geofísicas é possível. O leitor vai descobrir que este problema de soluções não-exclusivas permeia todos os capítulos desta tese. A estratégia geral para reduzir não-singularidade é encontrar maneiras de usar observações adicionais, que são sensíveis à estrutura interior, mas não são corrompidos pela gravidade e / ou a topografia.

Neste trabalho, estudamos três corpos do sistema solar: asteroide Vesta, planeta anão Ceres e Lua da Terra. Usando os dados da sonda Dawn, descobrimos que uma vez quente e hidrostática, Vesta já não é qualquer um. Foi retardando por duas colisões gigantes. Nós usamos os dados do princípio da sonda Dawn sobre gravidade / topografia, juntamente com dados de meteoritos para fornecer limites sobre a estrutura interna de Vesta. Ao contrário de Vesta, Ceres está perto do equilíbrio hidrostático. Com base no espectro topográfico de Ceres, concluímos que ele tem experimentado relaxamento viscoso limitado. Contrariamente às expectativas antes da sonda Dawn, descobrimos que a crosta Cereana é mecanicamente rochosa. Nós fornecemos os limites sobre a estrutura de reologia e densidade de Ceres, combinando dados de gravidade / topografia com finito-elemento de modelagem de relaxamento da litosfera. Além disso, descobrimos que a obliquidade de Ceres sofre grandes oscilações, o que tem implicações importantes para o transporte volátil. A missão GRAIL produziu modelos gravitacionais da Lua com uma precisão sem precedentes. Estudamos o conteúdo espectral de modelos gravitacionais e caracterizamos a sua resolução efetiva para fornecer aos usuários destes modelos as informações necessárias para compreender as limitações do modelo.

Professor Orientador: Maria T. Zuber
Título: E. A. Griswold Professor de Geofísica
Traduzido por: Alessandra Silva Xavier

(Portuguese)

Investigación geofísica del asteroide Vesta, el planeta enano Ceres y la Luna usando datos de la gravedad y la topografía.

por

Anton Ermakov

Presentado al Departamento de Ciencias Atmosféricas, Planetarias y de la Tierra el 31 de octubre de 2016, en cumplimiento parcial de los requisitos para el grado de Doctor en Filosofía en Ciencias Planetarias

Resumen

Tanto la forma como el campo de gravitatorio de un cuerpo planetario son propiedades fundamentales de este. La combinación de los conjuntos de datos acerca de la gravedad y la topografía es, sin duda, la más poderosa herramienta para estudiar el interior de un planeta desde la órbita. Sin embargo, incluso teniendo los datos mencionados, generalmente, se obtiene una amplia gama de posibles estructuras geofísicas posibles. El lector encontrará que estos problemas de soluciones no únicas aparecen en todos los capítulos de la presente tesis. La estrategia general para reducir el número de soluciones es encontrar maneras de utilizar observaciones adicionales que son sensibles a la estructura interior, pero no se degeneran con la gravedad o la topografía.

En este trabajo, estudiamos tres cuerpos del Sistema Solar: el asteroide Vesta, el planeta enano Ceres y la Luna. Utilizando los datos de la nave espacial Dawn se deduce que Vesta alguna vez estuvo caliente e hidrostática, sin embargo ha perdido estas propiedades. Sufrió un despun por dos colisiones gigantes. Se utilizaron los datos de la nave espacial Dawn respecto a la gravedad/topografía junto con los datos de meteoritos para proporcionar condiciones sobre la estructura interna de Vesta. A diferencia de Vesta, Ceres está cerca de equilibrio hidrostático. Basándonos en el espectro topográfico de Ceres, llegamos a la conclusión de que ha experimentado la relajación viscosa limitado. Contrariamente a las expectativas previas de la información brindada por Dawn, nos encontramos con que la corteza de Ceres es mecánicamente como una roca. Proporcionamos las condiciones sobre la estructura de la reología y densidad de Ceres mediante la combinación de datos de gravedad topografía con el modelado de elementos finitos de la relajación litosférica. Además, nos encontramos con que la oblicuidad de Ceres sufre grandes oscilaciones, lo cual tiene importantes implicaciones para el transporte volátil. La misión GRAIL ha producido modelos de gravedad de la Luna con una precisión sin precedentes. También se estudia el contenido espectral de los modelos de gravedad y se caracteriza su resolución efectiva para proporcionar a los usuarios de estos modelos la información necesaria para comprender las limitaciones del modelo.

Supervisor de tesis: Maria T. Zuber
Título: Profesor A. E. Griswold de Geofísica
Traducido por: Julio C. Castiglioni

(Spanish)

งานวิจัยด้านธรณีฟิสิกส์ของดาวเคราะห์น้อยเวสต้า, ดาวเคราะห์แคระเซเรส และดวงจันทร์ของโลก โดยใช้ข้อมูลแรงโน้มถ่วงและลักษณะภูมิประเทศ

โดย

อันโตน เยียร์มาคอฟ

ส่ง ภาควิชาวิทยาศาสตร์ โลก บรรยากาศ และดาวเคราะห์ ในวันที่ 31 ตุลาคม พ.ศ. 2559 เพื่อเป็นส่วนหนึ่งในการสำเร็จการศึกษาระดับปริญญาดุษฎีบัณฑิต ในสาขาวิทยาศาสตร์ดาวเคราะห์

บทคัดย่อ

รูปร่างและสนามแรงโน้มถ่วงเป็นคุณสมบัติพื้นฐานของวัตถุดาวเคราะห์ การใช้ชุดข้อมูลแรงโน้มถ่วง (gravity) ร่วมกับชุดข้อมูลลักษณะภูมิประเทศ (topography) ถือเป็นวิธีที่มีประสิทธิภาพที่สุดในการศึกษาโครงสร้างภายในของดาวเคราะห์จากวงโคจร อย่างไรก็ตาม แม้จะมีข้อมูลแรงโน้มถ่วงและลักษณะภูมิประเทศ แต่โครงสร้างทางธรณีฟิสิกส์ที่เป็นไปได้ก็มีความหลากหลายมากเช่นกัน ผู้อ่านจะพบว่าปัญหาที่มีคำตอบหลากหลายไม่ซ้ำกันนี้ ได้แทรกอยู่ในทุกบทของวิทยานิพนธ์ฉบับนี้ หลักการทั่วไปในการลดความหลากหลายของคำตอบ คือการหาวิธีที่จะใช้การสังเกตเพิ่มเติมซึ่งมีผลกระทบอย่างละเอียดอ่อนต่อโครงสร้างภายใน แต่ไม่ลดค่าแรงโน้มถ่วง และ/หรือ ลักษณะภูมิประเทศ

ในงานวิจัยนี้ เราศึกษาเทหวัตถุในระบบสุริยะสามดวง คือ ดาวเคราะห์น้อยเวสต้า (Vesta), ดาวเคราะห์แคระเซเรส (Ceres) และดวงจันทร์ของโลก ข้อมูลจากยานอวกาศ Dawn ทำให้เราพบว่าดาวเคราะห์น้อยเวสต้า ครั้งหนึ่งเคยร้อนและมีสภาวะอุทกสถิต (hydrostatic) แต่ปัจจุบันไม่มีสภาวะดังกล่าวแล้ว เนื่องจากมันถูกทำให้หมุนช้าลงโดยการชนครั้งใหญ่ถึงสองครั้ง เราใช้ข้อมูลแรงโน้มถ่วง/ภูมิประเทศ จากยานอวกาศ Dawn พร้อมกับข้อมูลอุกกาบาต เพื่อให้ข้อจำกัดของโครงสร้างภายในดาวเคราะห์น้อยเวสต้า ส่วนดาวเคราะห์แคระเซเรสมีสภาวะใกล้สมดุลอุทกสถิต (hydrostatic equilibrium) ซึ่งต่างจากดาวเคราะห์น้อยเวสต้า จากข้อมูลสเปกตรัมภูมิประเทศของดาวเคราะห์แคระเซเรส เราสรุปว่ามันเคยผ่านการคลายหนืดแบบจำกัด (limited viscous relaxation) เราพบว่าเปลือกของดาวเคราะห์แคระเซเรสเป็นกลไกคล้ายหิน ซึ่งขัดกับการคาดการณ์ก่อนการใช้ข้อมูลจากยานอวกาศ Dawn เราให้ข้อจำกัดวิทยาศาสตร์การไหล (rheology) และความหนาแน่นของโครงสร้างของดาวเคราะห์แคระเซเรส โดยใช้ข้อมูลแรงโน้มถ่วง/ลักษณะภูมิประเทศ ร่วมกับการสร้างแบบจำลองแบบองค์ประกอบจำกัดของการคลายธรณีภาค (finite-element modeling of lithospheric relaxation) นอกจากนี้เรายังพบว่าแกนเอียงของดาวเคราะห์แคระเซเรสมีการสายแกว่งอย่างมาก ซึ่งส่งผลกระทบสำคัญต่อการเคลื่อนย้ายที่ผันผวนง่าย ภารกิจ GRAIL ได้มีการผลิตแบบจำลองแรงโน้มถ่วงของดวงจันทร์ที่มีความถูกต้องอย่างไม่เคยมีมาก่อน เราศึกษาเนื้อหาด้านสเปกตรัมของหลากหลายแบบจำลองแรงโน้มถ่วง และอธิบายลักษณะการใช้งานที่มีประสิทธิภาพ เพื่อให้ผู้ใช้แบบจำลองเหล่านี้ มีข้อมูลที่จำเป็นในการเข้าใจข้อจำกัดของแต่ละแบบจำลอง

อาจารย์ที่ปรึกษาวิทยานิพนธ์: มาเรีย ที. ซูเบอร์
ตำแหน่ง: ศาสตราจารย์ (E. A. Griswold Professor) สาขาธรณีฟิสิกส์
แปลโดย: นางสาวปุญญพัฒน์ ศักดิ์สุภาพชน

(Thai)

Геофізичній аналіз Вести, Церери та Місяця з використанням даних гравітаційного поля й топографії

Антон Єрмаков

Дисертація передана в департамент земних, атмосферних та планетарних наук 31-го жовтня 2016 року на здобуття ступені Доктор Філософії з Палеонтології

Абстракт

Фігура і гравітаційне поле є фундаментальними характеристиками небесного тіла. Спільне використання даних про фігуру та гравітаційне поле є потужним інструментом для вивчення внутрішньої структури планет з орбіти. Але, навіть якщо фігура та гравітаційне поле небесного тіла відомі, неминуча неоднозначність в визначенні внутрішньої структури тіла. Читач з'ясує, що дана проблема неунікальних рішень присутня у всіх главах цієї дисертації. Загальна стратегія рішення цієї проблеми лежить в використанні додаткових даних, чутливих до внутрішньої структури, а також незалежні відносно гравітаційного поля і фігури.

В цій праці ми вивчаємо три тіла Сонячної системи: астероїд Весту, карликову планету Цереру та супутник Землі Місяць. З використанням даних з місії Dawn, ми дійшли до висновку, що Веста була гідростатична, знаходившись в розплавленому стані на початкових етапах свого життя. На даний момент, після охолодження, Веста не знаходиться в стані гідростатичного врівноваження. Швидкість її обертання була зменшена в результаті двох імпактних подій. Комбінування даних про гравітаційне поле і топографію з метеоритними даними дозволяє поліпшити модель внутрішньої структури Вести. На відміну від Вести, Церера близька до стану гідростатичного врівноваження. Виходячи зі спектру дисперсії топографії, поверхня Церери частково в'язкістно релаксована. Врозріз до уявлень до місії Dawn, ми зробили висновок, що кора Церери механічно подібна каменистій породі. Застосування методу кінцевих елементів в поєднанні з даними про гравітаційне поле й топографію дозволило поліпшити модель реології та розподіл густини Церери. Також мі з'ясували, що нахил вісі обертання Церери зазнає великих змін, що має важливі наслідки для переносу летючих речовин. Місія GRAIL провела визначення гравітаційного поля Місяця з безпрецедентною точністю. Ми вивчили спектральній контент моделей гравітаційного поля Місяця й охарактеризували ефективний дозвіл, що дозволяє краще зрозуміти їх обмеження та недоліки.

Науковий керівник: Марія Т. Зубер
Посада: Є.А. Грісволд, професор геофізики
Переклав: Олексій Смірнов

(Ukrainian)

Acknowledgments

These five years at MIT have been really interesting! First, I would like to thank my academic advisor Dr. Maria Zuber for accepting my application to the MIT's Ph.D. program and for guiding and tolerating me all this time. It was amazing to get to work with data from the current space missions. Maria has always been very supportive and very flexible on what topics I could work on; essentially I had full freedom on choosing the research direction. I would also like to thank Professor Jack Wisdom, it was always great to have him across the hall and be able to ask any science related or not related questions. Professors Tom Herring and Rick Binzel have helped by providing a critical review of my thesis. It has been a pleasure to have Professor Francis Nimmo on my thesis committee: numerous conversations with whom at conferences and meetings taught me a lot about planetary geophysics. Finally, Dr. Ryan Park has been critical in deriving the data products without which this work would not have been possible.

Over these five years at MIT, I have met so many people from all over the world as you saw from the abstract, it is impossible to mention them all in this short text, but I'll try. Zhandos Orazalin was my first roommate and has stayed my closest friend since my first day here, thanks for picking me and my mother from the airport that one time. Matt Talpe and Mike Sori – my first officemates – thank you guys a lot for helping me out so many times, especially Mike for reviewing tons of my emails to Maria. ZhenLiang Tian, who was the same year as me in the program, you have been an endless source of stories; it was great to see you grow as a scientist. Peter James was a great source of knowledge about geophysics, it was very surprising for me when you, with your typically calm personality, agreed on the spot to drive 1000 miles to see the Venus transit. Also, a lot of thanks to Frank Centinello for teaching me about orbit determination and, additionally, teaching me to fly a plane once in Hawaii. I am also grateful to Roger Fu who taught me a lot about how to write scientific papers, hours of conversations with him have contributed a lot to this thesis. Finally, Alex Evans and Yodit Tewelde have been great friends over these years. And yet another

finally, Sonia Tikoo-Schantz and Chris Schnatz, thanks a lot for buying my telescope.

We are not over with friends. His Highness (as he prefers to refer to himself) Alexander Tyshkovskiy and Aleksei Mikhalchenko who said they would stay for a couple of days at my place buy stayed for two weeks, in return they let me later stay in his place for two months. Aysylu Askarova has helped me many times and Valeriya Verkhovykh who were not at home at the right time. Anna Trukhan, who arrived to the States at the same time with me, it was a lot of fun to explore the US with you.

Of course, none of this would be possible without my mother Elena Ermakova, my father Ivan Ermakov, my grandmothers Nadezhda Nelubova and Olga Ermakova and my grandfathers Igor Nelubov and Valery Ermakov. This thesis is not worth a single day of yours. Finally, my fiancÃľe Dinara, at this moment still Zhussupova, what should I say about you? Last 1.5 years of adventures with you have made me happy and I love you, that's all.

Thank you all, guys!!!

Contents

List of Figures

List of Tables

Chapter 1

Introduction

1.1 Gravity and topography of rocky bodies

The shape and gravity field are fundamental properties of a planetary body. An accurate model of the shape has both practical and scientific applications. Practical aspects include the ability to land on or operate in close proximity to the body's surface. The work in this thesis focuses on the scientific applications, specifically on how the interior structure of a planetary body manifests itself in the shape and gravity field of the body. Gravity science complemented with the knowledge of topography is, arguably, the most powerful tool for studying deep interiors of rocky planetary bodies from the orbit.

In order to gain insight into the body's structure, the observational data of the body's gravitational field and surface shape must be compared to a geophysical model of the body. There are two main classes of modeling, which will be called here *forward* and *inverse*. The *forward* problem can be stated in the following way: what will the gravitational field and surface topography of a planetary body be given its internal structure? The simplest and most commonly employed assumption is hydrostatic equilibrium. Under the condition of hydrostatic equilibrium the surface of the body is an equipotential surface and there is no shear stress throughout the body. This means, in the absence of other processes that affect the long-wavelength shape of the surface, topography and gravity measurements provide the same information about

the interior structure. It is often said in scientific literature that a certain body either is or is not in hydrostatic equilibrium. The situation in reality is rarely so simple. There always exist deviations from the equilibrium state and such deviations must be quantified before employing the assumption of hydrostatic equilibrium.

The *inverse* problem can be stated in the following way: what is the interior structure of a planetary body given the observed surface topography and gravitational field? Practice shows that inverse problems are much harder to solve than forward problems. The situation with gravity and topography data is complicated by the problem of non-unique solutions, which can be demonstrated by the following simple example: the exterior gravity field of a point mass and a sphere of the same mass are identical. In fact, any radial density distribution, which sums up to the same mass, will have an identical exterior field. The non-uniqueness problem can be tackled by using additional and independent types of data such as radar, remote sensing or seismic observations. The hydrostatic equilibrium assumption can be employed as well.

The gravity and topography data can be obtained in a number of ways. Unless in-situ gravimetry observations are a possibility, the gravity data are typically obtained by monitoring the motion of a spacecraft, which acts as a test mass, in the gravity field of a planetary body. The shape data can be obtained by analysis of imagery or with an active remote sensing technique such as laser or radar altimetry. Combining gravity and topography data sets is essential in studying deep planetary interiors. However, even when gravity and topography data are in hand, typically a wide range of possible geophysical structures is possible. It is essential to bring new information to break this degeneracy.

Our work focuses on three solid Solar System bodies: asteroid Vesta, dwarf planet Ceres and the Earth's Moon. Recent space missions, namely Dawn and GRAIL, have acquired unique planetary data sets that allow insights into the geophysics of these bodies that were not previously possible. The Moon, being the only satellite of our Earth, carefully preserves a record of the processes acting in the Earth's vicinity over the history of the Solar System. Studying Vesta and Ceres is important as they

represent a unique class of objects – the protoplanets that survived to the present day providing clues about the violent environment of the early Solar System.

1.2 Vesta

Vesta is the second largest object in the main asteroid belt by mass. Due to its relatively high surface albedo and location in the inner part of the asteroid belt, Vesta is the brightest asteroid observable from the Earth. This high apparent brightness facilitated ground based observations of Vesta, which revealed the uniqueness of this asteroid. Vesta possesses a unique basaltic spectrum, which immediately points at a rich geophysical evolution of this body (McCord et al., 1970; Gaffey, 1983; Binzel and Xu, 1993). Moreover, there is a group of asteroids in the dynamical vicinity of Vesta that possess similar spectra. This led to an idea of the Vesta family – a group of asteroids (currently known as Vestoids) that originated on Vesta and were ejected into space in one or more violent collisional events (Binzel and Xu, 1993; Burbine et al., 2001). Pre-Dawn observations have revealed a large depression in the southern hemisphere of Vesta (Thomas et al., 1997) – a smoking gun of such collision. Additionally, there is a group of Howardite-Eucrite-Diogenite (HED) meteorites, whose reflectance spectra are identical to Vesta and Vestoids (McSween Jr et al., 2010). These observations constitute the strongest and most studied connection between a class of meteorites and an asteroidal family.

The Dawn mission has conducted a unique geophysical study of asteroid Vesta. Unlike terrestrial planets, large asteroids lack substantial surface modification, which makes it possible to preserve the evidence of the physical processes acting in the dawn of the solar system – thus the name of the space mission.

Using the data from the Dawn spacecraft, we infer that Vesta, once nearly hydrostatic due high interior temperatures (Fu et al., 2014), has departed from hydrostatic equilibrium due to two giant impacts (Ermakov et al., 2014). From the observed shape, gravity field and geochemical data available from the analysis of the HED meteorites, we derive models of the interior structure of Vesta. The largest gravity

anomaly is observed in Vestalia Terra – the region of the highest topography on the rim of the Rheasilvia basin. The power of this anomaly cannot be explained entirely by crustal thickness variations for plausible crust-mantle density contrasts, and implies lateral variations in crustal and/or mantle density, or alternatively, substantial lateral variations in impact-related porosity.

Our solution for Vesta's crust-mantle interface reveals a belt of thick crust around Rheasilvia and Veneneia. The thinnest crust is in the floor of the two basins and in the Vestalia Terra region. Our solution does not reveal an uplift of the crust-mantle boundary to the surface in the largest basins. This, together with the lack of olivine detected by the Visible and Infrared Spectrometer data in Rheasilvia and Veneneia (Ammannito et al., 2013), indicates that Vesta's presumed olivine mantle was either not brought to the surface by these large impacts or was covered by ejecta fallback from subsequent impacts.

1.3 Ceres

Ceres is the largest object in the main asteroid best. Discovered in 1801, Ceres enjoyed a planetary status for several decades until it was reclassified as an asteroid when many similar objects were discovered between the orbits of Mars and Jupiter. Later, it was once again reclassified as a dwarf planet given its large size and ellipsoidal shape.

Little was known about Ceres before the arrival of the Dawn spacecraft in 2015. Its mass was constrained from gravitational interactions with other bodies (Kovačević and Kuzmanoski, 2007; Kovačević, 2012). The spectrum had been measured and classified as an intermediate between C and G type asteroids (Carry et al., 2008; Milliken and Rivkin, 2009). Unlike Vesta, Ceres does not have a dynamically linked asteroidal family nor it does a meteoritic family associated with it. Prior to the Dawn mission, Earth-bound observations revealed that Ceres' shape, unlike that of Vesta, is consistent with a high degree of hydrostaticity (Drummond et al., 1998; Thomas et al., 2005; Carry et al., 2008; Drummond and Christou, 2008; Drummond et al.,

2014). Given its relaxed shape and low density, Ceres was thought to be similar to an icy satellite of the outer Solar System. It was expected that Ceres might possess an icy crust overlaying a rocky core. Given Ceres' position in the asteroid belt at $\approx$ 2.8 AU from the Sun, pervasive viscous relaxation of icy shell was expected prior to Dawn (Bland, 2013).

Contrary to the pre-Dawn expectations, we find that there is not much water ice in cerean crust (<30 vol%). We expand the shape of Ceres in a spherical harmonic series and compare the topographic spectrum of Ceres to that of Vesta. We observe that the topographic power of Ceres, unlike that of Vesta, deviates from a power law at low degrees and that the equatorial regions have lower topographic power. This indicates that viscous relaxation plays a role at Ceres. However, we find that viscous relaxation is important only at low degrees that correspond to spatial scales of more than $\approx$100 km. At smaller scales there is not a systematic latitude variation of the topographic power, nor there is a a deviation of the topography power from a power law, unlike the predictions of Bland (2013) based on the icy-shell model.

Because of its low obliquity, permanently shadowed regions (PSRs) can exist on Ceres, and have been identified using both images and shape models (Schorghofer et al., 2016; Platz et al., 2016). These observations make Ceres only the third body in the solar system with recognized PSRs after the Moon and Mercury. Some craters in Ceres' polar regions possess bright crater floor deposits (BCFDs). These crater floors are typically in shadow. However, they receive light scattered from the surrounding sunlit crater walls and therefore can be seen by the Dawn's Framing Camera. These bright deposits are hypothesized to be water ice accumulated in PSR cold traps, analogous to the Moon (Watson et al., 1961; Arnold, 1979). The temperatures in Ceres' cold traps can be low enough to accumulate and preserve volatiles over long time scales (Titus, 2015; Hayne and Aharonson, 2015b). It was shown that water ice can survive for 4.5 Gy at depths of only 10-100 m near the equator and less than 1-10 m at latitudes greater than 40° (Fanale and Salvail, 1989; Schorghofer, 2008).

The existence of the PSRs critically depends on the body's obliquity. Knowing past obliquity variations can shed light on the history of PSRs, and can help constrain

the water ice deposition time scales. As such, Ceres is unique in that the observation of volatiles on its surface can directly inform and be used to test its rotational dynamical models. Conversely an understanding of its dynamics can inform present-day rates of production, deposition and sublimation of volatiles in its polar regions.

1.4 The Moon

The NASA's GRAIL (Gravity Recovery and Interior Laboratory) mission has determined the gravity field of the Moon with unprecedented accuracy (Zuber et al., 2013). The gravity field model is recovered by processing line-of-sight (LOS) range-rate in combination with the Deep Space Network (DSN) tracking for precise orbit determination. Since the Moon does not have a notable atmosphere, it is possible for the spacecraft to orbit at much lower altitudes, which leads to higher sensitivity of satellite-satellite tracking to the body's gravity. Thus, the analysis of the GRAIL measurements has enabled for the first time development of a global planetary gravity model based solely on orbital observations at a resolution comparable to the shape model.

We study GRAIL gravity models using spectral analysis. First, we compute and compare the global spectral properties of the gravity, topography and gravity-from-topography models. We evaluate the global power spectral density (PSD) of gravity and gravity-from-topography. We find the the PSD of lunar gravity does not follow a single power law. In order to compare gravity and gravity-from-topography in the spectral domain, we compute correlation, isotropic ratio and effective density spectrum.

Second, we compute localized correlations using spectral-spatial localization method (Simons and Dahlen, 2006). This allows characterization of how the gravity field model is correlated with topography in both spatial and spectral domain. We find that the localized correlation is strongly influenced by the geophysical signal of the maria at low degrees ($n < 100$). At the intermediate range ($100 < n < 500$), the global correlation approaches unity. At high degrees ($n > 500$), the correlation gener-

ally decreases. The most important factor that controls the behavior of the correlation at high degrees is the average altitude of the spacecraft: in the low-lying maria the decrease of correlation starts earlier, whereas the Orientale basin exhibits a stronger correlation at high degrees ($n > 700$) due to the extremely low altitude arcs at the end of the mission.

Third, we compute the magnitude-squared coherence for the line of sight (LOS) acceleration time series produced by the gravity models and by the gravity-from-topography model on arc-per-arc basis. It is expected that at progressively higher spherical harmonic degrees the gravity signal is dominated by topographic variations as opposed to local density variations. The topography of the Moon is known to higher resolution than gravity due to Lunar Orbiter Laser Altimeter (LOLA) (Smith et al., 2010, 2016) onboard of Lunar Reconnaissance Orbiter (Chin et al., 2007). Therefore, the gravity created by topography provides a useful reference for gravity model determination. We find strong contributions of resonances to the coherence spectrum. The resonances occur at spherical harmonic degrees that correspond to integer multiples of spacecraft separation.

1.5 Thesis outline

In Chapter 2, we describe the methods of gravity and topography analysis. Then, In Chapter 3, we apply the gravity-topography analysis methods to study internal structure, composition and evolution of Vesta. In Chapter 4, we compare the shape models of Vesta and Ceres derived using stereophotogrammetry and stereophotoclinometry techniques. In Chapter 5, we investigate the GRAIL gravity models using spectral analysis. In Chapter 6, we apply the gravity-topography analysis methods to investigate the internal structure, evolution and composition of Ceres. In Chapter 7, we study the obliquity history of Ceres using the Dawn observations. Finally, we summarize the results of our work and discuss future work in Chapter 8.

Chapter 2

Methods

Abstract

In this chapter, we summarize the methods of working with gravity and topography data used throughout the thesis. First, we provide a summary of how gravity and topography data are represented. Then, we discuss the method of computing hydrostatic equilibrium. After that, we discuss the methods of gravity-topography spectral analysis and crustal thickness inversion. Finally, we briefly summarize the method of ellipsoid fitting based on the least-squares and conclude the chapter with discussing the method for computing gravity gradients.

2.1 Shape modeling

2.1.1 Gridded models

A geographic grid is the easiest and most common way to represent a planetary shape model. The main advantage of this method is its simplicity. In fact, to compute the spherical harmonic expansion of a shape, it is preferable to convert the shape model into the geographical grid format. However, this method has two major disadvantages. The first is the inability to effectively take into account the typically varying resolution of the shape model. Another is that geographic grids have higher concentrations of data points near the poles. This method might not be applicable for highly irregular bodies such as small asteroids or cometary nuclei.

2.1.2 Polyhedral models

A more complicated shape modeling approach is to tesselate the shape with polygons, typically triangles or quadrilaterals. In this approach, the shape model consists of the two data blocks. The first block contains the location of the vertices. The second block is the connectivity matrix that defines which vertices should be connected to form polygons. While programmatically this method is more complex, it offers more flexibility for shape representation, especially for highly non-spherical bodies.

2.1.3 Spherical harmonic expansion of topography

A shape model can be converted to a spherical harmonic expansion, which is desirable since it is the form of solution of Laplace's Equation on a sphere. In this case, the spherical harmonic coefficients represent the shape. This method, which is an analogue of a Fourier series on a sphere, allows study of spectral characteristics of the shape model. We represent the shape as a spherical harmonic series:

$$r(\phi,\lambda) = R\left[1 + \sum_{n=1}^{\infty}\sum_{m=0}^{n}\left(\bar{A}_{nm}\cos(m\lambda) + \bar{B}_{nm}(m\lambda)\right)\overline{P}_{nm}(\sin\phi)\right], \qquad (2.1)$$

where r is the radius vector of the shape model, ϕ is the planetocentric latitude, λ is the longitude, n is the degree, m is the order, $\bar{A}_{nm}$ and $\bar{B}_{nm}$ are normalized spherical harmonic coefficients, and $\bar{P}_{nm}$ are the normalized associated Legendre functions. The coefficient A_{00} is the mean radius of the body. The first-degree terms are typically non-zero because center-of-mass – center-of-figure (COM-COF) offset (see Section 3.2.1). This approach can be used to study cross-correlations between shape models produced by different methods. It also allows comparison of the spectral characteristics of the shapes of different planetary bodies. Maximizing the correlation reveals mutual orientation and offset parameters of the shape models.

2.2 Gravity modeling

2.2.1 Spherical harmonic expansion of gravity

The gravitational field is also modeled as a spherical harmonic expansion (e.g., Kaula, 1966)

$$U(r,\phi,\lambda) = \frac{GM}{r}\left[1 + \sum_{n=2}^{\infty}\sum_{m=0}^{n}\left(\frac{R_0}{r}\right)^n \left(\overline{C}_{nm}\cos(m\lambda) + \overline{S}_{nm}\sin(m\lambda)\right)\overline{P}_{nm}(\sin\phi)\right], \tag{2.2}$$

where U is the gravitational potential, GM is the gravitational constant times the mass of the body, $\bar{C}_{nm}$ and $\bar{S}_{nm}$ are the normalized spherical harmonic coefficients of the gravitational potential and R_0 is the reference radius for the gravity field model. R_0 it usually chosen to be either mean equarorial or volumetic radius of the body, however it can be chosen arbitrary. The spherical harmonic functions are normalized such that the integral of the harmonic squared is equal to 4π. The relationship between normalized and unnormalized coefficients is given by

$$\begin{pmatrix} C_{nm} \\ S_{nm} \end{pmatrix} = \left(\frac{(n-m)!(2n+1)(2-\delta_{0m})}{(n+m)!}\right)^{1/2} \begin{pmatrix} \bar{C}_{nm} \\ \bar{S}_{nm} \end{pmatrix}, \tag{2.3}$$

where δ_{0m} is the Kronecker delta function. The degree-one term is excluded from the expansion since the center of the coordinate system is chosen to be at the center of mass of the body. The zonal coefficients are given by $\bar{J}_n = -\bar{C}_{n0}$. The shape coefficients A_{nm} and B_{nm} are normalized in the same way. To shorten the notation we introduce $\alpha_{nm}$and σ_{nm}:

$$\begin{aligned} \alpha_{nm} &= \{A_{nm}, B_{nm}\}, \quad \bar{\alpha}_{nm} = \{\bar{A}_{nm}, \bar{B}_{nm}\} \\ \sigma_{nm} &= \{C_{nm}, S_{nm}\}, \quad \bar{\sigma}_{nm} = \{\bar{C}_{nm}, \bar{S}_{nm}\} \end{aligned} \tag{2.4}$$

The use of spherical harmonics for gravity field representation has one serious drawback. The spherical harmonic series formally diverges in the region below the minimum sphere that circumscribes the body (also known as the Brillouin sphere).

Therefore the spherical harmonic expansion cannot be used to map the gravitational potential and acceleration near the surface of the body. This is especially important for Vesta since difference between the lowest and the highest point on Vesta is $\approx$ 80 km. We estimate the divergence of the spherical harmonic expansion as follows. We find the closest distance to the body reference surface at which the divergence is less than the uncertainty in the gravity model. Using the icosahedron tessellation of a unit sphere, we find the location of vertices, and use the shape model expanded in spherical harmonics to degree 360 to compute the radius vectors at the vertices. To compute gravitational potential and acceleration, we use the algorithm developed by Werner (1994) and Werner and Scheeres (1996), in which the gravitational potential and acceleration of a constant-density polyhedral body can be expressed in a closed form.

This approach does not have the problem of divergence as the gravity potential is computed by summing over all tetrahedra that represent the shape model and the accuracy is defined by the size of the tetrahedra. One might construct a multilayered model of a body with tetrahedra, which would allow inverting for lateral density variations, as opposed to crustal thickness variations (Park et al., 2014b). We use the polyhedral approach to check the accuracy of the spherical harmonic expansion. For the Vesta shape model, we computed the difference between the gravitational acceleration of a constant density body expanded in spherical harmonics up to degree 20 and the exact acceleration computed from the polyhedral shape model. The divergence of the spherical harmonic expansion is illustrated in Fig. 2-1. The reference surface is defined as the volumetrically-minimal ellipsoid of revolution that approximates in a least-squares sense an equipotential surface (no centrifugal potential), and at which the divergence is smaller than the errors in the gravity field model. This ellipsoid lies partially inside the Brillouin sphere, but the divergence of the spherical harmonic expansion is not significant to a maximum spherical harmonic degree of 20.

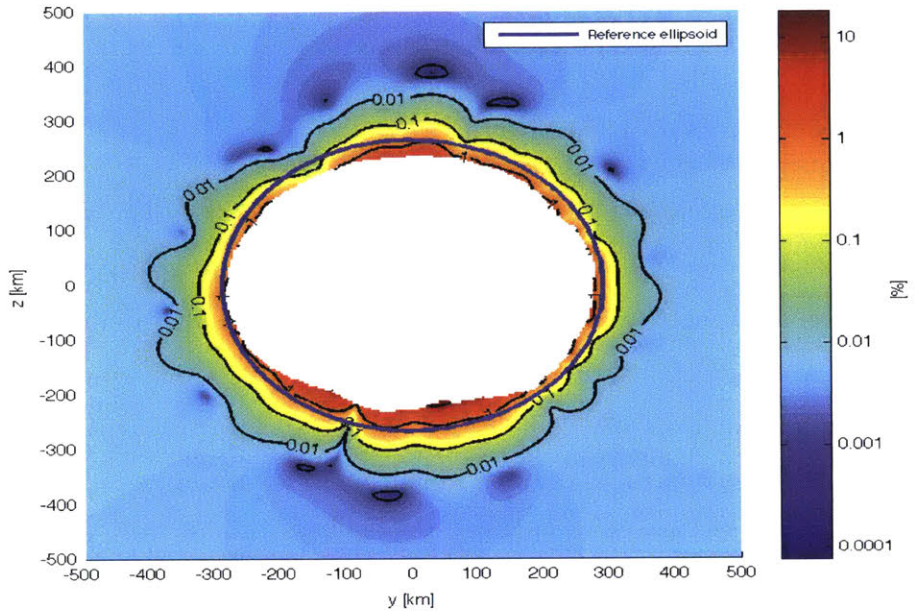

Figure 2-1 – Difference between the gravitational acceleration of Vesta computed using spherical harmonic expansion and polyhedral method in the YZ plane of the Claudia coordinate system.

2.2.2 Moments of inertia

The inertia tensor I contains six independent quantities. In the principal coordinate system, where the axes are aligned with the principal inertia axes, there are three independent inertia moments, which are called principal moments. By convention, they are usually called A, B and C, where $A \leq B \leq C$. On the other hand, there are only five degree-2 gravity coefficients, which can be reduced to two in the principal coordinate system. These two spherical harmonic coefficients are:

$$\begin{cases} C_{20} = \frac{1}{MR_0^2}\left(\frac{1}{2}(A+B) - C\right) \\ C_{22} = \frac{1}{4MR_0^2}(B-A) \end{cases}, \tag{2.5}$$

Note that here the coefficients are not normalized. It is not possible to uniquely determine the moments of inertia only from the degree-2 gravity coefficients. An additional constraint is required. Typically, this can come from the determination of the precession constant, which depends on the ratio C_{20}/C. Alternatively, hydrostatic

equilibrium can provide the extra constraint.

2.3 Hydrostatic equilibrium

Throughout this work, we have to deal with rapidly rotating bodies. The rotation period of Vesta is 5.34 hours and the rotation period of Ceres is 9.07 hours. Such rapid rotation requires an accurate method of computing figures of hydrostatic equilibrium. We use a numerical approach proposed by Tricarico (2014), which gives a solution for a multilayer body in hydrostatic equilibrium by approximating the equipotential surfaces with ellipsoids. In this approach, the equilibrium shape is found by minimizing the squared differences of the total gravitational potential $U_{tot}(x, y, z) = U_{ell} + U_{rot}$ at the outer surface and at the inner interfaces, where x, y and z are the cartesian coordinates with the z-axis aligned with the spin axis of the body. Here U_{ell} is the gravitational potential of an ellipsoid and $U_{rot} = \frac{1}{2}(x^2 + y^2)\omega^2$ is rotational potential. The sum of the squared potential differences Δ^2 is given by:

$$\begin{aligned}\Delta^2 &= \sum_{i=0}^{N}\{[U_{tot}(a_i, 0, 0) - U_{tot}(0, b_i, 0)]^2 + \\ &\quad [U_{tot}(a_i, 0, 0) - U_{tot}(0, 0, c_i)]^2\}\end{aligned}$$

where N is the number of layers and a_i, b_i, c_i are the longest, intermediate and shortest ellipsoidal axes, respectively. This form can be used both for finding the biaxial (Maclaurin) and triaxial (Jacobi) equilibrium ellipsoids (Chandrasekhar, 1967). To illustrate this, we compute Δ^2 for a Vesta-like homogeneous body. Fig. 2-2 shows Δ^2 as a function of the polar and equatorial flattening factors $f_p = (a - c)/a$ and $f_q = (a - b)/a$. Maclaurin and Jacobi equilibria are seen. At those points Δ^2 is minimized to a machine-precision zero.

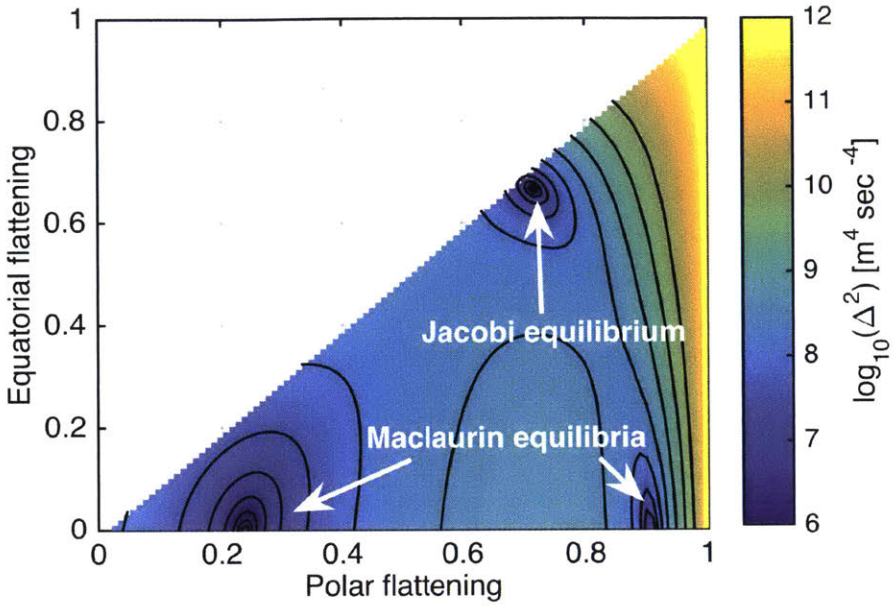

Figure 2-2 – Maclaurin and Jacobi equilibrium for a homogeneous body with a mass, mean density and rotation period of Vesta.

2.4 Gravity-topography analysis

2.4.1 Spectral analysis

To study how the power of either gravity or topography is distributed over various spatial scales, it is useful to define the power spectrum of the spherical harmonic expansion of gravity S_n^g , of topography S_n^t and the gravity-topography cross-power spectrum S_n^{gt}.

$$S_n^{gg} = \sum_{m=0}^{n} \bar{\sigma}_{nm}^2, \tag{2.6}$$

$$S_n^{tt} = \sum_{m=0}^{n} \bar{\alpha}_{nm}^2, \tag{2.7}$$

$$S_n^{gt} = \sum_{m=0}^{n} \bar{\sigma}_{nm}\bar{\alpha}_{nm}, \tag{2.8}$$

The power spectral density (PSD) of the gravity field or topography is defined through the power of the spherical harmonic expansion:

$$M_n^{gg} = \frac{S_n^{gg}}{2n+1}, \tag{2.9}$$

$$M_n^{tt} = \frac{S_n^{tt}}{2n+1}, \tag{2.10}$$

It was shown by Kaula (1963) and Lambeck (1976) that the power spectral density follows a power law assuming a random distribution of density anomalies at random depth.

2.4.2 Gravity from shape

We compute gravity-from-shape spherical harmonic coefficients $\bar{\sigma}_{nm}^{shape}$ as detailed by Wieczorek and Phillips (1998), where gravitational coefficients are expanded in a series of powers of shape.

$$\bar{\sigma}_{nm}^{shape} = \frac{3}{2n+1} \sum_{h=1}^{n+3} \frac{{}^h\bar{\alpha}_{nm}}{D^h h!} \cdot \frac{\prod_{j=1}^{h}(n+4-j)}{(n+3)} \tag{2.11}$$

where ${}^h\bar{\alpha}_{nm}$ are the spherical harmonic coefficients of shape raised to the power h. The first term in this expansion corresponds to the mass sheet approximation. Eq. 2.11 involves computation of the spherical harmonic coefficients of powers of topography. Although, the maximum power of topography needed is equal to $(n+3)$, where n is the degree of the gravity field expansion, we truncate the power of topography whose contribution to the gravitational field is less than the formal uncertainty in the gravity model. The terms with $h > 1$ in 2.11 are referred to as finite-amplitude correction (Wieczorek and Phillips, 1998). These terms become progressively important for highly non-spherical bodies and for high n.

2.4.3 Multilayer structures

Given the shape of internal interfaces, the gravity coefficients of a body can be computed as a weighted sum of the gravity coefficients of its component parts as

$$\bar{\sigma}_{nm} = \frac{\sum_{i=0}^{N} \bar{\sigma}_{nm}^{i} V_i \Delta\rho_i}{\sum_{i=0}^{N} V_i \Delta\rho_i}, \tag{2.12}$$

where i spans from 0 to N representing the layers within the body such as core, mantle and crust; V_i is the volume. For the case of a three-layer body, $\Delta\rho_0$ is the crustal density, $\Delta\rho_1$ is the crust-mantle density contrast and $\Delta\rho_2$ is the mantle-core density contrast (e.g. Ermakov et al., 2014; Park et al., 2014b). In our analysis of interior structure for Vesta and Ceres (Section 3.3.2 and Section 6.3.3, respectively), we will model the internal interfaces as triaxial ellipsoids to a first-order approximation. The degree-two coefficients of a triaxial ellipsoid with axes take the form (Balmino, 1994):

$$C_{20} = \frac{1}{5R_0^2}\left(c^2 - \frac{a^2+b^2}{2}\right), \tag{2.13}$$

$$C_{22} = \frac{1}{20R_0^2}\left(a^2 - b^2\right), \tag{2.14}$$

where a, b and c are the semiaxes of the ellipsoid aligned with the coordinate axes. In this case, the reference radius R_0 is equal to $(3/(a+b+c))^{1/2}$. Equations (2.13-2.14) are used to compute gravitational moments of the core and the mantle assuming an ellipsoidal shape. The coefficients with $n+m =$ odd are equal to zero because of the ellipsoidal symmetry.

2.4.4 Admittance and correlation

Admittance (Z) is a transfer function between gravity and topography. Admittance is defined as a function of spherical harmonics degree n. In this case, we refer to it as the admittance spectrum Z_n.

$$Z_n = \frac{\sqrt{S_n^{gg}}}{\sqrt{S_n^{tt}}} \tag{2.15}$$

It is a useful quantity because it depends on the state of isostatic compensation of topography. Therefore, it is possible to compute the admittance spectrum given a model of internal structure and compare it with the observed admittance spectrum. However, if either gravity or topography is not noiseless, Eq. 2.15 will give biased results. McKenzie (1994) shows that for the case where noise is primarily in the gravity model, the unbiased estimate of admittance will be:

$$Z_n = \frac{S_n^{gt}}{S_n^{tt}}, \tag{2.16}$$

where S_n^{gt} is the cross-power of gravity and topography. On the other hand, if the noise is primarily in the shape model, the unbiased admittance estimated is:

$$Z_n = \frac{S_n^{gg}}{S_n^{gt}} \tag{2.17}$$

If both gravity and topography have substantial noise, it is not possible to derive an unbiased estimate of admittance. For planetary applications, typically there is much more noise in the gravity model compared to topography. In other words, it is much easier to derive a shape model than a gravity model for a given resolution.

Since the spherical harmonic coefficients as defined in 2.1-2.2 are dimensionless, the admittance is so as well. To give admittance units of mGal/km, Z_n is multiplied by $(n+1)GM/R^3$:

$$Z_n = \frac{S_n^{gt}}{S_n^{tt}} \cdot \frac{GM}{R^3}(n+1) \tag{2.18}$$

The gravity-topography correlation spectrum is defined as:

$$R_n^{gt} = \frac{S_n^{gt}}{\sqrt{S_n^{tt} S_n^{gg}}} \tag{2.19}$$

The correlation spectrum is always between -1 and 1. For highly oblate bodies such as Vesta or Ceres or irregularly shaped bodies, the relationship between the shape and

the gravity coefficients becomes nonlinear (Wieczorek and Phillips, 1998; Balmino, 1994). Therefore, for a highly non-spherical body, even if it is homogeneous, the correlation coefficient between gravity and topography is not equal to unity. For such bodies it is more useful to compute the correlation between gravity and gravity induced by the shape:

$$R_n^{gg'} = \frac{S_n^{gg'}}{\sqrt{S_n^{gg} S_n^{g'g'}}}, \tag{2.20}$$

where $S_n^{g'g'} = \sum_{m=0}^{n} \left(\bar{\sigma}_{nm}^{shape}\right)^2$ and $S_n^{gg'} = \sum_{m=0}^{n} \bar{\sigma}_{nm} \bar{\sigma}_{nm}^{shape}$.

Another similar quantity called coherence is defined as $(R_n^{gt})^2$.

2.4.5 Isotropic ratio

The isotropic ratio introduced in Bills and Lemoine (1995) is a measure of directional isotropy of the variance. The mean squared North-South and East-West slopes are defined as follows:

$$S^{NS} = \frac{1}{4\pi} \int_{\Omega} \left(\frac{\partial U}{\partial s}\right)_{\phi}^2 d\Omega, \tag{2.21}$$

$$S^{EW} = \frac{1}{4\pi} \int_{\Omega} \left(\frac{\partial U}{\partial s}\right)_{\lambda}^2 d\Omega \tag{2.22}$$

Subscripts denote differentiation with respect to the corresponding spherical coordinate. As shown in Bills and Lemoine (1995), these integrals can be solved:

$$S_n^{NS} = \sum_{m=0}^{n} \left(n(n+1) - \frac{(2n+1)m}{2}\right) \left(\bar{C}_{nm}^2 + \bar{S}_{nm}^2\right), \tag{2.23}$$

$$S_n^{EW} = \sum_{m=0}^{n} \left(\frac{(2n+1)m}{2}\right) \left(\bar{C}_{nm}^2 + \bar{S}_{nm}^2\right), \tag{2.24}$$

The isotropy coefficient is the ratio of the North-South to the East-West mean squared slopes.

$$I_n = \frac{S_n^{NS}}{S_n^{EW}} \tag{2.25}$$

If the isotropic coefficient is greater than unity, the given field has more North-South variations, if the isotropic coefficient is less than unity the field has more variations in the East-West direction. An isotropic field is expected to have the isotropic ratio of unity.

2.4.6 Crustal thickness inversion

The shape of the mantle-crust interface and crustal thickness can be computed by minimizing the power of the residual anomaly (Wieczorek and Phillips, 1998) as

$$\bar{\alpha}'_{nm} = w_n \left(\frac{\bar{\sigma}_{nm}^{BA} M(2n+1)}{4\pi\Delta\rho(D')^2} \left(\frac{R_0}{D'} \right)^n - D' \sum_{h=2}^{n+3} \frac{{}^h\bar{\alpha}'_{nm} \prod_{j=1}^{h}(n+4-j)}{(D')^h h!(n+3)} \right), \tag{2.26}$$

where $\bar{\alpha}'_{nm}$ are the normalized coefficients of the crust-mantle interface, D' is the mean radius of the crust-mantle interface, $\Delta\rho$ is the crust-mantle density contrast and $\bar{\sigma}_{nm}^{BA}$ are the normalized spherical harmonic coefficients of the residual anomaly, D' is the zeroth order coefficient (mean radius) of the crust-mantle interface. The parameter is found as we expand the initial ellipsoidal shape of the crust-mantle interface in spherical harmonics. The first term in equation (2.26) can be computed directly using the residual anomaly coefficients; the second term should be computed iteratively. In the first iteration, the crust-mantle interface coefficients $\bar{\alpha}'_{nm}$ can be computed assuming an ellipsoidal shape of the interface that was derived before from mass balance and matching second-degree terms. The solution for the crust-mantle interface is not unique and depends on the assumed density contrast. As a result, the gravity data alone cannot be used to determine the mean crustal thickness.

In order to mitigate errors in the downward continuation of the residual anomaly, a low-pass filter should be applied (Wieczorek and Phillips, 1998):

$$w_n = (1 + \lambda K_n^2)^{-1}, \tag{2.27}$$

where $K_n = \left(\frac{M(2n+1)}{4\pi\Delta\rho(D')^2} \cdot \left(\frac{R_0}{D'}\right)^n\right)^2$. To find the filter parameter λ, we introduce a critical degree n_c defined as the degree at which $w_n = 0.5$, in which case we find $\lambda = K_n^{-2}$.

2.5 Spectral-spatial localization on a sphere

Wieczorek and Simons (2005); Simons and Dahlen (2006); Simons (2010) present an approach to locally estimate the spectral characteristics using Slepian functions that are both spatially and spectrally limited. The spherical harmonic expansion coefficients of the Slepian functions of a bandwidth L are found by maximizing the power in region R and spectral band L.

$$\lambda_1 = \frac{||g||_R^2}{||g||_\Omega^2} = \frac{\int_R g^2 d\Omega}{\int_\Omega g^2 d\Omega} \tag{2.28}$$

$$\lambda_2 = \frac{||g||_L^2}{||g||_\infty^2} = \frac{\sum_{l=0}^{L}\sum_{n=0}^{l} h_{lm}^2}{\sum_{l=0}^{\infty}\sum_{n=0}^{l} h_{lm}^2} \tag{2.29}$$

where λ_1 and λ_2 – the spectral power concentration factors – are sought to be maximized; Ω is the sphere. Simons and Dahlen (2006) presents a way to find λ_1 and λ_2 as a solution to an eigenvalue problem and shows that they are identical for harmonic degrees less than the bandwidth L. The resulting spectral-spatial tapers are called Slepian tapers.

2.6 Ellipsoid fitting

Figures of hydrostatic equilibrium can be approximated as ellipsoids. It is also instructive to fit the body's shape model with an ellipsoid to get a general sense of the body's asphericity. A general conic section is defined by:

$$f(x,y,z) = A_e x^2 + B_e y^2 + C_e z^2 + 2D_e xy + 2E_e xz + 2F_e yz + 2G_e x + 2H_e y + 2I_e z \quad (2.30)$$

$$f(x,y,z) = 1 \quad (2.31)$$

under the condition that $D_e^2 < 4A_eB_e$, $E^2 < 4A_eC_e$ and $F_e^2 < 4B_eC_e$. We can use this algebraic equation to derive a method of ellipsoid fitting in the least-squared sense. A general ellipsoid has nine degrees of freedom: three axes, three coordinates of the ellipsoid center and three orientation angles. The sensitivity matrix S is defined as:

$$S = \left\{ \left.\frac{\partial f(x,y,z)}{\partial A_e}\right|_{\{x,y,z\}=\{x_i,y_i,z_i\}}, \cdots, \left.\frac{\partial f(x,y,z)}{\partial I_e}\right|_{\{x,y,z\}=\{x_i,y_i,z_i\}} \right\}. \quad (2.32)$$

We can find the correction vector using least-squares as:

$$v = (S^T S)^{-1} S^T Q, \quad (2.33)$$

where v is a set of the algebraic coefficients $\{A_e, B_e, \cdots, I_e\}$ and Q is the vector of residuals, $Q = f(x,y,z) - 1$. It is possible to recover the ellipsoidal axes, ellipsoid center offsets and orientation from v (Gander et al., 1995).

2.7 Gravity gradients

Gravity gradients are second derivatives of the gravitational potential (Andrews-Hanna et al., 2013). They form the Eötvös tensor $\mathbf{E}$:

$$\mathbf{E} = \begin{pmatrix} U_{xx} & U_{xy} & U_{xy} \\ U_{yx} & U_{yy} & U_{yz} \\ U_{zx} & U_{zy} & U_{zz} \end{pmatrix}. \quad (2.34)$$

If the Eötvös tensor is computed in the local North-East-Up system, where x-axis is directed towards North, y-axis toward East and z-axis towards Up, the components of the Eötvös tensor take the following form (Petrovskaya and Vershkov, 2006):

$$\begin{aligned} U_{zz} &= U_{rr} \\ U_{xx} &= \tfrac{1}{r}U_r - \tfrac{1}{r^2}U_{\phi\phi} \\ U_{yy} &= \tfrac{1}{r}U_r - \tfrac{1}{r^2\cot\phi}U_\phi + \tfrac{1}{r^2\cos^2\phi}U_{\lambda\lambda} \\ U_{xy} &= -\tfrac{1}{r^2\cos\phi}U_{\phi\lambda} - \tfrac{\sin\phi}{r^2\cos^2\phi}U_\lambda \\ U_{xz} &= -\tfrac{1}{r^2}U_\phi + \tfrac{1}{r}U_{r\phi} \\ U_{yz} &= \tfrac{1}{r^2\cos\phi}U_\lambda - \tfrac{1}{r\cos\phi}U_{r\lambda} \end{aligned}, \tag{2.35}$$

where subscripts denote differentiation of potential with respect to spherical or local cartesian coordinates. The Eötvös tensor is symmetric and the sum of the second derivatives of potential is zero. Therefore, there are only five independent components of the Eötvös tensor. We introduce the horizontal Eötvös tensor, which contains derivatives only with respect to the horizontal coordinates x and y.

$$\mathbf{E}_h = \begin{pmatrix} U_{xx} & U_{xy} \\ U_{xy} & U_{yy} \end{pmatrix}, \tag{2.36}$$

Since this tensor is symmetric, its eigenvalues λ_1 and λ_2 can be easily found to be:

$$\begin{aligned} \lambda_1 &= \tfrac{1}{2}\left(U_{xx} + U_{yy} - \sqrt{U_{xx}^2 + U_{yy}^2 + 4U_{xy}^2 - 2U_{xx}U_{yy}}\right) \\ \lambda_2 &= \tfrac{1}{2}\left(U_{xx} + U_{yy} + \sqrt{U_{xx}^2 + U_{yy}^2 + 4U_{xy}^2 - 2U_{xx}U_{yy}}\right) \end{aligned} \tag{2.37}$$

We also introduce the maximum amplitude eigenvalue λ_{max}:

$$\lambda_{max} = \begin{cases} \lambda_1, & |\lambda_1| \geq |\lambda_2| \\ \lambda_2, & else \end{cases}. \tag{2.38}$$

The maximum amplitude eigenvalue λ_{max} represents the second horizontal derivative of maximum amplitude. For a linear gravity anomaly, λ_{max} will represent the gravity gradient orthogonal to the direction of this structure.

List of variables

Variable	Definition	Variable	Definition
a, b, c	ellipsoidal axes	S	Sensitivity matrix
A, B, C	principal moments of inertia	S_n^{gg}	gravity power
$\bar{A}_{nm}$, $\bar{B}_{nm}$	normalized spherical harmonic coefficients of shape	S_n^{gt}	gravity-topography cross-power
A_e,..., I_e	coefficients in the algebraic formula for an ellipsoid	S_n^{tt}	topography power
$\bar{C}_{nm}$, $\bar{S}_{nm}$	normalized spherical harmonic coefficients of gravity	S^{NS}, S^{EW}	mean squared North-South and East-West slopes
D'	zeroth order coefficient (mean radius) of the crust-mantle interface	U_{tot}	total potential of a hydrostatic layered body
$\mathbf{E}$	Eötvös tensor	U_{ell}	potential of an ellipsoid
f_p	flattening factor	U_{rot}	rotational potential
I_n	isotropic ratio	U_{xx}, ..., U_{zz}	second derivatives of potential
L	bandwidth	w_n	Bouguer anomaly filter
m	order	Z_n	admittance
M	body's mass	α_{nm}, $\bar{\alpha}_{nm}$	$\{A_{nm}, B_{nm}\}$, $\{\bar{A}_{nm}, \bar{B}_{nm}\}$
M_n^{gg}	power spectral density (PSD) of gravity	${}^h\bar{\alpha}_{nm}$	normalized spherical harmonic coefficients of topography raised to h-th power
M_n^{tt}	power spectral density (PSD) of topography	Δ^2	sum of squared potential differences
n	degree	λ	longitude
n_c	critical degree	λ_1, λ_2	eigen values of the horizontal Eötvös tensor
r	radius	λ_{max}	maximum amplitude eigen value of horizontal Eötvös tensor
R	mean radius	σ_{nm}, $\bar{\sigma}_{nm}$	$\{C_{nm}, S_{nm}\}$, $\{\bar{C}_{nm}, \bar{S}_{nm}\}$
R_n^{gt}	correlation between gravity and topography	ϕ	latitude
$R_n^{gg'}$	correlation between gravity and gravity-from-topography	ω	rotation rate
R_0	reference radius		

Table 2.1 – List of the main variables used in the chapter.

Chapter 3

Constraints on Vesta's interior structure using gravity and shape models from the Dawn missions

Published as: Ermakov, A.I., M.T, Zuber, D.E. Smith, C.A. Raymond, G. Balmino, R.R. Fu and B.A. Ivanov, Constraints on Vesta's interior structure using gravity and shape models form the Dawn mission, Icarus, 240, doi: 10.1016/j.icarus.2014.05.015, 146-160, 2014.

Abstract

Vesta is a differentiated asteroid as confirmed by gravity and spectroscopy measurements from the Dawn mission. We use the shape and gravity field of Vesta determined from observations of the Dawn spacecraft to develop models of the asteroid's interior structure. We compute a three-layer interior structure model by minimizing the power of the residual gravity anomaly. The densities of the mantle and crust are based on constraints derived from the Howardite-Eucrite-Diogenite (HED) meteorites.

Vesta's present-day shape is not in hydrostatic equilibrium. The Rheasilvia and Veneneia impact basins have a large effect on Vesta's shape and are the main source of deviation from hydrostatic shape. Constraining a pre-giant-impact rotation rate and orientation of the spin axis from an ellipsoidal fit to the parts of Vesta unaffected by the giant impacts, and using the theory of figures, we can constrain the shape of the core.

Our solution for Vesta's crust-mantle interface reveals a belt of thick crust around

Rheasilvia and Veneneia. The thinnest crust is in the floor of the two basins and in the Vestalia Terra region. Our solution does not reveal an uplift of the crust-mantle boundary to the surface in the largest basins. This, together with the lack of olivine detected by the Visible and Infrared Spectrometer (VIR) data in Rheasilvia and Veneneia, indicates that Vesta's presumed olivine mantle was either not brought to the surface by these large impacts or was covered by ejecta from subsequent impacts.

3.1 Introduction

Asteroid 4 Vesta resides in the inner region of the main asteroid belt, and is the second largest object by mass and third largest object by volume in the main belt. With its high albedo, it is the only asteroid that can be observed by naked eye from Earth. Telescopic observations revealed some characteristic properties of Vesta such as large-scale albedo variations as early as in 1929 (Bobrovnikoff, 1929). Spectroscopic observations pointed to a possible connection between Vesta and the Howardite–Eucrite– Diogenite (HED) meteorites (McCord et al., 1970) that allowed geochemical studies of Vesta's internal structure and composition (e.g., Ruzicka et al. (1997)).

Radiometric dating of the HED meteorites suggests that Vesta formed within 3 My of Solar System formation (Lugmair and Shukolyukov, 1998). Its large size and primordial basaltic crust indicates that it is a relatively intact survivor from the accretion phase of the Solar System (Russell et al., 2012). As such, the NASA Dawn mission (Russell et al., 2004; Russell and Raymond, 2011) was launched in 2007 to orbit the asteroids Vesta and Ceres in an effort to understand the accretion process of the Solar System via the composition and structure of earlyforming planetesimals.

In this paper we use the shape model constructed using images from Dawn's Framing Camera (FC) and the gravity model determined by radio tracking the spacecraft to place constraints on Vesta's internal structure and composition. The gravity models were produced by the Dawn gravity team at the Jet Propulsion Laboratory (JPL) (Konopliv et al., 2014a). The shape models of Vesta were produced independently by two research groups that employed different techniques: the German Aerospace Center (DLR) group using stereophotogrammetry (Jaumann et al., 2012) and Robert

Gaskell at the Planetary Science Institute (PSI) using stereophotoclinometry (Gaskell, 2012). We will refer to these methods as SPG and SPC, respectively.

This chapter is organized as follows: In Section 3.2.1 we describe the main properties of Vesta's shape in the space and frequency domains. Section 3.3.1 is devoted to the concept of hydrostatic equilibrium. Here, the effect of the impact basins on the flattening factor of Vesta, and the possibility of despinning and reorientation of Vesta due to giant impacts is discussed. In Section 3.3.2 we use the constraints from the observed shape, gravity field and HED meteorites to study the interior structure of Vesta. We discuss implications of our results on interior structure modeling and future research directions in Section 3.4. Results are summarized in Section 3.5.

3.2 Data

3.2.1 Shape models of Vesta

The shape model of Vesta as well as the spin vector orientation and rotation rate were obtained by Cellino et al. (1987) using photometric data, by Drummond et al. (1988), followed by Drummond and Hege (1989) using speckle interferometry and by McCarthy et al. (1994) using infrared speckle observations. The most accurate pre-Dawn estimate was made using Hubble Space Telescope (HST) observations Thomas et al. (1997). The HST shape model of Vesta can be approximated by a triaxial ellipsoid with semiaxes 280, 272 and 227 ($\pm$12) km. The HST data first revealed the large-scale topographic features on Vesta, specifically a basin of probable impact origin near the south pole that has since been named Rheasilvia. The HST shape model aided in estimating the illumination conditions on Vesta for the Dawn mission (Stubbs and Wang, 2011).

The Framing Camera (FC) onboard the Dawn spacecraft has permitted an improved determination of the shape of Vesta (Sierks et al., 2011). A shape model produced using SPC (Gaskell, 2012) is based on 17409 images from the FC and has a formal global vector position uncertainty of 26 m with respect to the center of mass

(Gaskell, personal communication). However, comparison of SPC and SPG-based (Preusker et al., 2012; Jaumann et al., 2012) shape models show systematic differences on the order of a few hundreds of meters, with greater discrepancies observed in deep craters. We consider the mismatch of the models to be a truer estimate of the uncertainty in the shape than the formal errors in either model. The uncertainty in the radius vector is not uniform because of poorer illumination conditions in the north. The radius vector ranges from 211.9 km to 292.8 km, with mean radius equal to 260.3 km. Thus, the range of topography is equal to 31% of the mean radius which is nearly two orders of magnitude larger compared to the highest topographic variation on the terrestrial planets (Wieczorek, 2007b). The topography ranges from -19.4 to +22.5 km with respect to the best-fit rotational ellipsoid centered at the center of mass.

The gridded shape model is produced with a resolution of 1/64 degree, which formally allows expansion up to spherical harmonic degree 11560. However, one must exercise extreme caution with such ultra-high order expansions because of the non-uniformity of the shape model's uncertainty and possible aliasing at short wavelengths. The topography power spectrum (Fig. 3-1) shows that the spectral slope of Vesta's topography is distinct from topographic spectra of the terrestrial planets (Wieczorek, 2007b). The power of Vesta's topography is higher at all wavelengths than that of the terrestrial planets, indicating rougher terrain at all scales, attributable to lower gravity and, at least in part, to the absence of weathering. The fractal dimension D of Vesta's topography on scales 10^1 – 10^3 km is approximately equal to 1.28. For Brownian noise topography the parameter $D = 1.5$ (Turcotte, 1987). The slope of the topography power is steeper at smaller wavelengths than at longer wavelengths.

The shape model can be fit by a rotational ellipsoid with semi-axes 280.9 and 226.2 km with the origin at the center of mass of the body. We use this ellipsoid as a reference surface for topography. The best-fit ellipsoid is found by minimization of the sum of the squares of the ellipsoidal heights. We also compute a more general ellipsoid fit for the shape model of Vesta. The general problem has 9 degrees of

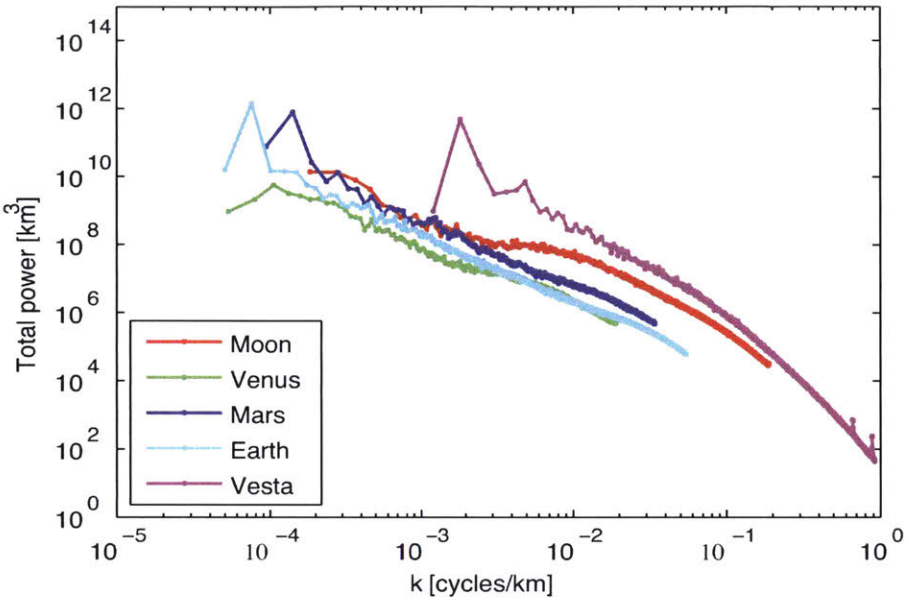

Figure 3-1 – Topography power spectra of Vesta and the terrestrial planets. The spikes at the shortest wavelengths for Vesta are numerical artefacts due to aliasing.

freedom: three axes, three angles that define the ellipsoid's orientation and three coordinates of the ellipsoid's center (Bertoni, 2010; Fu et al., 2014). We use a shape model (Gaskell, 2012) that is based on images from all stages of the Dawn mission including the northern hemisphere, that was not available in earlier shape models because of poor illumination conditions. Ellipsoid parameters estimated using the method of least squares are given in Tables 3.1 and 3.2. The range of topography in the undamaged northern part of Vesta with respect to the fossil (northern) ellipsoid is $\approx$ 20 km, which is approximately two times smaller that the global topography range with respect to the global ellipsoid. This indicates that the northern terrains are much closer to ellipsoidal shape and hydrostatic equilibrium.

3.2.2 Gravity models of Vesta

The gravitational field model of Vesta up to degree 20 was determined by radio tracking of the Dawn spacecraft (Konopliv et al., 2014a). The corresponding spatial resolution is $\approx$ 41 km. The gravity field power spectrum, error power spectrum and

Shape model	Semiaxes			Center of ellipsoid offset			Polar flattening
	a(km)	b(km)	c(km)	Δx	Δy	Δz	
SPC global shape (Gaskell, 2012)	284.895	277.431	226.838	0.151	1.177	0.134	0.1931
Northern shape (Fu et al., 2014)	280.61 ± 0.15	274.63 ± 0.10	236.77 ± 0.17	0.83 ± 0.15	0.20 ± 0.14	5.66 ± 0.18	0.1471 ± 0.0007

Table 3.1 – Best-fit ellipsoid dimensions. For the northern ellipsoid, standard deviations of the parameters are shown.

Shape model	Planetocentric coordinates of the axes		
	a	b	c
SPC global shape (Gaskell, 2012)	$\lambda = 40.5°$	$\lambda = -49.5°$	$\lambda = 65.2°$
	$\phi = 0.7°$	$\phi = 0.3°$	$\phi = 89.3°$
Northern shape (Fu et al., 2014)	$\lambda = 17.34° \pm 0.15°$	$\lambda = 107.30° \pm 0.60°$	$\lambda = -177.26° \pm 2.48°$
	$\phi = 2.91° \pm 0.15°$	$\phi = -0.75° \pm 0.10°$	$\phi = 87.00° \pm 0.14°$

Table 3.2 – Best-fit ellipsoid orientation in the Claudia system. Note that the polar axis of the northern shape deviates from the rotation axis of Vesta by 3.0. For the northern ellipsoid, standard deviations of the parameters are shown.

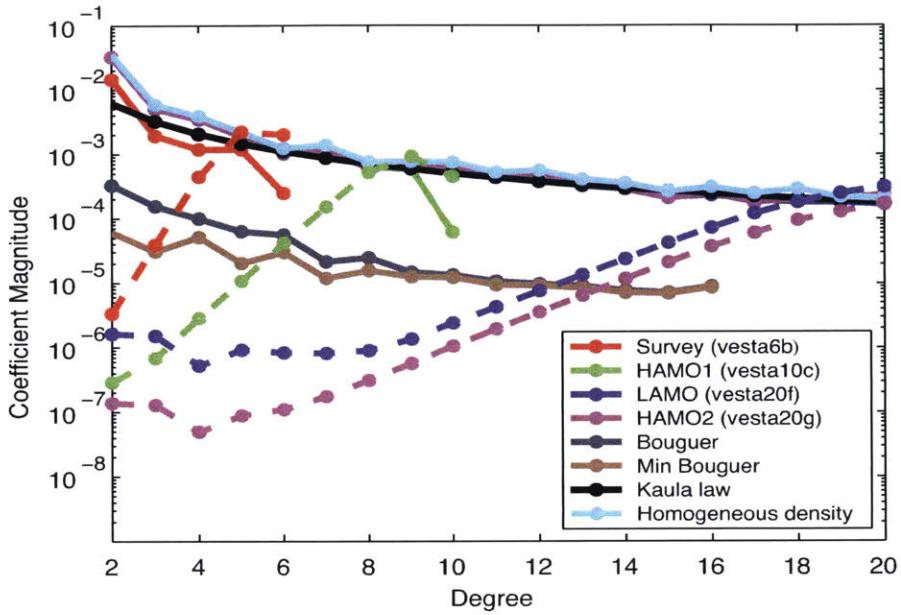

Figure 3-2 – Power spectra of different gravity models. The dashed lines show error spectra of the corresponding gravity models. The power of the residual gravity is about two orders of magnitude smaller than total gravity power. The power of the minimized residual anomaly ("Min Bouguer" on the legend) is shown in solid brown. For explanation of different orbits see Table 4.1.

the residual anomaly spectrum (see Section 3.3.2) are shown in Fig. 3-2. Analysis of Dawn's gravity and shape shows strong positive correlation between the geoid and topography (Fig. 3-3). The geoid height was calculated with respect to the ellipsoid that best approximates the equipotential surface. The reference ellipsoid size and potential on the geoid were chosen to satisfy three criteria: 1) the ellipsoid should be close to the surface, so that the amplitude of the anomalies is high; 2) the divergence of the spherical harmonic series should not produce artifacts when residual anomalies are plotted on the ellipsoid, in other words the divergence should be smaller than the errors in the gravity field model; and 3) the ellipsoid should be a least-squares approximation of a local equipotential surface. The ellipsoid axes are 293.2 km and 266.5 km. This ellipsoid will be used as a reference surface for the residual anomaly later in the paper.

A gravitational slope is the angle between the inward-pointing surface normal

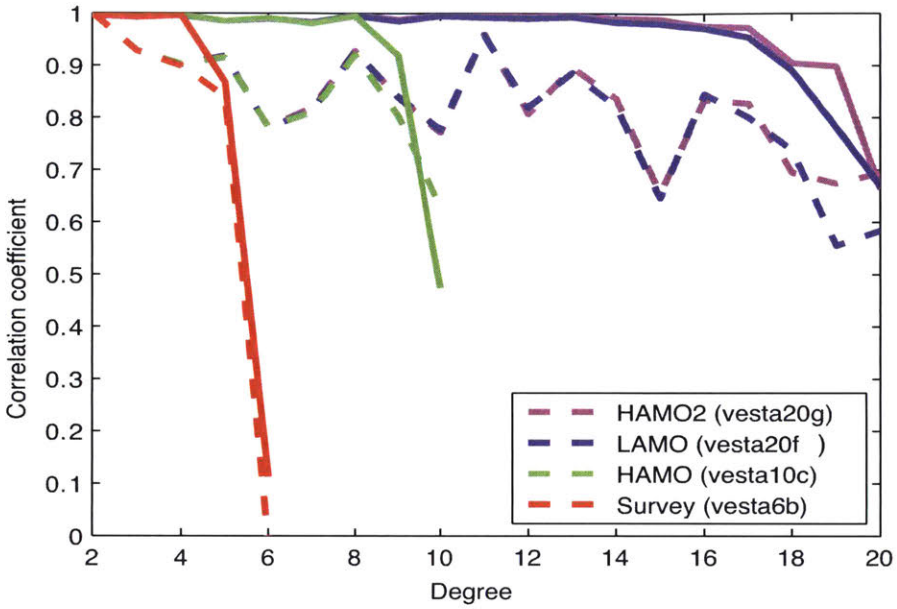

Figure 3-3 – Correlation between observed gravity and topography (dashed lines) between observed gravity and gravity induced by the homogeneous density shape (solid lines).

and the gravitational acceleration vector. If the gravity field is known, gravitational slopes can be computed (Tricarico, 2012). However, the divergence of the spherical harmonic expansion does not allow computation of the gravitational acceleration vector directly on the surface. Using the derived interior structure model (Section 3.3.2), we can compute gravitational acceleration by numerical integration at any point. The gravitational acceleration on Vesta surface ranges from 0.23 to 0.27 m/s^2. The centrifugal contribution is -0.03 m/s^2 at the equator. Computed slopes and the corresponding distribution are shown in Figs. 3-4 and 3-5, respectively. The maximum slope is $\approx 40°$, which is consistent with studies on the angle of repose of non-cohesive material with angular grains in reduced gravity environment (Kleinhans et al., 2011). Statistically, higher slopes are found in the southern hemisphere in the Rheasilvia basin. The main source of uncertainty in the computed slopes comes from the crust-mantle interface. By varying the critical degree n_c (see Section 2.4.6), we estimate that the global slope uncertainty is 1.4°. Note that in calculating the gravitational slope we used a high-resolution shape model but a low-resolution gravity field.

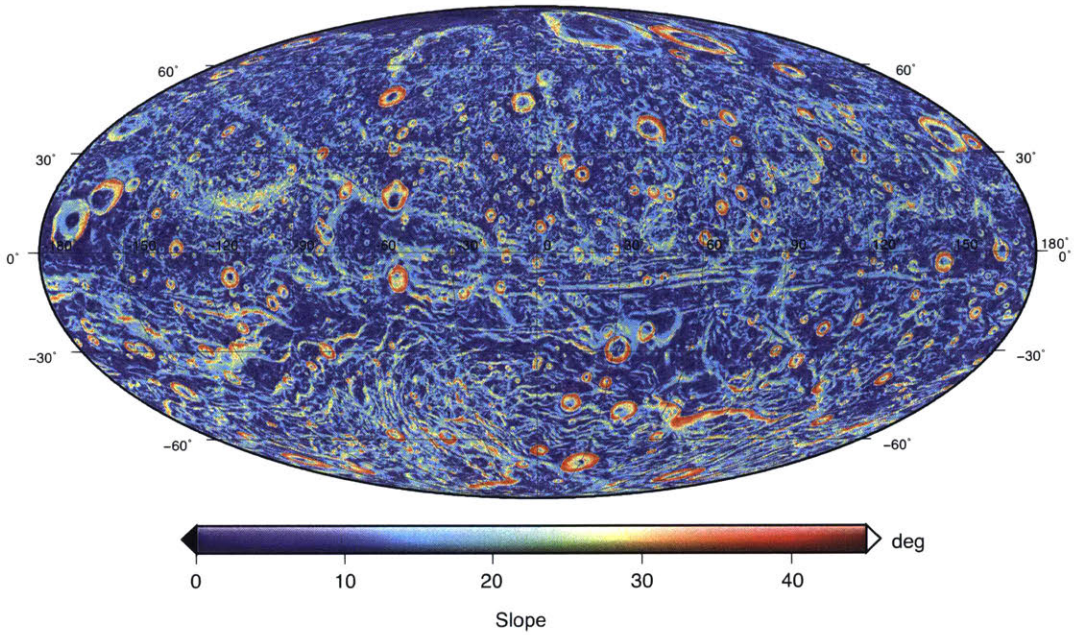

Figure 3-4 – Vesta gravitational slopes based on the computed interior structure model. The regions close to the North Pole appear to have lower slopes because of lower resolution due to poor illumination conditions.

Vesta possesses a significant center of mass – center of figure (COM-COF) offset (Russell et al., 2012). The offset vector lies surprisingly precisely in the equatorial plane of Vesta. The Z-component of the offset is only 2.5 meters. The XY component is equal to 1.44 km (Konopliv et al., 2014a) and is aligned approximately in the direction of Vestalia Terra, the highest point of the shape model. This, in combination with a strong gravity high, suggests that Vestalia Terra may have formed prior to the Rheasilvia and Veneneia basins.

3.2.3 Gravity from shape

We compute gravity-from-shape spherical harmonic coefficients $\bar{\sigma}_{nm}^{shape}$ as detailed by Wieczorek and Phillips (1998), where gravitational coefficients are expanded in a series of powers of shape. We find that due toVesta's significant non-sphericity eight terms need to be retained in Eq. 2.11 to compute gravity from shape with an accuracy matching the accuracy of the observed gravity (Fig. 3-6).

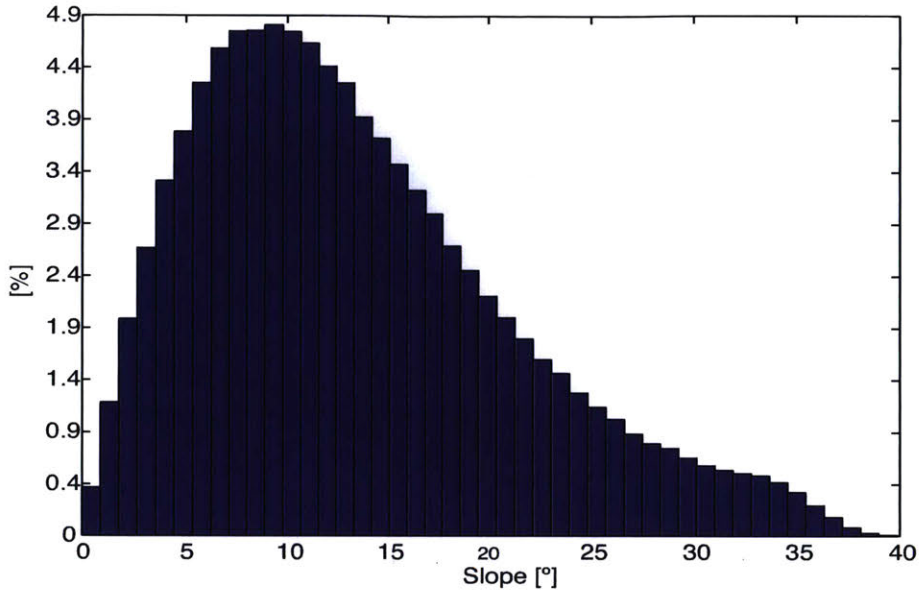

Figure 3-5 – Global distribution of slopes on Vesta. Mean slope is 13.5°. Median slope is 12.1°.

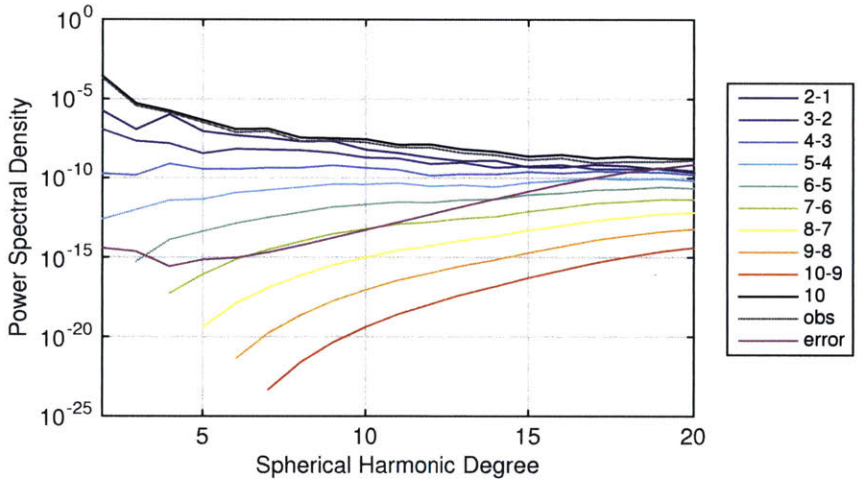

Figure 3-6 – Power spectral density contributions from the powers of topography. We show the power spectral density of the difference of the two gravity-from-shape expansion in which h and $h+1$ powers of topography were kept. Additionally, we show in black the power of the gravity-from-shape for $\max(h) = 10$. The grey curve is the power spectrum from the 20 degree JPL gravity model (JGV20G02) and the magenta curve is the error power spectrum of that model.

3.3 Results

3.3.1 Hydrostatic equilibrium

Given the shape, gravity field and rotation rate we can estimate the extent to which Vesta is currently in a state of hydrostatic equilibrium. We numerically compute the hydrostatic equilibrium figure of a three-layer Vesta by numerically minimizing the sum of potential differences squared (Equation 3.1) at the pole and at the equator of the internal interfaces. The method is described in Tricarico (2014).

$$\Delta^2 = \sum_{i=1}^{3} [U(0,0,c_i) - U(a_i,0,0)]^2 , \tag{3.1}$$

where $U(x,y,z)$ is the potential of a two-axial ellipsoid (see appendix A and B Tricarico (2014) for analytical expressions of potential), i runs from 1 to 3 representing the core-mantle, mantle-crust interfaces and the outer surface of Vesta. By fixing the volumes of the three layers, which gives a relationship between the semimajor axis a_i and semiminor axis c_i, we find the flattening factors $f_i = (a_i - c_i)/a_i$ that minimize Δ^2 . We explicitly assume in the expression for the gravitational potential that Vesta hydrostatic figures are ellipsoids of rotation.

The rotation period needed to make Vesta's present shape hydrostatic is 4.3 hours (Fig. 3-7); the present rotation period is 5.3 hours. This poses a problem in defining the geodetic reference surface for Vesta. The asteroid is too oblate for its rotation rate; therefore the equipotential surface will not follow the surface of Vesta. The reference-ellipsoid that approximates the equipotential surface and minimizes geoid heights of the terrain in a least-squares sense would be less oblate than the best-fit shape ellipsoid.

Vesta underwent significant melting during its early history that led to the formation of a basaltic crust (McCord et al., 1970). The extensive interior melting implies that early Vesta had a thin lithosphere, defined as the near-surface region where viscous relaxation does not occur on geologic timescales. Due to its low gravity, elastic deformation in this lithosphere is negligible. Significant relaxation of Vesta towards a

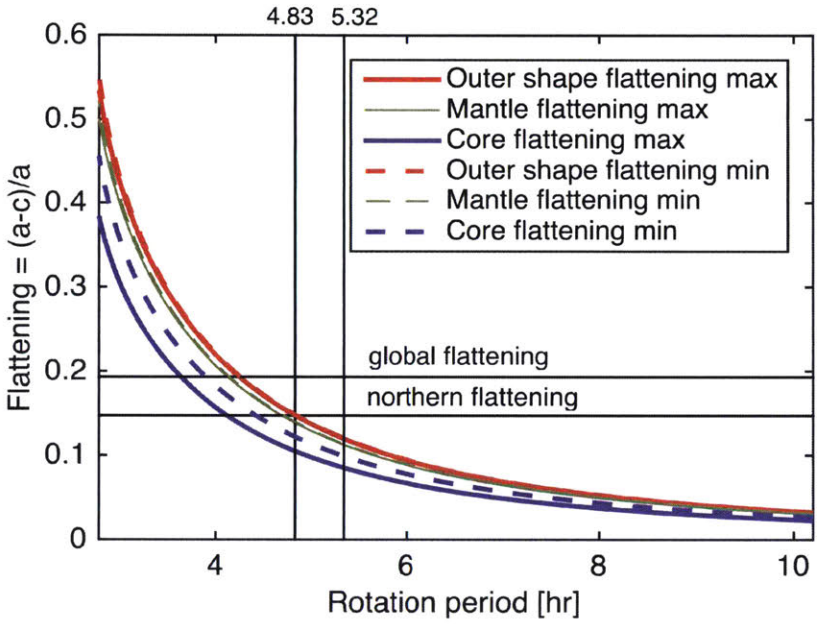

Figure 3-7 – Hydrostatic flattening of Vesta outer shape, mantle–crust and core–mantle interfaces. Two vertical lines show Vesta's current rotation period (5.342 h) and presumed pre-impact rotation period (4.83 h). The core has a density of 7800 kg/m^3 and a radius of 110 km for the maximum differentiation case and 6000 kg/m^3 and 135 km, respectively, for the minimum differentiation case. The crust has a density of 2700 kg/m^3. Crustal thickness is equal to 40 km.

more hydrostatic figure is only possible in the case of prevalent fracturing in the lithosphere leading to plastic behavior of the lithosphere (see also Johnson and McGetchin, 1973).

Finite element simulations of the early vestan lithosphere show that sufficient stresses existed in cases of substantial deviation from the hydrostatic state to cause extensive plasticity in the lithosphere and efficient hydrostatic relaxation (Fu et al., 2014). Relaxation to figures more hydrostatic than the present figure of Vesta ($f - f_{eq} = 0.065$) was possible within at least 40 My after the shut down of mantle convection (Fu et al., 2014), which likely occurred within $\approx$1 to a few My of the formation of Vesta (Sterenborg and Crowley, 2013). Inclusion of a thick (5-km) megaregolith extends this window of efficient hydrostatic relaxation to 200 My. After these times, Vesta effectively did not relax further. Higher degrees of hydrostatic equilibrium ($f - f_{eq} = 0.020$) were possible within the first 15 My after convective shut down (80 My assuming 5-km megaregolith). The deep interior reached temperatures that correspond to very low viscosities for both olivine-rich silicates and sulfur-bearing metal ($<10^{19}$ Pa$\cdot$s; Ghosh and McSween (1998); Hirth and Kohlstedt (1996); Dobson et al. (2000)); therefore, the early vestan core also approached closely to hydrostatic equilibrium. Due to the slow cooling of the interior, the shape of the core was frozen in at a later time than the outer shape.

In summary, during its early history, both the outer shape and the core mantle boundary of Vesta likely achieved figures close to hydrostatic equilibrium ($f - f_{eq} < 0.020$). The major impact events such as Rheasilvia and Veneneia are thought to have occurred much later in the history of Vesta (Schenk et al., 2012a; Marchi et al., 2012). These events affected the shape of Vesta and could have possibly changed its rotation rate and the orientation of the spin axis (Matsuyama and Nimmo, 2011; Fu et al., 2014). However, the asteroid would not have viscously relaxed from these late events since they occurred when Vesta was much cooler.

The Rheasilvia basin in the southern hemisphere has a significant effect on the global shape of Vesta. Rheasilvia makes the apparent shape of Vesta more oblate and changes the COM-COF offset. The hydrocode modeling of the Rheasilvia and

Veneneia impacts (Ivanov and Melosh, 2012, 2013) shows that the northern shape is not affected by the corresponding impacts and, consequently, is a reliable representation of Vesta's fossil shape. Eliminating regions south of the belt of high crustal thickness due to the Rheasilvia and Veneneia basins (see Section 3.3.2), a fit of an ellipsoid to the undisturbed northern terrains leads to constraints on the pre-impact global figure and rotation rate of Vesta (Fu et al., 2014). A similar approach, i.e., mirroring the northern hemisphere, was used in Zuber et al. (2011) to estimate the change of moments of inertia and subsequent reorientation. However, mirroring of the northern hemisphere makes the center-of–figure in the Z-direction equal to zero. Another physical unknown that affects reorientation is the angular momentum of the ejecta, which is strongly dependent on the impact angle.

Instead, we estimate reorientation from a different perspective. Based on finite element simulations (Fu et al., 2014) we assume that the pre-impact figure of Vesta was close to hydrostatic equilibrium. We then fit a triaxial ellipsoid with 9 degrees of freedom (three axes, three orientation angles and three coordinates of the origin) to the terrains unaffected by the late giant impacts. The northern shape ellipsoid parameters are given in Table 3.1. The northern shape is less oblate than the overall shape. The flattening is equal to 0.147, whereas the flattening of the overall Vesta shape is $\approx$ 0.193. The northern shape appears to be much closer to the state of hydrostatic equilibrium for the current rotation rate (Fig. 3-7).

In order to constrain the paleorotation rate, we considered the hydrostatic figures for two end-member cases, which correspond to the most and least differentiated internal structures that agree with the J_2 and total mass constraint. The most differentiated case is a three-layer model that has a 110-km core with a density of 7800 kg/m^3 and 40 km thick crust with a density of 2700 kg/m^3. The least differentiated case is a two-layer model with a 135-km core that has a density of 6000 kg/m^3. The outer shape flattening is equal to the northern ellipsoid flattening at rotation periods of 4.83 and 4.93 hours for the most and least differentiated cases, respectively. Fig. 3-7 shows the flattening factors as a function of rotation period for the most differentiated case. Fu et al. (2014) estimates the paleorotation period to be 5.02 hours, which

is slightly longer than in this work. This is mainly caused by different assumptions about the core density and radius, which for this estimate was taken from Russell et al. (2012).

The volume of the paleo-ellipsoid is 2% larger than the present volume of Vesta, which is consistent with estimates of the volume of excavated material due to giant impacts (Schenk et al., 2012a). The polar axis of the total shape ellipsoid closely matches the rotation axis of Vesta. However, the polar axis of the ellipsoidal fit for the northern shape is off by $\approx 3.0^{\circ}$ (Table 3.2). This value is robust with respect to the definition of the region unaffected by the giant impact and constitutes evidence for possible reorientation. The magnitude of this value is consistent with the results of hydrocode impact simulations (Jutzi and Asphaug, 2011; Jutzi et al., 2013). The orientation uncertainties are also given in Table 3.2.

Hydrocode impact simulations showed that the giant impacts on Vesta could not have significantly changed the shape and position of the core inside the body. The displacement of the core-mantle boundary was <1 km (Ivanov and Melosh, 2013). Therefore the core effectively preserved its pre-impact hydrostatic shape. If we interpret the COM-COF offset by offsetting the center of core from the center of mass, given its small mass, the equivalent center of core offset is equal to 7-9 km, depending on the assumed densities. The relationship between core offset and core density is shown in Fig. 3-8. Shifting the core results in a degree-one change in the gravitational anomaly and our solution for the interior structure model.

We can estimate the flattening and orientation of the core using either the theory of figures or using a numerical algorithm assuming the rotation rate that corresponds to hydrostatic equilibrium of the northern shape. This affects the lower-degree gravity coefficients of our interior structure model.

3.3.2 Interior structure modeling

The interior structure of Vesta can be estimated using three constraints. The first is that the total mass of the interior structure model should be equal to the observed mass of Vesta. The second constraint involves matching the long-wavelength

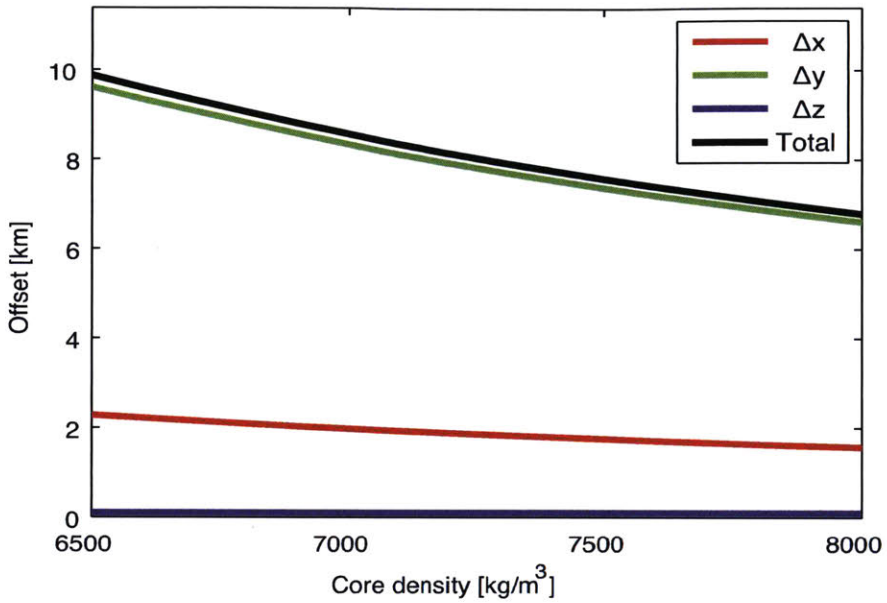

Figure 3-8 – The COM–COF offset can be interpreted as the core offset from the center of mass. The figure shows the center of core offset as a function of the average core density. The mantle and crust densities are fixed to 3200 and 2900 kg/m3 respectively. The core density ranges from 6500 to 7800 kg/m3.

component of observed gravity field with the gravity field calculated from an interior structure model (Eq. 2.13-2.14). The interior structure interfaces can be modeled as ellipsoids. The third constraint is based on the fact that Vesta is the likely parent body of the HED meteorites (McCord et al., 1970; Takeda et al., 1983; McSween Jr et al., 2010). Chemical composition and siderophile element contents in HED meteorites provide a constraint on of the likely degree of metal depletion in the asteroid mantle and, therefore, the size of the metal core. Estimates of the core size in Ruzicka et al. (1997) are consistent with the gravity data. Microporosity can also be estimated from meteoritic and geochemical evidence.

Since the core mass is relatively small and its flattening is smaller than the global flattening (see Section 3.3.1), the core contributions are 1.07% for J_2 and 0.13% for J_4. Therefore, we interpret the rest of the gravity signal at higher harmonics, as coming from the outer shape, the shape of the crust-mantle interface and from internal density variations.

The residual anomaly is defined as the difference between the observed gravitational acceleration and the gravitational acceleration produced by the internal structure model computed at the reference surface. A similar definition was used for the Bouguer anomaly for Vesta in Konopliv et al. (2014a) and Park et al. (2014b) and for asteroid 433 Eros (Garmier et al., 2002). We use the term "residual gravity anomaly" to distinguish it from the conventional definition of Bouguer anomaly that is used in terrestrial geodesy.

Due to extensive impact bombardment of Vesta's surface, the crust and upper mantle of the asteroid likely have non-negligible macroporosity. However, due to Vesta's higher gravity, the vestan crust likely has lower macroporosity than small asteroids ($\approx$ 20%; Consolmagno S.J. et al. (2008)). The deep interior of Vesta likely has nearly zero macroporosity. Some fractures could occur in the core due to the giant impacts, but the magnitudes of transient stresses in the impact modeling were not high enough to create a significant porosity (Ivanov, personal communication). Due to the relatively small mass of the core (<20%), small changes in its porosity should not influence the densities and structure of the overlying layers presented in this work. Therefore, we adopt a macroporosity of zero for the core. Porosity for the silicate portion can be estimated by comparing the mean density of Vesta and the expected mean density computed from geochemical and thermodynamic constraints (Toplis et al., 2013). We adopt a porosity of 8% for the silicate potion of the body, realizing that the uncertainty in porosity can be as high as 50% (Toplis, personal communication). The mantle and crust macroporosity as well as lateral density variations can significantly affect the interior structure, especially if the crust-mantle density contrast is small.

Vesta was first proposed to be the parent body of HED meteorites more than four decades ago (McCord et al., 1970). Analyses of meteorites from the HED suite shows that they are spectroscopically, geochemically and dynamically connected to Vesta (Ruzicka et al., 1997; Binzel and Xu, 1993; Zuber et al., 2011). Spectroscopic mapping of the vestan surface from the Dawn mission has confirmed its affinity to the HED meteorites and identified terrains on Vesta, where howardites, eucrites and

diogenites are each most abundant (De Sanctis et al., 2012; Reddy et al., 2012). In addition, Vesta's surface elemental composition was found to be consistent with the HED meteorites from the gamma ray measurements by Dawn's Gamma Ray and Neutron Detector (GRaND), reinforcing the link between Vesta and the HEDs (Prettyman et al., 2013). In summary, Dawn observations have strengthened the hypothesis that HEDs represent the upper layers (crust and upper mantle) of Vesta.

The likely provenance of the HED meteorites from Vesta allows for inferences of Vesta's interior properties via geochemical studies of the HEDs. The observed chemical composition and modal mineralogy of the eucrites and diogenites suggest that they are the end products of both equilibrium and fractional crystallization of liquids from an extensively-melted interior (Righter and Drake, 1997; Elkins-Tanton et al., 2011). Petrological modeling of these crystallization processes suggests that the vestan mantle should consist predominantly of olivine, which has a grain density of $\approx$ 3200 - 3400 kg/m^3 (Britt et al., 2010; Beck and McSween Jr, 2010). The eucrites and diogenites, which represent the upper and lower crust of Vesta, have measured hand sample densities of between 2900 and 3300 kg/m^3 (Britt and Consolmagno S.J., G., 2003b; Elkins-Tanton et al., 2011). However, the geochemical difference in density can be masked by porosity variations (see Section 3.4). In fact, if the porosity is order of 10% it results in a density contrast comparable or even higher than the pure geochemical density contrast. This poses a problem in interpretation of gravity anomalies.

Russell et al. (2012) showed that, assuming the core has a density similar to that of iron meteorites, a core with a mean radius of 110 km is required to match the observed value of J_2 for the present-day rotation rate. This value is approximately in the middle of the possible range of core sizes derived from geochemical data (Ruzicka et al., 1997). However, due to the non-uniqueness of the inverse gravitational problems, the gravity and topography date alone are not enough to uniquely determine the parameters of even a simple two-layer model. See the discussion of Russell et al. (2012) result in Bills et al. (2014). In order to break this degeneracy, assumptions on the densities should be made. The density of the vestan core, although not directly constrained

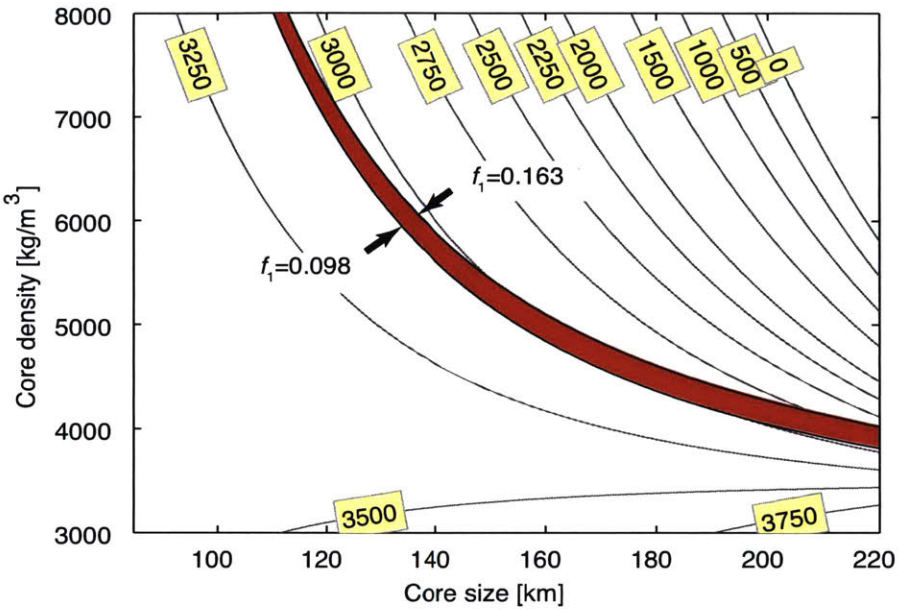

Figure 3-9 – Core size–density relationship for a two-layer internal structure model. The abscissa is the core volume-equivalent radius. The red region shows the solution for the internal structure that satisfies the observed mass and J_2 of Vesta. Gray contours are the density of the outer (silicate) layer in kg/m3. For a given rotation rate, the core flattening factor (f_1) can be computed from hydrostatic equilibrium and plotted in contours similar to the silicate portion density. The minimum value of f_1 corresponds to the smallest core size, highest core density and longest rotation period (4.93 h). The maximum value of f_1 corresponds to the largest core size, lowest core density and shortest rotation period (4.83 h).

by meteorite samples (McSween Jr and Huss, 2010; Buchwald, 1975), is likely to be similar to that of iron meteorites, which have characteristic hand sample densities between 7700 and 8000 kg/m^3. The amount of sulfur, which is unknown, can reduce the density of the core. Toplis et al. (2013) predict core densities as low as 6000 kg/m^3 for some bulk compositions. For the core density range of 6000 – 8000 kg/m^3, the core size ranges from 110 to 138 km. Fig. 3-9 shows the core density-size relationship computed by matching J_2 and total mass of the two-layer model to the corresponding observed values. The core flattening range was chosen taking into account hydrostatic equilibrium of the core figure.

The above constraints are not sufficient to define the axes of the core and mantle ellipsoids uniquely. The shape of the core should satisfy hydrostatic equilibrium for

the rotation rate at the moment of its freezing (see Section 3.3.1). This paleorotation rate can be constrained by the flattening of the northern shape (Fu et al., 2014). However, the sensitivity of the gravity field to the core flattening or orientation is small because of the small mass fraction of the core (Asmar et al., 2012; Russell et al., 2012). We solve for the semiaxes of the mantle ellipsoid (and therefore) by assuming the core radius and crustal density and computing the hydrostatic shape of the core with a numerical algorithm (Tricarico, 2014). This solution provides a baseline interior structure model.

To avoid non-physical solutions for the crust-mantle interface, we choose the critical degree $n_c = 5$. This value of n_c most effectively minimizes the power of the residual anomaly. At higher values of n_c, the power of the residual anomaly at high degrees becomes larger than the original, which indicates that there is not a satisfactory solution to the residual anomaly in the least-squares minimization problem. The resulting low-pass filter w_n is shown in Fig. 3-10. Since the power of the residual anomaly is significantly smaller than the power of the total gravity field, the residual anomaly power spectrum (Fig. 3-2) intersects the error power spectrum at degree 15, which corresponds to the spatial resolution of $\approx$ 55 km. Using equation (2.26), we iteratively minimize the residual anomaly field and find the spherical harmonic coefficients α'_{nm}, that represent the crust-mantle interface. The power of the minimized residual anomaly is also shown in Fig. 3-2.

We observe a significant contribution of non-zonal, second-degree terms in the residual gravity anomaly, which indicates spatial variability of the internal interfaces. The residual anomaly is shown in Figs. 3-11 and 3-12. The residual anomaly in Rheasilvia has a local high at the central peak but is asymmetric in the floor of the basin. A major positive anomaly is apparent in the Vestalia Terra region. For a given crust-mantle density contrast we can estimate the minimum crustal thickness at which the Vestalia Terra anomaly can be explained by crustal thinning. For a density contrast of 300 kg/m^3, if the mean crustal thickness is less than 25 km; the magnitude of the anomaly is high enough that it cannot be explained by crustal thickness variation, indicating a local density increase. For density contrasts of 400

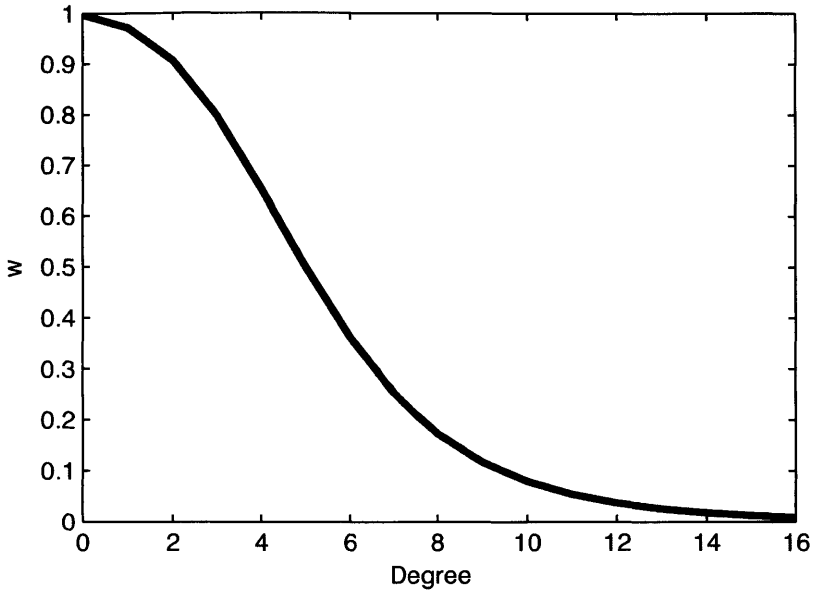

Figure 3-10 – The filter applied to the residual anomaly.

and 500 kg/m^3, the corresponding minimum mean crustal thicknesses are 22 and 18 km, respectively.

Given only gravity and topography data, an absolute mean crustal thickness cannot be computed. However, we can choose densities based on the geochemistry of HEDs to invert for the crust-mantle interface to study relative crustal thickness variations. We adopt values given in Table 3.3; the core volume is adopted from Russell et al. (2012). A characteristic solution for the crustal thickness of Vesta is shown in Figs. 3-13 and 3-14. Alternatively, we show the deviation of the mantle from ellipsoidal shape in Figs. 3-15 and 3-16. The thinnest crust is observed in the floors of the Rheasilvia and Veneneia basins, which correspond to a diogenite-rich region as inferred from the Dawn VIR (McSween et al., 2013). Areas of thickest crust are associated with the rims of the impact basins and could be at least partially associated with impact ejecta.

In this model, there is not a degree-one term in crustal thickness since the COM-COF offset was compensated by shifting the core from the center of mass (see Fig. 3-8). However, the COM-COF offset can also be interpreted as due to a hemispheric-

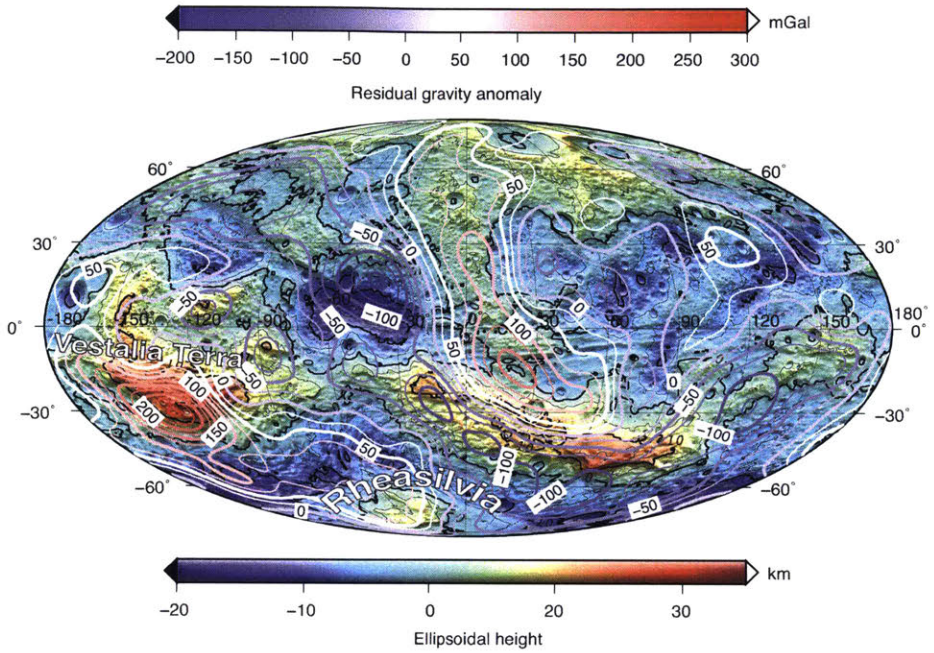

Figure 3-11 – Topography and the residual gravity anomaly in Mollweide projection. The reference ellipsoid for the residual gravity anomaly is 293.2 km × 266.5 km. The reference ellipsoid for topography is 280.9 km x 226.2 km.

Unit	Density (kg/m^3)	Size (km)	Mass fraction (%)
Core (iron)	7800	102.3 × 114.1	16.8
Mantle (olivine)	3200	198.8 × 253.3	66.0
Crust (HED)	2900	226.2 × 280.9	17.2

Table 3.3 – Interior structure model parameters that were used to derive crustal thickness and the deviation of the mantle from ellipsoid.

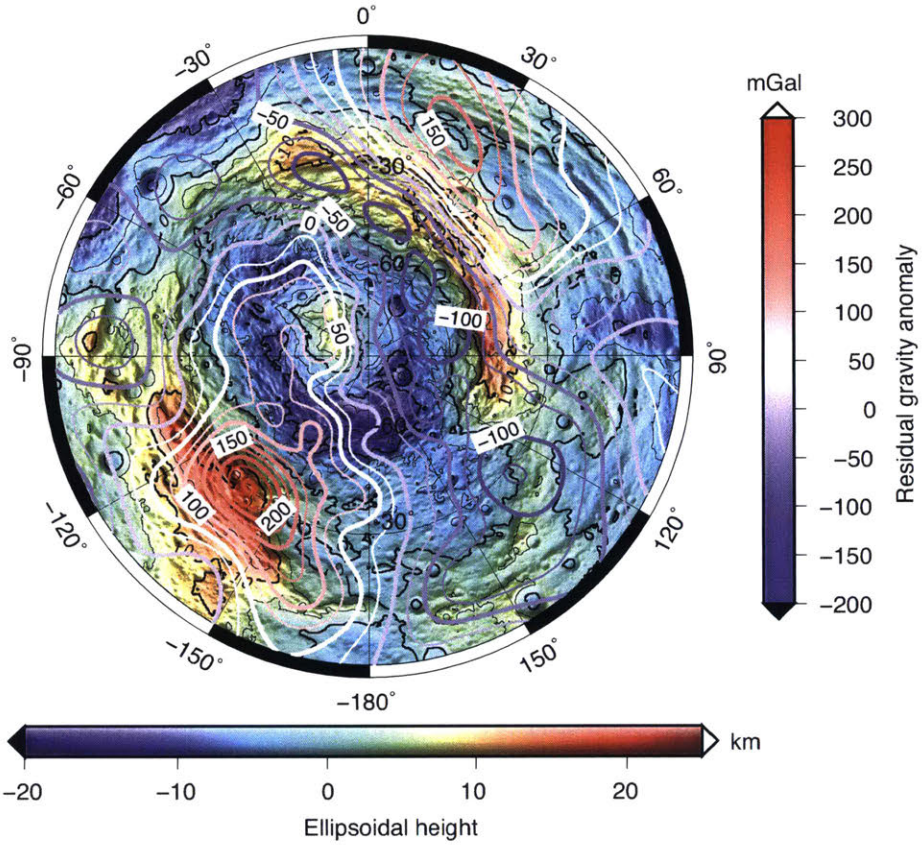

Figure 3-12 – Topography and the residual gravity anomaly in stereographic projection of the southern hemisphere. The reference ellipsoid for the residual gravity anomaly is 293.2 km × 266.5 km. The reference ellipsoid for topography 280.9 km × 226.2 km.

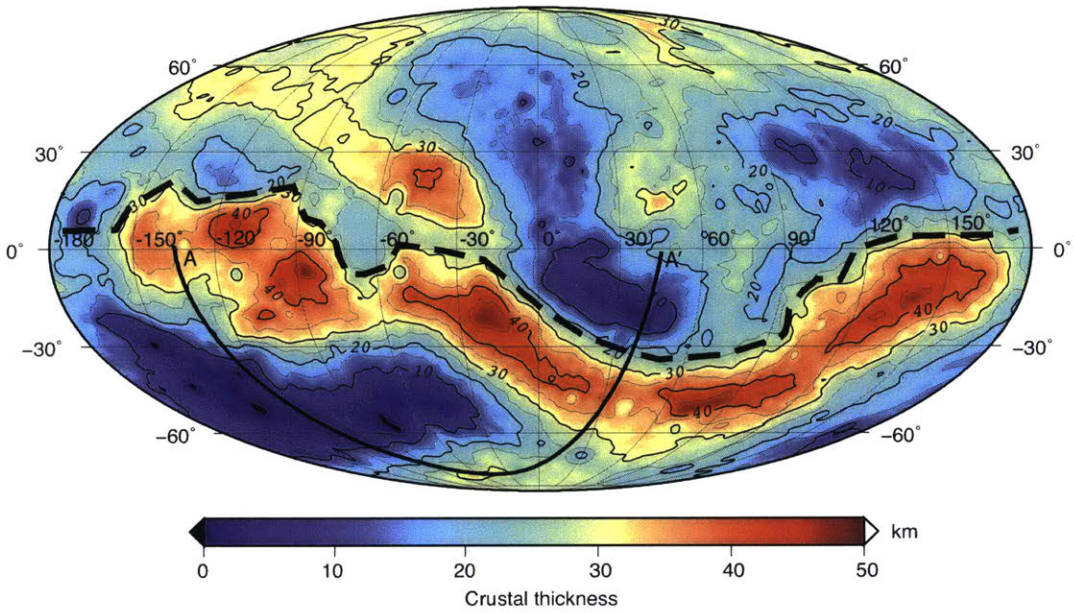

Figure 3-13 – Crustal thickness of Vesta in Mollweide projection based on the internal structure from Table 3.3. The mean crustal thickness is 23.9 km. The thick dashed black curve shows the boundary of the northern terrain, which we define as unaffected by the giant impacts. The black curve (AA_0) shows of the location of the profile across the Rheasilvia basin (see Fig. 3-18).

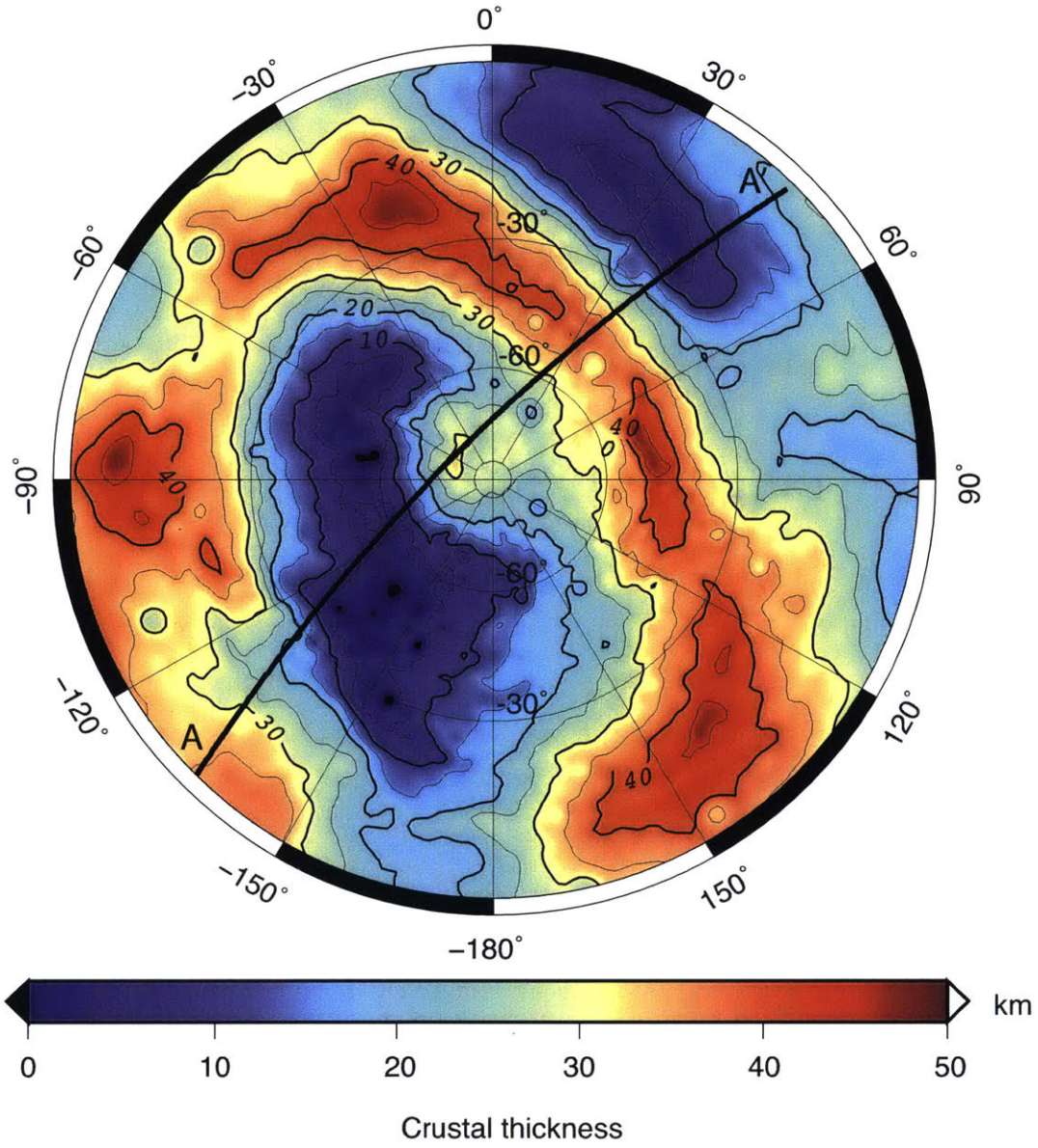

Figure 3-14 – Crustal thickness of Vesta based on the internal structure from Table 3.3. Stereographic projection of the southern hemisphere.

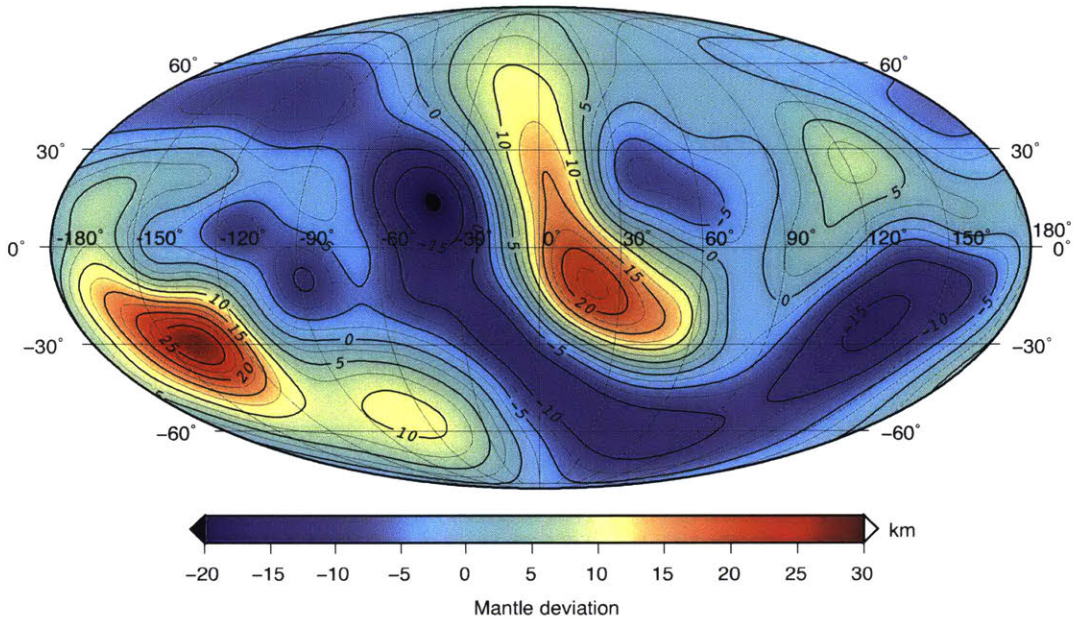

Figure 3-15 – Deviation of the mantle from ellipsoid in Mollweide projection.

scale (degree-one) difference in the crustal thickness. One possibility is that the core's center is at the current center of mass. The other possibility is that the core's center is at the center of the northern ellipsoid (see Table 3.1). In the first case the COM-COF offset directly goes into a degree-one term in crustal thickness. In the second case, the degree-one term in crustal thickness is defined by a combination of mostly southward offset of the core (see Table 3.1) and the COM-COF offset that points approximately towards Vestalia Terra. Crustal thickness was computed for these two cases. The main characteristic feature common to both models is the belt of thicker crust around the Rheasilvia and Veneneia basins. The main difference compared to the maps shown in Figs. 3-13 and 3-14 is a region of thin crust in northern latitudes of the eastern hemisphere. This crustal thinning in the North-East is of the same magnitude or even greater than crustal thinning in the impact basins. Ruesch et al. (2014) shows that most of the olivine detections at Vesta's surface are located in a lobe of diogenite-enriched material that extends north from Matronalia Rupes. If the core center is placed in the center of the northern ellipsoid, most of the olivine detections would correspond to a region with thin crust.

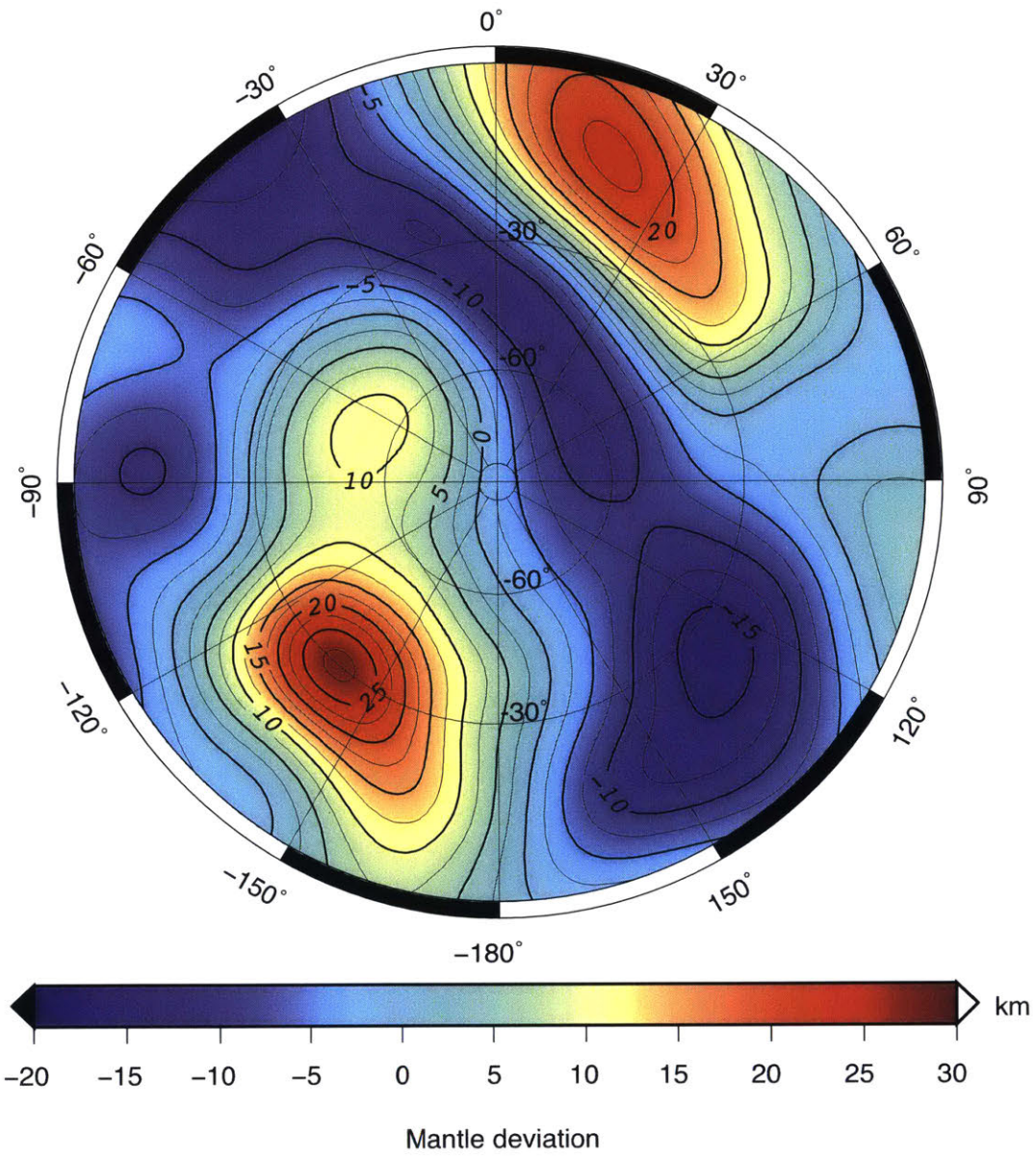

Figure 3-16 – Deviation of mantle from ellipsoid in stereographic projection of the southern hemisphere.

The average crustal thickness for the densities adopted in Table 3.3 is equal to 23.9 km. For a crust mass fraction less that 15%, we observe a region of negative crustal thickness in the Rheasilvia basin towards Vestalia Terra. The core is computed to be approximately 15-17% by mass, which is consistent with Russell et al. (2012). However, the choice of densities shown in Table 3.3 is not unique. We explore the range of possible crust, mantle and core densities. The mean crustal thickness as a function of the three densities is shown in Fig. 3-17. The core size is fixed and corresponds to the volume-equivalent sphere with a radius of 110 km. This size was chosen because it is in agreement with most representative geochemical models (e.g. Toplis et al. 2013). If we assume that the crustal thickness cannot be negative, the minimum mean crustal thickness is estimated (Fig. 3-17) to be 16 km. The maximum crustal thickness, in general, cannot be estimated only from gravity/topography data. Geochemical models place an upper limit on crustal thickness to be 42 km (Ruzicka et al., 1997), 41 km (Mandler and Elkins-Tanton, 2013), and 21 km (Toplis et al., 2013). Note that these authors differ in their definition of the crustal layer. In Toplis et al. (2013), only the eucritic portion is defined as crust; whereas in Mandler and Elkins-Tanton (2013) and Ruzicka et al. (1997), the crust comprises both eucritic and diogenitic layer.

3.4 Discussion

We used spherical harmonics representations of gravity and topography to investigate the interior structure of Vesta. For an oblate body such as Vesta, spherical harmonics have a significant limitation in that the expansion converges only outside of the Brillouin sphere. An alternative approach is to use ellipsoidal harmonics that converge outside of the Brillouin ellipsoid (Garmier et al., 2002; Hobson, 1931; Park et al., 2014b). For Vesta, the volume of the Brillouin ellipsoid is about 80% of the Brillouin sphere volume. With ellipsoidal harmonics it is possible to map gravity anomalies closer to the surface, which amplifies the geophysical signal in the gravity anomaly and eliminates the divergence problem. Our approach allows us to rapidly

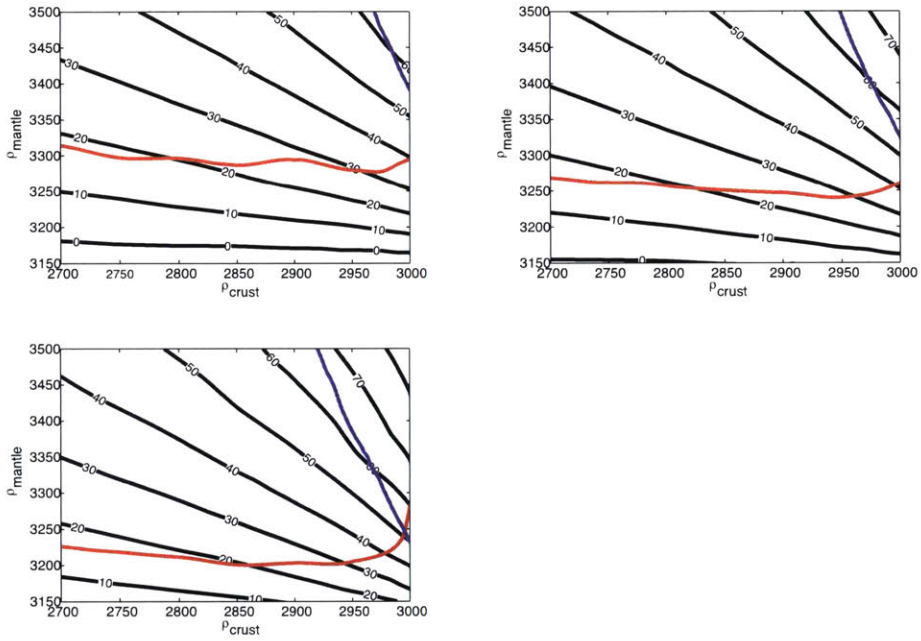

Figure 3-17 – Mean crustal thickness as a function of mantle and crustal densities. The core mean radius is 110 km. The core density is 7800 kg/m^3 (bottom), 7400 kg/m^3 (top right), and 7100 kg/m^3 (top left). For the densities below the red line, the minimum crustal thickness is less than zero. For the densities right to the blue line, the maximum crustal thickness is greater than 100 km.

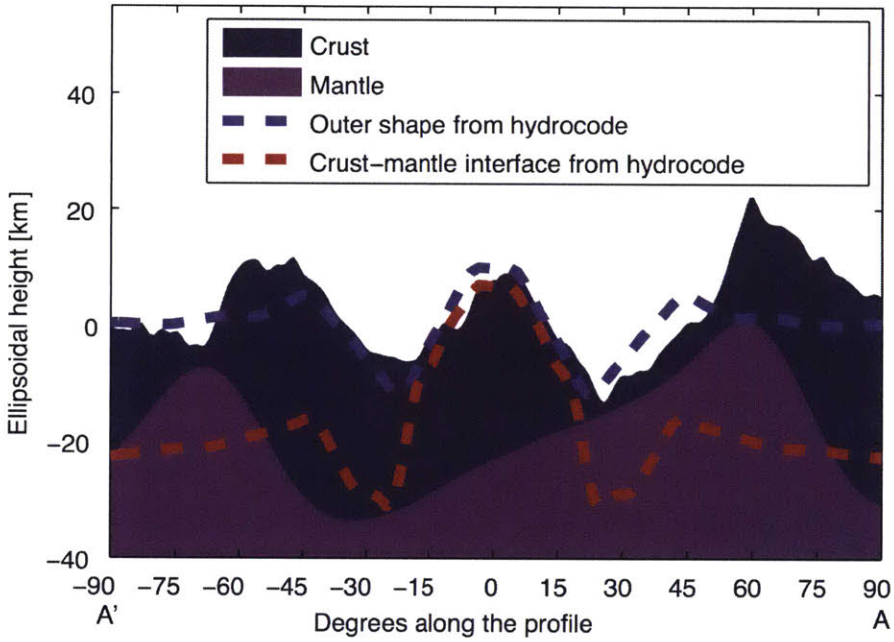

Figure 3-18 – Crustal profile of the Rheasilvia and Veneneia basins derived from this paper (solid profiles in background, compared to the results of hydrodynamic impact simulations (Ivanov and Melosh, 2013) shown as dashed lines.

converge on a solution for the interior structure and is not affected by the slightly lower resolution relative to an elliptical harmonic model.

Vesta's global shape and gravity field are not in hydrostatic equilibrium (Konopliv et al., 2014a; Park et al., 2014b; Bills et al., 2014). Given Vesta's high oblateness and rapid rotation, using the first-order theory (Dermott, 1979) to assess the hydrostatic state of Vesta could be inaccurate; hence we used a numerical approach (Tricarico, 2014) to compute hydrostatic equilibrium of a multilayered body. Vesta's global flattening factor corresponds to a faster rotation ($\approx$4.3 hours). The flattening factor of the northern terrains is smaller but still requires more rapid rotation ($\approx$4.9 hours) for hydrostatic equilibrium.

The 1.4-km COM-COF offset in the equatorial plane can be interpreted as an offset of the core from the present day center of mass, which implies that the position of the core is not in equilibrium, or it could represent a degree-one crustal thickness variation in which thin crust dominates the eastern hemisphere. Further hydrodynamic impact simulations could establish if the COM-COF offset can be the result of core disequilibrium resulting from a high-angle impact, and therefore the possibility that the core was displaced as a result of the giant impact(s).

Vesta's degree-two gravity coefficients are also inconsistent with hydrostatic equilibrium. Matsuyama and Nimmo (2011) estimated reorientation and despinning due to the south polar (Rheasilvia) impact event based on the pre-Dawn HST shape model. The discrepancies between their prediction and the observed gravity coefficients are plausibly due at least in part to the low resolution and errors in the HST shape model. With second-degree gravity coefficients accurately measured by Dawn, it is possible to redo the reorientation analysis. Our analysis of the northern shape Vesta does not show an evidence of significant reorientation.

The local analysis of the gravity field reveals regions of major geophysical interest, one of which is the Vestalia Terra region. Distinctive attributes of Vestalia Terra include the fact that it is the region of highest topography on the surface, it lies in the direction of the COM-COF offset, and it has the highest positive gravity anomaly on Vesta. Given density constraints from the HEDs, the anomaly cannot be explained

by thinning of the crust. Alternative possibilities include piling up of ejecta that was excavated from the deep mantle (Jutzi et al., 2013; Jutzi and Asphaug, 2011) and was subsequently covered by thick regolith (Schenk et al., 2012a), or a primordial intrusive body (Raymond et al., 2013a).

Another region of interest is the south polar area that is the site of two giant impact basins: Rheasilvia and Veneneia. Our crustal thickness models confirm that these are the regions of the thinnest crust. Based on the derived crustal thickness, we can identify which craters are most likely to penetrate into the mantle. These craters are concentrated on the floors of Rheasilvia and Veneneia. No olivine has been detected within these craters, indicating a pure olivine mantle was not sampled by these impacts. This likely means that there is no pure olivine mantle at the depth expected for a magma ocean scenario (30-41 km based on Mandler and Elkins-Tanton 2013).

A number of hydrocode simulations have been produced of the Rheasilvia and Veneneia basins (Ivanov and Melosh, 2012, 2013; Jutzi and Asphaug, 2011; Jutzi et al., 2013), which predict substantial mantle uplift in the basins (Fig. 3-18). The redistribution of mass in the impact basins as predicted from hydrocode simulations results in a characteristic gravitational anomaly – positive in the basin's peak and negative in the floor. Our crustal thickness inversion shows a moderate mantle uplift in the Rheasilvia basin. However, it does not show evidence for uplifted mantle in the Veneneia basin. The central peak of the Rheasilvia basin, particularly on its northwestern side, is associated with a modest gravity high of $\approx$100 mGal, which is consistent with the predictions from hydrocode modeling.

Central positive mass concentrations or mascons have been observed for large impact basins on the Moon (Muller and Sjogren, 1968), Mars (Smith et al., 1993) and Mercury (Smith et al., 2012), and reflect contributions from mantle uplift beneath the basin, and in some cases flooding by volcanic material within the basin cavity (cf. (Neumann et al., 1996; Melosh et al., 2013)). Uplift is consequently believed to be a characteristic feature of basin formation on solid planetary bodies. The fact that the Veneneia basin lacks evidence for such uplift implies either a sufficiently

thick crust such that mantle uplift cannot be detected at the resolution of Vesta's gravity field, which would be inconsistent with geochemical constraints from HEDs as discussed above, or that the crust-mantle boundary has subsequently relaxed due to viscous flow (cf. Fu et al. 2014). Additionally, the relaxation could have had a non-thermal nature. For a relatively small body impact shaking may result in a slow creep of granular material (Richardson et al., 2005). Another possibility is that the younger Rheasilvia impact could have destroyed all preexisting structures associated with older Veneneia.

It is also worth considering whether porosity variations, rather than compositional variations, are the main source of the observed gravity anomalies on Vesta. If so, the upper two layers of our three-layer model could be interpreted as a higher-porosity shell that overlies a lower-porosity shell instead of compositionally different crust and mantle. The gravity discrepancy with hydrocode in the Veneneia basin might indicate that the porosity of the impacted region is higher, which would decrease the bulk density of uplifted mantle material. This could occur due to dilatancy of the material in the two giant basins. Collins (2013) predicts a greater porosity increase for low-gravity environments. The prediction for the Moon is for porosity as high as 17% beneath a 60-70 km crater, assuming zero initial porosity. The GRAIL gravity measurements revealed a high mean porosity of 12% with local variations between 6% and 18% (Wieczorek et al., 2012). In the case of Vesta, the porosity variations and the local density decrease due to dilatancy can be even higher due to a lower surface gravity (g = 0.2–0.27 m/s^2, 6-8 times lower than on the Moon), and less volcanic activity. Therefore, we conclude that porosity variations on Vesta can be an important source of gravity anomalies because they can create density contrasts comparable to the geochemical density contrast. A porosity of $10 - 15\%$ results in a density contrast of $300 - 500$ kg/m^3, assuming HED densities.

The hydrocode modeling showed that the displacement field is not very sensitive to the crust-mantle density contrast. The dry friction coefficient as well as parameters of the acoustic fluidization model are the dominant parameters that control the impact displacement geometry (Ivanov and Melosh, 2013). In our future work, we plan to use

the derived displacement field in combination with a set of density profiles to find a match between the Dawn-observed and hydrocode-predicted gravity anomaly in the basins.

Hydrocode impact simulations by Jutzi et al. (2013) predict excavation depth to be about 60-100 km, and the maximum excavation depth is located in the region where the two basins overlap. The models predict a large area of exposed mantle olivine in the basins and olivine ejecta extending into the northern hemisphere. However, olivine was not detected in the impact basins, although the detectability threshold is estimated at 25% olivine concentration (McSween et al., 2013; Beck et al., 2013). A possible explanation could be much thicker eucritic crust ($\approx$100 km) intruded by diogenitic plutons. However, this would contradict geochemically-derived constraints on maximum crustal thickness, which are based on the assumption that initial composition of Vesta was chondritic (e.g. Toplis et al. 2013; Mandler and Elkins-Tanton 2013; McSween et al. 2013).

If the mantle material was not brought to the surface in association with Vesta's large impacts, then the existence of ultamafic vestoids (Reddy et al., 2011) requires alternative interpretation. Ivanov and Melosh (2013) propose that the absence of olivine-rich ejecta could be explained by the two subsequent giant impacts. The first impact (Veneneia) produces an uplift of mantle material; the second impact (Rheasilvia) launches the uplifted mantle material into space. Since Veneneia does not show a sign of mantle uplift, the existence of mantle vestoids is another challenge in making a self-consistent Vesta model.

One obvious simplification in our model is that we treat the interior density distribution as three constant-density regions. This allows a simple solution for the crust-mantle relief from the residual anomaly (Wieczorek and Phillips, 1998). However, there surely exist density perturbations in the crust and probably to a lesser extent in the mantle. Tricarico (2012) suggests an alternative algorithm for interior structure inversion, where the density field is represented as an expansion using Chebyshev polynomials. This inversion produces the exact gravity field, unlike that of Wieczorek and Phillips (1998) which gives a least-squares, minimized-misfit approxi-

mation. However, the inversion problem is underdetermined and possesses an infinite number of solutions. Tricarico (2012) shows possible ways to eliminate non-physical solutions (such as ones with negative density), but even so, the results are highly unconstrained. The two approaches can be combined. The first-level solution can be found from a three constant-density layer inversion. This solution can be refined using the Chebyshev polynomial algorithm. For example, the algorithm can be forced to seek density variations only in the upper layer leaving constant density core and mantle. This approach would help to constrain intracrustal density variations and to estimate the effect of the density variations in the mantle on the gravity field.

Despite the above-discussed crust and mantle density perturbations, the surface of Vesta appears to be more laterally homogeneous than the terrestrial planets, as demonstrated by the correlation between the observed gravity and the gravity due to shape at the observed wavelengths. In a contrasting example, the gravity/topography correlation on the Moon is substantially reduced at spatial scales corresponding to the maria-filled major impact basins; the maria are negative topographic features that possess a strong positive gravity signature (e.g.: Zuber et al. (2013); Wieczorek (2007b)).

Future work will include assessment of reorientation and despinning of Vesta from the observed gravity field and moments of inertia. The spectral characteristics and roughness of Vesta topography at different scales will be compared for the SPG and SPC shape models as well as to that of the planetary analogues. Also, regional spectral topography analysis based on local geology should be conducted. It would also be useful to perform analytical calculations of viscous relaxation on the interior structure in spherical or ellipsoidal symmetry.

3.5 Conclusions

The topographic spectrum of Vesta is distinctive compared to those of the terrestrial planets; with its smaller mass and gravitational attraction Vesta is rougher at all length scales. Vesta is currently not in a state of hydrostatic equilibrium. Low

degrees of the topographic model are dominated by the Rheasilvia basin, which is the primary non-hydrostatic perturbation of the shape. The pre-impact rotation rate of Vesta derived from the shape of the northern hemisphere that lacks comparable large impact structures, allows new constraints on the shape of the vestan core. Refined calculation of moments based on Dawn data provide quantitative support for pre-Dawn analysis that suggested that Vesta may have reoriented due to the giant impacts. The reorientation is estimated by fitting an ellipsoid to the northern part of Vesta. We conclude that up to 3° of reorientation is consistent with the Dawn data. From the observed shape, gravity field and geochemical data available from the analysis of the HED meteorites, we derive models of the interior structure of Vesta. The largest gravity anomaly is observed in the Vestalia Terra region. The power of this anomaly cannot be explained entirely by crustal thickness variations for plausible crust-mantle density contrasts, and implies lateral variations in crustal and/or mantle density, or alternatively, substantial lateral variations in impact-related porosity.

Chapter 4

Comparison of the SPG and SPC shape models of Vesta and Ceres

Frank Preusker and Ryan Park contributed to this work.

Abstract

The shapes of Vesta and Ceres were constructed using the images from the Framing Camera (FC) of the Dawn spacecraft. The shape models were developed by two different groups using two techniques: stereophotogrammetry (SPG) and stereophotoclinometry (SPC). The SPC models were produced by Planetary Science Institute (Gaskell, 2012) for Vesta and by JPL for Ceres (Park et al., 2016). The SPG models of Vesta and Ceres are produced by the German Aerospace Center (DLR) (Preusker et al., 2012, 2015, 2016). In this chapter, we provide an analysis of the systematic and stochastic differences between the shape models. After subtracting the systematic difference, we assess the remaining residual difference, which appears to have less structure and therefore better reflects statistical noise in the shape reconstruction. The main goal of this chapter is to inform the future users of the shape models of their effective resolution, possible artifacts and systematic differences that might affect the results of geophysical analysis.

4.1 Introduction

Knowledge of a body's shape is crucial for geophysical, geological and geomorphological studies. The Dawn mission images have been used to construct the shape models of Vesta and Ceres. The Dawn mission has the following mission requirements

pertaining to the shape (Rayman et al., 2006; Russell and Raymond, 2011)

- Obtain images of $\geq$ 80% of the surface of Vesta with a sampling of $\leq$ 100 m per pixel, and a signal-to-noise ratio of at least 50 in the clear filter and in $\geq$ 3 color filters.
- Obtain images of $\geq$ 80% of the surface of Ceres with a sampling of $\leq$ 200 m per pixel, and a signal-to-noise ratio of at least 50 in the clear filter and in $\geq$ 3 color filters.
- Obtain a topographic map of $\geq$ 80% of the surface of Vesta, with a horizontal spatial resolution of $\leq$ 100 m, and a vertical accuracy of $\leq$ 10 m.
- Obtain a topographic map of $\geq$ 80% of the surface of Ceres, with a horizontal spatial resolution of $\leq$ 200 m, and a vertical accuracy of $\leq$ 20 m.

In this Chapter, we describe the orbits of the Dawn mission from which the images were collected. Second, we compare the basic characteristics of the shape models such as dimensions of fitted ellipsoids. Third, we compare the shape models in spatial domain and identify the systematic differences between shape models. Additionally, we study the crater depth differences for Vesta. Finally, we compare the models in the spectral domain and provide conclusions of our findings.

4.2 Shape models

4.2.1 Vesta shapes

The Dawn spacecraft collected data on the orbit around Vesta from July 2011 to September 2012. Table 4.1 summarizes the parameters of the Dawn science orbits at Vesta.

Orbit name	beginning	end	altitude (km)	pixel scale (m)
Survey	11-08-2011	30-08-2011	2750	258
HAMO 1	27-09-2011	28-10-2011	680	63
LAMO	07-12-2011	10-04-2012	210	20
HAMO 2	24-05-2012	12-06-2012	680	63

Table 4.1 – Parameters of the Dawn science orbits at Vesta.

4.2.1.1 Stereophotoclinometry – SPC

The SPC technique (Gaskell et al., 2008) has previously been applied to produce shape models of the Earth's Moon (Gaskell and Mastrodemos, 2008), asteroid 433 Eros (Gaskell et al., 2007), Martian moons Phobos and Deimos (Ernst et al., 2015) and will be used for the future OSIRIS-REx mission to characterize the shape of asteroid Bennu (Palmer and Gaskell, 2015). Table 4.6 summarized the SPC shape models of Vesta built over the course of the Dawn mission.

Model name	a (km)	b (km)	c (km)	$\|\Delta r\|$ (km)
GASKELL_SHAPE_SURV_CYC3	285.014	277.564	226.678	2.850
GASKELL_SHAPE_SURV_CYC4	285.118	277.577	226.645	2.830
GASKELL_SHAPE_SURV_CYC7	285.275	277.670	226.252	2.523
GASKELL_SHAPE_VTH_OPNAV2	285.190	277.733	226.283	2.528
GASKELL_SHAPE_HAMO_CYC1	285.381	277.785	225.642	1.129
GASKELL_SHAPE_HAMO_V1	285.059	277.517	226.767	1.459
GASKELL_SHAPE_HAMO2_07_09	285.083	277.432	226.743	1.276
GASKELL_SHAPE_HAMO2	285.099	277.507	226.582	1.245
HASTA_LA_VESTA_SHAPE	284.959	277.501	226.554	1.293
GASKELL_CLAUDIA_2013_02_13	284.915	277.512	226.571	1.245
GASKELL_CLAUDIA_2013_05_22	285.003	277.519	226.531	1.193
GASKELL_SHAPE_POST_VESTA	284.945	277.551	226.548	1.246
GASKELL_CLAUDIA_2014_05_13	285.067	277.439	226.540	1.233

Table 4.2 – List of SPC shape models of Vesta. The semimajor axes (a, b and c) and the magnitude of the center-of-ellipsoid–center-of-mass offset of the ellipsoidal fits with 9 degrees of freedom are shown.

4.2.1.2 Stereophotogrammetry – SPG

Table 4.3 summarized the SPG shape models of Vesta built over the course of the Dawn mission. The SPG technique used for constructing the shape model of Vesta is summarized in Jaumann et al. (2012).

Model name	a (km)	b (km)	c (km)	$\|\Delta r\|$ (km)
2013-06-29 HAMO-1-2	285.145	277.615	226.611	1.231

Table 4.3 – List of SPG shape models of Vesta. The semimajor axes (a, b and c) and the magnitude of the center-of-ellipsoid–center-of-mass offset of the ellipsoidal fits with 9 degrees of freedom are shown.

4.2.2 Ceres shapes

The Dawn spacecraft have been collecting data on the orbit of Ceres from March 6. Table 4.4 summarizes the parameters of the Dawn science orbit at Ceres.

Orbit name	beginning	end	altitude (km)	pixel scale (m)
RC3	23-04-2015	09-05-2015	13500	1300
Survey	06-06-2015	30-06-2015	4400	410
HAMO	17-08-2015	23-10-2015	1450	135
LAMO	16-12-2015	-	375	35

Table 4.4 – List of the Dawn science orbits at Ceres

4.2.2.1 SPC

Table 4.5 summarizes the shape models of Ceres built over the course of the Dawn mission. The methods used for constructing the shape model of Ceres are presented in Park et al. (2016).

Model name	a (km)	b (km)	c (km)	$\|\Delta r\|$ (km)
OpNav5	484.161	481.421	447.784	0.896
Ceres_SPC_2015-05-28_through_RC3	483.529	481.74	445.422	11.484
CERES_150604_GRAVITY_SPC	483.806	481.646	445.590	0.910
CERES_SURVEY_150702_GRAVITY_SPC	483.456	481.408	445.690	0.719
CERES_SURVEY_150716_GRAVITY_SPC	483.403	481.334	445.640	0.787
CERES_SURVEY_150828_GRAVITY_SPC	483.001	481.316	446.029	0.960
CERES_HAMO_151123_GRAVITY_SPC	483.20	481.067	445.883	0.981

Table 4.5 – List of SPC shape models of Ceres. The semimajor axes (a, b and c) and the magnitude of the center-of-ellipsoid–center-of-mass offset of the ellipsoidal fits with 9 degrees of freedom are shown.

4.2.2.2 SPG

Table 4.6 summarizes the shape models of Vesta built over the course of the Dawn mission.

Model name	Data included	a (km)	b (km)	c (km)	$\|\Delta r\|$ (km)
PreSurvey	up to RC3	483.004	480.880	446.502	1.002
Survey	up to HAMO	483.069	480.891	446.086	1.039
HAMO	up to LAMO	483.233	481.005	445.947	1.027

Table 4.6 – List of SPG shape models of Ceres. The semimajor axes (a, b and c) and the magnitude of the center-of-ellipsoid–center-of-mass offset of the ellipsoidal fits with 9 degrees of freedom are shown.

4.3 Comparison in the spatial domain

4.3.1 Height difference

4.3.1.1 Vesta

We first compare the shape models in the spatial domain. Fig. 4-1 shows the difference of ellipsoidal heights between the SPG and SPC Vesta shape models. The first systematic difference that we notice is an offset between the prime meridians. After making the latitude dependent adjustment for this mutual rotation (see Sec.4.5), the height difference is somewhat smaller as seen in Fig. 4-4. However, the main systematic difference is a J_2-like offset. It can be seen in Fig. 4-2 that the SPG model is more oblate than the SPC model. After fitting this latitude dependent signal and subtracting it, we produce a map presented in Fig.4-3. This map better represents the statistical difference between the two shape models and allows identification of finer scale systematic differences. The most apparent difference can be seen in the high

north latitudes. The illumination conditions in the north high regions were poorer because the sub-solar point was in the southern hemisphere for the most part of the mission. In the north pole region there is a systematic difference in the crater depths. The craters are systematically shallower in the SPC shape model.

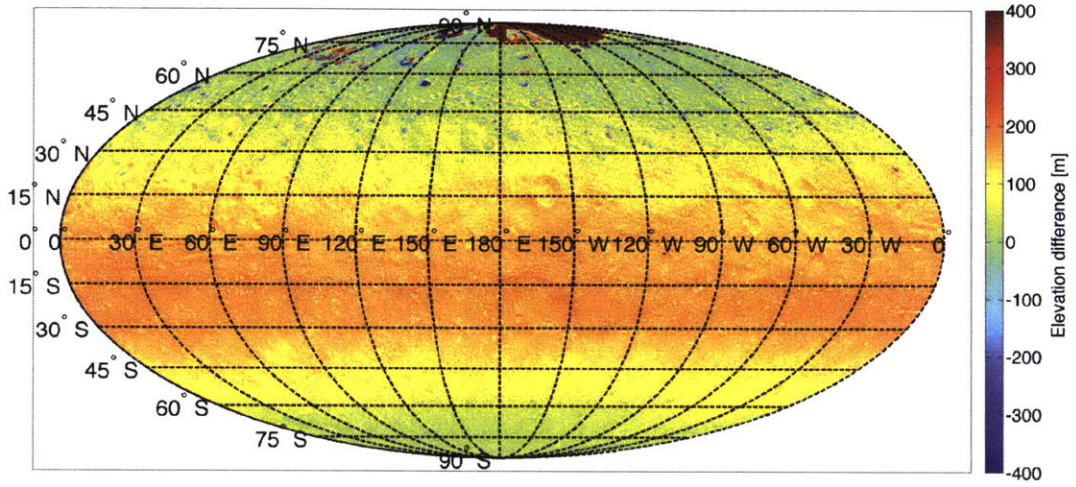

Figure 4-1 – Vesta height difference map (SPG - SPC). The 2013-06-29 HAMO-1-2 and GASKELL_CLAUDIA_2014_05_13 models were used (SPG and SPC, respectively)

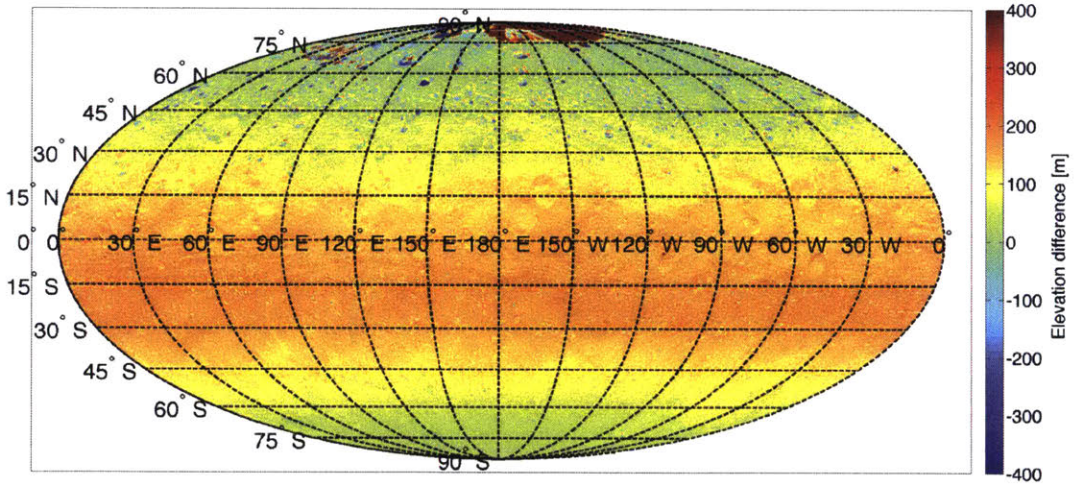

Figure 4-2 – Vesta height difference map after correcting the prime meridian (SPG - SPC).

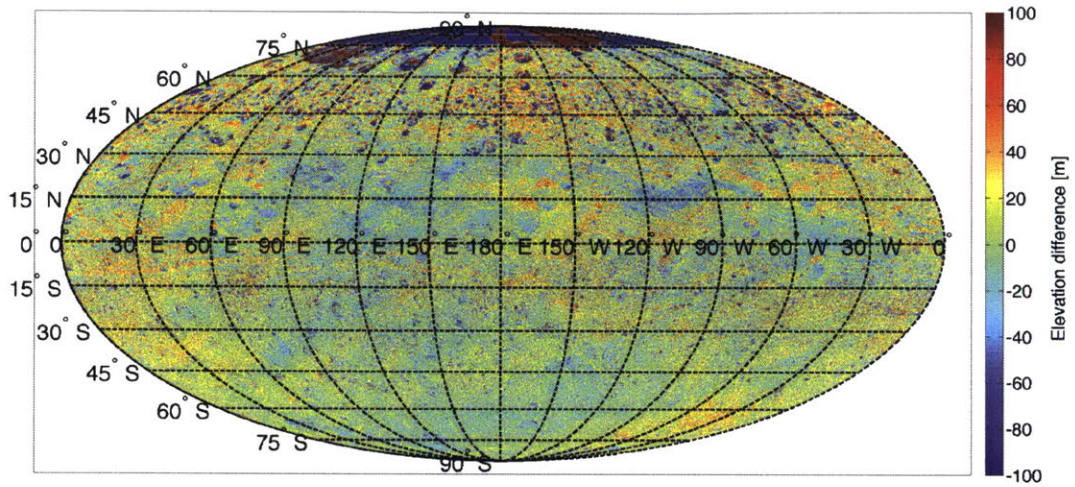

Figure 4-3 – Vesta height difference map after correcting the prime meridian and adjusting the J_2-like offset (SPG - SPC). Notice the change of color scale.

Fig. 4-4 shows how the difference between the two shape models changes as we subtract the systematic effects.

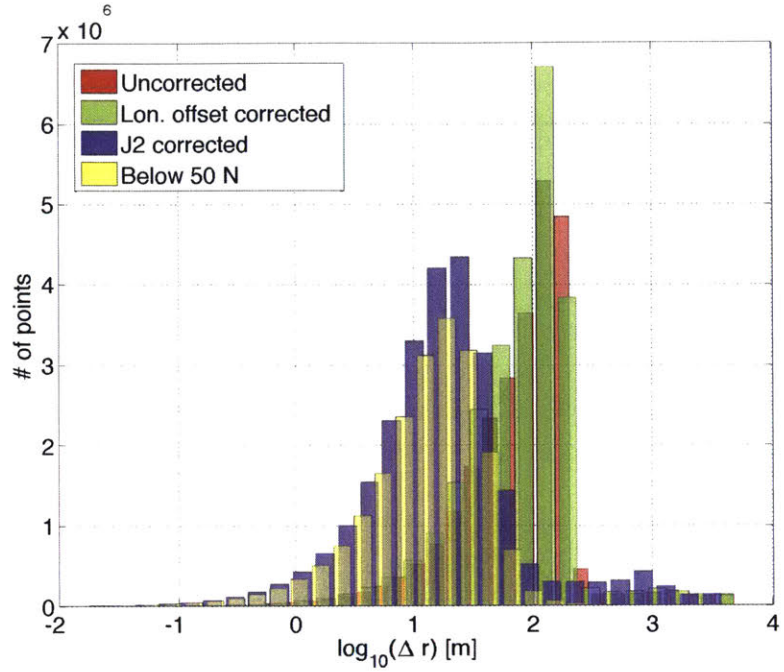

Figure 4-4 – Vesta height difference histograms. The red histogram corresponds to the uncorrected shape models. The green histogram corresponds to the shape models after a latitude-dependent prime meridian offset was applied. The blue histogram corresponds to the shape models after the J_2-like difference was empirically fit and subtracted. Finally, the yellow histogram is shown for the data points that lie below 50°N to eliminate the poor illumination regions.

4.3.1.2 Ceres

We have also performed similar analysis for the Ceres shape models. The height difference map for the Ceres shape models is dominated by the craters (Fig. 4-5). The craters are systematically shallower in the SPC shape model. This is observed both for the Survey and HAMO shape models. However, the difference is less apparent in the HAMO shape. Besides the systematic crater depth difference, there are extended regions with a consistent height difference that cannot be attributed to impact features. The most noticeable example of such a feature is located near the equator at a longitude of 180° E. Such extended regions are mostly present in the Survey height difference map (Fig. 4-5a). However, they are still visually noticeable in the HAMO height differences (Fig. 4-5b).

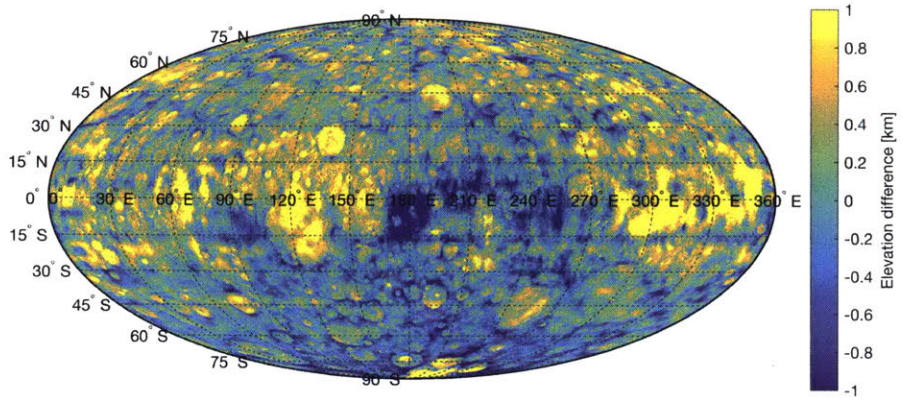

(a) Ceres height difference map for the shape models from the Survey models.

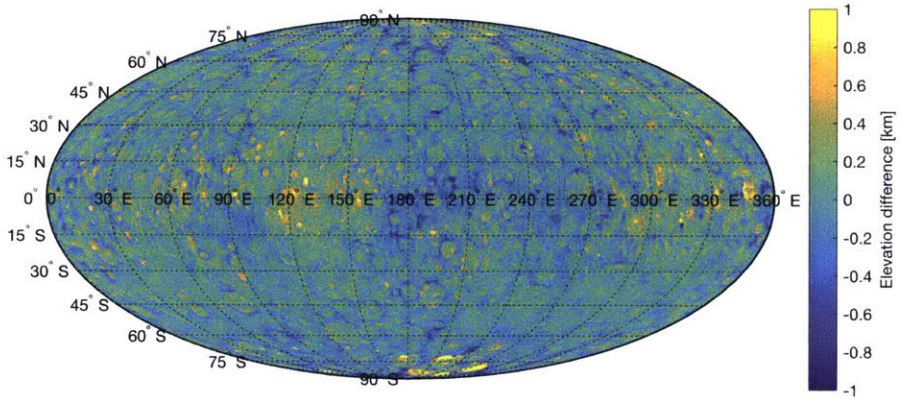

(b) Ceres height difference map for the shape models from the HAMO models.

Figure 4-5 – Ceres height difference maps from the Survey and HAMO models.

Fig. 4-6 shows the histogram of the height difference for the Ceres shape models. The standard deviation of the difference is 510 m for the Survey models and 342 m for the HAMO models.

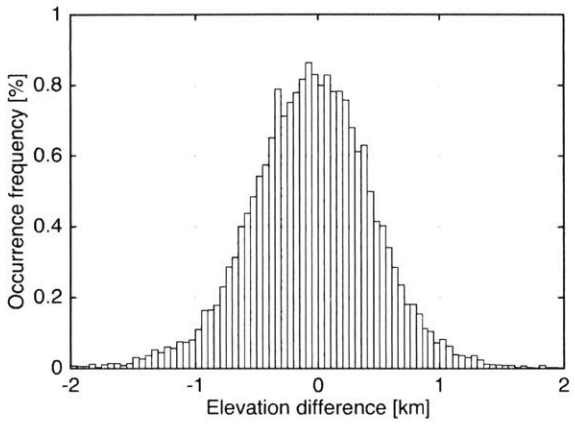

(a) Height difference histogram for the Ceres shape models from the Survey orbit.

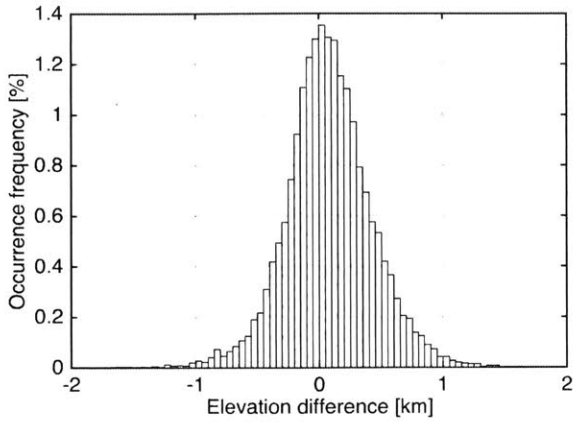

(b) Height difference histogram for the Ceres shape models from the HAMO orbit.

Figure 4-6 – Ceres height difference histogram.

4.3.2 Vesta Crater depths

Craters are the most abundant and easily observable landforms on the asteroidal surfaces. Circular forms of craters make them a very useful tool for visual inspection of the height difference maps. For example, a small solid rotation between the shape models creates a characteristic positive and negative difference at the opposing crater walls. To compute the crater depths, we used a crater catalogue (Marchi et al., 2012) for craters bigger than 1 km in diameter. For each crater we computed 50 radial profiles from the center of the crater. We find the minimum point in the portion of the profile that extends from the center to the half of the crater radius. We also find the maximum point in each profile between 0.8 and 1.2 crater radius. We define the crater depths as the difference between the averaged maximum and minimum height. The spread in the minimum and maximum point heights allows to assign an uncertainty to crater depths as:

$$\sigma^2_{depth} = \sigma^2_{bottom} + \sigma^2_{top}, \tag{4.1}$$

$$\sigma^2_{top/bottom} = \frac{1}{N-1}\sum_{i=1}^{N}(h_i - \bar{h}_{top/bottom})^2, \tag{4.2}$$

$\bar{h}_{top/bottom}$ is the mean and $\sigma^2_{top/bottom}$ is the variance of the topographic height of either the lowest point on the floor or the highest point on the crater rim, respectively. In our analysis, we keep only craters where this uncertainty is less than 20% of the determined crater depth. The main source of this uncertainty is "geological noise" and not the errors in the shape model. Fig. 4-7 shows an example of crater determination for a vestan crater.

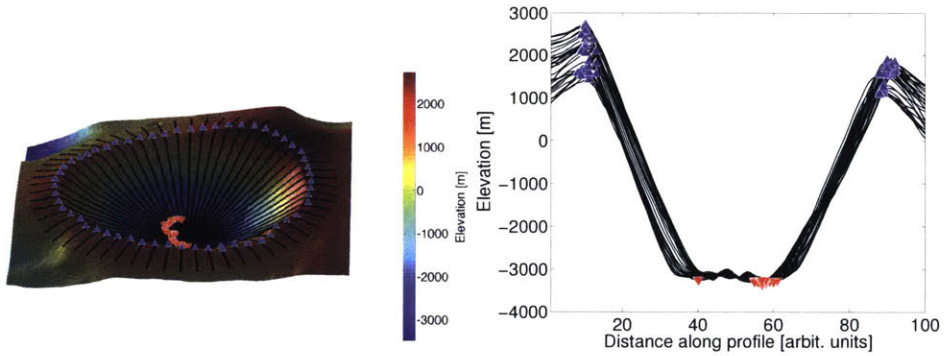

(a) Oblique view of a crater. Azimuthal profiles are shown as black lines.

(b) All azimuthal profiles.

Figure 4-7 – Illustration of average crater depth determination. The blue triangles show the maximum height at the rim. The red triangles show the minimum height at the crater floor.

We computed crater depths for 5631 craters on Vesta using the SPG and SPC shape models. The difference in crater depths is shown in Fig. 4-8.

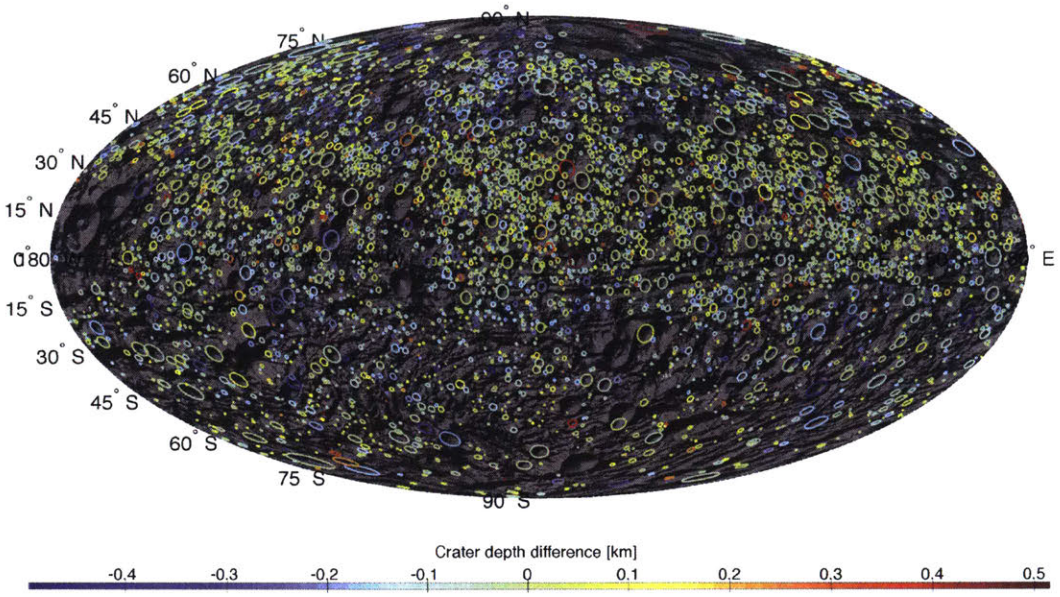

Figure 4-8 – Vesta crater depth difference map. Each circle represents a crater color-code according to the crater depth difference.

As expected, the crater depth difference is larger near the polar regions where the illumination conditions were poor. Fig. 4-9 summarizes the results of the crater depth study. It can be seen in Fig. 4-9a, that the crater depth difference are typically less than 100 m. The standard deviation of the crater depth difference is 133 m. The standard deviation of the crater depth difference are typically higher at high south polar latitudes (Fig. 4-9b and Fig. 4-9d). There is not a systematic trend of crater depth difference as a function of crater size (Fig. 4-9c), at least for the crater diameters over 1 km.

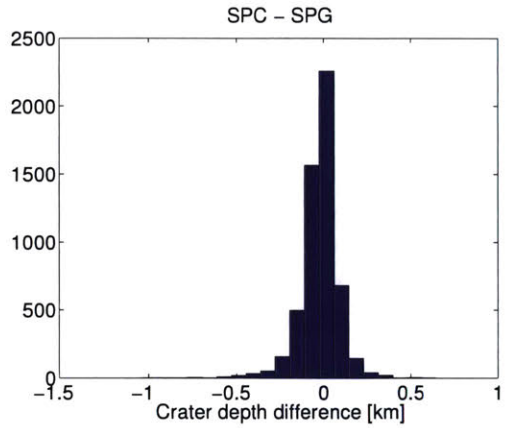

(a) Vesta crater depth difference histogram.

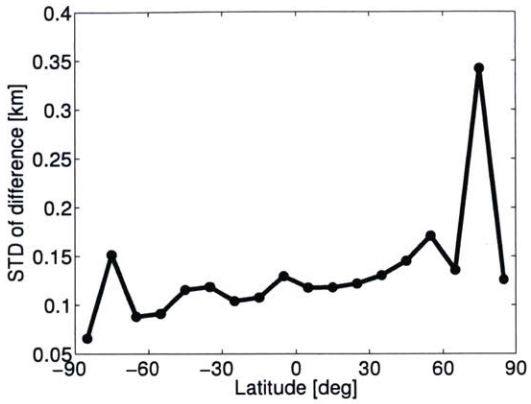

(b) Standard deviation of crater depth per latitude bins.

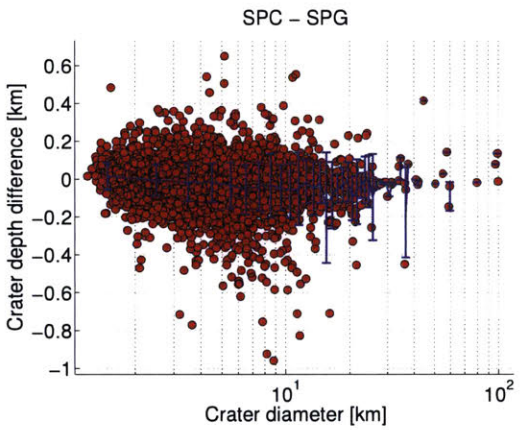

(c) Crater depth difference as a function of crater diameter.

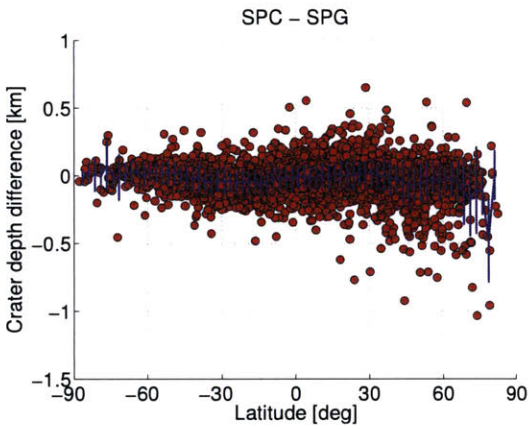

(d) Crater depth difference as a function of latitude.

Figure 4-9 – Statistics of Vesta crater depth difference.

4.4 Comparison in the spectral domain

We use SHTOOLS software (Wieczorek, 2014) to expand the shape models of Vesta and Ceres in a spherical harmonic series. SHTOOLS allows expansions up to degree 2800.

4.4.1 Power spectral density

The power spectral density or PSD is proportional to the total magnitude of spherical harmonic coefficients (Eq. 2.10). Typically, PSDs of rocky planetary bodies as a function of spherical harmonic degree follow a power law (Turcotte, 1987). Deviations from the power law might occur due to inaccuracies in the shape model as well as due to geophysical processes such viscous relaxation (Fu et al., 2016) or isostasy (Nimmo et al., 2011). It can be seen in Fig. 4-10a-4-10b that as more images are collected from progressively lower altitude orbits, the PSD spectra pick up more power at the high spherical harmonic degrees.

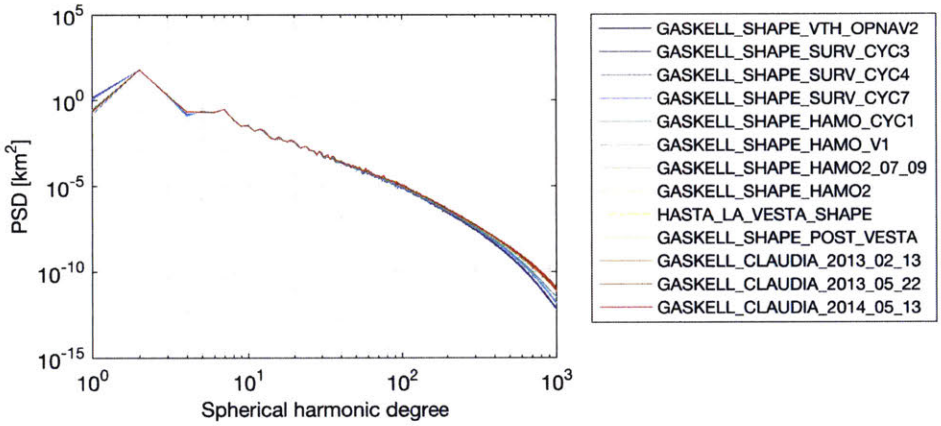

(a) Vesta SPC shape power spectral density.

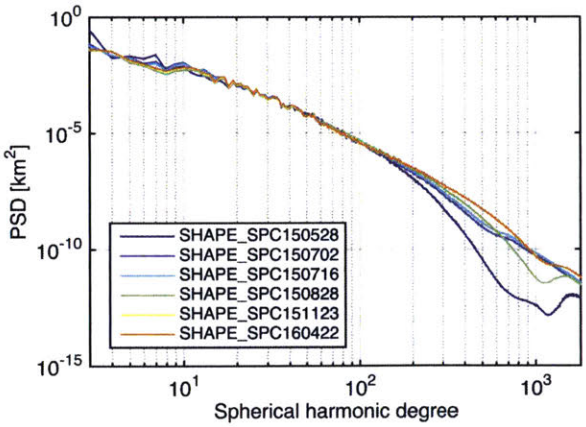

(b) Ceres SPC shape power spectral density.

Figure 4-10 – Power spectral density for various shape models.

4.4.2 Correlation

The correlation function is a measure of phase agreement between the two shapes. The correlation between the SPG and SPC models is shown in Fig. 4-11a. The correlation decreases to $\frac{1}{2}$ at the degrees of 1100 and 800 for Vesta and Ceres, respectively. Due to lower orbits and therefore higher image resolution the shape models of Vesta have higher mutual correlation compared to those of Ceres.

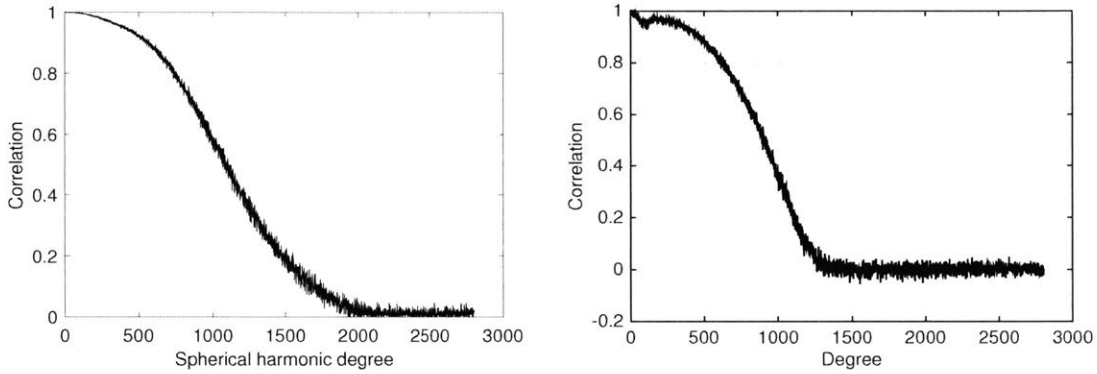

(a) Correlation between SPC and SPG models of Vesta.

(b) Correlation between SPC and SPG models of Ceres.

Figure 4-11 – Correlation between SPC and SPG models.

4.4.3 Isotropic ratio

The isotropic ratio is a ratio of the mean squared North-South to the East-West slope. It is a measure of isotropy of the shape (See Section 2.4.5). This ratio is expected to be close to unity. The isotropic ratios for Vesta and Ceres are presented in Fig. 4-12a and 4-12b. As can be seen in Fig. 4-12a-4-12b, both for the models of Vesta and Ceres, the SPG shape model strongly deviates from isotropy at high spherical harmonic degrees.

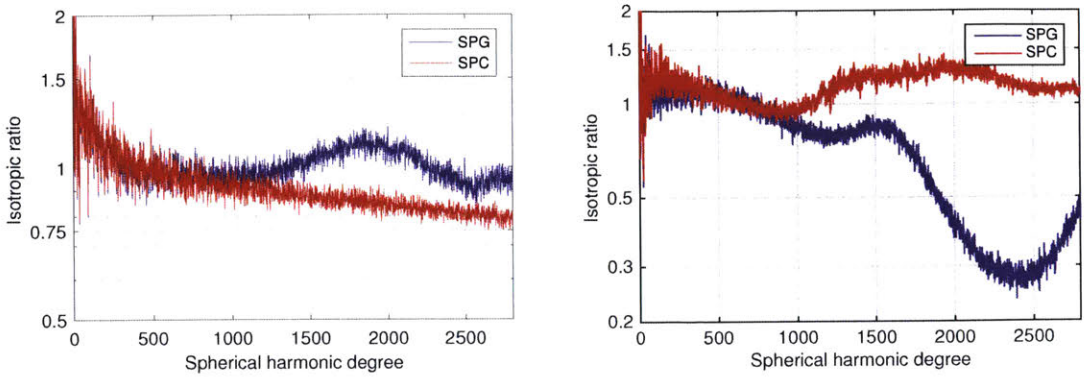

(a) Vesta shape shape isotropic ratio

(b) Ceres shape shape isotropic ratio

Figure 4-12 – Isotropic ratio.

4.5 Potential artifacts

4.5.1 J_2-like pattern

We have observed a number of potential artifacts while comparing the SPG and SPC shape models. However, it is hard to determine what model these artifacts originate from. First, we observe a systematic torsion between the two Vesta shapes. In other words, one model is rotated with respect to the other one around the z-axis, however the amount of rotation is latitude-dependent. The maximum rotation is at the poles and the minimum is at the equator (Fig. 4-13).

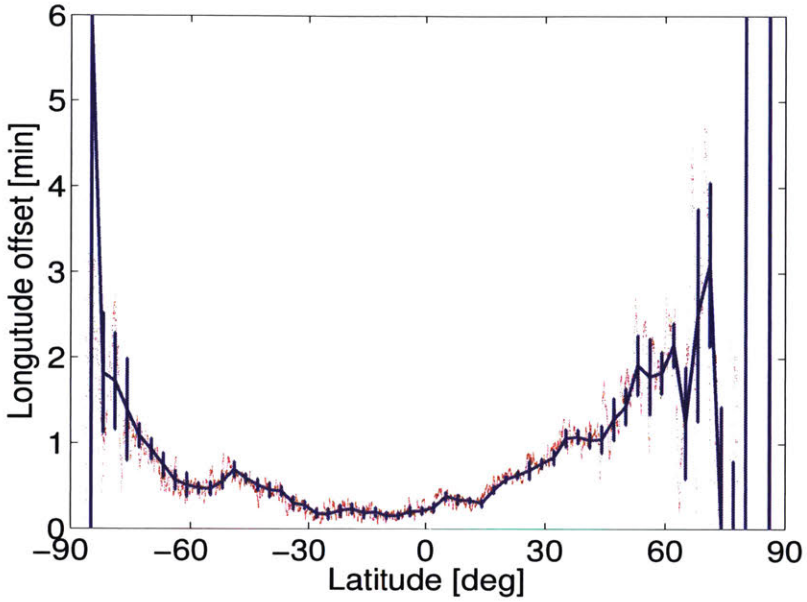

Figure 4-13 – Prime meridian offset as a function of latitude. The red points show the prime meridian offset which minimizes the sum of squared difference of heights. The blue error bars represent the found offsets binned into 3 degree bins.

Another, more significant effect is the J_2-like difference between the SPG and SPC Vesta shapes. The SPG model is more oblate than the SPC model as seen in Fig. 4-14. However, this systematic difference does not exactly follow the J_2-pattern. The maximum difference is centered at a latitude of $\approx -15°$. Moreover, we observe a similar pattern if we difference the two subsequent SPC models, which might indicate the source of this systematic difference is in the SPC modeling. It is curious that the latitude of $-15°$ is the latitude of the sub-solar point during the HAMO phase of the mission.

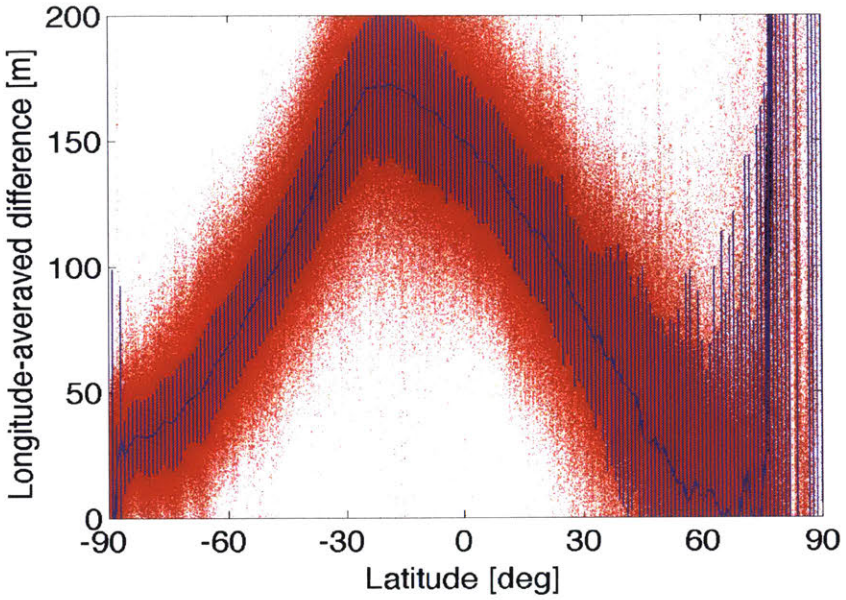

Figure 4-14 – Longitude-averaged height difference map. The scattered red points represent the data points in the shape model. The blue error bars represent the shape model data points binned into 1-degree bins.

4.5.2 Discontinuities at the poles

The SPG model of Vesta has problems with a discontinuity near both poles as well as in polar regions along the prime meridian as seen in Fig. 4-15. Such artifacts, being essentially very high-frequency features, affect the spectral characteristics of the shape models that increase unrealistically the power in the high degrees due to the amplification of noise.

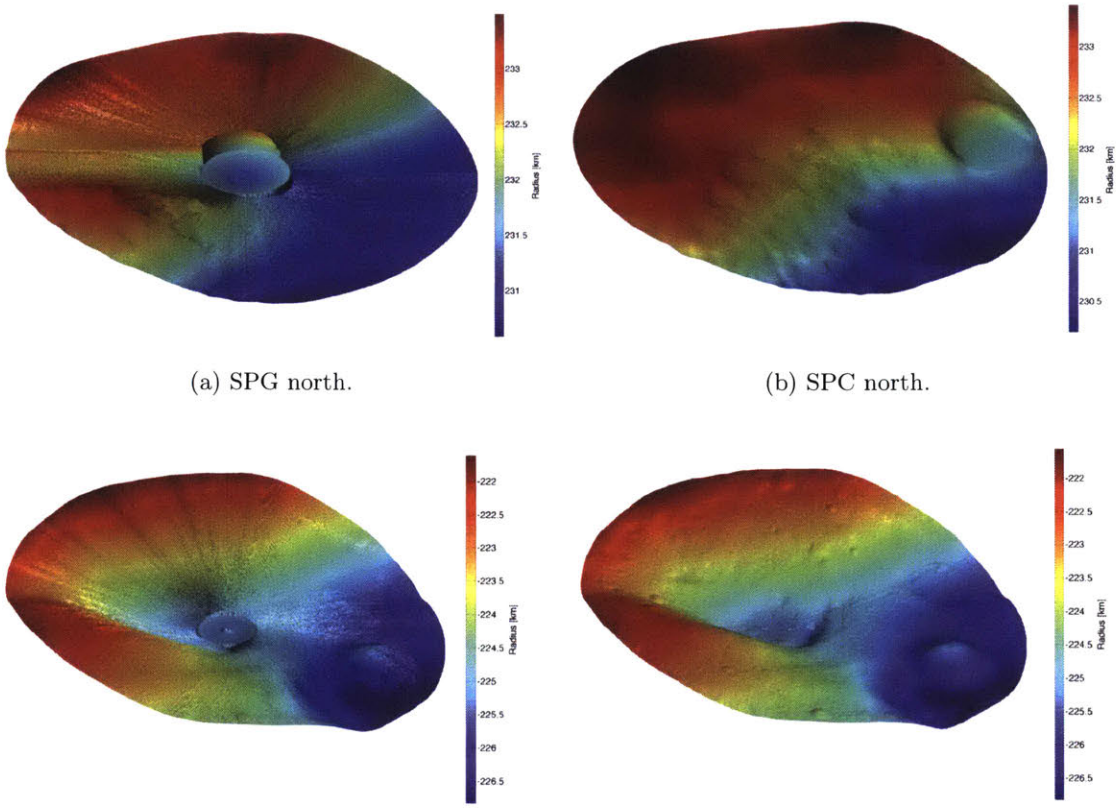

(a) SPG north.

(b) SPC north.

(c) SPG south.

(d) SPC south.

Figure 4-15 – Discontinuity at the poles is present for the SPG models. The heights of Vesta polar regions are shown in a stereographic polar projection.

4.6 Conclusions

We have analyzed the difference between the SPG and SPC shape models of Vesta and Ceres in the spectral and spatial domains. The main conclusion even after subtracting the apparent systematic differences between the SPG and SPC models, the residual differences are greater than the stated formal uncertainties of the model. After the observed systematic effects were removed:

- For the LAMO shape models of Vesta, 24% of the shape model data points have height differences between SPC and SPG less than 10 m.

- For the HAMO shape models Ceres, 5% of the shape model data points have height differences between SPC and SPG less than 20 m. A better agreement is expected for the subsequent LAMO shape models.

The SPG shape models of both Vesta and Ceres strongly deviate from isotropy at high spherical harmonic degrees. For Vesta shape models, we have observed a number of potential artifacts while comparing the SPG and SPC models. We observe a systematic torsion between the two shape models of Vesta. Additionally, there is the J_2-like difference between the SPG and SPC Vesta shapes. The SPG model is more oblate than the SPC model, the magnitude of this systematic deviation reaches as high as 150 meters. There are no such systematic differences for Ceres. The largest differences in Vesta's crater depths are in high northern latitudes where the Dawn illumination conditions were poorer. The difference reaches several kilometers in deep craters due different methods of gap filling.

While this relative analysis is useful in pointing out inconsistencies between models, it does not and cannot distinguish which model is closer to truth, because image-derived topography lacks an absolute reference. In models where image-derived topography has been compared to topographic observations from laser altimetry, long wavelengths in image-derived models are the most poorly determined.

Chapter 5

Evaluation of the GRAIL gravity models using line-of-sight data and spectral analysis

Ryan Park, Alex Konopliv and Gregory Neumann contributed to this work.

Abstract

The GRAIL (Gravity Recovery and Interior Laboratory) was NASA's mission to determine the gravity field of the Moon with unprecedented accuracy (Zuber et al., 2013; Konopliv et al., 2013; Lemoine et al., 2014). The GRAIL twin spacecrafts were launched to the Moon on a low-energy transfer trajectory on September 10th , 2011. The primary mission started on March 1st 2012 and finished on May 29th, 2012 with mean orbital altitude of 55 km and measurement cadence of 5 seconds. The extended mission started on August 30th, 2012 and finished on December 14th, 2012 with mean altitude of 23 km and measurement cadence of 2 seconds. The gravity field model is recovered by processing line-of-sight (LOS) range-rate in combination with the Deep Space Network (DSN) tracking for orbit determination. Over 6 million range-rate measurements were collected. At the time of this writing, degree and order 1200, 1500 and 1620 gravity models were produced. The goal of this chapter is to evaluate GRAIL gravity models using LOS acceleration data. First, we compute and compare the global spectral properties of the gravity and gravity from topography models. These spectral properties include power spectral density (PSD), correlation, isotropic ratio and effective density spectrum. Second, we compute localized correlation using the spectral-spatial localization method. This, in combination with the LOS magnitude squared coherence, allows the characterization how the gravity field model is correlated with topography both in spatial and spectral domain. Third, we compute

the magnitude-squared coherence for the LOS acceleration time series produced by the gravity models and by the gravity from topography model on arc-per-arc basis. It is expected that at progressively higher spherical harmonic degree (i.e. smaller spatial scale) the gravity signal is dominated by topographic variations as opposed to local density variations. The topography of the Moon is known to higher resolution than gravity due to Lunar Orbiter Laser Altimeter (LOLA) (Smith et al. (2016) and references therein) onboard of Lunar Reconnaissance Orbiter (LRO, (Chin et al., 2007)). Therefore, the gravity created by topography provides a useful reference for gravity model determination. The caveat, however, is that the density of the topographic masses is not independently known. This precludes direct comparison of the magnitudes of topographic and observed gravity potential. We find strong contributions of resonances to the coherence spectrum. The resonances occur at spherical harmonic degrees that correspond to integer multiples of spacecraft separation.

5.1 Introduction

The first model of lunar gravity dates back to the Soviet Luna-10 mission (Akim, 1966), which determined the full degree-2 field, degree-3 field except the $n = 3, m = 3$ term and the zonal degree-4 term. After that, the data from four Lunar Orbiter missions have been used to further improve the knowledge of lunar gravity (Muller and Sjogren, 1969; Lorell and Sjogren, 1968). Muller and Sjogren (1968) using a new technique of differentiating the Doppler residuals produced a gravity map of the near side and showed that the low-lying maria regions are associated with positive gravitational anomalies, which were called "mascons" for mass concentrations. The data from the Apollo 15 and 16 were also subsequently used for gravity field determination (Sjogren et al., 1974; Muller et al., 1974). Improved computational resources in the 1990s allowed determination of lunar near-side gravity up to degree-60 using the above-mentioned historical data (Konopliv et al., 1994). Later, the combination of Clementine laser altimetry data (Smith et al., 1997) with the S-band tracking data for gravity (Lemoine et al., 1994, 1997) gave new insights intro the geophysics of the Moon. It was revealed that lunar highlands are nearly compensated, whereas the impact basins possess a variety of compensation states. The crustal thickness was determined to be lower under the impact basins. In late 1990s and early 2000s, Lunar Prospector data led to further improvement of the lunar gravity models (Konopliv

et al., 2001). However, it was until the Japanese Kaguya mission that there was a large discrepancy between the precision of the gravity models for the near and far sides of the Moon due to lack of tracking data for far side. In 2007, four-way radio tracking of the main satellite in the far side and a subsatellite for very long baseline interferometry enabled for the first time a determination of the far-side gravity (Goossens et al., 2011). The Kaguya-derived models achieved global determination of the gravity field up to degree-70 (Wieczorek, 2007a). Finally, in 2011-2012 the inter-satellite tracking of the dual GRAIL spacecraft – a technique with a major heritage from the Earth's Gravity Recovery and Climate Experiment (GRACE) mission (Tapley et al., 2004) – has been used to improve the accuracy and precision of the gravity model of the Moon by an order of magnitude in terms of the achieved spherical harmonic resolution and two to three orders of magnitude in terms of accuracyZuber et al. (2013); Lemoine et al. (2013, 2014); Konopliv et al. (2013, 2014b).

The goals of this Chapter are to evaluate spectral characteristics of the GRAIL gravity models of the Moon, compute the coherence between gravity and gravity-from-topography, reveal possible artifacts in the gravity models and inform the users of the gravity models of the model limitations. We begin with the description of the available data in Section 5.2. Then, we describe methods of computing the line of sight accelerations in Section 5.3. Our results are discussed in Section 5.4. Finally, we summarize our findings in Section 5.5.

5.2 Data

5.2.1 Gravity models

We used three GRAIL gravity models produced at the Jet Propulsion Laboratory and expanded up to degree-1200, 1500 and 1620. The models were constructed by analysis of primary and extended mission data. The three gravity models used in this study differ, apart from the maximum spherical harmonic degree of expansion, in the a priori constraint applied to the gravity field spectrum. For the 1200 model,

model name	maximum degree	R_{ref} (km)	PM weights (μm/sec)	XM weights (μm/sec)
JGGRAIL_1200C12A_SHA	1200	1738.0	0.03 to 0.06	0.05
JGGRAIL_1500C13A_SHA	1500	1738.0	0.03 to 0.06	0.05
JGGRAIL_1620C14_SHA	1620	1738.0	0.03 to 0.06	0.05

Figure 5-1 – Summary of the GRAIL gravity models.

a constant constraint (10^{-9}) was applied starting at $n = 701$. For the 1500 model, a constant constraint (8×10^{-10}) was applied starting at $n = 701$. For the 1620 model, a constraint is applied starting after $n = 501$ with a zero a priori value and the a priori uncertainty of 1.25 times the gravity from topography coefficient value.

5.2.2 Gravity from shape

The gravity from topography model was provided by Greg Neumann (Goddard Space Flight Center). The model was computed keeping 15 powers of topography in the expansion using a gridded LOLA dataset. In order to estimate how many powers of topography should be kept in the expansion, we recompute gravity from topography. We estimate contributions of the powers of topography to the power spectral density and compare them to the error spectrum of the gravity model. We conclude that keeping at least 8 powers of topography is required in order to achieve the accuracy of the gravity models (Fig. 5-2).

5.3 Methods

5.3.1 Gravity acceleration

Gravitational acceleration is the gradient of the gravitational potential

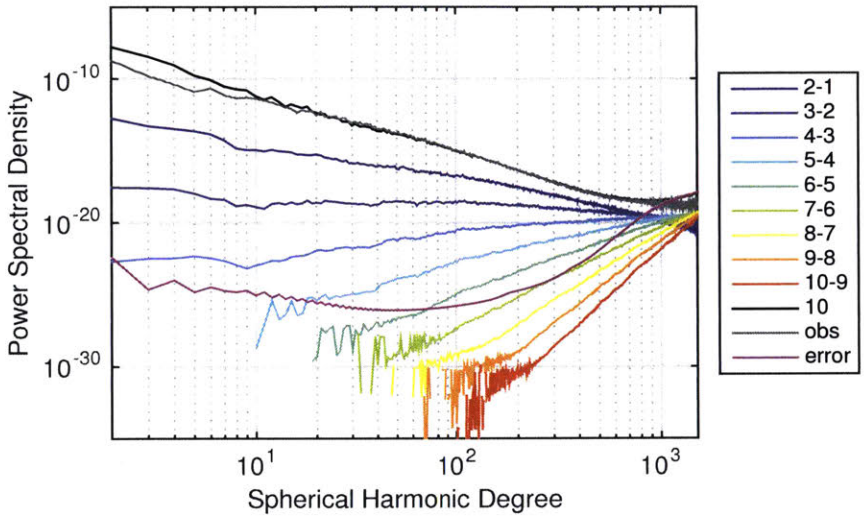

Figure 5-2 – Power spectral density contributions from the powers of topography. We show the power spectral density of the difference of the two gravity-from-shape expansion in which h and $h+1$ powers of topography were kept. Additionally, we show in black the power of the gravity-from-shape for $\max(h) = 10$. The grey curve is the power spectrum from the 1620 degree gravity model (JGGRAIL_1620C14_SHA) and the magenta curve is the error power spectrum of that model.

$$\vec{a} = \left\{ \begin{array}{c} a_x \\ a_y \\ a_z \end{array} \right\} = \vec{\nabla} U, \tag{5.1}$$

To compute the gravitational acceleration we first compute the derivatives of potential with respect to spherical coordinates. We then multiply the potential derivatives by the Jacobian of the spherical coordinates to obtain the gravity acceleration vector.

$$\vec{a} = J \left\{ \begin{array}{ccc} \frac{\partial U}{\partial \phi} & \frac{\partial U}{\partial \lambda} & \frac{\partial U}{\partial r} \end{array} \right\}^T, \tag{5.2}$$

where J is the Jacobian matrix of partial derivatives:

$$J = \left(\begin{array}{ccc} \frac{\partial \phi}{\partial x} & \frac{\partial \lambda}{\partial x} & \frac{\partial r}{\partial x} \\ \frac{\partial \phi}{\partial y} & \frac{\partial \lambda}{\partial y} & \frac{\partial r}{\partial y} \\ \frac{\partial \phi}{\partial z} & \frac{\partial \lambda}{\partial z} & \frac{\partial r}{\partial z} \end{array} \right). \tag{5.3}$$

The column of J are given by expressions:

$$\frac{\partial r}{\partial \overrightarrow{r}} = \left\{ \begin{array}{ccc} x/r & y/r & z/r \end{array} \right\}^T, \tag{5.4}$$

$$\frac{\partial \phi}{\partial \overrightarrow{r}} = \frac{1}{\sqrt{x^2+y^2}} \left\{ \begin{array}{ccc} -xz/r^2 & -yz/r^2 & 1-z^2/r^2 \end{array} \right\}^T, \tag{5.5}$$

$$\frac{\partial \lambda}{\partial \overrightarrow{r}} = \frac{1}{x^2+y^2} \left\{ \begin{array}{ccc} -y & x & 0 \end{array} \right\}^T. \tag{5.6}$$

To simplify notation we introduce:

$$\bar{A}_{nm} = \bar{C}_{nm} \cos(m\lambda) + \bar{S}_{nm} \sin(m\lambda), \tag{5.7}$$

$$\bar{A}'_{nm} = -\bar{C}_{nm} \sin(m\lambda) + \bar{S}_{nm} \cos(m\lambda). \tag{5.8}$$

The derivatives of potential are given by:

$$\frac{\partial U}{\partial \phi} = \frac{GM}{r} \left(1 + \sum_{n=2}^{\infty} \sum_{m=0}^{n} \left(\frac{R_0}{r} \right)^n \bar{A}_{nm} \frac{\bar{P}_{n+1,m} \sin(\phi)(m-n-1)\Phi_{nm} - (n+1)\sin(\phi)\bar{P}_{nm}\sin(\phi)}{\cos(\phi)} \right) \tag{5.9}$$

$$\frac{\partial U}{\partial \lambda} = \frac{GM}{r} (1 + \sum_{n=2}^{\infty} \sum_{m=0}^{n} \left(\frac{R_0}{r} \right)^n m \bar{A}'_{nm} \bar{P}_{nm} \sin(\phi) \tag{5.10}$$

$$\frac{\partial U}{\partial r} = \frac{GM}{r^2} \left(1 + \sum_{n=2}^{\infty} \sum_{m=0}^{n} \left(\frac{R_0}{r} \right)^n (n+1) \bar{A}_{nm} \bar{P}_{nm} \sin(\phi) \right). \tag{5.11}$$

where $\Phi nm = \sqrt{\frac{(2n+1)(n+m+1)}{(2n+1)(n-m+1)}}$ is the ratio of normalization factors for degree n and $n+1$.

5.3.2 Line-of-sight acceleration and range-acceleration

To derive the range-acceleration we follow Kim (2000). We start with the LOS vector:

$$\vec{\rho}_{12} = \vec{r}_1 - \vec{r}_2, \tag{5.12}$$

which can be also written as range ρ_{12} multiplied by a unit vector:

$$\vec{\rho}_{12} = \rho_{12}\hat{e}_{12}, \tag{5.13}$$

Range rate is obtained by differentiating the expression for range:

$$\dot{\rho} = \dot{\vec{r}}_{12} \cdot \hat{e}_{12}, \tag{5.14}$$

By differentiating range-rate, we obtain range acceleration:

$$\ddot{\rho} = \ddot{\vec{r}}_{12} \cdot \hat{e}_{12} + \dot{\vec{r}}_{12} \cdot \dot{\hat{e}}_{12} \tag{5.15}$$

Range acceleration can be simplified to the following expression:

$$\ddot{\rho} = \ddot{\vec{r}}_{12} \cdot \hat{e}_{12} + \frac{1}{\rho}(|\dot{r}_{12}|^2 - \dot{\rho}^2) \tag{5.16}$$

where the first term is just the LOS acceleration $g_{LOS} = \ddot{\vec{r}}_{12} \cdot \hat{e}_{12}$

5.4 Results

5.4.1 Spectral analysis

Fig. 5-3 shows the spectral density for the two gravity models as well as for the gravity from topography model as a function of spatial scale. The power of the gravity of topography model levels off at the shortest scales (≈10 km).

5.4.1.1 Correlation between gravity and topography

Fig. 5-4 shows the global correlation between the gravity models and topography as well as between gravity and gravity-from-topography. It can be seen in Fig. 5-4a that the correlation between gravity and topography quickly approaches zero at

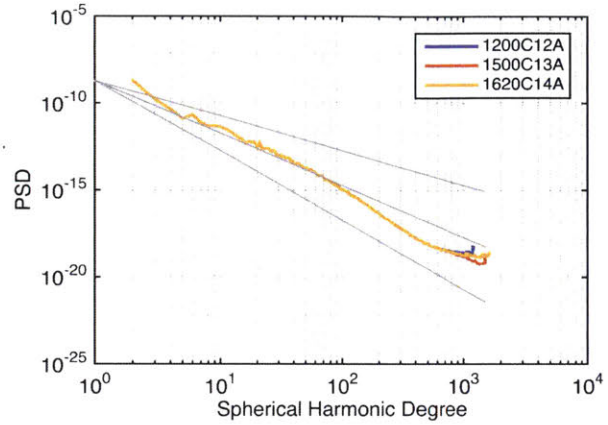

(a) Power spectra on the 1200, 1500 and 1620 degree gravity models. The grey lines are shown for the spectral slopes of -2, -3 and -4.

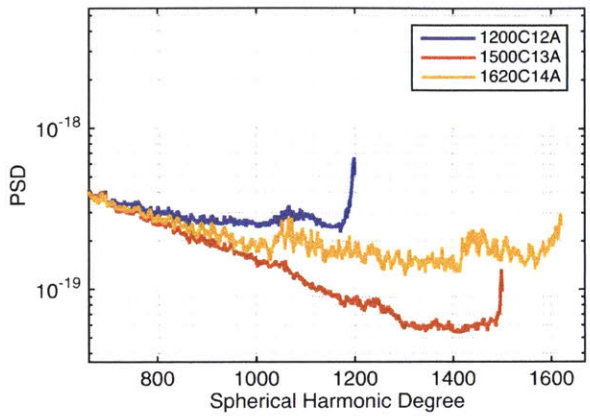

(b) Zoom-in at the high degrees.

Figure 5-3 – Power spectral density of the gravity models.

high degrees ($n > 100$), whereas the correlation between gravity and gravity-from-topography (Fig. 5-4b) is close to unity for $100 < n < 600$ and decreases at $n > 600$. This difference between the correlation spectra arises due to the importance of the finite-amplitude correction at progressively higher n. As evidenced in Fig. 5-2, the contribution of higher powers of topography is more important for high n than for low n, which leads to a strong non-linearity of gravity coefficients as a function of topography coefficients.

5.4.2 Isotropy

The isotropic ratio was in Bills and Lemoine (1995) and is a measure of directional isotropy of the variance. The North-South and East-West power are defined as follows. The isotropy coefficient is the ratio of the North-South to the East-West power. If the isotropic coefficient is greater than unity, the field has more North-South variations, if the isotropic coefficients is less than unity the field has more variation in the East-West direction.

$$I_n = \frac{I_n^{NS}}{I_n^{EW}} \tag{5.17}$$

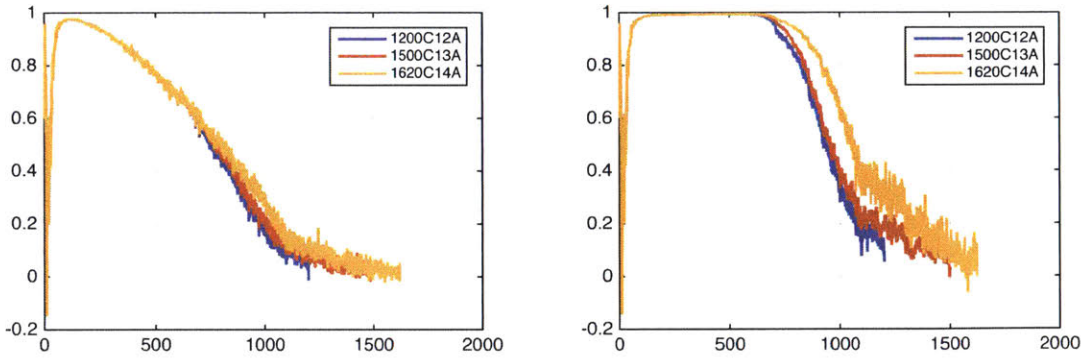

(a) Correlation between gravity models and topography.

(b) Correlations between gravity models and gravity-from-topography.

Figure 5-4 – Correlation spectrum of the gravity models.

We computed the isotropy coefficient of the GRAIL gravity modes (Fig. 5-5), LOLA-based topography model as well as for the LOLA-based gravity-from-topography model. The topography isotropic coefficient is close to unity. It becomes larger than unity at high degrees. The possible cause of this might be the fact that LOLA tracks are meridionally aligned, therefore making the North-South resolution better. However, the gravity from topography isotropic ratio steadily decreases. The isotropic ratio of the GRAIL gravity models decreases as well up to approximately degree 700. After degree 700, the isotropic ratio of the GRAIL gravity models exhibits a complex behavior with a local maximum at degree 1000 and local minimum at degree 1100.

In order to understand this significant anisotropy of the Moon's gravity and gravity-from-shape, we decided to compute isotropic ratio for the other planetary bodies that have their shape measured to high accuracy, namely for Venus, Earth and Mars. Fig. 5-6 shows the isotropic ratio for these bodies. Interestingly, Earth and Mars have strong deviations between the isotropic ratio of the shape and of the gravity-from-shape whereas Venus does not. The key characteristic that makes Venus different from the Earth and Mars is its near-sphericity due to slow rotation. In fact, if we remove the rotational flattening from the Earth and Mars, the isotropic ratio of gravity-from-shape and of the shape become closer to each other and closer to unity.

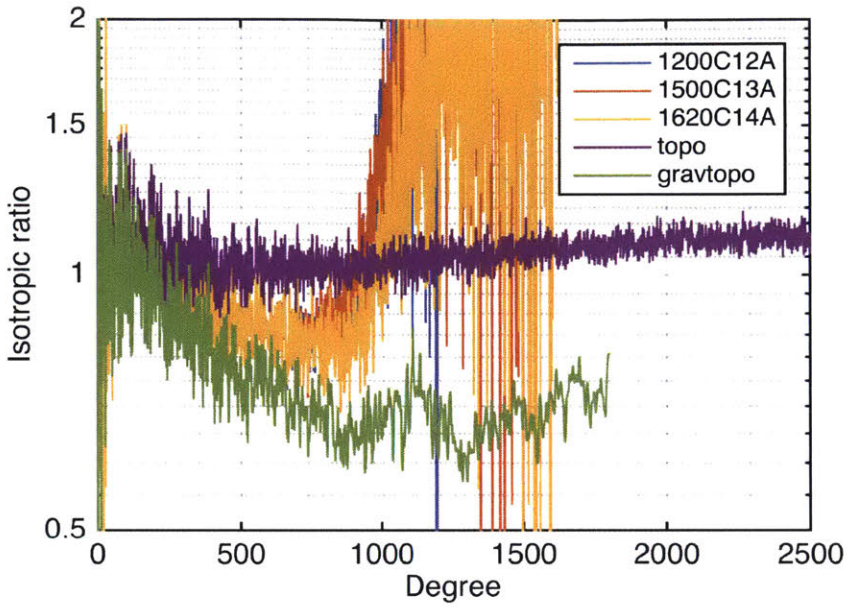

Figure 5-5 – Isotropic ratio of the gravity models and gravity from topography model.

We conclude that for highly non-spherical bodies, the gravity-from-shape is intrinsically non-isotropic according to the Bills and Lemoine (1995) definition of isotropy. Moreover, for highly non-spherical bodies, the isotropic ratio of gravity-from-shape might deviate from the isotropic ratio of the shape.

5.4.3 Effective density

The effective density spectrum is defined as the ratio of the gravity power to the gravity from topography power multiplied by the mean density of the body:

$$\rho_n = \frac{M_n^G}{M_n^{GT}} \bar{\rho} \tag{5.18}$$

Given an assumption about the character of the density profile (e.g. linear or exponential increase of density with depth), the effective density spectrum can be used to invert for the density structure (Besserer et al., 2014). Fig. 5-7 shows the effective density spectra for the GRAIL gravity models. The lower degrees have rapid oscillations of the effective density due to the density anomaly effect from the maria.

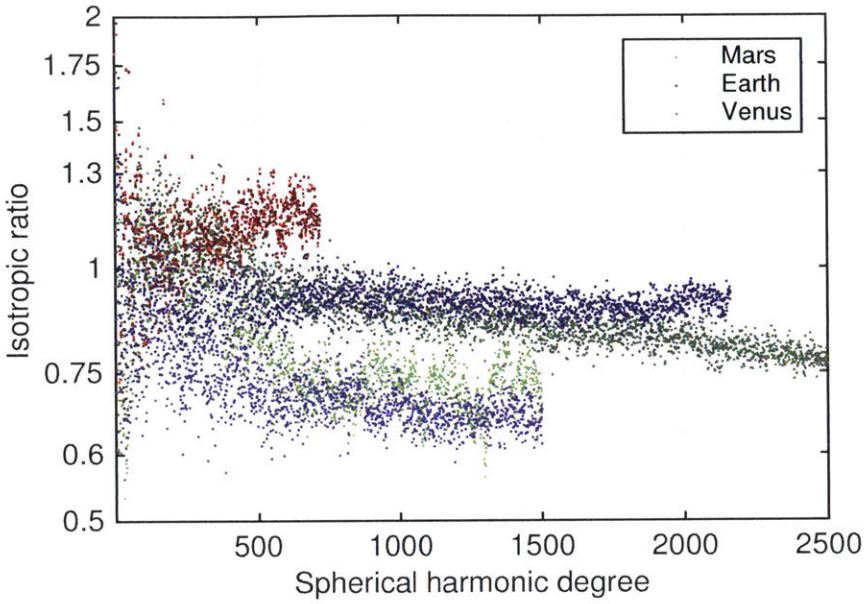

Figure 5-6 – Isotropic ratio for the gravity-from-shape of Mars, Earth and Venus. The brighter colors correspond to the isotropic ratio of the gravity-from-shape. The darker colors correspond to the isotropic ratio of the shape.

The higher harmonics sample shallower structures, therefore in the band from degree 100 to 700 the effective density spectrum shows a steady decrease. After degree 700, the effective density spectra start to diverge. This can be explained by the fact that the different constraints were applied to the models after degree 700.

The Bouguer anomaly is the difference between the observed gravity and gravity induced by topography. In order to compute the Bouguer anomaly, a crustal density needs to be assumed. Typically, a constant density crust is assumed. However, as can be seen in Fig. 5-7, the effective density decreases with spherical harmonic degree. This leads to a bias in the Bouguer anomaly if a constant density is assumed: the low degrees get underweighted and the high degree overweighted. As a result, the Bouguer anomaly is correlated with topography (Fig. 5-9). The Bouguer anomaly is positively correlated with topography at low degrees and negatively correlated at high degrees. The correlation spectrum crosses zero at the spherical harmonic degree at which the effective density is equal to the assumed crustal density.

We propose a correction to the Bouguer anomaly in order to compensate for the

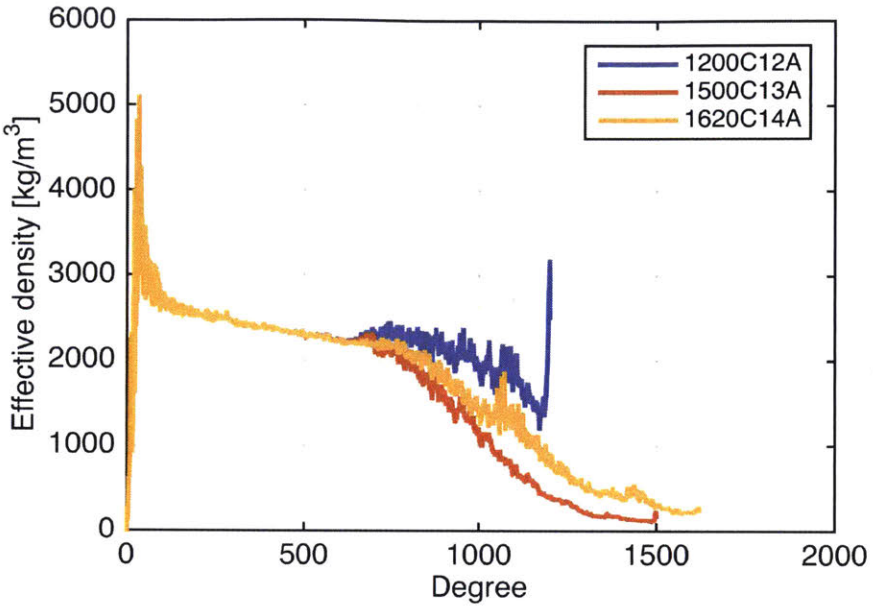

Figure 5-7 – Global effective density spectrum for the three JPL GRAIL gravity models.

degree dependence of the effective density spectrum. In order to do so, we first fit the global effective density spectrum with a polynomial within the range where the effective density spectrum behaves linearly (see Fig. 5-8) and then weight the gravity-from-topography according to the fit of the effective density:

$$\sigma_n^{corrected\,BA} = \sigma_n^{obs} - \sigma_n^{shape}(\rho_{crust}) \cdot \frac{\rho_n}{\bar{\rho}}, \tag{5.19}$$

where $\sigma_n^{shape}(\rho_{crust})$ are the coefficients of the gravity-from-shape computed for the crustal density ρ_{crust}.

This effectively decorrelates the Bouguer anomaly from topography (Fig. 5-9). Alternatively, a corrected Bouguer anomaly can be computed regionally given a localized effective density spectrum.

Correlation of the Bouguer anomaly with topography is problematic for studies that focus on comparing the Bouguer anomaly of features at different spatial scales. For example, Soderblom et al. (2015) studied the residual Bouguer anomaly in the highland craters and found that the residual Bouguer anomaly has a weak dependence

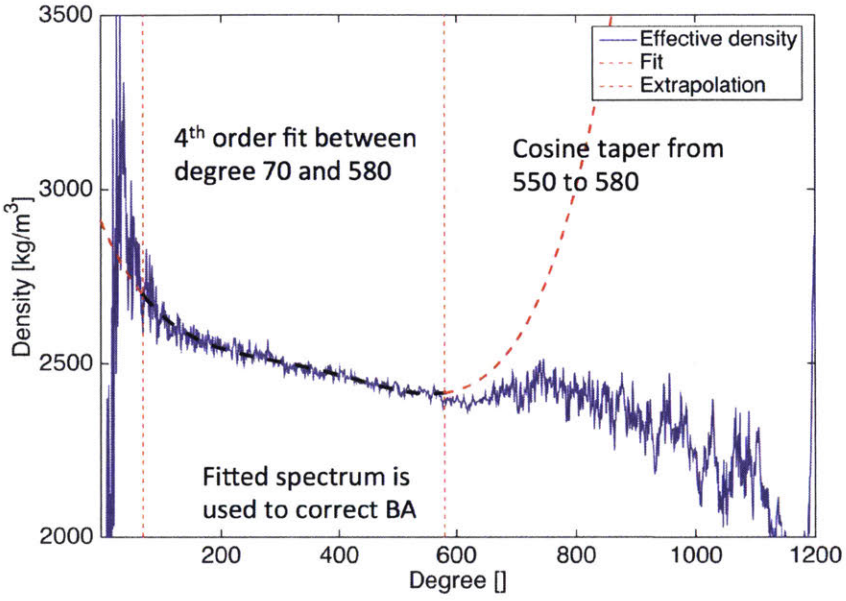

Figure 5-8 – Fitting global effective density spectrum with a 4-th order polynomial.

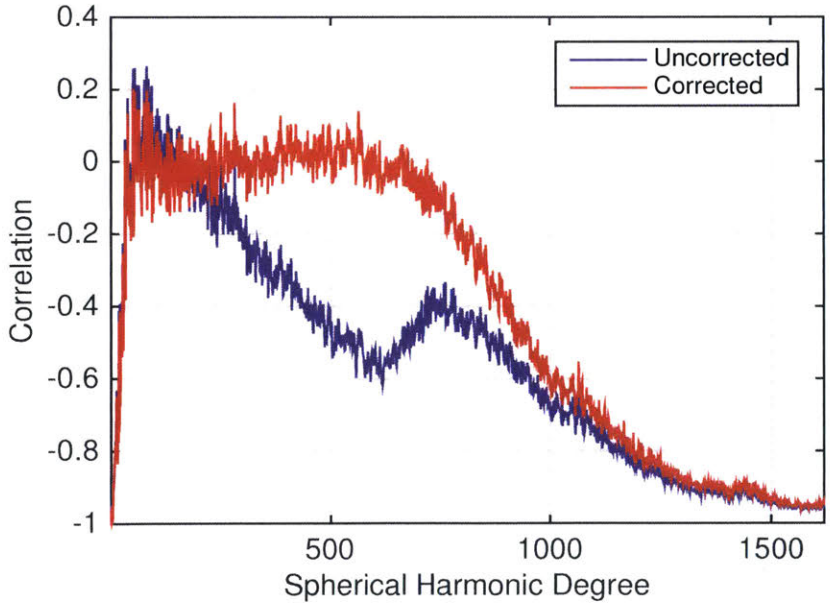

Figure 5-9 – Correlation of the uncorrected and corrected Bouguer anomaly with gravity-from-topography. The uncorrected Bouguer anomaly was computed for $\rho = 2550$ kg/m^3.

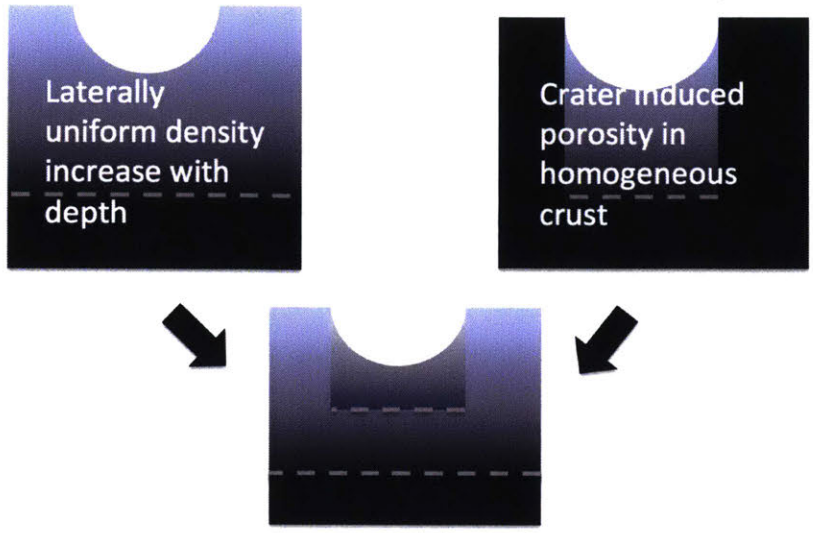

Figure 5-10 – Nature of porosity in the crust and under a crater.

on the crater diameter (Fig. 5-11a). We have repeated the analysis of Soderblom et al. (2015) with a corrected Bouguer anomaly field. As seen in Fig. 5-11, the correlation of the residual Bouguer anomaly with crater diameter is reduced but not vanished when the corrected Bouguer anomaly field is used. (Fig. 5-11). This leads us to a better understanding of the intracrustal porosity field. The porosity field is composed of two components: the first is the bulk decrease of porosity with depth, the second is the impact induced porosity under individual craters (Fig. 5-10).

5.4.4 Spectral-spatial localization using Slepian functions

We used the spectral-spatial localization technique (Wieczorek and Simons, 2005; Simons and Dahlen, 2006; J.S., 2014) to find the localized correlation spectra with help of Slepian functions. Slepian functions have been previously used for localized gravity-topography analysis of the GRAIL and LOLA data (Besserer et al., 2014; Gong et al., 2016). First, we used icosahedron tessellation of a sphere to find the centers of localization windows (Fig. 5-12) The use of icosahedron tessellation has two main advantages. First, it is easily implementable in a recursive procedure. Second,

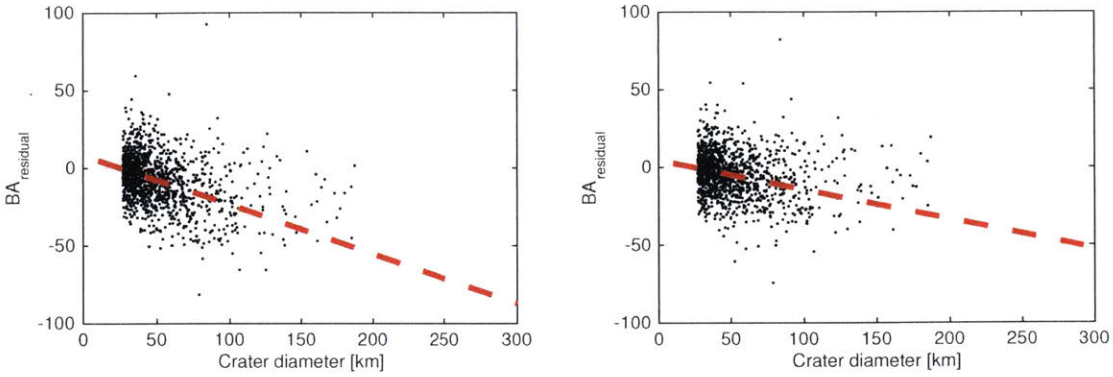

(a) Residual Bouguer anomaly in the highland crater for the Bouguer anomaly.

(b) Residual Bouguer anomaly in the highland crater for the corrected Bouguer anomaly.

Figure 5-11 – Residual Bouguer anomaly in the highland crater for the Bouguer anomaly and corrected Bouguer anomaly.

it allows quasi-uniform sampling of a sphere as opposed to geographic grid sampling. The gravity and gravity from topography fields were localized in spherical cap windows with a radius of 9 degrees. The localized correlation spectra were interpolated from the localization centers to a regular grid using spherical harmonic expansion of degree 45. Fig. 5-13 shows all 2556 localized spectra. Fig. 5-14-5-16 show the interpolated correlation coefficient for degrees 50, 300, 900, respectively.

At lower degrees, the correlation is dominated by the maria signal (Fig. 5-14). The correlation approaches unity after degree 100 almost uniformly over the surface of the Moon (Fig. 5-15). The correlation starts to decrease first on the near side, most noticeably in the maria regions in the South Pole-Aitken basin at degree 500 and higher (Fig. 5-16). The topography in these regions is low with respect to the mean sphere, therefore spacecraft altitudes were larger making GRAIL less sensitive to the gravity signal. On the other hand, the strongest correlation is observed in the highlands.

5.4.5 Gravity gradiometry

The spatial pattern of correlation (Fig. 5-14–5-16) manifests itself in the gravity gradients which are particularly sensitive to small-scale structures. Gravity gradients

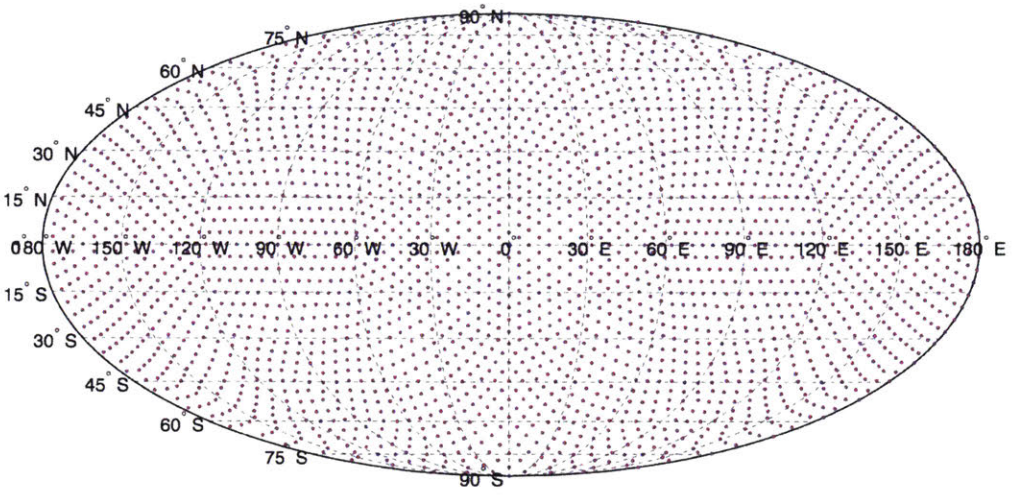

Figure 5-12 – Localization window centers. Uniformity is achieved with a icosahedron tessellation.

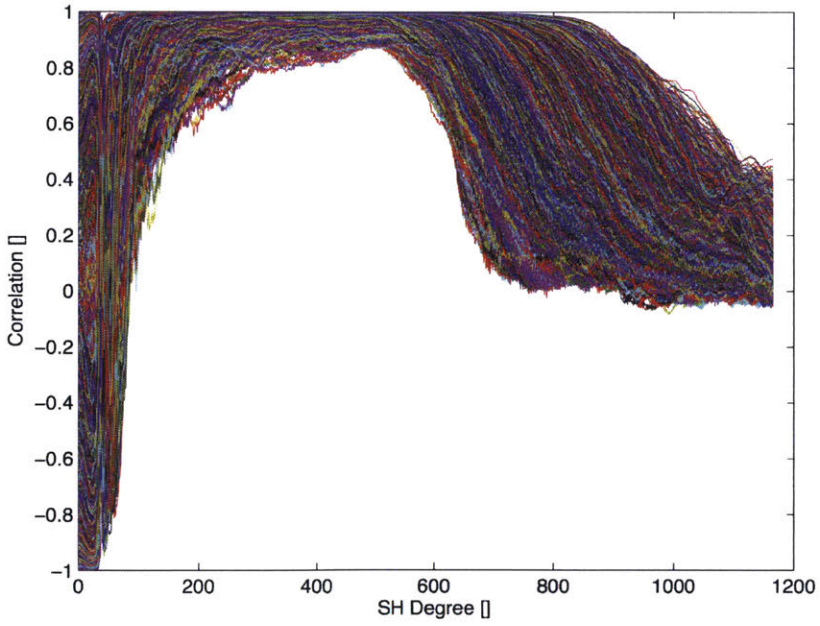

Figure 5-13 – Localized correlation spectra.

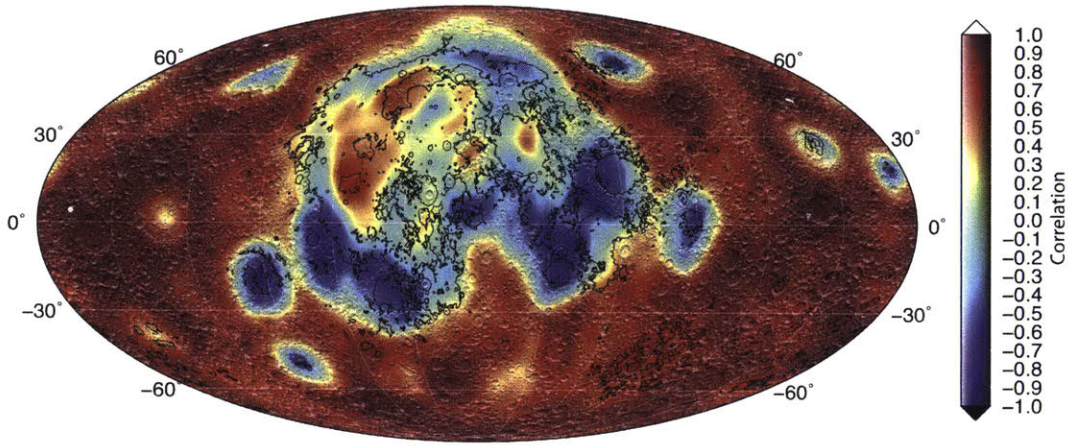

Figure 5-14 – Localized correlation at degree 50. Black contours are the maria outlines.

Figure 5-15 – Localized correlation at degree 300. Black contours are the maria outlines.

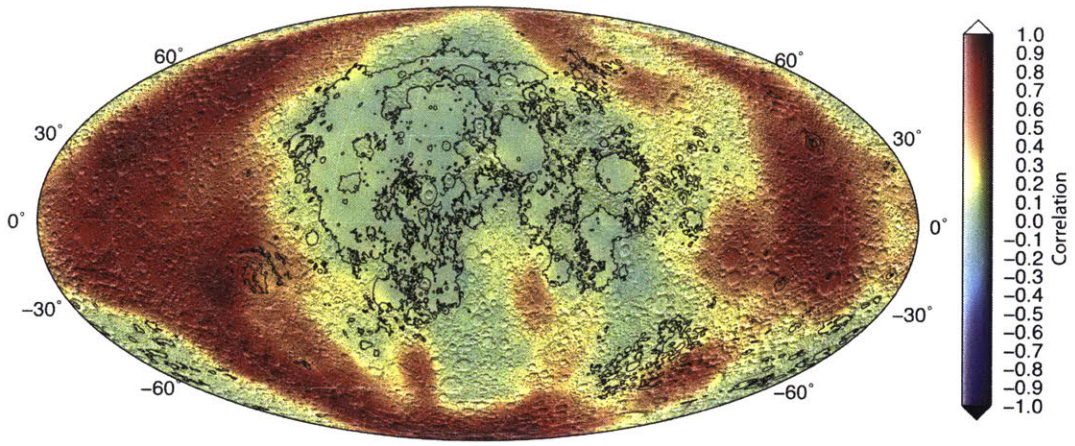

Figure 5-16 – Localized correlation at degrees 900. Black contours are the maria outlines.

are second derivatives of the gravitational potential (see Section 2.7). Fig. 5-17 shows the two ways of computing the gravity gradients and illustrates characteristic numerical problems. In Fig. 5-17a, the maximum amplitude gravity gradient eigenvalue λ_{max} (see Eq. 2.38) is mapped onto a sphere with a radius of 1738 km. The lunar highlands lie typically 5-10 km above this sphere. Therefore, the high frequency geological noise is significantly amplified due to downward continuation in these regions making such a map useless in the highlands. To tackle this problem we can compute the λ_{max} at the actual surface of the Moon, which results in the map shown in Fig. 5-17b. Apparent noisiness is reduced and is more uniformly distributed. However, another problem is evident: there is still significant noise in the regions with low degree strength and low correlation (Fig. 5-16), primarily in the maria and the South Pole-Aitken (SP-A) basin.

5.4.6 Coherence on arc-per-arc basis

Up to this point we have used the global expansions of the GRAIL gravity models. However, it is advantageous to evaluate the gravity models at the locations where the inter-satellite measurements were collected in order to avoid the errors associated with off-track interpolation. Computing LOS accelerations between the GRAIL spacecraft

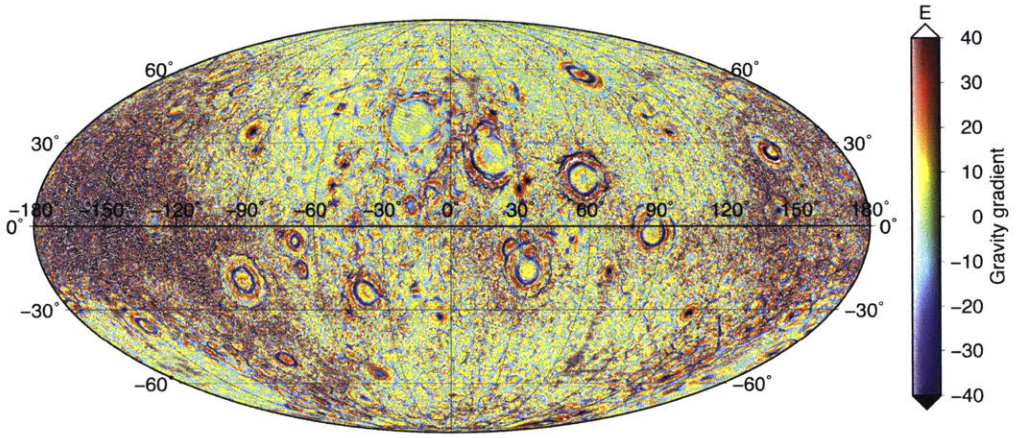

(a) Maximum amplitude gravity gradient computed at the spherical surface with a radius of 1738 km.

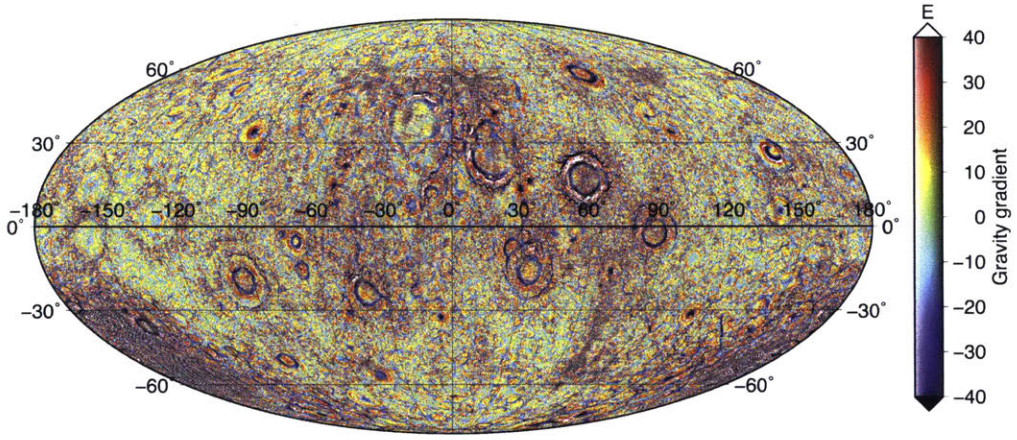

(b) Maximum amplitude gravity gradient computed at the actual surface of the Moon.

Figure 5-17 – Map of the maximum amplitude eigen value λ_{max} of the horizontal Eötvös tensor

provides a way to investigate the surface and subsurface structures at the highest possible resolution achievable with GRAIL data.

We computed the range-acceleration for the primary (PM) and extended mission (XM) using the gravity and gravity from topography models. Range accelerations have been previously used to estimate local density and porosity variations (Han, 2013; Han et al., 2014). We compute the magnitude-squared coherence for the two time series using the Welch's periodogram method Welch (1967). This allows us to study the gravity-topography relationship on arc-per-arc basis. Since the spacecraft orbit is nearly circular, the orbital velocity (v_{orb}) of the spacecraft is nearly constant.

$$v_{orb} = \sqrt{\frac{GM}{R+h}}, \tag{5.20}$$

where h is the spacecraft altitude, M is the mass of the Moon, R is the radius of the Moon and G is the gravitational constant. Therefore, we can easily translate the time frequency of measurements f to spatial frequency and spherical harmonic degree:

$$n = \frac{2\pi(R+h)f}{v_{orb}}. \tag{5.21}$$

We can compute the maximum spherical harmonic degree for which the Nyquist sampling condition is satisfied. Taking the appropriate values for the XM ($v_{orb} \approx 1.6$ km/s, h=23 km, and $f = 0.5$ Hz), we get $n_{Nyquist} = 1656$.

The coherence was computed using Matlab mscohere routine with a segment length of 4096 samples using the Hamming window and 50% overlap. Fig. 5-18-5-20 show coherence computed for two arcs of the XM. The drops of coherence occur at the degrees that correspond to integer multiples of the spacecraft separation. It is interesting to note that the drops of coherence are not observed in all arcs (e.g Fig. 5-20). The resonant degrees n_{res} are shown as green vertical lines. The resonant degrees are defined as:

$$n_{res} = \frac{2\pi R}{d}m, \tag{5.22}$$

where d is the spacecraft separation and m – the resonance order – is a positive

integer. The coherence drops occur only at degrees higher than 500 where the model is dominated by the XM data (Fig. 5-18-5-19).

5.5 Conclusions

The GRAIL gravity models are not consistent with a single power law. We analyzed degree 1200, 1500 and 1620 GRAIL gravity models. The gravity models power spectra are similar up to degree 700. After degree 700 the difference in power spectra is caused by different constraints applied to the models. The improvement in coherence between 1200 and 1620 is not uniform. The biggest improvement is in the low altitude Orientale arc. The near side always has a lower coherences than the far side due to the presence of low-lying maria.

The isotropic ratio is puzzling; it decreases at smaller spatial scales for both gravity models and the gravity-from-topography model. However, the isotropic ratio of lunar topography remains at nearly unity. We conclude that for highly non-spherical bodies, the gravity-from-shape is intrinsically non-isotropic according to the Bills and Lemoine (1995) definition of isotropy. Moreover, for highly non-spherical bodies, the isotropic ratio of gravity-from-shape can deviate from the isotropic ratio of the shape.

Spectral-spatial localization with Slepian functions allowed us to study correlation of gravity and topography both spectrally and spatially. The correlation coefficient starts to decrease at degrees between 500 and 800, first in the maria and SP-A regions and later in the highlands. We computed the magnitude-squared coherence for all arcs of the mission.

Perhaps, the most interesting effect is observed in the XM arcs. For certain arcs the coherence spectrum drops substantially at degrees corresponding to integer multiples of the spacecraft separation. The spacecraft separation was variable during the PM but relatively constant during the XM. Therefore, the coherence drops are observed only at degrees after 500 where the models are dominated by XM data. The arc coherence is highly variable: coherence can be as high as 0.9 at $n = 1200$ for certain arcs and be as low as 0.5 at $n = 800$ for other arcs.

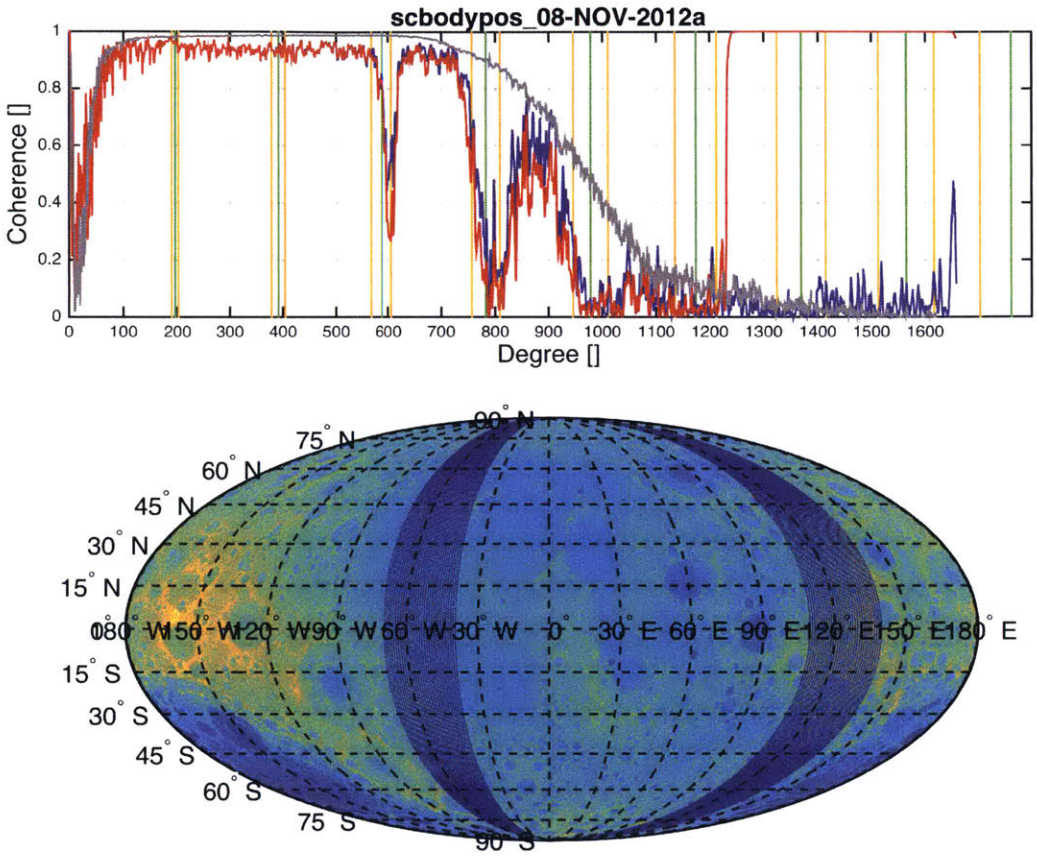

Figure 5-18 – Magnitude-squared coherence for the 08-NOV-2012 arc. The vertical green lines at the top graph represent the resonant degrees that correspond to the mean spacecraft separation and the yellow vertical lines correspond to the minimum and maximum separation for this arc. The red and blue curves are coherences for the 1200 and 1620 degree gravity models. The grey curve is the global coherence. The bottom graph shows the ground track of the arc.

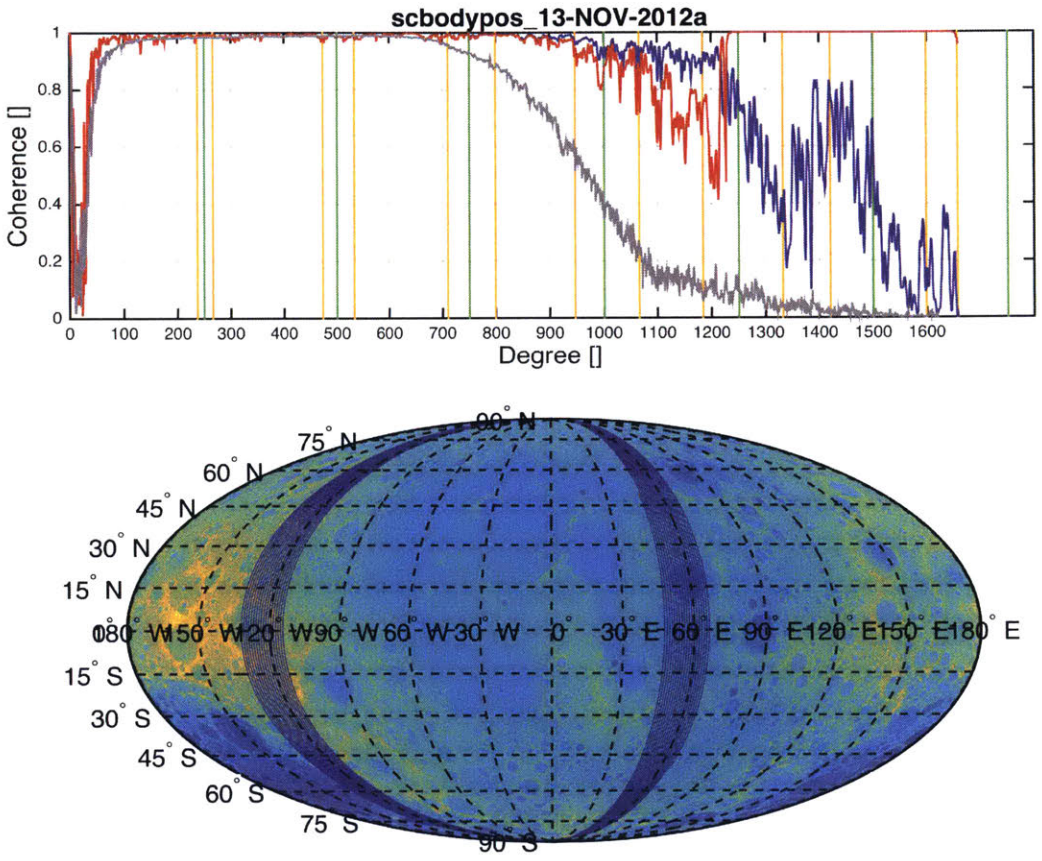

Figure 5-19 – Magnitude-squared coherence for the 13-NOV-2012 arc. For this arc, the arc coherences are significantly larger than the global coherence. The vertical green lines at the top graph represent the resonant degrees that correspond to the mean spacecraft separation and the yellow vertical lines correspond to the minimum and maximum separation for this arc. The red and blue curves are coherences for the 1200 and 1620 degree gravity models. The grey curve is the global coherence. The bottom graph shows the ground track of the arc.

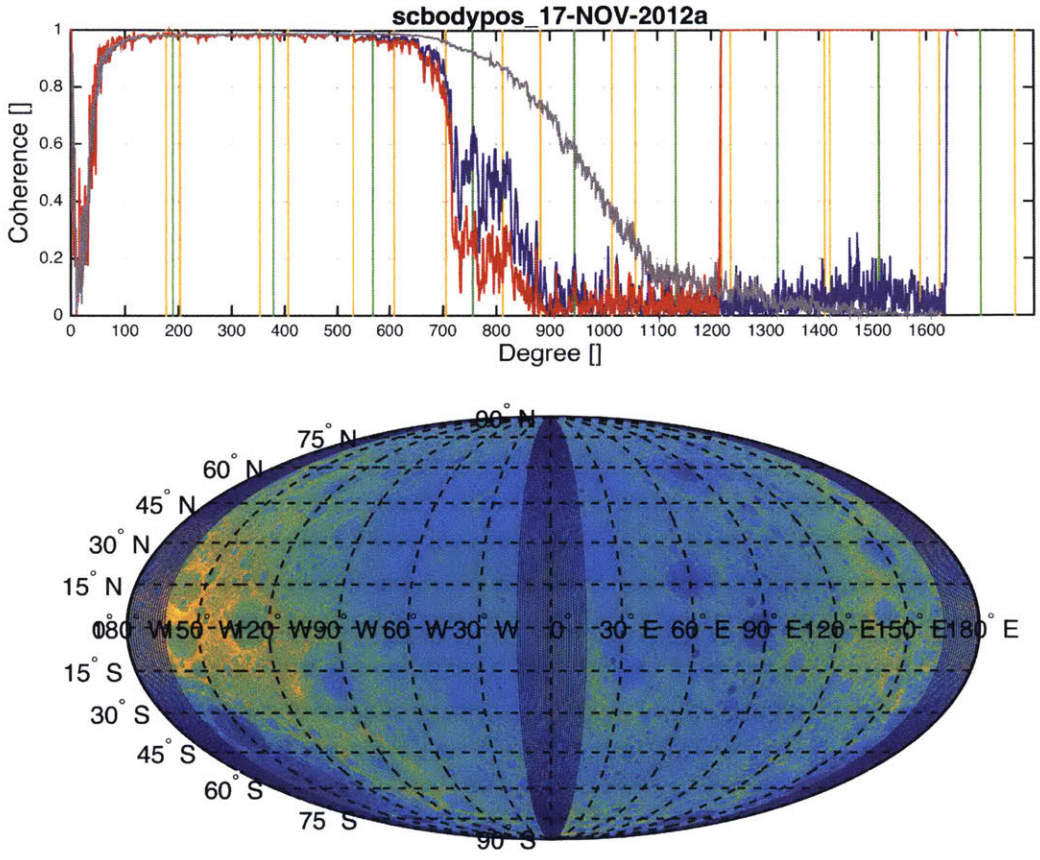

Figure 5-20 – Magnitude-squared coherence for the 17-NOV-2012 arc. For this arc, the arc coherences are significantly lower than the global coherence. The vertical green lines at the top graph represent the resonant degrees that correspond to the mean spacecraft separation and the yellow vertical lines correspond to the minimum and maximum separation for this arc. The red and blue curves are coherences for the 1200 and 1620 degree gravity models. The grey curve is the global coherence. The bottom graph shows the ground track of the arc.

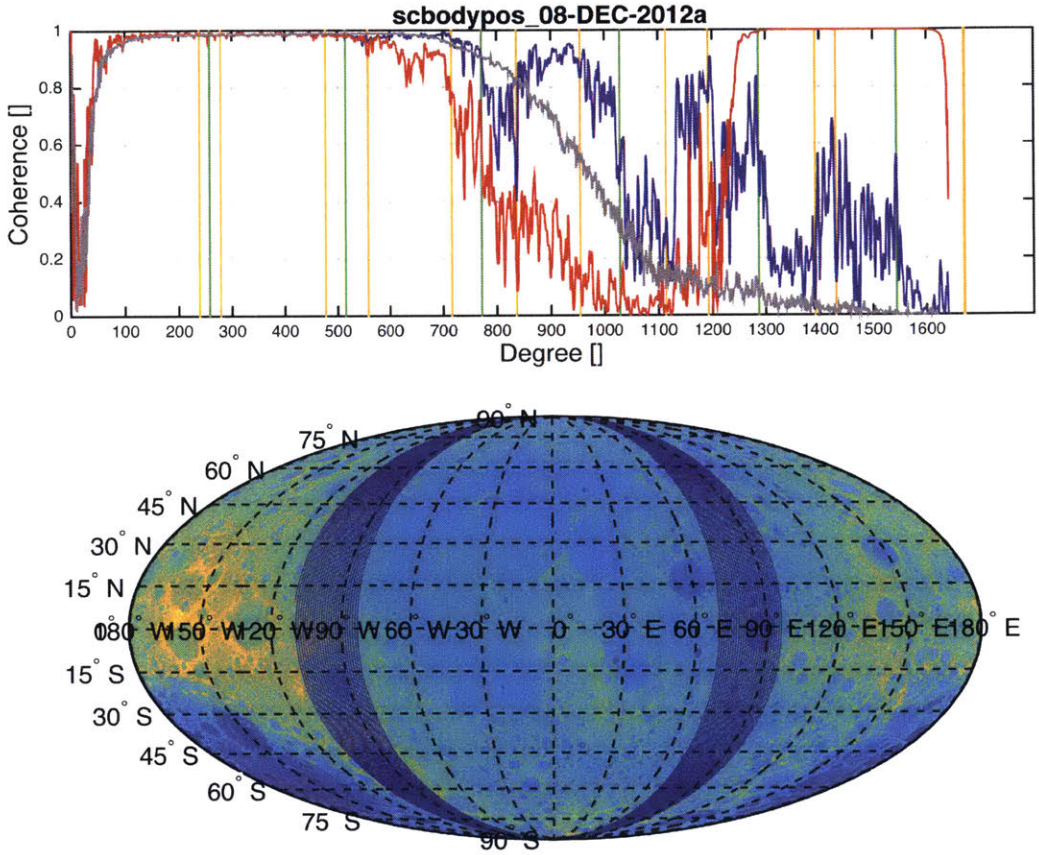

Figure 5-21 – Magnitude-squared coherence for the 08-DEC-2012 arc. This is one of last arcs in the XM. The mean altitude for this arc was 8.8 km for the near side and 12.8 km for the far side. The vertical green lines at the top graph represent the resonant degrees that correspond to the mean spacecraft separation and the yellow vertical lines correspond to the minimum and maximum separation for this arc. The red and blue curves are coherences for the 1200 and 1620 degree gravity models. The grey curve is the global coherence. The bottom graph shows the ground track of the arc.

Chapter 6

Constraints on Ceres' internal structure and evolution from its shape and gravity measured by the Dawn spacecraft

Roger Fu, Carol Raymond, Ryan Park, Frank Preusker and Julie Castillo-Rogez contributed to this work.

Abstract

Ceres is the largest body in the asteroid belt with a radius of approximately 470 km. In part due to its large mass, Ceres more closely approaches hydrostatic equilibrium than other major asteroids. Pre-Dawn mission shape models of Ceres revealed a shape consistent with a hydrostatic ellipsoid of revolution. Since March 2015, images from the Framing Camera (FC) of the Dawn spacecraft have been used to construct shape models of Ceres with a resolution of 130 meters/pixel, while the gravity field of Ceres has been accurately determined to a spherical harmonic (SH) degree-12 (Park et al., 2016; Konopliv, 2016).

Here we use these shape and gravity models to constrain Ceres' internal structure. We find a negative correlation and admittance between topography and gravity at degree-2 and order-2. Low admittances between SH degrees 3 and 12 are well explained by an Airy isostasy mechanism with a $46.3^{+4.9}_{-5.0}$ km thick shell that has a density of 1379^{+50}_{-45} kg/m^3, overlying a $423.7^{+5.0}_{-4.9}$ km radius core with a density of 2442^{+56}_{-52} kg/m^3. At the same time, the topographic power spectrum of Ceres and

its latitude-dependence suggest that viscous relaxation occurred at the longest wavelengths (>100 km). Viscoelastoplastic finite element (FE) modeling of the viscous relaxation process on Ceres suggests that the rheology of the shallow surface is most consistent with a rock, ice, salt and methane clathrate mixture (Fu et al., 2016). Based on this constraint, we show that the minimum density of the cerean core is 2415 kg/m^3 while the shell has a minimum thickness of 29 km, which is consistent with the thickness inferred from admittance analysis.

6.1 Introduction

Ceres possesses both asteroid- and planet-like properties. It is sufficiently large to attain a shape close to hydrostatic equilibrium, similar to planets. However, its surface is uniformly heavily cratered, more resembling asteroid surfaces. Ceres' mean density of 2161 kg/m^3 (Park et al., 2016) and its location in the Solar System ($\approx$2.8 AU from the Sun) indicate that it likely consists of a combination of silicates and water ice. McCord and Sotin (2005) estimate that Ceres has from 17% to 27% of free water by mass. In this respect, Ceres is similar to icy satellites or even Trans-Neptunian Objects (TNOs, see McKinnon 2008). Important factors in the evolution of Ceres as identified in McCord et al. (2011); Castillo-Rogez and McCord (2010); Neveu and Desch (2015) include: 1) the abundance of water in its interior, which controls internal dynamics and energy transport; 2) the time of accretion, which determines the abundance of short-lived radioactive nuclides (^{26}Al, ^{60}Fe) constituting the dominant heat source during the early epoch of evolution; 3) the amount of long-lived radioactive elements (^{40}K,^{232}Th,^{235}U,^{238}U) that provide a continuous heat source throughout all of Ceres evolution; and 4) the surface temperature, an important boundary condition. In this paper, we address constraints on the internal structure and composition of Ceres from shape and gravity measurements from the Dawn mission.

Two end-member models of Ceres' internal structure have been proposed. In the model proposed by McCord and Sotin (2005) and elaborated in Castillo-Rogez and McCord (2010), Ceres accreted as a mixture of ice and rock just a few My after the condensation of Calcium Aluminum-rich Inclusions (CAIs), and later differentiated into a water mantle and a mostly hydrated silicate core. The possibility of an inner

iron core was excluded based on the pre-Dawn shape measurements (Thomas et al., 2005). In the second model presented in Zolotov (2009), Ceres formed relatively late from planetesimals consisting of hydrated silicates. This model suggests that Ceres could have undergone little internal evolution and is today made up of porous hydrated silicates and has no free volatiles. These two end-member models predict different degrees of physical differentiation: the former being more differentiated and the latter more homogeneous.

The two models also predict different surface morphologies. In the first model, viscous relaxation is expected to be important in the outer icy shell whereas little viscous relaxation is expected for the second model. Bland (2013) predicts that craters as small as 4 km in diameter should be substantially relaxed and, in addition, suggests that there should be a strong latitude-dependent variation of crater morphology due to the change in surface temperature within the icy shell.

A number of techniques had been used prior to Dawn to determine Ceres' radius and shape (see Section 6.2). Ground and space-based telescopic observations revealed that Ceres has a shape consistent with hydrostatic equilibrium to the measurement accuracy (Thomas et al., 2005; Carry et al., 2008; Drummond et al., 2014). Images from the Dawn spacecraft Framing Camera (FC) suggest that there is a substantial non-hydrostatic component in the shape of Ceres.

Gravity and shape data provide constraints on the internal structure and the degree of physical differentiation. Internal structure models can be parameterized in a number of ways. For this paper, we chose a two-layer model with uniform density layers, which is the most parsimonious model of a differentiated Ceres than can explain the data. Such a model has only five parameters: two densities, two radii and the rotation rate of the body. While some previous work (e.g., Castillo-Rogez and McCord (2010)) has invoked more complicated internal structure models, we stress the inherent problem of solution non-uniqueness when solving for free parameters given constraints only from gravity and shape data, particularly when only low degree data is available.

This chapter is organized as follows: we describe the available data in Section

6.2; results are presented in Section 6.3; we discuss the implications of our results in Section 6.4 and make conclusions in Section 6.5.

6.2 Data

6.2.1 Shape model

Size and shape determinations of Ceres have been documented previously in the literature beginning with filar micrometer measurements by Barnard (1895). Later, lunar occultations (Dunham et al., 1974), polarimetry (Morrison and Zellner, 1979), radio (Johnston et al., 1982), infrared imaging (Brown et al., 1982; Lebofsky et al., 1984), stellar occultations (Millis and et al., 1987), adaptive optics systems (Saint-Pe et al., 1993; Drummond et al., 1998; Carry et al., 2008; Drummond et al., 2014), radar (Mitchell et al., 1996), and Hubble Space Telescope observations (Parker et al., 2002; Thomas et al., 2005) were used to determine Ceres' size and shape. Some of the methods were sensitive only to Ceres' radius, others were able to constrain the body's shape, typically approximating it with an ellipsoid of revolution, with an exception of Drummond et al. (1998), who attempted to solve for a triaxial ellipsoid. Table 6.1 summarizes pre-Dawn Ceres' shape determinations in the chronological order.

Source	r_{vol} (km)	$a = b$ (km)	c (km)	$(a - c)/a$
Barnard (1895)	391 ± 44	–	–	N/A
Dunham et al. (1974)	600 ± 125	–	–	N/A
Morrison and Zellner (1979)	508 ± 25	–	–	N/A
Johnston et al. (1982)	409 ± 41	–	–	N/A
Brown et al. (1982)	477 ± 25	–	–	N/A
Lebofsky et al. (1984)	481 ± 15	–	–	N/A
Millis and et al. (1987) (solution 1)	468.9 ± 2.1	479.6 ± 2.2	453.4 ± 4.5	0.0546 ± 0.0103
Millis and et al. (1987) (solution 2)	470.9 ± 1.7	481.6 ± 2.4	450.1 ± 2.0	0.0644 ± 0.0062
Saint-Pe et al. (1993)	489 ± 14	499 ± 20	469 ± 20	0.0601 ± 0.0550
Mitchell et al. (1996)	471 ± 14	480 ± 11	454 ± 5	0.0542 ± 0.0454
Drummond et al. (1998) (solution 1)	486.3 ± 6.4	490.4 ± 8.3	445.5 ± 5.0	0.0915 ± 0.0184
Drummond et al. (1998) (solution 2)	486.0 ± 6.0	489.4 ± 7.6	445.5 ± 5.0	0.0897 ± 0.0174
Parker et al. (2002)	478.6 ± 3.9	484.8 ± 5.1	466.4 ± 5.9	0.0380 ± 0.0158
Thomas et al. (2005)	476.2 ± 1.3	487.3 ± 1.8	454.7 ± 1.6	0.0669 ± 0.0045
Carry et al. (2008)	467.6 ± 1.6	479.7 ± 2.3	444.4 ± 2.1	0.0736 ± 0.0062
Drummond et al. (2014)	470.6 ± 3.7	483.5 ± 5.0	446.0 ± 5.0	0.0776 ± 0.0141

Table 6.1 – Ceres' shape determinations prior to Dawn. 1σ uncertainties are shown.

Since the arrival of the Dawn spacecraft at Ceres in May 2015, images from the Framing Camera were used to construct Ceres shape model using two techniques. The first technique is stereophotogrammetry (SPG) used by the German Aerospace Center (DLR) (Preusker et al., 2015, 2016). The second technique is stereophotoclinometry

used by NASA's Jet Propulsion Laboratory (JPL) (Park et al., 2016). We compute ellipsoidal fits to the shape models. The results of these fits are shown in Table 6.2 and 6.3.

Model	R_{vol} (km)	a (km)	b (km)	c (km)	$(a-c)/a$	$(a-b)/a$	volume (10^8 km^3)	mean density (kg/m^3)
SPC Survey (JPL)	469.79	483.02	481.29	446.01	0.0766	0.0036	4.3429	2161
SPG Survey (DLR)	469.71	483.05	480.90	446.10	0.0765	0.0044	4.3403	2162

Table 6.2 – Parameters of ellipsoid fits for Ceres' shape models constructed from the FC images. R_{vol} is the radius of a sphere that has the same volume as the best-fit ellipsoid.

Model	Δx (km)	Δy (km)	Δz (km)	$\Delta \vec{r}$ (km)	λ_a (°)	λ_b (°)	λ_c (°)	ϕ_a (°)	ϕ_b (°)	ϕ_c (°)
SPC Survey (JPL)	-0.66	-0.33	0.60	0.95	46.49	136.50	132.82	-0.01	-0.81	89.19
SPG Survey (DLR)	-0.85	-0.41	0.38	1.02	45.50	135.50	133.55	-0.04	-0.67	89.33

Table 6.3 – Ellipsoid center coordinates and axes' orientation for Ceres' shape models constructed from the FC images. λ is longitude and ϕ is latitude.

Observations prior to the Dawn mission indicated that Ceres' shape is oblate and consistent with a hydrostatically-relaxed body. However, the accuracy of the pre-Dawn shape determinations did not allow a robust estimation of non-hydrostatic ef-

fects such as tri-axiality. Nevertheless, the determined rotationally-symmetric shapes in combination with the hydrostatic equilibrium assumption have been cited as evidence for differentiation of the body (Thomas et al., 2005; Carry et al., 2008). In all pre-Dawn shape determinations the formal error of the ellipsoidal fits was likely dominated by the noise in the measurements as opposed to non-hydrostatic effects in the shape.

The images acquired by the Dawn spacecraft enable Ceres' shape determination to much higher accuracy and precision. The residuals of the ellipsoidal fits are dominated by actual non-hydrostatic topography rather than measurement noise. Dawn data reveal that Ceres' shape is significantly triaxial. The difference between the two equatorial axes a and b is on the order of 2 km, which corresponds to an equatorial flattening factor $f_q = (a - b)/a$ of 0.004. The equatorial flattening factor f_q is a proxy for the body's non-hydrostaticity as a body in hydrostatic equilibrium would have $f_q = 0$ at the Ceres' rotation rate. It can be seen from Fig 6-4 that Ceres is less oblate than expected for a homogeneous body. However, Ceres deviates from homogeneity by the same order as it deviates from hydrostaticity. Therefore, non-hydrostatic effects need to be taken into account when interpreting Ceres' shape and gravity field.

Ceres also possesses a moderate center-of-mass – center-of-figure (COM–COF) offset. We define the COM–COF offset as the vector between the body's center of mass and the center of mass of the body assuming it has uniform density. The COM–COF offset can be loosely used as a metric for planet's general deviation from spherical symmetry with regard to interior structure. The magnitude of the offset is 1.0 km or 0.2% of Ceres' radius. This value is substantially larger than the COM–COF offsets for the terrestrial planets but smaller than for Vesta (Table 6.4). This observation again demonstrates the intermediate nature of dwarf planet Ceres. A global map of Ceres topographic heights computed with respect to the best-fit ellipsoid with five degrees of freedom (polar and equatorial axes and offset vector) confirms its tri-axiality, which is evident as regions of alternating positive and negative topography (Fig. 6-1).

Body	Offset magnitude (km)	Fraction of radius	Reference
Mercury	0.144	0.0059%	Perry et al. (2015)
Venus	0.19	0.0031%	Yoder (2013)
Earth	0.8	0.0126%	Yoder (2013)
Moon	1.982	0.1141%	Yoder (2013)
Mars	2.501	0.0738%	Yoder (2013)
Vesta	1.44	0.5517%	Ermakov et al. (2014)
Eros	0.83	12.077%	Zuber et al. (2000)
Ceres	1.02	0.2128%	This paper

Table 6.4 – COM–COF offsets for terrestrial planets, Moon, Vesta and Ceres.

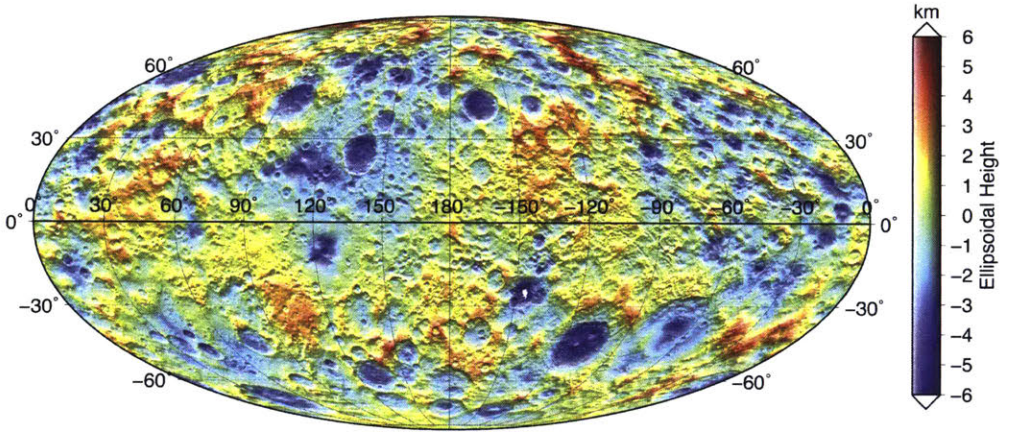

Figure 6-1 – Map of Ceres ellipsoidal heights based on the SPG HAMO model. The reference ellipsoid of revolution has axes 482 and 446 km.

Even though it might seem from Fig. 6-1 that Ceres possesses highlands and lowlands, the histogram of Ceres elevations (Fig. 6-2) is unimodal.

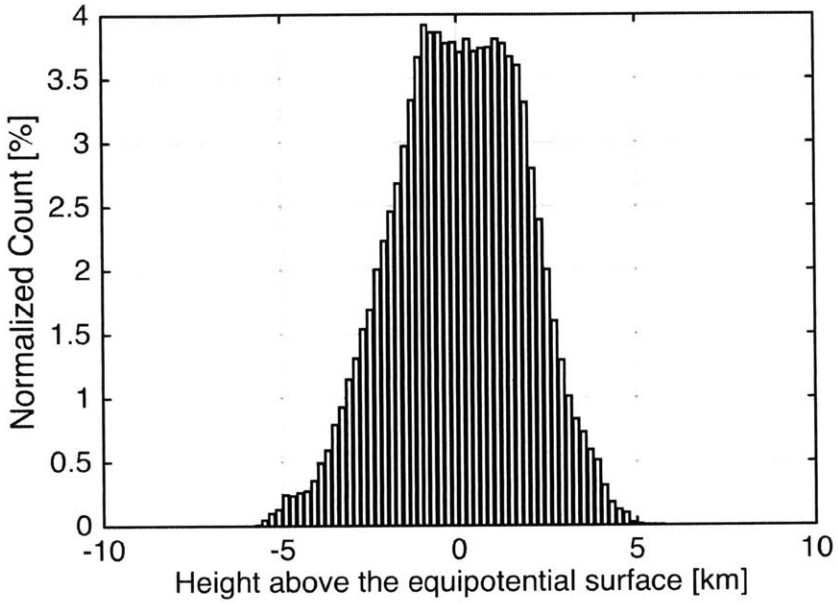

Figure 6-2 – Histogram of Ceres heights with respect to the equipotential surface.

6.2.2 Gravity field model

We use a degree-18 gravity field model derived from Dawn's radio-tracking data from the approach phase to LAMO. The model is accurate up to degree 9-12. Observed degree-2 gravity spherical harmonic coefficients (Park et al., 2016) as well as the coefficients computed assuming a homogeneous interior are shown in Table 6.5

Comparing the magnitude of the sectorial to zonal degree-2 coefficients power, it should also be noted that Ceres' gravity is non-hydrostatic at a 3% level at degree-2. On the other hand, Ceres' tri-axiality $(a-b)/a$ is 6% of its polar flattening $(a-c)/a$. Therefore, Ceres is more non-hydrostatic in its shape compared to its gravity, which indicates that degree-2 topography is largely compensated (see Section 6.3.4).

n	m	$\bar{C}_{nm}$	$\bar{S}_{nm}$	$\bar{C}_{nm}^{SPC}$	$\bar{S}_{nm}^{SPC}$	$\bar{C}_{nm}^{SPG}$	$\bar{S}_{nm}^{SPG}$
2	0	$-1.19 \cdot 10^{-2}$	–	$-1.3279 \cdot 10^{-2}$	–	$-1.3180 \cdot 10^{-2}$	–
2	1	$-8.35 \cdot 10^{-7}$	$7.02 \cdot 10^{-7}$	$-1.7327 \cdot 10^{-4}$	$-2.1191 \cdot 10^{-4}$	$2.0139 \cdot 10^{-4}$	$-2.1778 \cdot 10^{-4}$
2	2	$2.47 \cdot 10^{-4}$	$-2.74 \cdot 10^{-4}$	$-3.8998 \cdot 10^{-5}$	$5.7610 \cdot 10^{-4}$	$-5.3365 \cdot 10^{-6}$	$7.3199 \cdot 10^{-4}$

Table 6.5 – Degree-2 gravity model from the HAMO orbit and computed from the SPC and SPG shape models. (Park et al., 2016)

6.2.3 Gravity from shape

We compute gravity-from-shape spherical harmonic coefficients $\bar{\sigma}_{nm}^{shape}$ as detailed by Wieczorek and Phillips (1998), where gravitational coefficients are expanded in a series of powers of shape. We find that due to Ceres' significant non-sphericity three terms need to be retained in Eq. 2.11 to compute gravity from shape with an accuracy matching the accuracy of the observed gravity (Fig. 6-3).

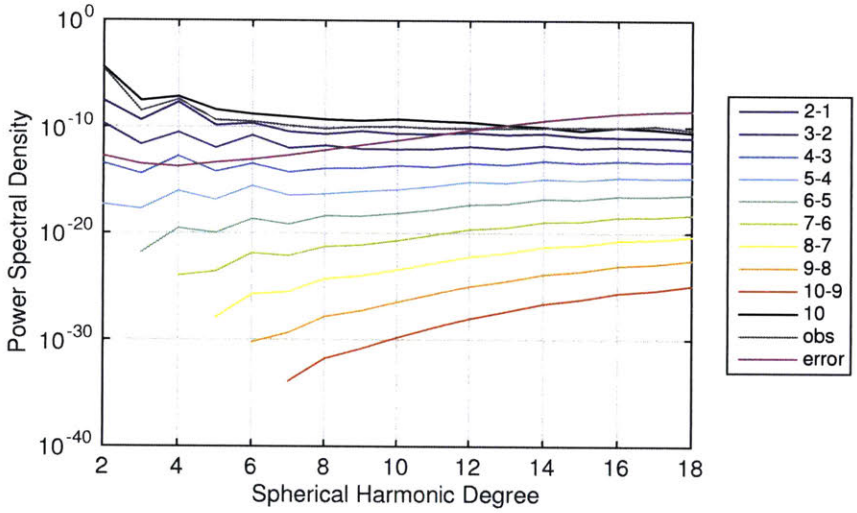

Figure 6-3 – Power spectral density contributions from the powers of topography. We show the power spectral density of the difference between the two gravity-from-shape expansions in which h and $h+1$ powers of topography were retained. Additionally, we show in black the power of the gravity-from-shape for $\max(h) = 10$. The grey curve is the power spectrum from the degree-18 JPL gravity model (CERES18B01) and the magenta curve is the error power spectrum of that model.

6.3 Results

6.3.1 Hydrostatic equilibrium

Fig. 6-4 shows the flattening factor of Ceres assuming homogeneous interior as a function of rotation period. Due to Ceres' fast rotation, it is necessary to take into account high-order effects when computing the body's equilibrium shape. The accuracy of first order theory of figure methods such as Dermott (1979) is not sufficient

for rapid rotators such as Ceres or Vesta.

Even so, Ceres rotates sufficiently slowly such that it is in the Maclaurin regime, i.e., its equilibrium shape is an ellipsoid of revolution. In this case, we should note that the shape of an equipotential surface can be an ellipsoid only for a homogenous body. This fact is known as the Hamy-Pizzetty theorem: Hamy (1889); Moritz (1990); Pohánka (2011); Rambaux et al. (2015). However, we find that the accuracy of the Tricarico (2014) approximation using ellipsoids of revolution to represent equipotential surfaces is on the order of 10 m for a Ceres-like multilayer body. This estimate is found by evaluating the potential at ellipsoidal interfaces and converting it to equipotential surface heights.

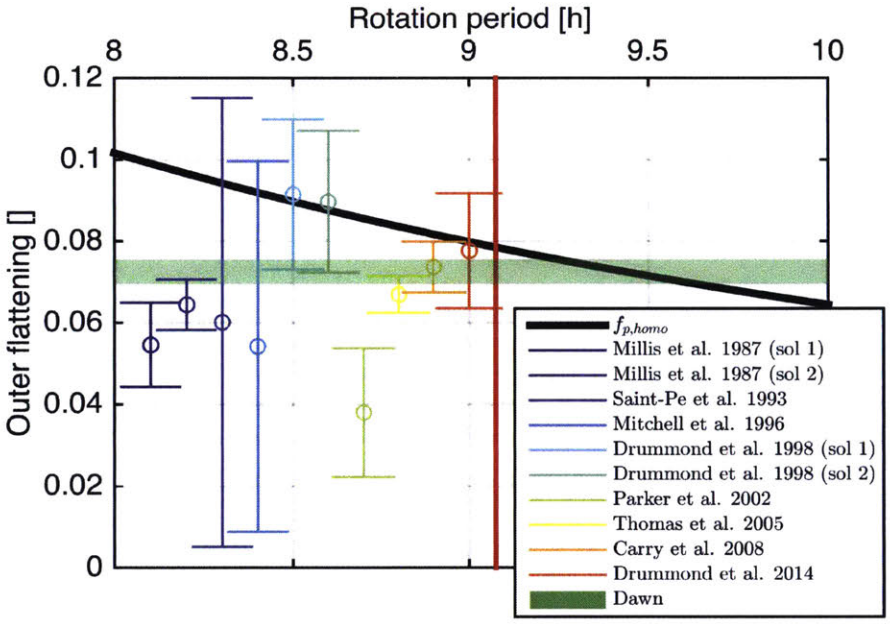

Figure 6-4 – Ceres' hydrostatic equilibrium polar flattening as a function of rotation period assuming a homogeneous interior is shown in thick black. Also shown are Pre-Dawn Ceres shape flattening determinations with their corresponding 1σ error bars. The pre-Dawn data points are shown in chronological order from left to right and do not correspond to different rotation periods. The green region corresponds to the flattening of the Dawn-derived shape. The width of the region is due to the tri-axiality of Ceres, i.e., range between $(a-c)/a$ and $(b-c)/b$. The vertical red line indicates Ceres' current rotation period. It can be seen that the body's deviation from hydrostaticity (the width of the green region) is of the same order as its deviation from homogeneity.

6.3.2 Shape harmonic analysis

6.3.2.1 Comparison with terrestrial planets

Fig. 6-5 shows the power spectrum of Ceres' topography compared to those of the terrestrial planets and asteroid 4 Vesta. Vesta is perhaps the most useful body to be compared against Ceres due to its location in the asteroid belt, which suggests a similar impact history (O'Brien and Sykes, 2011; Fu et al., 2016). The spectrum of Ceres lies below that of Vesta indicating that Ceres' topography is smoother. As the main process in building topography is impact cratering on both Vesta and Ceres, the difference in the topography power is likely due to different target properties. Ceres appears to be a weaker target than Vesta. We also note that the Vesta spectrum at the lowest degrees displays substantial variability, which is likely due to the effect of the two giant impact basins Rheasilvia and Veneneia. The spectra shown in Fig. 6-5 are integral characteristics; they contain information from all acting physical processes that can affect bodies' shape. For example, the spikes at degree-2 (second data point in all spectra) mostly represent the hydrostatic response to rotation. In subsequent figures we remove this hydrostatic signal from the spectra. The power spectra for Ceres and Vesta curve down at high frequencies ($k > 2 \cdot 10^{-3}$ km^{-1}) as they reach the resolution limit of the shape reconstructing process.

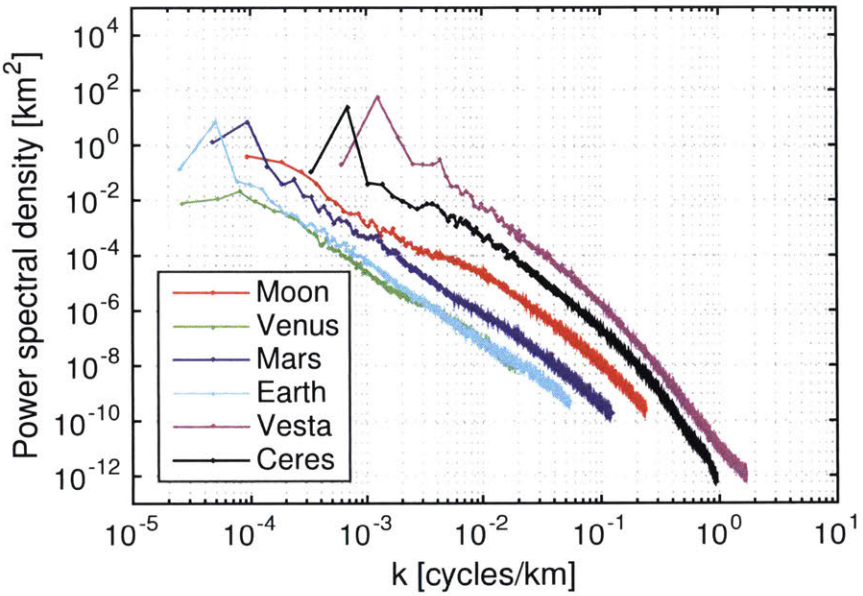

Figure 6-5 – Topographic spectral density spectrum of Ceres compared with spectra of the terrestrial planets, the Earth's Moon and Vesta. Data for the Moon, Venus and Mars are taken from Wieczorek (2007a). Data for the Earth is are taken from Hirt and Kuhn (2012).

6.3.2.2 Viscous relaxation in the spectral domain

Bland (2013) argued that if Ceres contains an outer water ice layer, craters as small as 4 km should be significantly relaxed at the equatorial regions. At mid-latitudes, all craters older than 10 Ma and larger than 16 km should be completely relaxed. On the other hand, if Ceres is a rocky body, Bland (2013) predicted that crater relaxation should be negligible.

The topographic power of Ceres behaves as a power law (Fig 6-5). However, we observe a decrease of power at low degrees with respect to the power law. In order to assess the statistical significance of the deviation of the power spectrum from a power law at low degrees, we performed a least-squares linear fit and computed confidence intervals, which are shown in Fig. 6-6. The hydrostatic signal was removed from the spectrum in order not to bias the fits. As shown in Fig. 6-6, the deviation of the observed spectrum from a power law at low degrees is statistically significant, i.e.,

the spectrum lies outside of the 95% confidence interval.

We interpret the decrease of power at low degrees to be due to viscous relaxation. The observed topographic spectrum then implies that viscous relaxation does occur on Ceres but, unlike modeled in Bland (2013), it is important only at the lowest degrees that correspond to scales of several hundreds of km. There are only a few features on Ceres of that size and at least one of them (a hexagonal-shaped basin named Kerwan with a diameter of 275 km and Coniraya crater with a diameter of 131 km) is morphologically relaxed (Hiesinger et al., 2016; Bland et al., 2016). Therefore, due to a low sample size and the lack of confirmed craters at longer wavelengths, crater morphology cannot be effectively used as a statistical means to study viscous relaxation on Ceres at the low degrees ($n < 20$) where most deviation from the power law is observed. In reality, the topographic power spectrum reflects all ongoing processes (e.g., impact cratering, internal activity such as convection, tectonic processes) which could balance viscous relaxation contribution to the spectrum (Fu et al., 2016).

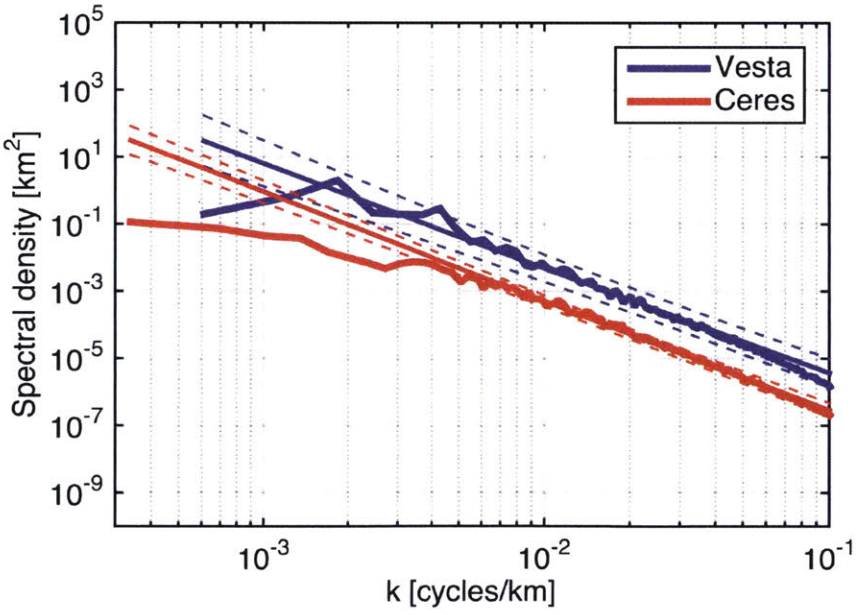

Figure 6-6 – Ceres and Vesta topographic power spectral density with hydrostatic signal removed. A linear fit is shown. The dashed curves indicate the 95% confidence interval. It can be seen that Ceres' power spectrum, unlike that of Vesta, deviates from the power law at long wavelengths.

6.3.2.3 Regional variations of viscous relaxation

To confirm the occurrence of viscous relaxation on Ceres, we studied regional variations of the topographic power spectrum. Since Ceres has a low obliquity ($\approx 4°$), a strong systematic difference exists in the insolation between the polar and equatorial regions. As such, equatorial regions are expected to have more relaxed topography due to their higher temperatures Bland (2013). Latitude-dependent crater relaxation at the scale that was modeled in Bland (2013) has not been observed on Ceres by Dawn from crater morphology Marchi et al. (2016). However, an insufficient number of confirmed impact basins may exist in the wavelength range affected by viscous relaxation (see above). Furthermore, crater morphology might be affected by processes other than viscous relaxation, such as infilling with ejecta from subsequent impacts. Therefore, we focus on a more basic surface property, the localized topography power spectrum, using a spectral-spatial localization algorithm described in Simons and Dahlen (2006). We adopted a spherical cap localization window with a radius of 20 degrees and a bandwidth of 20 spherical harmonic degrees and computed the topographic power within each window. We tesselate a unit sphere using the 3rd order icosahedron tessellation to find centers of the localization windows. This gives 642 points uniformly distributed on a sphere.

Fig. 6-7 shows a strong dependence of topographic power at low spherical harmonic degrees on latitude. Specifically, topographic power is lower near the equator and increases poleward for degrees $n < 40$. This observation is consistent with the geometry of viscous relaxation as calculated by Bland (2013). However, it is not consistent with the magnitude of relaxation in the case of a water ice-dominated shell, which would predict nearly no topography at equatorial latitudes. The observed latitudinal dependence of topographic power is an indication that Ceres' outer shell cannot be supported by water ice rheology as was modeled by Bland (2013). We observe that viscous relaxation is important only at large scales (over 100 km). At very high latitudes ($> 80°$), the topographic power is constant to slightly decreasing. This can be explained by the fact that Ceres' shape models have lower resolution near the

poles due to poorer illumination conditions and therefore lack topographic power in these regions. Fig. 6-8 shows topographic spectral density localized in latitude bands. It is evident that the difference between the topographic spectra is more pronounced at the low degrees. The power spectra are essentially statistically indistinguishable at spherical harmonic degrees higher than 40. The fact that Ceres' equatorial regions have a reduced topographic power also implies that the dwarf planet has not experienced a true polar wander or obliquity change that would significantly affect the insolation pattern over the geologic time scale.

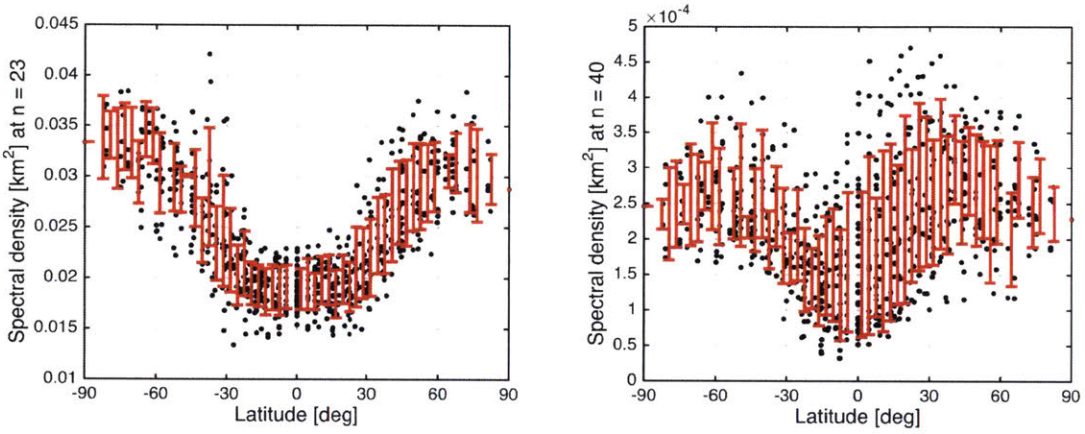

Figure 6-7 – The spectral density of Ceres' localized topography as a function of latitude at spherical harmonic degrees 23 (wavelength of 123 km) and 40 (wavelength of 74 km). The error bars correspond to data points binned into 5-degree bins.

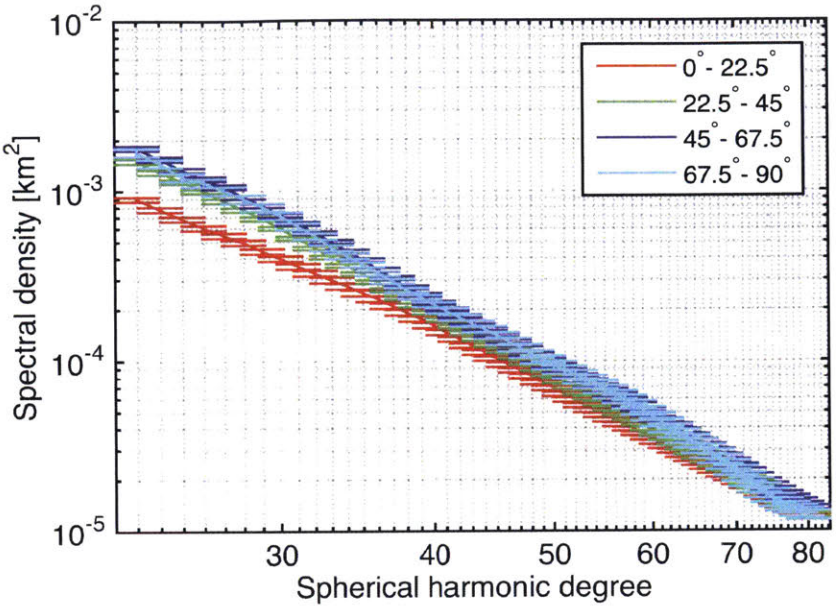

Figure 6-8 – Topography power spectral density localized at different latitude bands

6.3.3 Internal structure constraints

As indicated above, a two-layer model is the most parsimonious structure possible to explain the topography and gravity data. We therefore adopt this basic structure and explore the parameter space of two-layer models constrain the permitted range of plausible internal density structures. Fig. 6-9 shows the parameter space for the two-layer model and a family of hydrostatic solutions given the observed shape and gravity field of Ceres. The difference between the equatorial axes and the difference between shape and gravity solutions demonstrates the degree of Ceres' non-hydrostaticity. Since Ceres is triaxial, we choose to use the reduced flattening factor $f_{p,red} = \left(\sqrt{ab} - c\right)/\sqrt{ab}$ in our hydrostatic computation for the shape solution. The family of solutions lies above the homogeneous line indicating an increase of density towards the center of Ceres. The two-layer model solution based on the gravity field appears to be more differentiated than the solution based on the shape. This is likely due to some topography being compensated at degree-2 (see below).

The polar moment of inertia factor $\lambda = C/Ma_{HE}^2$[1] is ≈ 0.373 (which corresponds to $C/MR_{vol}^2 \approx 0.392$) based on the gravity solution and ≈ 0.390 based on the shape solution. This value is greater than that of the Earth (0.33), Mercury (0.35) and Mars (0.366), but more similar to that of the Moon (0.39). As observed by Dawn, Ceres appears to be less differentiated than based on some of the pre-Dawn shape models (Thomas et al., 2005).

Also, we note that the contour lines for constant λ on Fig. 6-9 do not exactly correspond to the contour lines of constant $\bar{J}_2$ or f_p. The shell densities between 900 kg/m^{3}and 1800 kg/m^3 correspond to λ between 0.3734 and 0.3738 (Fig. 6-16). This range is rather small. Effectively, this means that for Ceres' mean density and rotation rate there is a one to one correspondence between λ and $\bar{J}_2$ or f_p. The Radau-Darwin (RD) relation is typically used to find the relationship between the polar moment of inertia and $\bar{J}_2$ (Zharkov and Trubitsyn, 1978). For the case of Ceres, RD gives C/Ma^2 of 0.370 or, equivalently, $C/MR_{vol}^2 = 0.390$.

[1] a_{HE} refers to the equatorial axis of the ellipsoid in hydrostatic equilibrium. a_{HE} is different from the observed a.

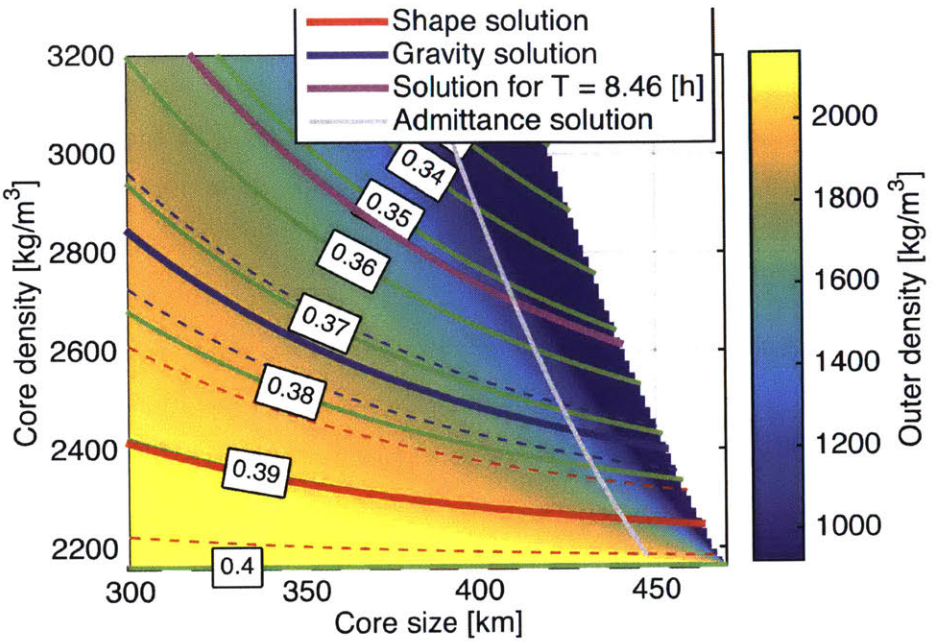

Figure 6-9 – Parameter space of the 2-layer internal structure model. The green lines indicate the moment of inertia factor $C/(Ma_{HE}^2)$. The dashed line at the bottom corresponds to a homogeneous model. Two solution families for the present rotation period ($T = 9.07$ hours) are shown: gravity solution from the $\bar{J}_2$ coefficient in blue and shape solution from f_p in red. The two solutions are noticeably different. Notice the larger uncertainty in the shape solution compared to the gravity solution. Since some of the degree-2 shape can be compensated, we later adopt the gravity solution to derive constraints on the internal structure. The uncertainty in the shape solution comes from the difference between $(a-c)/a$ and $(b-c)/b$. The uncertainty in the gravity solution due to non-hydrostaticity is taken to be 3%, which is the ratio of the total magnitude of the non-hydrostatic sectorial degree-2 term to the hydrostatic zonal term $\sqrt{\bar{C}_{22}^2 + \bar{S}_{22}^2}/\bar{J}_2$. Changing the rotation period affects the gravity and shape solutions. At a rotation period $T = 8.46$ hours, the two solutions are identical, which is shown as a magenta curve. The faster rotation rate solution corresponds to a smaller value of C/Ma_{HE}^2 and therefore yields a more differentiated structure. Finally, the gray curve shows the locus of points at which the isostatic admittance matches in the least-squared sense with the observed admittance. We note that the moment of inertia factor λ shown in this figure is normalized using the hydrostatic equilibrium semimajor axis a_{eq} which is not constant at different points on the figure. We chose to normalize the moment of inertia in such way in order for the homogeneous model to have $\lambda = 0.4$.

Fig. 6-15 shows the shell thickness as a function of shell density as well as the core offset required to compensate for the COM–COF offset. Ceres is more oblate in its topography than in its gravity. Therefore, Ceres' internal structure solution is more

differentiated based on gravity compared to topography. If Ceres was perfectly in hydrostatic equilibrium, the two solutions would be identical. Some of this degree-2 topography can be compensated. However, the mechanism for creating such degree-2 pattern in shell thickness is unclear. The negative correlation between gravity and topography at $\{n = 2, m = 2\}$ is also a puzzle. It is possible that viscosity at great depths increases due to a compositional boundary, therefore making this deep interior resistant to relaxation and able to support a significant deep interface topography over geologic time-scales. This could potentially explain the observed non-hydrostaticity.

Also, see the supplementary materials Table 6.6 for the two-layer solution in a table form.

6.3.3.1 Possible despinning

As seen in Fig. 6-9, the hydrostatic solutions from the gravity and shape are different. Mao and McKinnon (2016) suggests than the gravity and topography can be simultaneously hydrostatic by changing the rotation period. In fact, the solution for the internal structure from gravity ($\bar{J}_2$) and shape ($f_{p,red}$) are identical for a rotation period of 8.46 hours. The moment of inertia of such hydrostatic equilibrium model is smaller ($C/Ma_{HE}^2 \approx 0.353$) than for the shape or gravity solutions given the present rotation rate implying stronger differentiation. The required dispinning is significant (≈7.2%). The most likely mechanism capable of imparting the necessary angular momentum is a giant impact. However, Ceres lacks big impact features on its surface. Marchi et al. (2016) suggests that the low topography region centered at 135°E and 20°N is an ancient, heavily eroded basin some 700 km in diameter. However, the observational evidence is so far inconclusive whether this topographic depression is an impact feature. The impactor that formed this hypothetical basin could have potentially been large enough to change the rotation rate of Ceres by 7%.

Mao and McKinnon (2016) stated that the faster rotation hydrostatic solution is applicable for modeling Ceres' internal structure if the fossil bulge is frozen in. In other words, Ceres' polar flattening factor f_p and gravity coefficient $\bar{J}_2$ should not have appreciably changed since the despinning event, which likely happened more

than 4 Gy ago. However, finite element modeling of Ceres' relaxation (Fu et al., 2016) suggests that the fossil bulge quickly relaxes to isostatic equilibrium. The topography power spectrum suggests a decrease of viscosity with depth. Therefore, the deeper structures, having lower viscosity, are involved in a faster relaxation. This results in the gravity anomalies relaxing faster than the outer shape features. As such, the frozen in condition is violated and the faster rotation rate solution (shown in magenta in Fig. 6-9) is likely not representative of the internal structure of Ceres.

6.3.4 Admittance and correlation

Admittance (Z) and correlation (R) are spectral characteristics that allow to cross-analyze gravity and shape data. The admittance estimate Z_{n} is a ratio of gravity-shape cross power to the power of shape. This definition of admittance is appropriate for the case when noise in the gravity data dominates noise in the topography data (McKenzie, 1994). In order to give admittance units of mGal/km, we multiply the ratio by $GM/R^3(n+1)$.

$$Z_n = \frac{S_n^{gt}}{S_n^{tt}} \cdot \frac{GM}{R^3}(n+1) \tag{6.1}$$

$$R_n = \frac{S_n^{gt}}{\sqrt{S_n^{tt} S_n^{gg}}} \tag{6.2}$$

where S_n^{gt} is gravity topography cross-power.

Even though Ceres is close to hydrostatic equilibrium, its fast rotation distorts the shape to the degree that non-linear effects in computing gravity from the shape become important. Non-linearity also affects admittance and correlation. The correlation between observed gravity and gravity-from-shape for the degree-2 sectorial term is ≈ -0.7. The admittance is therefore also negative ≈ -57 mGal/km. This term dominates the non-hydrostatic signal at degree-2. Negative admittances are rare (see discussion in Hemingway et al. 2013). A possible explanation of the negative admittance at degree and order 2 could be a combination of a buoyant bottom loading and a thick/rigid shell. The load's contribution to the gravity is negative and the

surface uplift contribution is positive. However, if the shell is rigid it would not bend enough to compensate the negative contribution of the load and the total effect will be negative. This hypothesis will be further tested with higher degree gravity models.

6.3.5 Bouguer anomaly and shell thickness variations

The Bouguer anomaly (BA) is computed as a difference between the observed gravity coefficients and the gravity coefficients of the model:

$$\bar{\sigma}_{nm}^{BA} = \bar{\sigma}_{nm}^{obs} - \bar{\sigma}_{nm}^{hydrostaticmodel} \tag{6.3}$$

Similarly to Ermakov et al. (2014), model gravity is computed as a weighted sum of gravity-from-shape and gravity of the internal layers. Since the model is assumed to be hydrostatic, the degree-2 zonal term in the Bouguer anomaly is zero. The Bouguer anomaly is presented in Fig. 6-10, which shows that regions of negative Bouguer anomaly correspond to regions of positive topography. Fig. 6-11 shows a map of Ceres' shell thickness based on the solution for the shell-core interface that minimizes the Bouguer anomaly. Gravity and shape data do not allow an absolute estimation of the shell thickness since either densities of layers or the shape of the interface between different density layers must be assumed. A core density of 2442 kg/m^3 and shell density of 1379 kg/m^3 were assumed to compute shell thickness shown in Fig. 6-11. This choice of densities lies in the range allowed by rheological constraints (Fu et al., 2016) and is justified further below. We would also like to note that, the choice of densities affects the amplitude of the Bouguer anomaly and the amplitude of the shell-core interface variations, it does not affect the pattern of the anomalies.

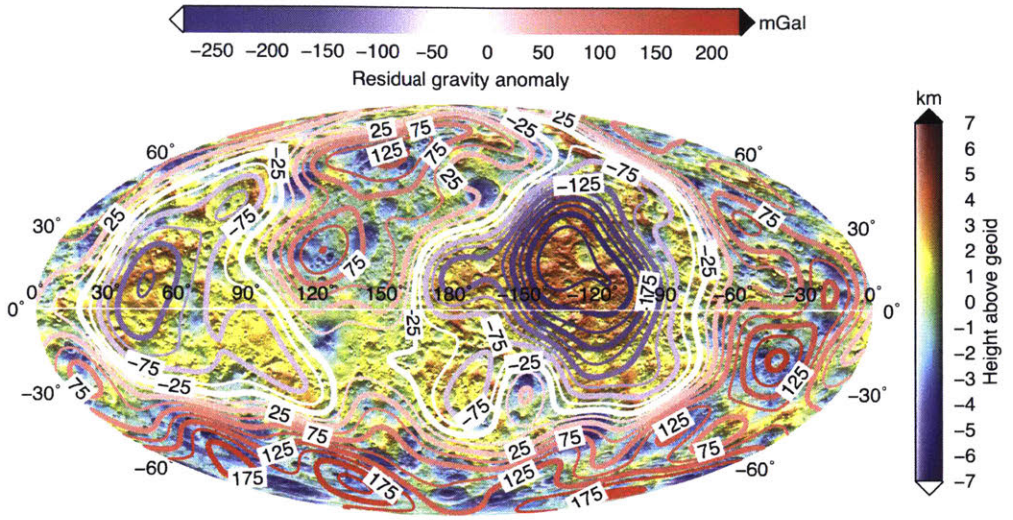

Figure 6-10 – Bouguer anomaly based on the HAMO SPC shape model and degree-12 gravity model.

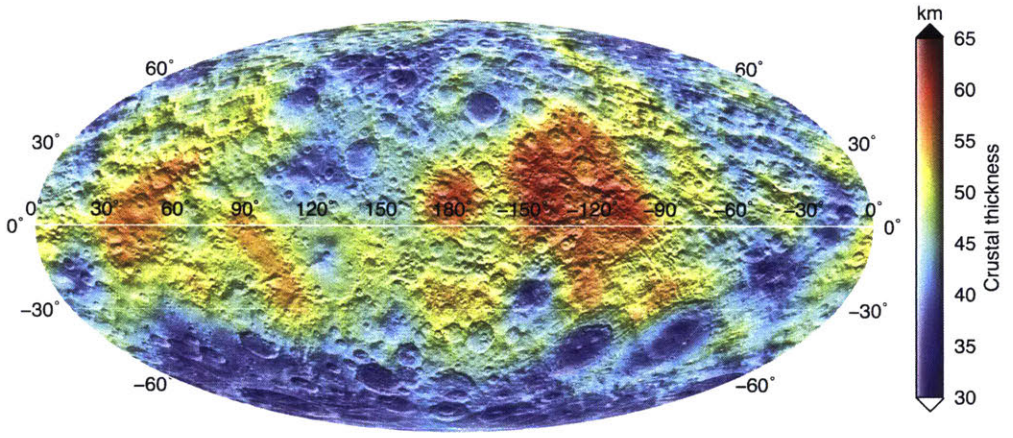

Figure 6-11 – Ceres' relative shell thickness.

6.3.6 A self-consistent two-layer isostatic model

It is clear from the Bouguer anomaly map (Fig 6-10) that there is a negative correlation between the Bouguer anomaly and topography, which implies compensation

of topography. FE modeling of Fu et al. (2016) constrains the rheological structure of Ceres, which, given the existence of plastic failure, is consistent with no significant intact elastic lithosphere at 4 Gy time scale; therefore, full isostatic compensation is expected for Ceres. Low values of admittance are also suggestive of isostatic compensation. In the case if Airy isostatic compensation, admittance can be computed as follows

$$Z_n^{Airy} = \frac{GM}{R^3}\frac{3(n+1)}{2n+1}\frac{\rho_{shell}}{\rho_{mean}}\left(1-\left(1-\frac{D_{comp}}{R}\right)^n\right), \tag{6.4}$$

where D_{comp} is the depth of compensation, which is taken to be the mean shell thickness in our two-layer model. Equation 6.4 is valid if the departure from sphericity is small. We compute isostatic compensation following Rummel et al. (1988). Firstly, we compute an equipotential surface based on the gravity field and shape models. Secondly, assuming Airy compensation mechanism, we find the crustal root t as a function of equipotential height. The isostatic equilibrium condition presented in (Rummel et al., 1988) reduces to a third-order equation in t. With a change of variables it can be written as:

$$T^3 - 3T^2 + 3T - \eta\left(H^3 + 3H^2 + 3H\right) = 0 \tag{6.5}$$

where $T = \frac{t}{R-D}$, $H = h/R$ and $\eta = \frac{\rho_1}{\rho_2-\rho_1}\left(\frac{R}{R-D}\right)^3$; D is the depth of compensation, h is the height with respect to the equipotential surface, which can be found using the gravity and shape models. We numerically solve this third order polynomial equation for t. We assume a model in which compensation occurs at the interface between the layers. We can choose which part of the hydrostatic family (Fig. 6-9) fits best with isostasy. Once we find t, we know the shape of the isostatic interface between the inner and outer layer and can use Equation 2.11 to find its gravitational attraction. We find the best-fit isostatic solution by varying the shell density between 1200 kg/m^3 and 1800 kg/m^3 to minimize the power of the isostatic anomaly (IA), which is found in a similar manner to the Bouguer anomaly, i.e. by subtracting the gravitational attraction of a isostatic model from the observed gravitational attraction:

$$\bar{\sigma}_{nm}^{IA} = \bar{\sigma}_{nm}^{obs} - \bar{\sigma}_{nm}^{isostatic\,model} \tag{6.6}$$

Due to non-hydrostaticity, the exact hydrostatic value of $\bar{J}_2$ is uncertain. In order to estimate the uncertainty in the isostatic solution, we varied the $\bar{J}_2$ by 3% and found the confidence intervals for the shell and core density as well as the core radius. We choose to minimize the isostatic power at degrees from 3 to 12, since degree-2 has a negative admittance and cannot be explained purely by isostasy (Fig. 6-12). The power of the isostatic anomaly is minimized for the shell density of 1379^{+50}_{-45} kg/m^3. This corresponds to a shell thickness of $46.3^{+4.9}_{-5.0}$ km and a core radius of $423.7^{+5.0}_{-4.9}$ km.

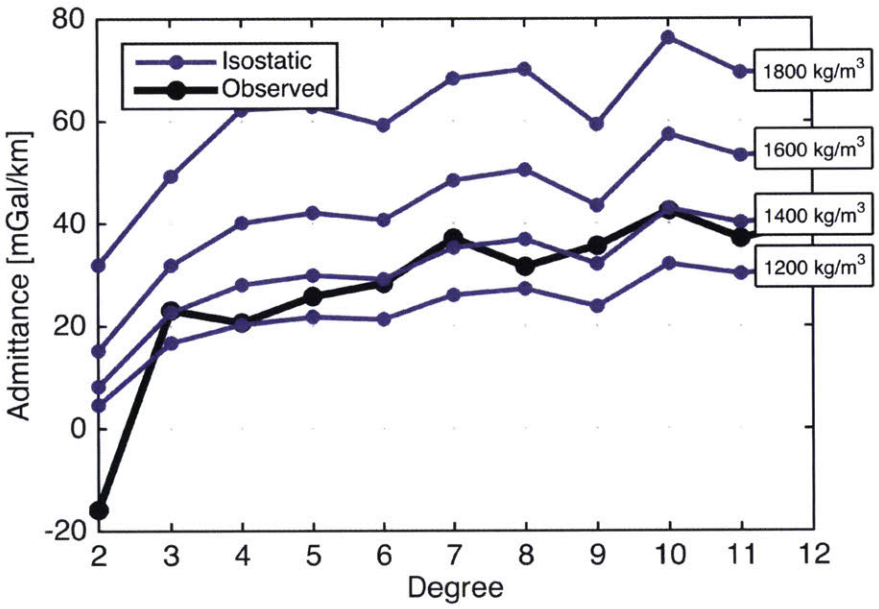

Figure 6-12 – Gravity-topography admittance of Ceres. The observed admittance (black curve) is negative at degree-2 after hydrostatic contribution is removed. The admittance at degrees 3 to 12 is positive. Blue curves are isostatic admittances for different shell densities.

We show a map of the isostatic anomalies for degrees from 1 to 12 in Fig. 6-13. The range of the isostatic anomaly (from -104 mGal to +104 mGal) is much smaller than that of the Bouguer anomaly (from -270 mGal to +207 mGal), indicating that isostasy can indeed explain the great majority of the Bouguer anomaly. The sectorial

degree-2 component dominates the isostatic anomaly. Possible sources of this signal include core fossil topography or a bottom buoyancy-driven load (see Section 6.4) If we compute the isostatic anomaly for degrees from 3 to 12 (Fig. 6-14), the range is smaller (from -59 mGal to +69 mGal). Interestingly, the biggest basins (Kerwan, Yalode and Urvara) appear to have isostatic negative anomaly, which could be evidence for a localized volatile enrichment and/or increased impact induced porosity in these regions.

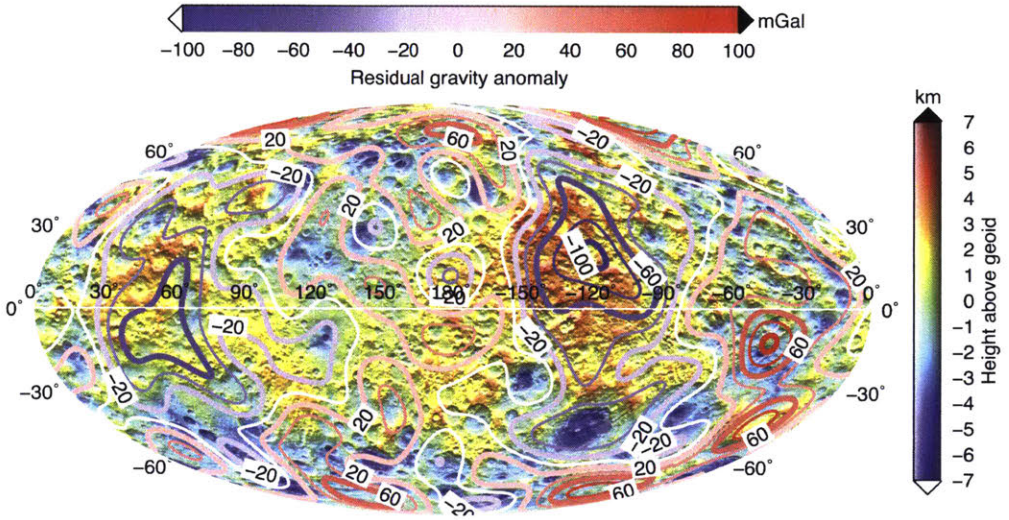

Figure 6-13 – Ceres' isostatic anomaly including all degrees.

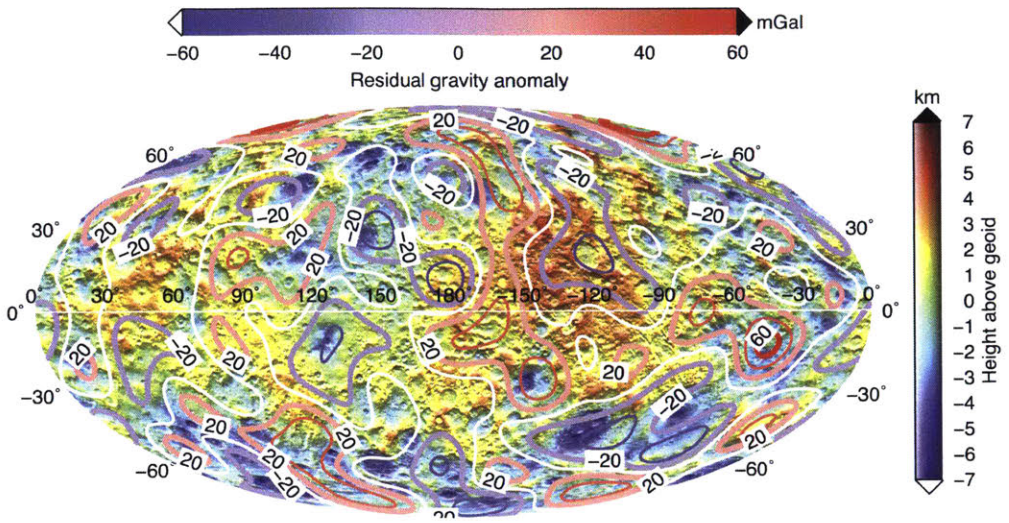

Figure 6-14 – Ceres' isostatic anomaly from degree-3 to degree-12.

6.4 Discussion

Based on the observed latitudinal patterns of topography power and comparison to rocky bodies such as Vesta, we attribute the reduction of topographic power at low degrees as due to viscous relaxation. We also explore other processes that may contribute to the observed topography. For instance, Nimmo et al. (2011) discussed how a flexural response can reduce low-degree power. We repeated the analysis of Nimmo et al. (2011) for Ceres. We multiplied the power law fit for Ceres' topography (Fig. 6-6) by the factor $F_n^2 = 1/\left(1 + \frac{\rho_c}{\rho_{m-\rho_c}} C_n\right)^2$, where C_n is the degree of compensation (Turcotte et al., 1981) for a spherical harmonic degree n. The parameter C_n depends on such lithospheric properties as Young's modulus, effective elastic thickness, Poisson's ratio, as well as shell and mantle densities. We varied the effective elastic thickness between 0.1 km and 100 km, Young's modulus between its ice value of 9 GPa to a typical rock value of 40 GPa. Shell and core densities were taken according to Fig. 6-15. Given these reasonable ranges, we were not able to achieve a satisfactory fit to the observed Ceres topography spectrum. Therefore, a flexural response is likely not the source of the low-degree topography power reduction.

Crustal inversions show the magnitude regional heterogeneity of Ceres' crust. Two regions with larger crustal thickness are centered near equator at 45°E and 135°W. The magnitude of the crustal thickening in the two regions is different (Fig. 6-11) due to the non-zero COM–COF offset. The 135°W high topography region has a larger crustal thickness and contains a crater named Occator that has a unique set of bright spots in its topographic center. Furthermore, the regions of high topography and negative Bouguer anomaly surrounding the Occator crater are associated with so called "bluish material". This material is presumed to be Occator's ejecta. Another region with bluish material is the flanks of Ahuna Mons - a pyramid shaped mountain located at 11.5°S and 44.2°W. Paradoxically, unlike the Occator region, the region around Ahuna Mons has one of the strongest positive Bouguer and isostatic anomalies. The Occator and Ahuna Mons regions have been proposed to be sources of cryovolcanic activity on Ceres. Having the strongest negative and positive gravity anomalies, the physical mechanism responsible for these two features appears to be fundamentally different.

The topographic spectrum indicates that there is substantial salt and/or silicate content in the outer shell of Ceres (Fu et al., 2016). This claim will be further tested with the spectroscopic measurements by the VIR and elemental abundance measurements by the GRaND instrument onboard Dawn.

The negative gravity-topography correlation for the sectorial degree-2 term is puzzling. A possible mechanism is a combination of bottom buoyant loading with a rigid shell. This could imply a present-day global-scale convection or a frozen-in anomaly for such convection in the past. Travis et al. (2015) suggested that liquid water could still be present and active in Ceres' interior and that hydrothermal convection in a mud ocean and wet rocky core is currently ongoing. The Travis et al. (2015) model can potentially explain the observed negative correlation, although further modeling is necessary to establish that the magnitude of the gravity and topography anomaly due to this source is quantitatively consistent with the data. Another interpretation of the negative anomaly in the 135°W high topography region region around the Occator crater is salt tectonics. (Buczkowski et al., 2016) identifies extensional features

that are consistent with the salt dome interpretation. This mechanism would imply a local salt diapir rising due to its lower density and bending the surface. A possible connection of such salt tectonics mechanism to the bright spots in Occator, the composition of which is still to be spectrally identified, is intriguing and merits a separate study. A higher-degree gravity model will be highly advantageous in determining a possible source of the anomaly.

Higher-degree gravity field models expected from Dawn's Low Altitude Mapping Orbit (LAMO) will allow improved localization of the gravity anomalies. It is expected that the Dawn measurements will enable the determination of a degree 13-14 (Park et al., 2016; Konopliv, 2016) gravity model, which corresponds to a wavelength of approximately 220 km. Ceres lacks large-scale topographic features that can be morphologically identified with high confidence. However, the gravity signature of the putative giant impact basins Marchi et al. (2016) will likely be resolvable in the future gravity data and will allow constraining the magnitude of the uplift of the subsurface layers.

6.4.1 Rheological constraints

Ceres' topographic power spectrum provides an important constraint on the rheologic structure of the interior. Finite-element modeling of viscous relaxation (Fu et al., 2016; Bland et al., 2016) (Add new Bland's paper here) shows that a pure icy shell is not consistent with the observed spectrum, as relaxation in an icy shell would occur too quickly. The simplest explanation is that Ceres' outer shell is not purely ice (the case studied in Bland, 2013) nor purely rock but an ice-rock-salt mixture that allows some relaxation at the longest wavelengths. Such a heavily-contaminated icy shell is required to support the observed topographic spectrum. Shell contamination with respect to pure water ice also increases its density, implying that the shell density must exceed a minimum value to provide the required mechanical strength. Given this minimum density, we can thereby constrain the minimum shell thickness.

Without invoking any geochemical evolution models to constrain the maximum salt to rock ratio, we can adopt 40% ice and 60% meridianiite with density 1504 kg/m^3

(Fortes et al., 2008). This is essentially the lightest salt, and yields an absolute minimum mean shell density of 1273 kg/m^3. This density corresponds to a shell thickness of 44 km and minimum core density of 2460 kg/m^3. If we assume the 60% is half meridianiite and half phyllosilicates (2500 kg/m^3), then the minimum shell density is 1573 kg/m^3. This composition yields a shell thickness of 68 km. An alternative constraint is to assume that the salt content is similar to that of a CI chondrite, the most aqueously-altered type known. The density of these meteorites is 2260 kg/m^3 after removing the effect of porosity (Britt and Consolmagno S.J., G., 2003a). This density yields a minimum shell density of 1730 kg/m^3, which corresponds to a shell thickness of 95 km. Clathrates are also a possible constituent of Ceres' outer shell. Methane clathrate has a density of 950 kg/m^3 similar to that of water ice and is rheologically strong. Mixing 40% water ice with 60% methane clathrate gives a density of 938 kg/m^3, which would correspond to a low bound of the shell thickness of 29 km.

While insight from the topographic spectrum shows that Ceres' outer shell is not currently consistent with a fully ice composition, it could have had more ice in its early history. Bowling et al. (2015) predicts removal of order of 10 km of ice due to impact-driven sublimation in a Gy time scale. This scenario would imply a bulk density change on the order of 10%. Castillo-Rogez et al. (2016) updates this estimate to 50 km in the case if Ceres formed in the outer Solar System. Alternatively, Ceres' low density was hypothesized due to its porous interior in the absence of a substantial ice content Neumann et al. (2015). However, Castillo-Rogez (2011) argues that high interior porosity is unlikely. However, the porosity of the upper layers can be greater due to impact gardening.

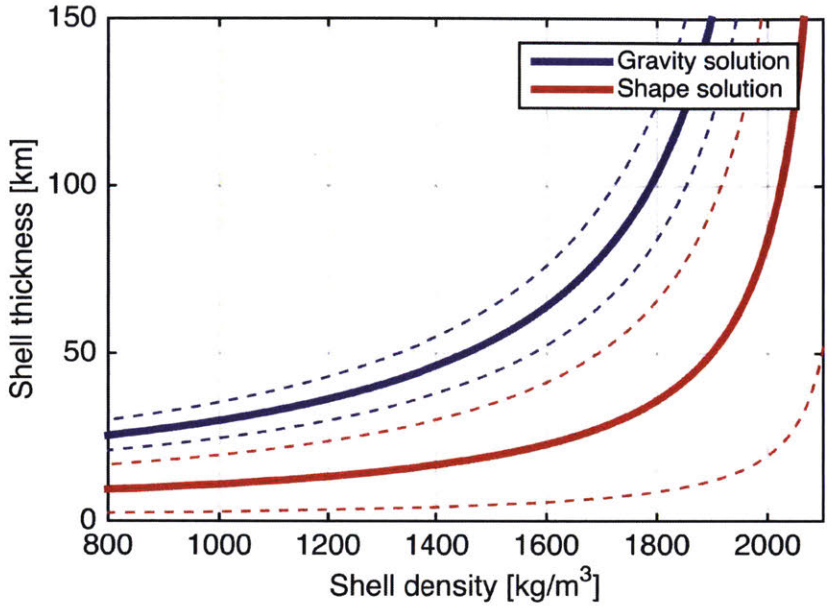

Figure 6-15 – Ice shell thickness as a function of shell density. The dashed curves represent our estimate of uncertainty due to non-hydrostaticity.

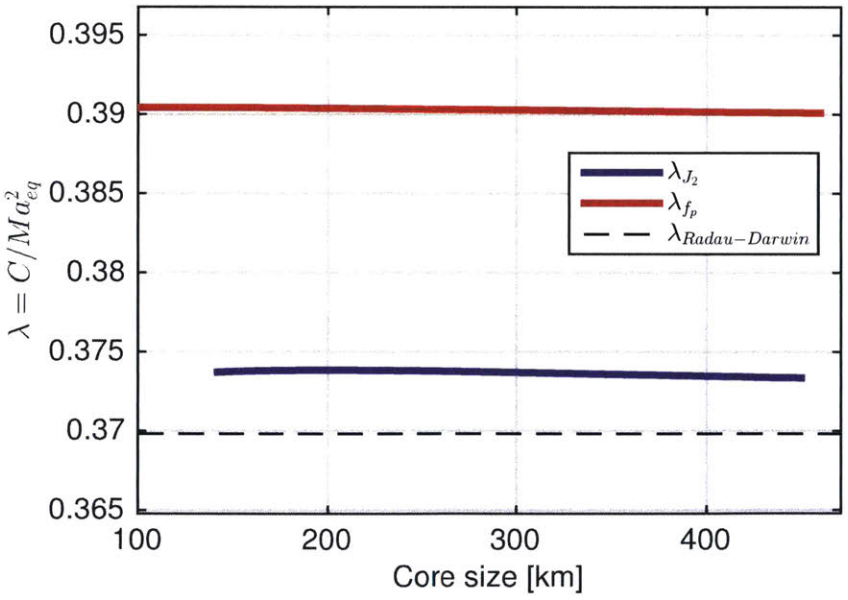

Figure 6-16 – Hydrostatic solution for the normalized moment of inertia (C/Ma_{HE}^2) as a function of the core size derived from the gravity and shape constraints. The dashed line is the solution from the Radau-Darwin relationship.

6.4.2 Isostatic constraints

While rheology can give a lower bound on the shell density, isostasy can give the upper bound. Isostatic admittances are low compared to the uncompensated case. However, if there is a lithosphere, it will be able to, at least partially, support topographic loads. Therefore, admittance will be higher in the presence of an elastic lithosphere. Therefore, as can be seen in Fig. 6-12, a lower shell density will be required to match the observed admittance.

We find that a density of 1379^{+50}_{-45} kg/m^3 is most consistent with full isostatic compensation at degrees 3 to 12. This gives a shell thickness of $46.3^{+4.9}_{-5.0}$ km and core density of 2442^{+56}_{-52} kg/m^3. Surprisingly, the range of shell densities/thicknesses allowed both by rheological and isostatic constraints is quite small. However, we want to emphasize that given all simplifications in our model (two constant density layers, compensation happens at the only internal interface), the small range allowed by rheological and isostatic constraints should be taken with a grain of salt, as perhaps the best manifested by the negative admittance for the sectorial degree-2 component, which cannot be explained within the framework of an isostatic model.

Several models with inverted density structure have been proposed (Neveu and Desch, 2015). In such models, primordial crust overlays either pure water ice or ice-rock mixture layer. For such structure, the density of the top layer is higher than the density of the lower layer, therefore it is gravitationally unstable. Formisano et al. (2016) studied whether or not Rayleigh-Taylor instability could reverse all or part of the crust. A range of structures was identified for which the crust is stable over the age of the Solar System. We note that the concept of isostasy is inconsistent with such inverted structure. Therefore, either the instability occurred and the primordial crust foundered or such inverted structure never existed.

6.4.3 Occator and Hanami planum

Hanami planum is the region of high standing terrain around the Occator crater. The Occator crater corresponds approximately to the the location where the eleva-

tions are the highest within the Hanami planum. This region is associated with the strongest negative Bouguer anomaly. Hanami planum is large enough (≈600 km) to be resolved in current the gravity model, that is accurate up to degree from 9 to 12. Since the region has positive topography and a negative gravity anomaly, it is expected that, at least partially, this negative anomaly is a consequence of isostatic compensation. However, even after computing isostatic correction, the isostatic anomaly is also negative, indicating supercompensation. Alternatively, a regional density decrease can create such a negative isostatic anomaly.

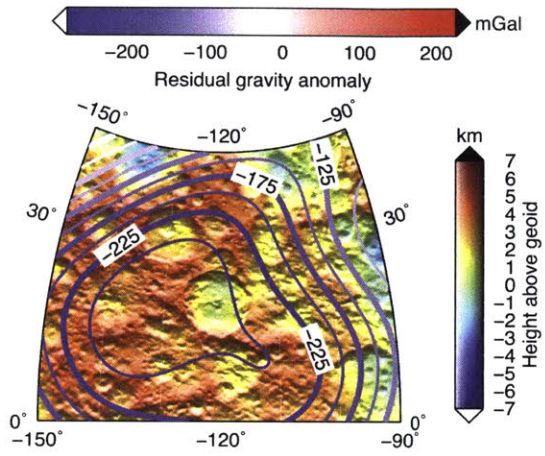

(a) Bouguer anomaly plotted over the height with respect to the geoid.

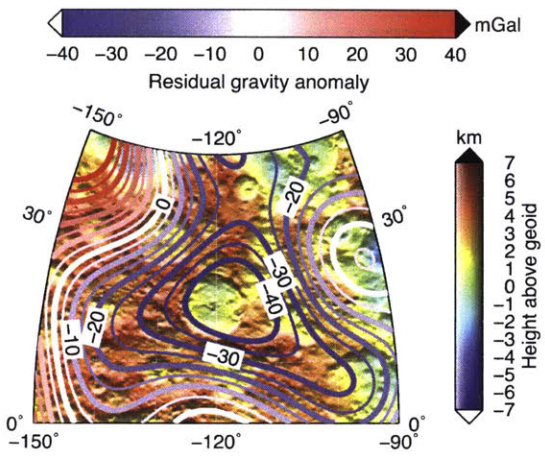

(b) Isostatic anomaly plotted over the height with respect to the geoid.

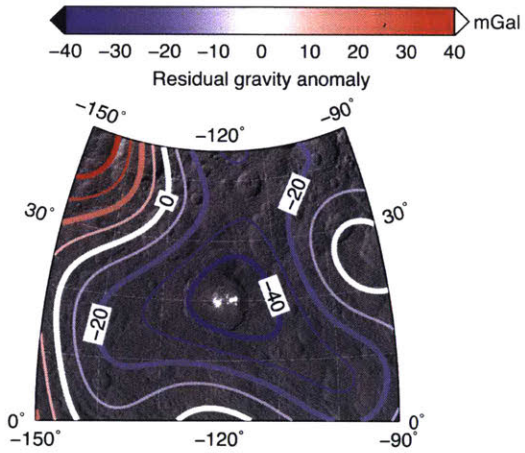

(c) Isostatic anomaly maps plotted over projected Dawn clear filter mosaic.

Figure 6-17 – Occator and Hanami planum.

6.4.4 Kerwan

With a diameter of 281 km, Kerwan is the biggest unambiguous impact basin on Ceres (Fig. 6-18). It is located near the equator in Ceres' eastern hemisphere. Its subdued topography could indicate that this feature has experienced viscous relation. The negative isostatic anomaly within the basin indicates that the basin is subisostatic. Bland et al. (2016) argued that viscous relaxation of Kerwan can only be achieved if the ice content in the subsurface is enhanced relative to the rest of Ceres, which would be consistent with a negative isostatic gravity anomaly.

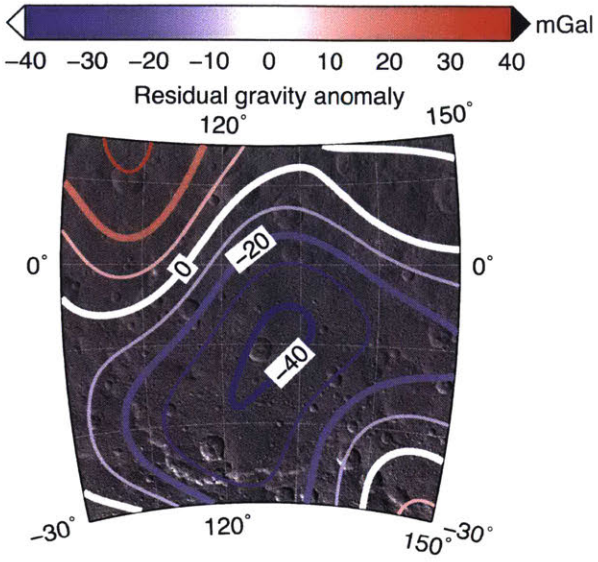

(a) Isostatic anomaly maps plotted over projected Dawn clear filter mosaic.

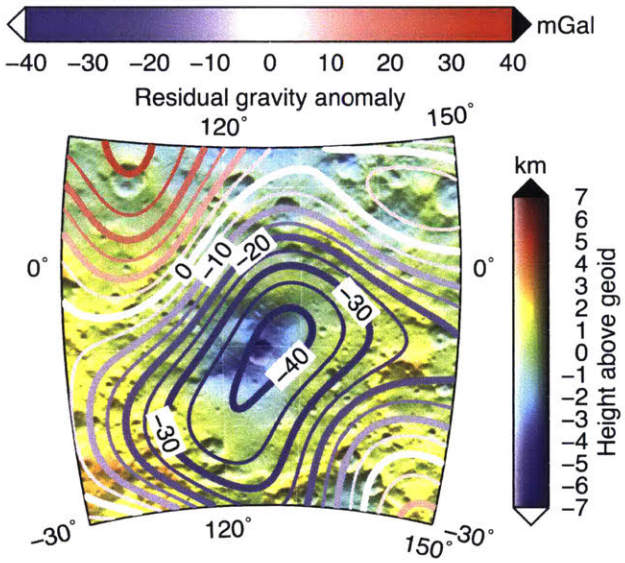

(b) Isostatic anomaly plotted over the height with respect to the geoid.

Figure 6-18 – Kerwan crater

6.4.5 Urvara and Yalode

Urvara and Yalode are the two adjacent impact features in the southern hemisphere. Their diameters are 163 and 271 km, respectively. Similarly to Kerwan, the two basins have negative isostatic anomalies indicating subisostasy.

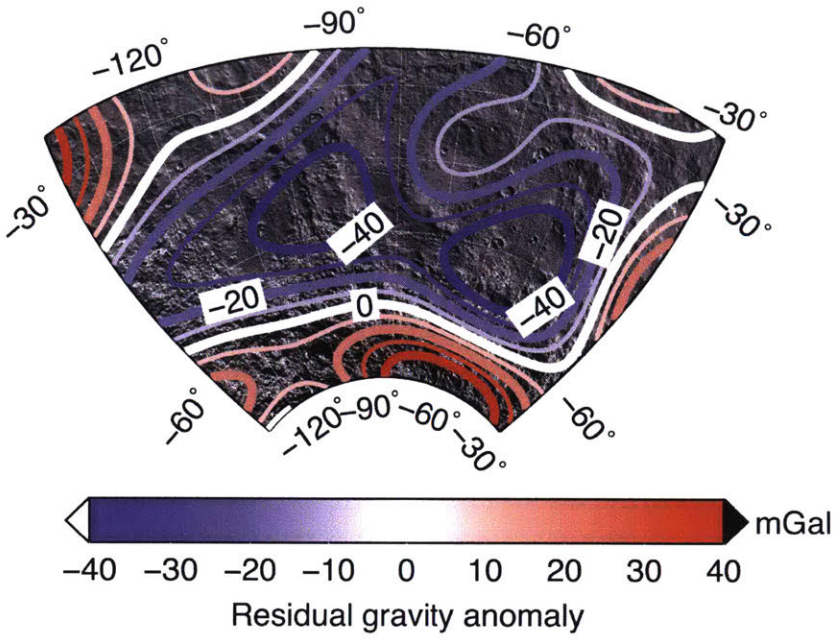

(a) Isostatic anomaly maps plotted over projected Dawn clear filter mosaic.

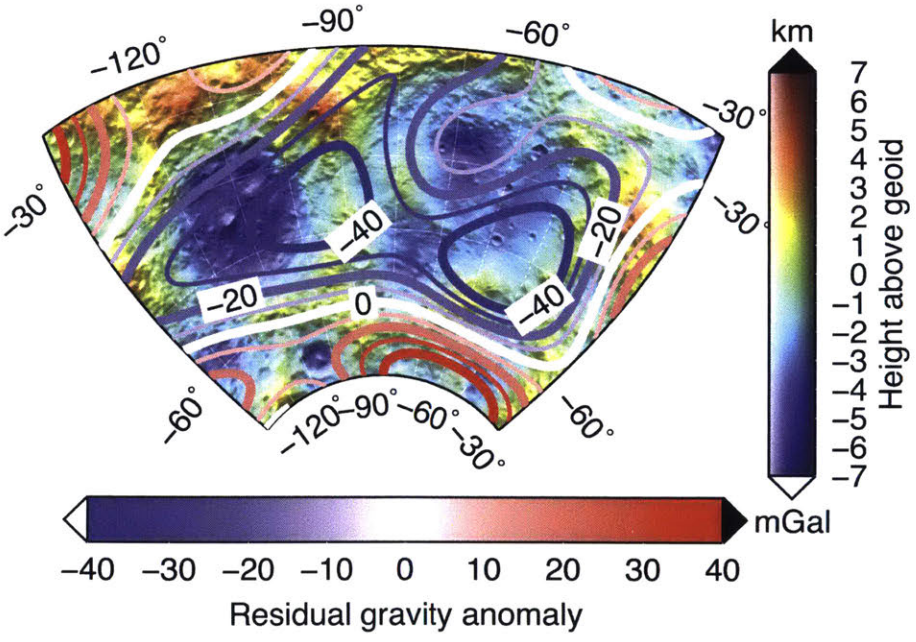

(b) Isostatic anomaly plotted over the height with respect to the geoid.

Figure 6-19 – Urvara and Yalode basins.

6.4.6 Ahuna Mons

Ahuna Mons is a pyramid-shaped mountain near the equator in the western hemisphere of Ceres. This feature has a unique morphology that cannot be found anywhere else on Ceres. This curious feature is associated with a strong positive Bouguer and isostatic anomaly. However, since the feature is only 20 km wide, it is not possible to associate the anomaly with the feature itself, rather with the general surrounding area.

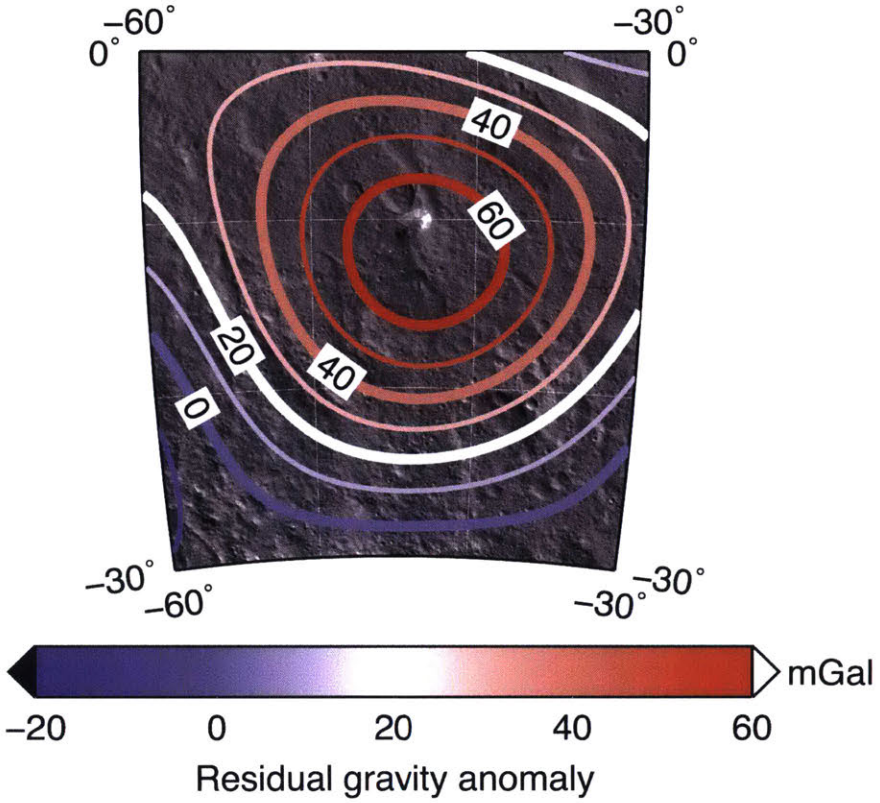

Figure 6-20 – Ahuna mons isostatic anomaly maps plotted over projected Dawn clear filter mosaic.

6.5 Conclusions

The gravity and shape indicate that Ceres is a physically-differentiated object. However, the extent of differentiation is less than based on some of the pre-Dawn

shape data (Thomas et al., 2005) and is more consistent with more recent ground telescope-based studies Drummond et al. (2014); Carry et al. (2008). The tri-axiality of Ceres indicates the magnitude of the non-hydrostatic influence is on the order of its deviation from a uniform body. Ceres' topography at degree-2 appears to be overcompensated as indicated by the negative correlation between sectorial gravity and topography at degree-2. A possible explanation for this observation could be a combination of a buoyancy-driven anomaly with a high-rigidity/thick shell at the time scales relevant to the buoyant process.

We observe that the topographic power of Ceres deviates from a power law at low degrees and that equatorial regions have lower topographic power. This indicates that viscous relaxation plays a role at Ceres. However, we find that viscous relaxation is important only at low degrees that correspond to spatial scales of more than 100 km. At smaller scales, or, equivalently, higher spherical harmonic degrees, there is not a systematic latitude variation of the topographic power nor there is a deviation of the topography power from a power law.

An isostatic model reproduces the observed gravity very well as demonstrated by the low magnitude of isostatic gravity anomalies compared to the Bouguer anomaly. The best fit two-layer isostatic model has the shell density of 1379^{+50}_{-45} kg/m^3 and shell thickness of $46.3^{+4.9}_{-5.0}$ km. Finite element modeling of Ceres' topography (Fu et al., 2016) shows that the topographic power cannot be supported by a solely ice rheology over billion year timescales. Shell contamination by silicates is required for strengthening, and doing so increases its density. Using a lower bound for shell density based on rheology, we derive constraints on the shell thickness using the assumption of hydrostatic equilibrium. Using the mixture of methane clathrate and water ice, we find the minimum plausible shell thickness to be 29 km, which is consistent with the above-derived isostatic constraints.

Supplementary materials

Two-layer internal structure solution

ρ_1 (kg/m^3)	$\rho_2^{central}$ (kg/m^3)	ρ_2^{min} (kg/m^3)	ρ_2^{max} (kg/m^3)	$r_2^{central}$ (km)	r_2^{min} (km)	r_2^{max} (km)
900	2414	2367	2464	441.86	437.10	446.52
1000	2418	2370	2469	439.35	434.09	444.42
1100	2423	2373	2476	436.35	430.57	441.89
1200	2428	2377	2484	432.69	426.25	438.84
1300	2435	2381	2494	428.14	420.93	435.08
1400	2444	2387	2508	422.33	414.06	430.29
1500	2458	2396	2529	414.65	404.95	423.99
1600	2478	2409	2560	403.98	392.22	415.18
1700	2512	2430	2614	388.20	373.23	402.31
1800	2581	2469	2731	362.35	341.75	381.51
1900	2785	2572	3149	311.54	277.74	341.56
1960	3347	2780	5260	245.58	183.94	292.64
1990	5064	3118	–	178.29	–	249.01
2020	–	5089	–	–	–	167.05

Table 6.6 – Two-layer internal structure model solution based on the observed value of $\bar{J}_2$ and observed non-hydrostaticity for the present-day rotation rate. The minimum and maximum values are the solutions corresponding to the value of $\bar{J}_2$ varied by $\pm 3\%$. ρ_1 and ρ_2 are the densities of the shell and the core, respectively; r_2 is the core radius.

Chapter 7

Ceres obliquity history and implications for the permanently shadowed regions

Erwan Mazarico, Stefan Schröder, Uri Carsenty, Frank Preusker and Norbert Schorghofer contributed to this work.

Abstract

Because of the small current obliquity of Ceres ($\epsilon \approx 4°$), permanently shadowed regions (PSRs) exist on the surface of Ceres. Some craters in Ceres' polar regions possess bright crater floor deposits (BCFDs), which are hypothesized to be volatiles that accumulated in PSR cold traps. The existence and persistence of the PSRs depends on Ceres' obliquity. We integrate the obliquity of Ceres over the last 3 My and find that it undergoes large oscillations with a period of 24.5 ky and a maximum of $\epsilon_{max} \approx 19.7°$. At such large obliquity most of the present-day PSRs receive direct sunlight. We find an apparent correlation between BCFDs and the most persistent PSRs. In the north, we find that only two PSRs remain at ϵ_{max}. These PSRs contain BCFDs. In the south, we find that only one crater with a BCFD remains in shadow at ϵ_{max}. Our results support the cold trapping mechanism for formation of the observed BCFDs.

7.1 Introduction

7.1.1 Pre-Dawn Ceres pole determinations

The location of the Ceres spin pole had been constrained in several studies prior to the Dawn mission (Thomas et al., 2005; Drummond and Christou, 2008; Carry et al., 2008; Drummond et al., 2014). The uncertainties of these determinations were typically on the order of 5°.

Skoglöv et al. (1996) conducted a study of the obliquity variations of ten large asteroids including Ceres using the then available spin vectors and ellipsoidal shape models from the ground-based observations and concluded that orbital evolution characteristic frequencies are typically higher than precession frequencies. No indication of chaos in 2 My integrations was found.

Bills and Nimmo (2011b) predicted that Ceres has a tidally-damped obliquity. If the obliquity is tidally damped, it presents an additional constraint on the internal structure, as it would depend on the moments of inertia. However, Rambaux et al. (2011) argued that the damping period is on the order of 10^{17} years, much longer than the Solar System age, and, therefore, it is highly unlikely that the present-day obliquity is damped.

7.1.2 Ceres' permanently shadowed regions

Images from the Dawn spacecraft's Framing Camera (FC) and radio tracking of the spacecraft from ground-based stations have allowed the precise determination of the Ceres' rotational pole (Park et al., 2016) and, therefore, of Ceres' obliquity (ϵ). Presently, Ceres obliquity is about 4°. Because of this low obliquity, permanently shadowed regions have been detected on Ceres' surface using the Dawn Framing camera images and shape-based illumination modeling (Schorghofer et al., 2016; Platz et al., 2016). This makes Ceres only the third body in the Solar System after the Moon (Zuber and Smith, 1997; Mazarico et al., 2011) and Mercury (Chabot et al., 2012; Neumann et al., 2013) with identified PSRs.

Additionally, some craters at high northern and southern latitudes on Ceres possess bright crater floor deposits, or BCFDs, (Platz et al., 2016). Despite being in shadow in the Dawn FC images, these crater floors are partially illuminated by light scattered from the crater rims. We hypothesize that BCFDs are volatile deposits accumulated in the PSR cold traps similarly to the Moon and Mercury (Watson et al., 1961; Arnold, 1979; Paige et al., 2010; Sanin et al., 2012; Moores, 2016). Temperatures in Ceres' PSRs are low enough to retain volatiles for long durations (Fanale and Salvail, 1989; Schorghofer, 2008; Titus, 2015; Hayne and Aharonson, 2015b). In at least one of such deposits (later referred to as NP5), water has been detected spectrally (Platz et al., 2016).

The observation of BCFDs on Ceres is similar to the observations within Mercury's PSRs by the MESSENGER spacecraft (Chabot et al., 2014). The MESSENGER images show regions with higher reflectance inside some PSRs, with the boundary of the higher-reflectance units matching the PSR boundaries well (Deutsch et al., 2016). The critical difference between the PSR inventory from the MESSENGER and Dawn data is that the heights of Mercury's topography were derived from laser altimetry (Cavanaugh et al., 2007; Zuber et al., 2012), which is independent of the illumination conditions, whereas Ceres' elevations are derived from stereo-analysis of the FC images.

The analysis of the Gamma Ray and Neutron Detector (GRaND) data shows that Ceres' regolith is rich in hydrogen (Prettyman et al., 2016). Neutron and gamma ray count data reveal a strong latitude variation with suppressed counts at high latitudes. The lower bound of H concentration near the poles exceeds that found in carbonaceous chondrites, which are thought to be the best meteoritic analogues of Ceres. Therefore, the GRaND observations indicate that water ice and/or other volatile species may be concentrated in the polar regions on or very near ($\approx$1 m) the surface.

Siegler et al. (2016) provides an example of a feedback between knowledge of volatile distribution and body orientation history. The existence of the PSRs critically depends on the body's obliquity. Understanding temporal obliquity variations in the past can shed light on the history of PSRs and can help constrain the time scales

required for water ice deposition and its lifetime on the surface (Schorghofer, 2008).

7.1.3 Outline

We start with describing the integrator and illumination modeling in Section 7.2. We then summarize the available shape and orientation data as well as observations of Ceres' BCFDs in Section 7.3. The results on Ceres' obliquity and PSR history and their relation to BCFDs are presented in Section 7.4. We discuss the implications our results in Section 7.5 and summarize our findings in Section 7.6.

7.2 Methods

7.2.1 N-body dynamics

The symplectic mapping for the N-planet problem was developed by Wisdom and Holman (1991). It has been proven to be an efficient algorithm for long-term integrations of planetary systems. The mapping requires that the Hamiltonian can be split into two individually solvable parts.

$$H = H_1 + H_2. \tag{7.1}$$

In the case of the N-planet problem, $H_1 = H_{Kepler}$ corresponds to the Keplerian unperturbed motion and $H_2 = H_{Interaction}$ includes mutual interactions between planets and satellites. H_2 is viewed as a perturbation and is required to be much smaller than H_1, which is why the term "N-body problem" is not used. In order to obtain the mapping Hamiltonian, we multiply H_2 by a periodic sequence of Dirac delta functions:

$$H_{map} = H_1 + 2\pi\delta_{2\pi}(\Omega t)H_2, \tag{7.2}$$

with

$$\delta_{2\pi}(t) = \sum_{n=-\infty}^{\infty} \delta(t - 2\pi n) = \frac{1}{2\pi} \sum_{n=-\infty}^{\infty} \cos(nt), \tag{7.3}$$

where Ω is the mapping frequency. The time step size h is related to Ω as $h = 2\pi/\Omega$.

The Hamiltonian for the N-planet problem can be written as

$$H = \sum_{i=1}^{n-1} \frac{p_i^2}{2m_i} - \sum_{i<j} \frac{Gm_i m_j}{r_{ij}}, \tag{7.4}$$

where G is the gravitational constant, n is the number of bodies, m_i is the mass of the i-th body. This Hamiltonian can be split into the Keplerian part, which can be efficiently solved using the Gauss f and g functions and the interactions part, which would depend only on the bodies' coordinates. The Kepler Hamiltonian has the usual form

$$H_{Kepler} = \frac{p^2}{2m} - \frac{\mu}{r}. \tag{7.5}$$

We use Jacobi coordinates to eliminate the central object dynamics. We first designate each body with a tuple of the body's mass and position in heliocentric coordinates $(m_i, \mathbf{r}_i)$. Then we define a tuple of n bodies $(b_0, b_1, ..., b_{n-1})$. The linking transformation $\mathcal{L}_{jk}$ takes a tuple of n bodies and returns a new tuple, where all the bodies are the same $b'_i = b_i$ except bodies j and k:

$$(m'_j, \mathbf{r'}_j) = (m_j m_k/(mj + mk), \mathbf{r}_k - \mathbf{r}_j), \tag{7.6}$$

$$(m'_k, \mathbf{r'}_k) = (m_j + m_k, (m_j \mathbf{r}_j + m_k \mathbf{r}_k)/(m_j + m_k)). \tag{7.7}$$

The velocities and accelerations are transformed in the same way as coordinates. The complete transformation from the heliocentric to Jacobi coordinates is done as a composition of n linking transformations:

$$\mathcal{L}_{n-1,n} \circ \mathcal{L}_{1,2} \circ \ldots \circ \mathcal{L}_{0,1}. \tag{7.8}$$

The Hamiltonian in Jacobi coordinates takes the form (Wisdom and Holman, 1991):

$$H_{Translation} = H_{Kepler} + H_{Interaction}, \tag{7.9}$$

with

$$H_{Kepler} = \sum_{i=1}^{n-1} \left(\frac{p_i'^2}{2m_i'} - \frac{Gm_i m_0}{r_i'} \right), \tag{7.10}$$

and

$$H_{Interaction} = \sum_{i=1}^{n-1} Gm_i m_0 \left(\frac{1}{r_i'} - \frac{1}{r_{i0}} \right) - \sum_{0<i<j} \frac{Gm_i m_j}{r_{ij}} + \sum_{i \neq c} W_{ci}, \tag{7.11}$$

where the Jacobi coordinates are primed, r_{ij} is the geometric distance between bodies i and. In our case, we take into account the second degree potential of Ceres in the MacCullagh form (Touma and Wisdom, 1994):

$$W_{ci} = -\frac{Gm_i}{2r_{ci}^3} \mathrm{Tr}(\mathbf{I}) + \frac{3}{2} \frac{Gm_i}{r_{ci}^5} \mathbf{R}_i \mathbf{I} \mathbf{R}_i, \tag{7.12}$$

where r_{ci} is the distance between i-th body and Ceres and m_i is the mass of the i-th body. To include the effect of Ceres' triaxiality, we introduce a new coordinate system $\mathbf{R}$ linked to Ceres. The coordinate axes of $\mathbf{R}$ are aligned with the principal axes of inertia of Ceres. In this coordinate system, $\mathbf{I}$ – the inertia tensor of Ceres – is diagonal, and its components can be estimated from the measured gravity coefficients of Ceres (Park et al., 2016). However, there is not a one-to-one correspondence between the measured second degree coefficients and moments of inertia. The situation is complicated by any non-hydrostaticity of Ceres. Therefore, we decided to explore a range of moment of inertia values.

The choice of the time step h is crucial for the accuracy of the mapping. In our work, we choose the time step to be $1/20$ of the fastest periodic motion considered. We performed integrations both with biaxial and triaxial Ceres. For the case of triaxial Ceres, the shortest period is the rotational period of Ceres (9.07 hours). Therefore, for these integrations we set $h = 1620$ seconds. For the case of a biaxial Ceres, the

shortest period is the orbital period of Mercury (≈88 days). In this case, we set $h = 4.4$ days.

7.2.2 Rotational dynamics

The symplectic mapping for the rigid body dynamics was developed by Touma and Wisdom 1994. We already introduced the coordinate system **R** linked to Ceres principal axes of inertia. The coordinate system **R** is related to the heliocentric inertial coordinate system **r** by:

$$\mathbf{r} = \mathbf{C}\mathbf{R}, \tag{7.13}$$

where **C** is the rotation matrix. To produce the opposite transformation, **C** should be replaced by $\mathbf{C}^{-1} = \mathbf{C}^T$. In the coordinate system **R**, the Hamiltonian that governs rigid body dynamics takes a simple form

$$H_{Euler} = \frac{L_A^2}{2A} + \frac{L_B^2}{2B} + \frac{L_C^2}{2C}, \tag{7.14}$$

where I_i are the principal moments of inertia of the body and L_i are angular momenta projected onto the principal inertia axes. As it is shown in (Touma and Wisdom, 1994), we can split this Hamiltonian into an unperturbed axisymmetric term and a triaxial term that acts as a perturbation:

$$H_{Euler} = H_{Axisymmetric} + H_{Triaxial} = \underbrace{\frac{L_A^2 + L_B^2}{2B} + \frac{L_C^2}{2C}}_{H_{Axisymmetric}} + \underbrace{\frac{L_A^2}{2}\left(\frac{1}{A} + \frac{1}{B}\right)}_{H_{Triaxial}}. \tag{7.15}$$

The two parts are individually integrable. The solution method is given in (Touma and Wisdom, 1994). However, we notice that the Hamiltonian splitting (7.15) proposed in (Touma and Wisdom, 1994) is not symmetric in A and B. It can be shown using formula (7.1.14) from (Touma and Wisdom, 1994) that for $A < B < C$ and assuming principal rotation (about the axis of highest inertia), the mapping produces

an evolution with a biased rotation frequency. The apparent rotation is faster by a factor of $AB/(AB - AC + BC)$, which is ≈ 0.997 for Ceres. We propose a different Hamiltonian splitting, that is symmetric in A and B:

$$H_{Euler} = H_{Axisymmetric} + H_{Triaxial} = \underbrace{\frac{L_A^2 + L_B^2}{A+B} + \frac{L_C^2}{2C}}_{H_{Axisymmetric}} + \underbrace{\frac{L_A^2}{2}\left(\frac{1}{A} - \frac{2}{A+B}\right) + \frac{L_B^2}{2}\left(\frac{1}{B} - \frac{2}{A+B}\right)}_{H_{Triaxial}}. \tag{7.16}$$

The axisymmetric term has a solution of the same form as before, but with the correct frequency. The triaxial term is a sum of two quadratic monomials, each of which are of the same order. Using the Poisson bracket from (Touma and Wisdom, 1994), we find that the solution of the triaxial term, in general, can be found in terms of elliptic integrals. We choose not to use the exact solution of the triaxial term, rather we solve $H_{Triaxial}$ by parts. We split it into two quadratic monomials $H_{Triaxial,1}$ and $H_{Triaxial,2}$. The two terms are individually solvable and their solutions are simple rotations (Touma and Wisdom, 1994). The fact that the two terms are of the same order does not affect the overall accuracy of the algorithm since $H_{Triaxial}$ itself is regarded as a perturbation. We choose to solve the two parts using a leap-frog scheme (see Section 7.2.3).

We should note that the derived splitting is still not symmetric with respect to C - the highest moment of inertia. Such splitting can cause problems with a biased rotation frequency for the bodies with significant deviations from the principal axis rotation. However, this is not the case for Ceres.

7.2.3 Mapping description

We use a symplectic leap-frog algorithm, in which an accuracy of $\mathcal{O}(h^2)$ is achieved by shifting the phase of the Dirac delta functions by a half of the mapping period. General leap-frog mapping for the Hamiltonian splitting (7.1) can be written in the form:

$$\mathcal{A}(h/2) \circ \mathcal{B}(h) \circ \mathcal{A}(h/2), \tag{7.17}$$

where $\mathcal{A}(h/2)$ corresponds to the evolution governed by H_1 for a half of the time step and $\mathcal{B}(h)$ corresponds to the evolution according to H_2 for the whole time step. Our total Hamiltonian consists of the translational and rotational Hamiltonians:

$$H = H_{Translation} + H_{Rotation}. \tag{7.18}$$

$H_{Rotation}$ is of Euler form (7.14). $H_{Translation}$ has the form as in Eq. (7.9). The term W that couples rotational and translational dynamics can be included either in $H_{Translation}$, as we did in (7.11), or in $H_{Rotation}$, or can be even treated as an independent term. Each Hamiltonian is split into two parts. Therefore, the complete mapping can be written as the rotational dynamics leap-frog mapping nested into the translational dynamics leap-frog mapping:

$$\mathcal{A}_K(h/2)\circ\mathcal{A}_2(h/4)\circ\mathcal{B}_3(h/2)\circ\mathcal{A}_2(h/4)\circ\mathcal{B}_{TI}(h)\mathcal{B}_{RI}(h)\mathcal{A}_K(h/2)\circ\mathcal{A}_2(h/4)\circ\mathcal{B}_3(h/2)\circ\mathcal{A}_2(h/4), \tag{7.19}$$

where $\mathcal{A}_K$ is the Keplerian motion, $\mathcal{A}_2$ is the axisymmetric rigid body motion, $\mathcal{B}_3$ is the perturbation in the rigid body motion due to the body's triaxiality, $\mathcal{B}_{TI}$ is the translational interactions between the bodies, $\mathcal{B}_{RI}$ is the rotational interactions between Ceres and other bodies, i.e. the Sun and the planets. In our case, the spit-orbit coupling term W acts in $\mathcal{B}_{TI}$.

7.2.4 Wobble damping

Non-principal rotation adversely grows as the numerical integration proceeds. We implemented an ad-hoc wobble damping procedure to suppress non-principal rotation growth based on the analytically computed time scale of wobble damping. The time scale of wobble damping is given by Burns et al. (1973):

$$\tau = \frac{\mu Q}{\rho K_3^2 R^2 \omega^3}, \tag{7.20}$$

where μ is the rigidity; Q is the quality factor; ρ is the mean density; K_3^2 is the shape factor, which is about 10^{-2} for nearly spherical bodies and $10^{-1}f^2$ for non-spherical bodies with oblateness f (Burns et al., 1973). Taking $\mu = 4 \cdot 10^9$ Pa, $Q = 100$, $K_3^2 = 10^{-2}$, we get τ=374 years. To damp the non-principal rotation, at each integration step, we first multiply the angular momentum components L_a and L_b by the damping factor $\exp(-h/\tau)$, where h is the time step of integration. This modifies the total magnitude of the angular momentum. We upscale each component of L to preserve the total magnitude. Then, we make sure that the orientation of the angular momentum in inertial space is unchanged. We do so by modifying the configuration matrix $\mathbf{C}$ using the matrix form of the Rodrigues rotation formula:

$$\mathbf{J} = \mathbf{I} + \sin(\theta)\mathbf{K} + (1 - \cos(\theta))\mathbf{K^2} \tag{7.21}$$

where θ denotes the angle of between the undamped and damped angular momenta and $\mathbf{K}$ is the cross-product matrix. The elements of $\mathbf{K}$ are vector components of the normalized cross-product of the undamped and damped angular momentum vectors in space.

$$\mathbf{K} = \begin{pmatrix} 0 & -k_3 & k_2 \\ k_3 & 0 & -k_1 \\ -k_2 & k_1 & 0 \end{pmatrix} \tag{7.22}$$

To preserve the orientation of the angular momentum in space, we adjust the configuration matrix, multiplying it by the inverse of $\mathbf{J}$:

$$\mathbf{C_{adjusted}} = \mathbf{J^{-1}C} \tag{7.23}$$

Additionally, we tested how non-principal rotation damping affects the obliquity history by varying Q from 1 to 1000. We concluded that it does not have any measurable impact on the obliquity history.

7.2.5 Validation of the integrator

In order to check the accuracy of the integrator, we performed several numerical tests. The method of Touma and Wisdom (1994) should conserve the angular momentum and the energy error should be periodic and bounded. We test numerically the conservation of angular momentum for the case of Ceres on a fixed circular orbit around the Sun. We find that $\Delta L/L = 10^{-11}$. For such an orbit, as shown in Wisdom (1987), a Jacobi-like integral exists. The conservation of this integral can be used to validate the integrator's accuracy. Fig. 7-1 shows that the Jacobi-like integral is conserved to 3×10^{-10} (Fig. 7-1).

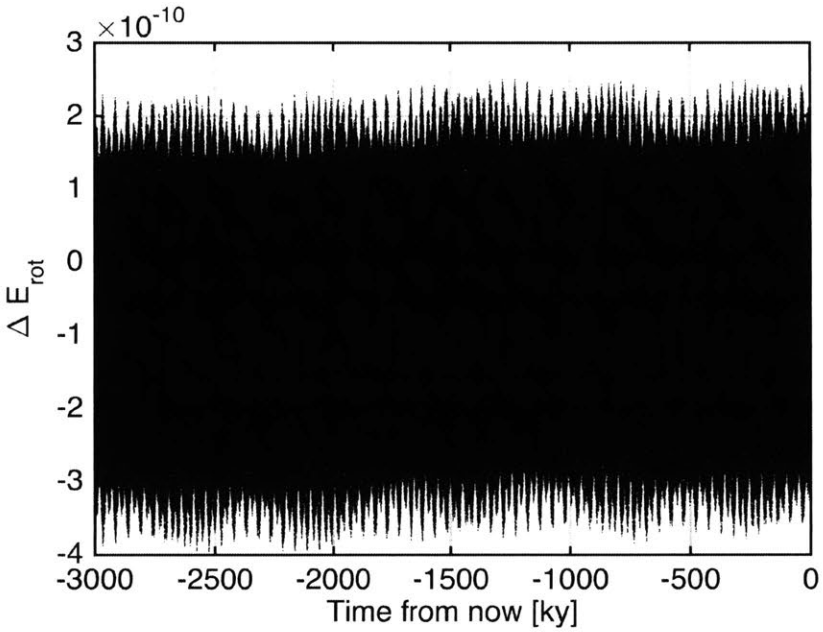

Figure 7-1 – Jacobi-like integral conservation.

We also compute the conservation of the $H_{Translation}$ in the absence of the orbital-rotational coupling. As seen in Fig. 7-2, the total mechanical energy is conserved to 10^{-10}.

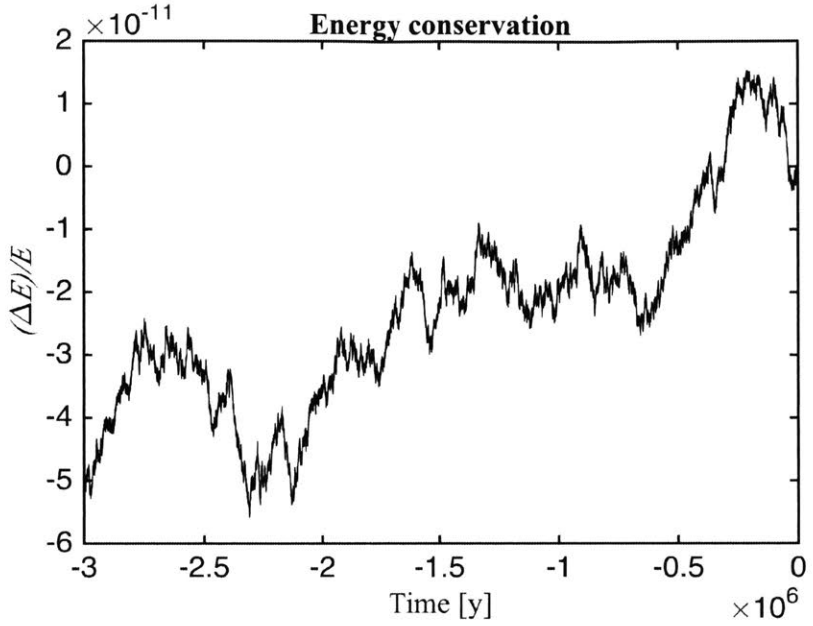

Figure 7-2 – Energy conservation.

As a further validation of our integrator in a more realistic case, we performed an integration of the obliquity of Mars over the last 4.5 My and compared our results with Laskar et al. (2004). There is excellent agreement between the two obliquity histories, and the growing divergence is likely due to the difference in the initial condition and the fact that the martian obliquity is known to be chaotic.

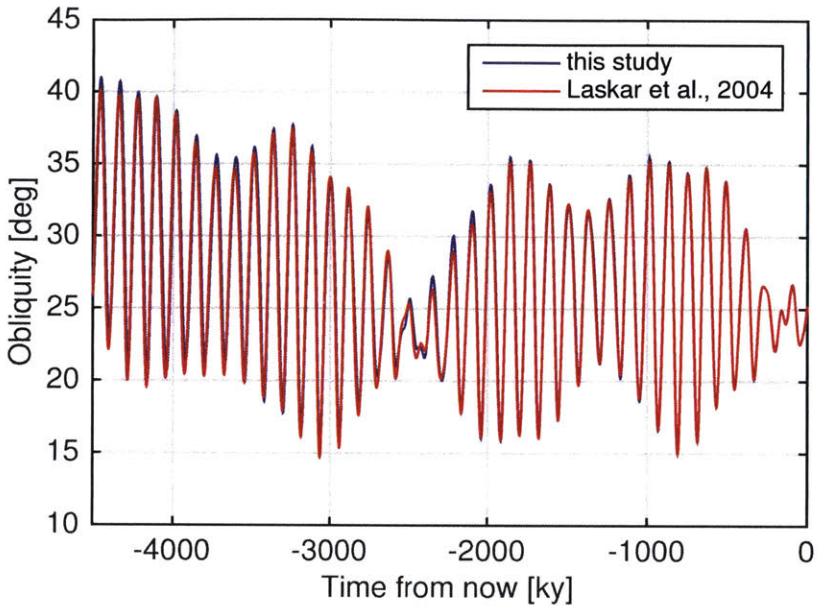

Figure 7-3 – Obliquity of Mars over the last 4.5 My.

7.2.6 Illumination modeling using DTM

In order to assess the illumination conditions at Ceres over a range of past obliquities, we performed numerical illumination modeling using a shape model of Ceres. This approach has been used in the past for the Moon and Mercury, using a shape model derived from laser altimetry data (Mazarico et al., 2011; Neumann et al., 2013). We follow the approach described in Schorghofer et al. (2016) using raytracing over multi-level, multi-resolution triangulated meshes. The extended nature of the Sun as a light source is handled by discretizing its disc into 500 point sources. For the present-day orientation of Ceres, we use the current best estimates consistent with the adopted shape model (Preusker et al., 2015, 2016). While Schorghofer et al. (2016) resampled the HAMO-derived Digital Terrain Model (DTM) onto a grid of points uniformly spaced in north polar stereographic projection, we took advantage of the full resolution of the DTM high-level products by implementing the Lambert-Azimuthal Equal Area projection (Snyder, 1982) and performing the simulations in that projection at a resolution of 135 m/pixel down to $\approx 53.5°$ latitude. For com-

putational reasons and because of Ceres' fast spin (rotational period ≈9.07 h) and long orbital period (4.6 years), we restricted our simulations to a full rotation at each pole's respective solstice, which is the time that provides the best constraint regarding the presence of long-lived shadows.

7.3 Data

7.3.1 Ceres shape

The shape model of Ceres was produced using a stereophotogrammetry technique applied by the German Aerospace Center (DLR) (Preusker et al., 2015, 2016). The stereophotogrammetric (SPG) method of shape reconstruction is purely geometrical and does not rely on simultaneously solving for surface heights and albedo. The global shape model used here was computed from images acquired during Dawn's HAMO phase (6 weeks at ≈1500 km altitude), at a resolution of ≈135 meters/pixel. Thanks to the high sensitivity of the Dawn's Framing Camera (Sierks et al., 2011; Schröder et al., 2013)) it is possible to utilize features seen in scattered light to constrain the shape of the floors of shadowed polar craters, despite larger ray intersection errors and the need for some interpolation near those locations. The comparison of the area in permanent shadow derived from numerical illumination simulations performed with a shape model (Schorghofer et al., 2016) and that obtained from a survey of minimum shadows observed by FC near northern solstice (Platz et al., 2016) shows an agreement to ≈2%, which brings confidence in the modeling methodology and DTM quality for illumination modeling. However, we find that the HAMO DTM resolution and accuracy are typically not sufficient to model the conditions within small craters (<4 km). We also used the shape reconstructed for the southern hemisphere. Despite the unfavorable lighting conditions, as Dawn visited Ceres during southern winter, the HAMO DTM allows illumination modeling, outside of the immediate polar region (85°–90°S) which was poorly illumination and in seasonal darkness.

7.3.2 Ceres rotational pole and rotation rate

The arrival of the Dawn spacecraft to Ceres made it possible to substantially improve the accuracy of Ceres' pole position and rotation rate. The present day obliquity of Ceres is $\approx 4°$. For the present study, we used the spin pole location derived from the Dawn measurements (Table 7.1). [1]

δ (°)	α (°)	σ_δ (°)	σ_α (°)
66.75988	291.42592	0.01	0.01

Table 7.1 – Ceres pole position at JD = 2451545.0. δ and α are the declination and right ascension of the spin axis in the J2000 frame, respectively; σ_δ and σ_α are the corresponding uncertainties. NEED TO CHECK UNCERTAINTIES

7.3.3 Ceres moments of inertia

We can constrain the moments of inertia of Ceres using the observed degree-2 gravity field coefficients and a hydrostatic equilibrium assumption. It was shown in subsection 6.3.3 that Ceres' polar moment of inertia factor $C/MR_{vol}^2 \approx 0.392$ (Ermakov et al., 2016), where $R_{vol} = 469.7$ km – the radius of a sphere that has the volume equivalent to the volume of Ceres. Using the relations between moments of inertia and unnormalized gravity coefficients (Park et al., 2016), we have:

$$\begin{Bmatrix} A/(MR_{vol}^2) \\ B/(MR_{vol}^2) \end{Bmatrix} = \left(C/(MR_{vol}^2) - J_2\right) + \sqrt{C_{22}^2 + S_{22}^2} \cdot \begin{Bmatrix} -2 \\ +2 \end{Bmatrix}. \tag{7.24}$$

We used a two-layer model and hydrostatic equilibrium method from Tricarico (2014) to derive moments of inertia from the observed gravity coefficients. The major uncertainty in deriving the moments of inertia from the observed gravity coefficients is due to non-hydrostaticity of Ceres. The non-hydrostatic effects can change C/MR_{vol}^2 by as much as 0.005, which corresponds to 3% of non-hydrostaticity in the degree-2 gravity field. We, therefore, chose to vary C/MR_{vol}^2 between 0.387 and 0.397 for our

[1] A PCK SPICE kernel dawn_ceres_SPC160422.tpc was used for Ceres' initial orientation.

orbital integrations. For the triaxial Ceres, the equatorial moments of inertia A and B are computed according to 7.24. For the biaxial case, we take the equatorial moment to be $(A + B)/2$.

7.3.4 Bright crater floor deposits

A number of bright crater floor deposits (BCFDs) in PSRs have been identified (Table 7.2). In general, BCFDs are rare: only 5 out of 49 present-day PSRs greater than 10 km^2 contain BCFDs. All of the deposits considered for this study lie entirely within the present-day PSRs, except NP5. Light reflected from the high-standing, illuminated crater rims allows identification of the surface features within the shadows. However, this illumination is much weaker than direct sunlight and resolving the surface requires substantial stretching of the image. This inevitably enhances the image noise and artifacts due to image compression. Careful visual inspection of images taken with different illumination geometries and compression ratios is therefore required to recognize real surface brightness variations.

The surface brightness of the BCFDs, with a exception of NP5, is typically 1.4 – 3.0 times higher than the surrounding area. It is important to note that the deposits are seen in diffuse, secondary, illumination. As such we cannot derive an albedo, which is defined at phase angle zero. The fact that NP5 is not entirely in permanent shadow possibly indicates that the nature of this deposit may be different from the others considered in this study.

ID	ϕ (°)	λ (°)	BCFD area (km^2)	brightness ratio	crater diameter (km)	comments
NP4 central part	+86.2	79.3	16.9	3.0±0.8	6.5	contains a PSR up to $\epsilon = 20°$
NP4 outer part			2.4	1.4±0.3		
NP7	+77.6	353.9	0.9	1.8±0.3	4.6	contains a PSR up to at least $\epsilon = 12°$
NP5 shadowed part	+69.9	114.0	2.4	2.7±0.2	3.5	No PSR at DTM resolution.
NP5 illuminated part				2.8±0.2		Water ice detected by VIR (Platz et al., 2016)
NP26	+79.0	259.1	16.0	-	8.6	contains a PSR up to at least $\epsilon = 20°$
NP19	+81.3	313.9	10.8	-	6.5	contains a PSR up to at least $\epsilon = 12°$
SP1	-71.3	31.2	6.9	1.6±0.2	6.9	contains a PSR up to at least $\epsilon = 20°$
SP2	-69.7	168.5	< 1	-	2.2	not well resolved in DTM

Table 7.2 – Summary of the BCFDs.

7.4 Results

7.4.1 Obliquity history

We performed a number of orbital integrations with triaxial and biaxial Ceres, as well as with different number of perturbing planets. As long as Jupiter and Saturn are included and interact with Ceres, we get a essentially the same obliquity history. The initial positions and velocities of planets were taken from the DE430 ephemeris (Folkner et al., 2014) using the SPICE ancillary information system (Acton, 1996). We find that the obliquity history is not sensitive to the triaxiality of Ceres. This allows us to use much longer integration time steps because there is no need to resolve the Ceres' rotation period, and the triaxial step $\mathcal{B}(h)$ can be skipped. Our integrations show that the obliquity history is essentially identical for biaxial and triaxial Ceres. The results are also not sensitive to the relativistic effects, which were modeled as an additional velocity kick.

Currently, the value of the osculating obliquity of Ceres is 4.03° and is on an increasing trend. The Ceres obliquity passed its local minimum 1340 years ago when the obliquity was 2.42°. The most recent obliquity maximum of 18.56° was reached 13950 years ago (Fig. 7-4).

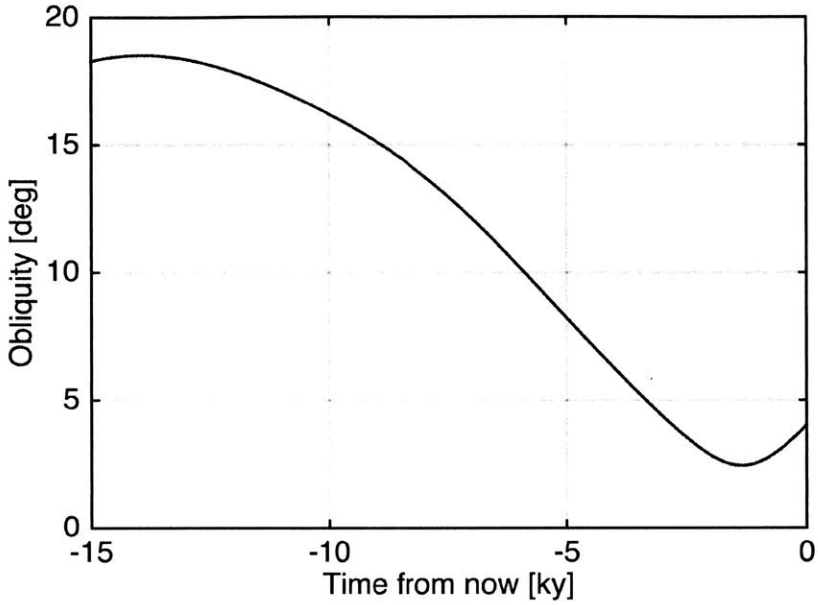

Figure 7-4 – Recent Ceres obliquity history for $C/MR_{vol}^2 = 0.392$.

Our long-term integrations show that the obliquity of Ceres undergoes large oscillations (Fig. 7-5-7-7). The main period of the oscillation is 24.5 ky (Fig. 7-8). Obliquity can reach $\approx 20°$, which is much larger than the present day 4°. The pattern of oscillations is very regular and with no evidence of chaos even past 3 My. The Ceres obliquity is skewed towards the higher values (Fig. 7-9), with a mean obliquity of Ceres of 12.26° and a median of 13.27°. The obliquity is greater than 15° more than 40% of the time. Curiously, nature has given us a unique opportunity to observe Ceres at the time when the polar winters are minimal, which enables more and higher quality observations of the polar areas.

The range of obliquity oscillations does not have a strong dependence on the assumed moments of inertia within the limits considered given the Dawn gravity measurements (Table 7.3). The obliquity oscillations are driven by the periodic change in Ceres' orbit inclination which happens with a period of 22 ky and the pole precession period which is 210 ky. The obliquity cycle period is therefore close the synodic period between the precession period T_p and inclination period T_i. This synodic period is $(T_i T_p) \,/\, (T_p - T_i) \approx$24.6 ky. The Dawn observations disagree with the prediction of

Bills and Nimmo (2011a): the obliquity of Ceres is not tidally damped to the lowest energy state. However, this might not be surprising given the long tidal damping period of the obliquity (Rambaux et al., 2011).

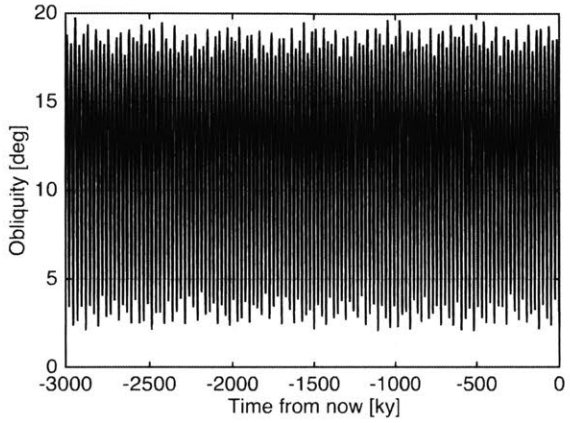

Figure 7-5 – Ceres obliquity history for $C/MR_{vol}^2 = 0.387$.

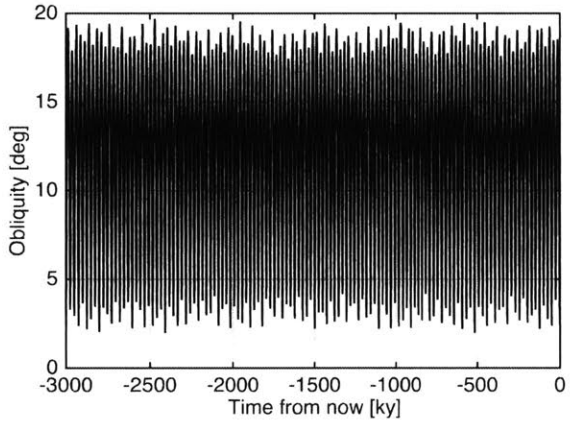

Figure 7-6 – Ceres obliquity history for $C/MR_{vol}^2 = 0.392$.

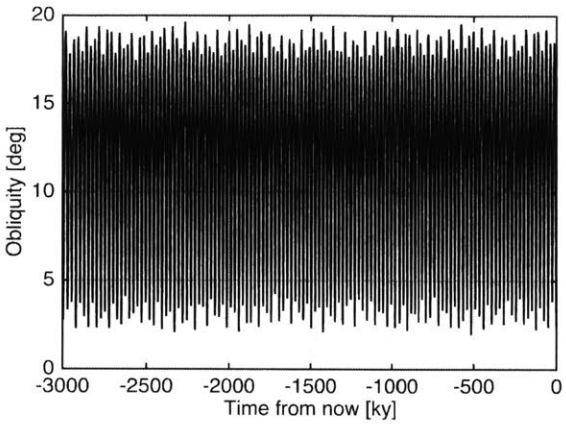

Figure 7-7 – Ceres obliquity history for $C/MR_{vol}^2 = 0.397$.

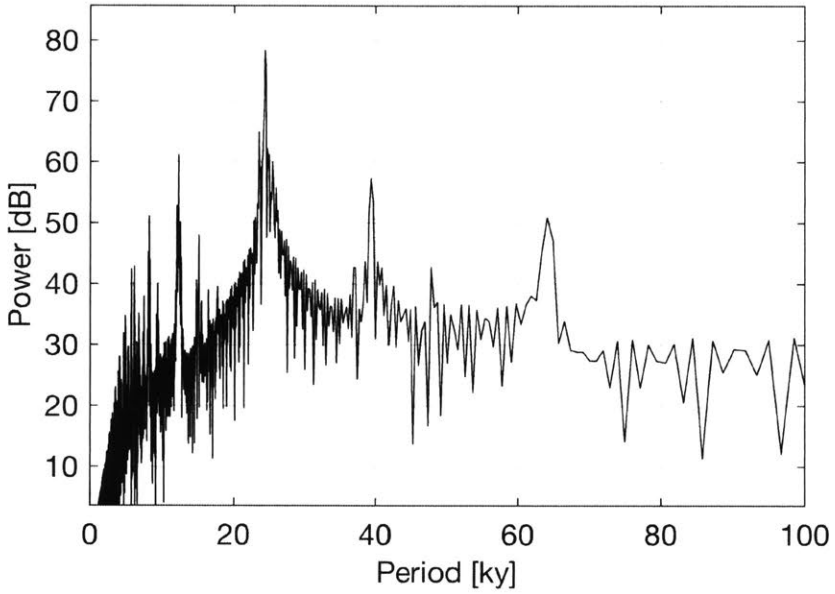

Figure 7-8 – Periodogram of Ceres' obliquity for $C/MR_{vol}^2 = 0.392$.

C/MR_{vol}^2	min (ϵ)	max (ϵ)
0.387	2.06°	19.76°
0.392	1.97°	19.71°
0.397	1.95°	19.64°

Table 7.3 – Range of obliquity (ϵ) variations for the 3 My integration.

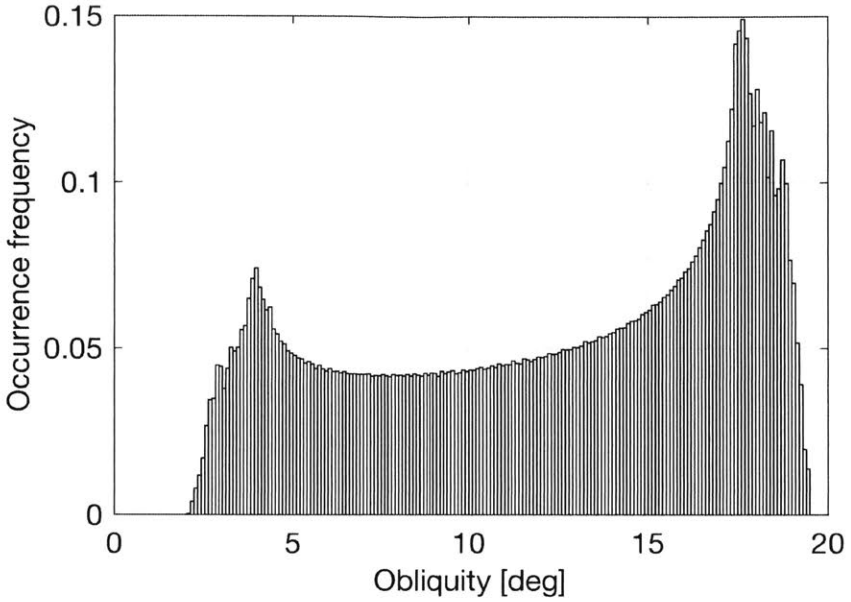

Figure 7-9 – Ceres obliquity histogram over 3 My for $C/MR_{vol}^2 = 0.392$.

We also find that there is no a hemispheric asymmetry in terms of insolation over long (100 ky and longer). The distribution of the sub-solar point latitude at the perihelion is symmetric with respect to the equator.

7.4.2 PSR history

The initial illumination modeling by Schorghofer et al. (2016) revealed dozens of craters hosting PSRs. The total area of PSRs is a strong function of the body's obliquity. As expected, the total area in permanent shadow decreases at larger obliquity. As illustrated in Fig. 7-10, simulations performed over a range of obliquity values ($2° - 20°$) indicate a reduction in PSR area from $\approx$3400 km^2 at $\epsilon = 2°$ to only $\approx$2.4 km^2 at $\epsilon = 18.56°$ and $\approx$1.6 km^2 at $\epsilon = 20°$.

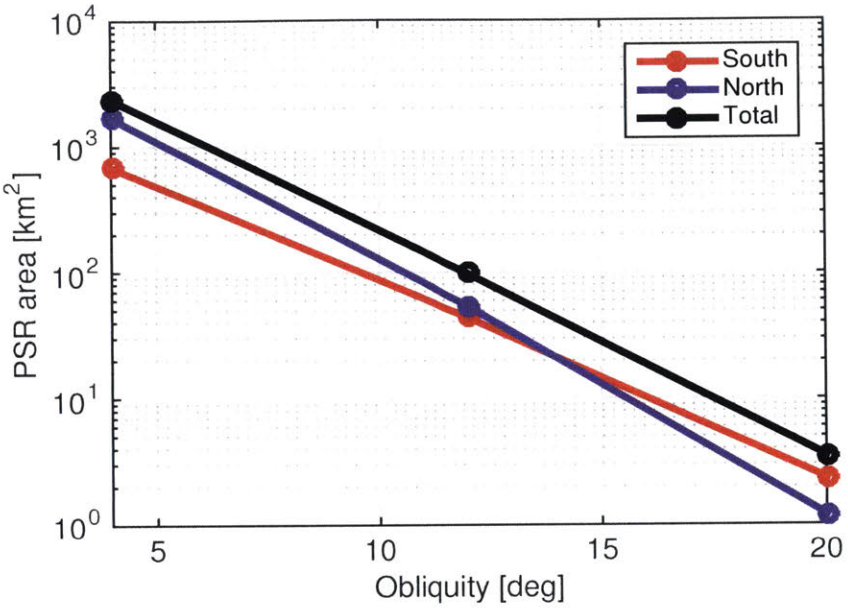

Figure 7-10 – Area of PSRs.

In the northern hemisphere (Fig. 7-11), we find that only two crater floors remain partly in permanent shadow at $\epsilon = 20°$: NP4 ($D = 6.6$ km) and NP26 ($D = 4.5$ km). Fig. 7-13 shows the shrinking outlines of the shadow at NP4 as obliquity increases. Among the other identified northern BCFDs, NP7 ($D = 4.6$ km) maintains an area of permanent shadow up to $\epsilon = 12°$, while NP5 is likely too small ($D = 3.5$ km) to be resolved by the DTM with confidence.

In the southern hemisphere, we find that part of the floor of crater SP1 remains in permanent shadow at the maximum obliquity. Although we did not identify other areas in permanent shadow at $\epsilon = 20°$, due to severe DTM artifacts near the South Pole (Fig. 7-12), it is an intriguing fact that SP1 is the only such example in our results. The other southern bright deposit (SP2) is inside a very small crater (~2.2 km), below what the DTM can confidently model. Both NP4 and SP1 are 6-7 km craters with steep walls (40°–45° slope), the primary reason for the persistence of their shadowed floor at high obliquity.

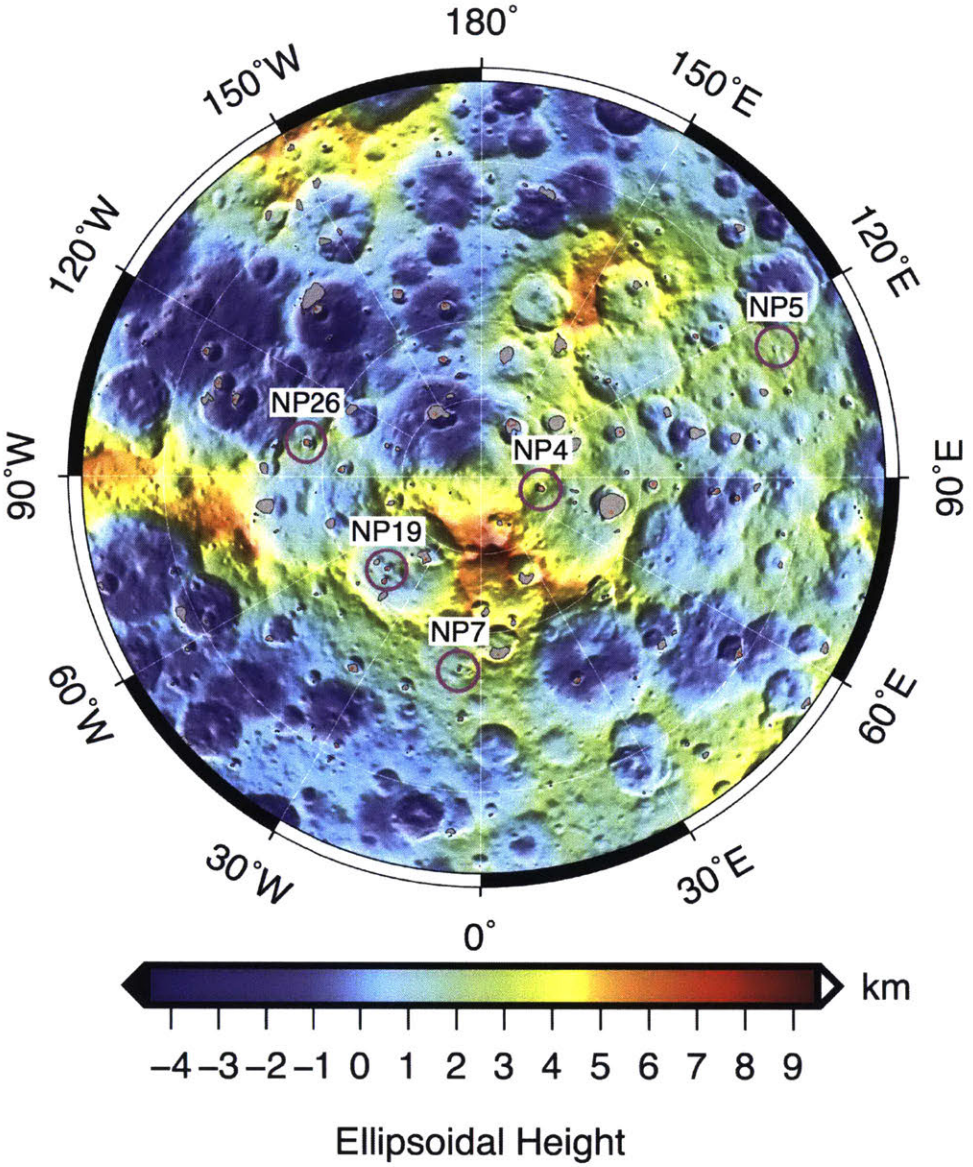

Figure 7-11 – The PSR areas at $\epsilon = 4°$ in the northern hemisphere are shown as filled gray areas. The boundaries for the PSRs at $\epsilon = 12°$ are shown as red contours. The heights are with respect to a 482 km × 446 km ellipsoid.

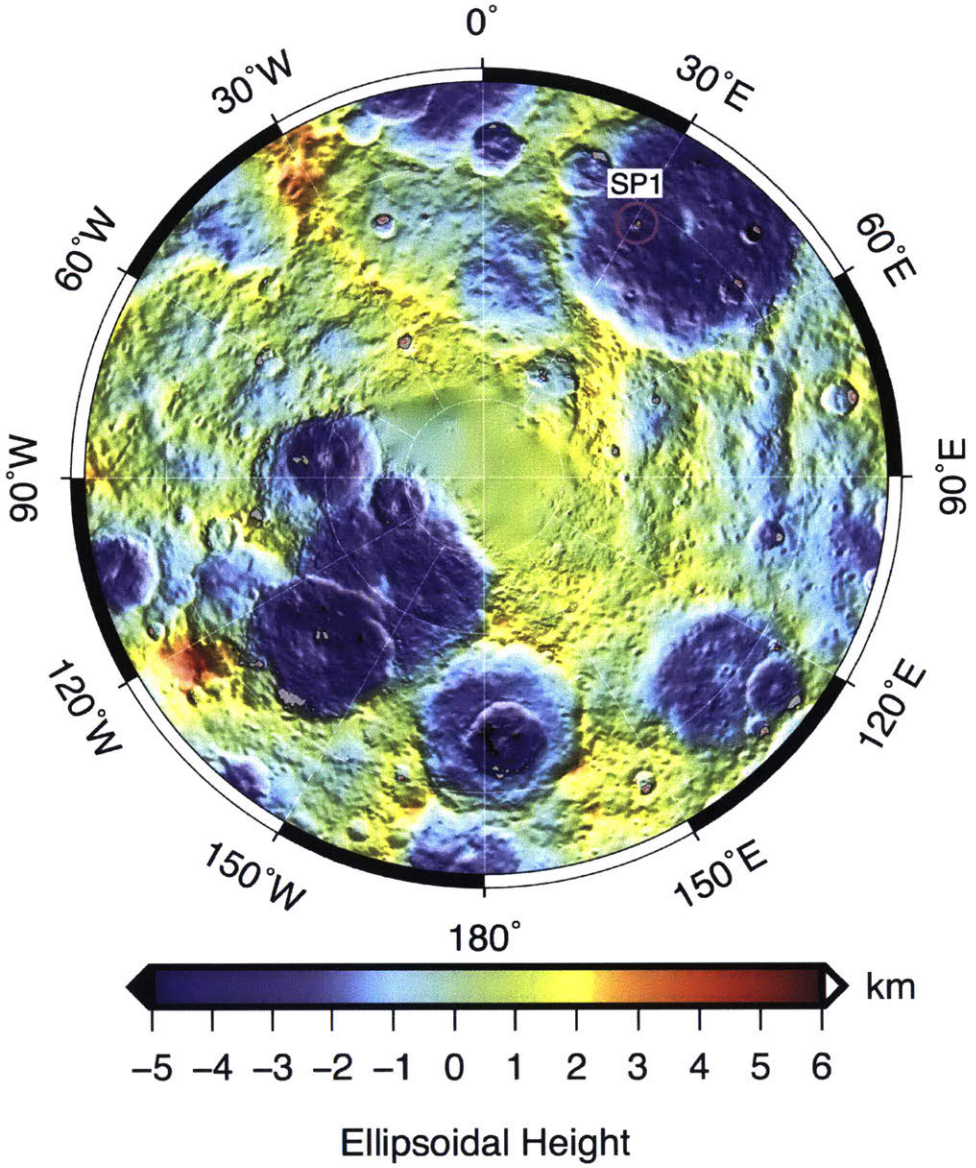

Figure 7-12 – The PSR areas at $\epsilon = 4°$ in the southern hemisphere are shown as filled gray areas. The boundaries for the PSRs at $\epsilon = 12°$ are shown as red contours. The heights are with respect to a 482 km × 446 km ellipsoid.

7.4.3 Relationship of persistent PSRs and BCFDs

We will an apparent correlation between the most persistent PSRs, i.e. regions that stay in permanent shadow at the maximum obliquity of 20° and BCFDs. Fig.

7-13 shows FC images of the BCFDs and the outlines of PSRs computed using illumination modeling. The grey scale of the images is piecewise linear. This is done in order to show both the shadowed and illuminated parts of the surface.

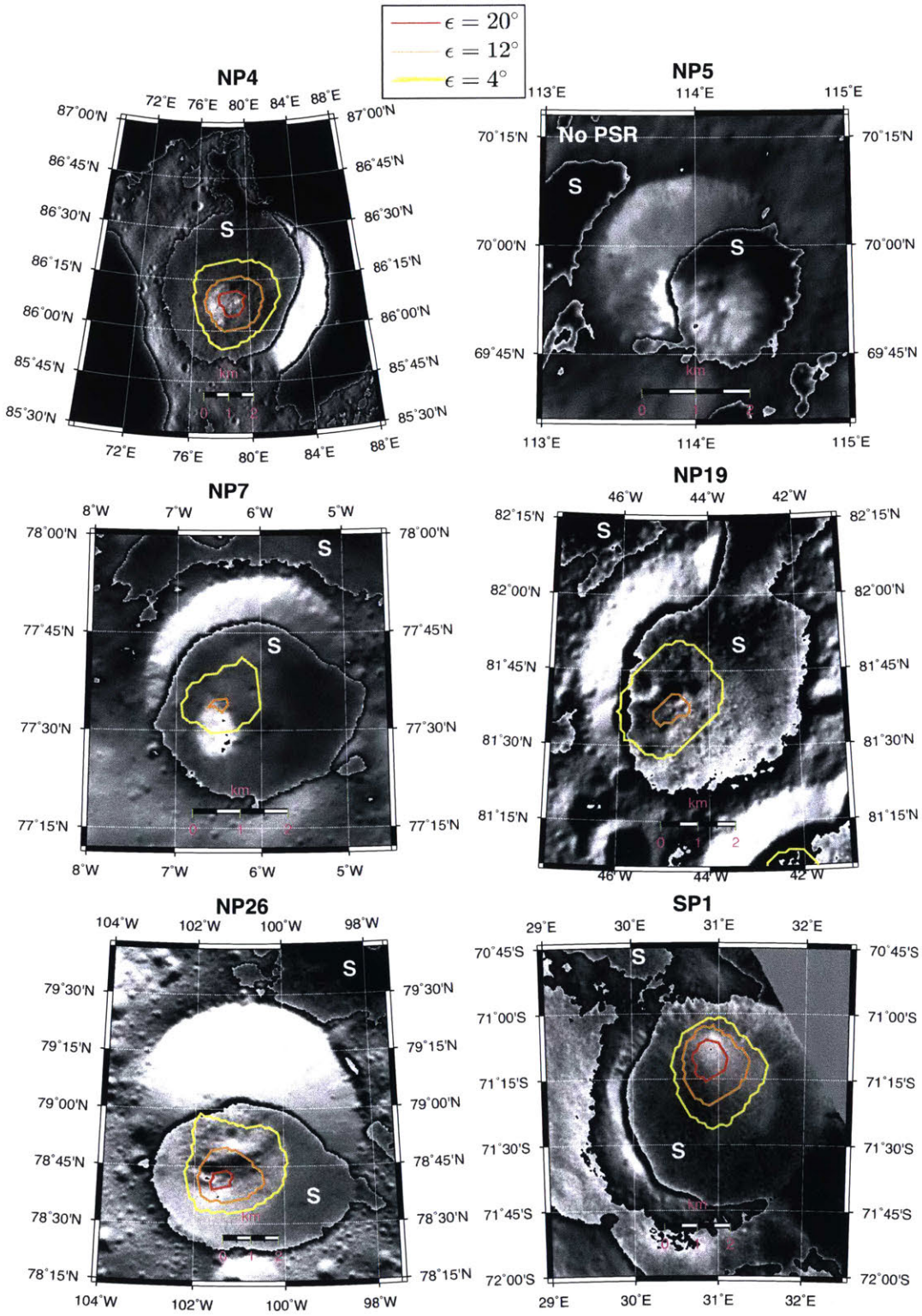

Figure 7-13 – Projected images of BCFDs and the outlines of PSRs for different obliquities ($\epsilon = 4°$, $\epsilon = 12°$, $\epsilon = 20°$). The regions in shadow are marked with the letter S.

7.4.3.1 NP4

The outline of the PSR in crater NP4 corresponds to boundary of the BCFD at the maximum obliquity (Fig. 7-13). Interestingly, the NP4 deposit appears to have two brightness gradations of the bottom which will be referred to as *central deposit* and the *outer deposit.* The central deposit is XX times brighter than the outer one and lies in the center of the PSR. The outer deposit appears to have a well defined boundary that approximately coincides with the PSR boundary at an obliquity of 2°.

7.4.3.2 NP7

The appearance of the BCFD in NP7 (Fig. 7-13) is similar to that in NP4. The NP7 crater remains in shadow up to an obliquity of 12°. However, it is possible that due the crater's smaller size (D = 4.6 km), its real depth is larger than the depth derived from the HAMO DTM and thus possible that permanent shadow remains at higher obliquity.

7.4.3.3 NP5

The NP5 crater is not permanently shadowed at the resolution of the DTM, but the shadow-stacking method reveals a small PSR (Platz et al., 2016). The brightness of the BCFD in NP5 is significantly larger than those of the other BCFDs in this study. Part of the BCFD in NP5 sticks out of the shadow (Fig. 7-13) and is known to be water ice from the VIR spectroscopic measurements (Platz et al., 2016).

A standard one-dimensional thermal model is used to estimate the sublimation rate of an ice deposit at 70° latitude (Schorghofer, 2008). Assuming a Bond albedo of 0.2 and thermal properties appropriate for bulk ice, the sublimation rate of ice exposed on the surface is $\approx 10^{-3}$ kg m^{-2} yr^{-1}. In this case the peak temperature is $\approx$135 K and the mean temperature $\approx$130 K. For lower thermal inertia, appropriate if the ice is not in bulk form, the peak temperature would be higher and the sublimation loss faster. This calculation demonstrates that a sunlit macroscopic ice deposit at this latitude must be geologically young.

7.4.3.4 NP19

The NP19 crater remains in shadow at an obliquity of 12° (Fig. 7-13). Its bright deposit is qualitatively similar to the one of NP26 and the outer deposit of NP4. We should note that the BCFD inside NP19 has the weakest brightness contrast with respect to the surrounding terrain among the deposits considered in this study.

7.4.3.5 NP26

The NP26 crater remains in shadow up to the maximum obliquity of 20°. Its floor deposit is offset from the crater center and lies partially on the crater wall. The deposit has a sharp and round boundary. There appears to be no morphological difference in the region covered by the bright deposit compared to the surrounding terrain indicating a low thickness of the deposit. The apparent brightness contrast of the deposit in crater NP26 with respect to the surrounding area is lower than for features NP7, NP5 and the central deposit of NP4. Qualitatively, it is similar to the outer deposit in crater NP4 or to the deposit in NP19.

7.4.3.6 SP1

The SP1 crater is one of the two regions in the southern hemisphere that remains in shadow at an obliquity of 20°. The brightest part of the BCFD well corresponds to the location of the PSR at $\epsilon = 20°$. Further identification of PSRs and BCFDs in the southern polar region will critically depend on the subsequent observing campaign as the sub-solar point moves southward.

7.5 Discussion

Unlike the Moon or Mercury, Ceres' obliquity undergoes rapid and large periodic oscillations. The unique set of crater floor deposits in Ceres appears to be correlated with the most persistent of PSRs, i.e. the area that remain in shadow even at the highest obliquity ($\epsilon = 20°$). In the northern hemisphere, at an obliquity of 20°,

only two PSRs remain, which were shown to host bright deposits. In the southern hemisphere, despite poorer data from Dawn at the time of writing, there remain two PSRs at an obliquity of 20° and, one of them has a definite bright deposit. The second most prominent BCFD in the southern hemisphere is located in a 2 km crater that is not well resolved in the HAMO shape model.

Craters NP4, NP19, NP26 and SP1 also possess weaker brightness contrast deposits. Interestingly, the boundaries of those areas approximately correspond to the PSR boundary at the present-day obliquity of 4°. We suggest that we could be due to events of mass waisting that might expose the ground ice. Once the PSR boundary shrinks due to increasing obliquity, these weak constant deposits are likely to sublimate due to an increased solar incidence flux.

A Monte-Carlo model of thermal ballistic hops is used to estimate the fraction of water molecules that will ultimately fall into cold traps. For present-day Ceres this fraction is 0.14% (Schorghofer et al., 2016). We carried out the same type of Monte-Carlo calculation for an obliquity of 10° and a corresponding PSR area of 167 km^2. We find that the fraction trapped is proportional to the PSR area. Hence, the ratio of fraction trapped to the cumulative PSR area, also known as trapping efficiency, is independent of obliquity. This suggests that permanent shadow at maximum obliquity is a necessary condition for the formation of the BCFDs, which are likely composed of volatiles deposited via the cold trapping mechanism.

7.6 Conclusions

We have integrated the obliquity of Ceres over the last 3 My for a range of moments of inertia constrained by the Dawn gravity observations. We discovered that obliquity undergoes large oscillations with a period of ≈25 ky. Within the range of the Dawn-constrained moments of inertia, our integrations show that obliquity goes to values as high as ≈ 20°. At such high obliquity, most of the present day PSRs receive direct sun light. However, there are still PSRs at an obliquity of 20°. We find a correlation between BCFDs and the most persistent PSRs. In the northern hemisphere, we find

that only two PSRs remain at ϵ_{max}; these two PSRs contain BCFDs. In the southern hemisphere, we also find that only one crater with a BCFD remains in shadow at ϵ_{max}. Our results support the permanent shadow cold trapping mechanism of volatiles for formation of the observed BCFDs.

Chapter 8

Conclusions and future work

8.1 Conclusions

We have investigated Vesta, Ceres and the Moon using gravity and topography data. Gravity and topography provide insight into a planetary body's internal structure. We find that Vesta was once hot and hydrostatic and is no longer either. It was despun by two giant collisions that produced the two largest basins on the asteroid's surface – Rheasilvia and Veneneia. These two basins in the southern hemisphere represent the largest deviation of Vesta from a hydrostatic equilibrium shape. On the other hand, the northern hemisphere is well approximated by an ellipsoid and represents the fossil shape of Vesta prior to the giant impacts. We used a combination of gravity/topography data with geochemical data from the HED meteorites and find constraints on the core size. Taking densities similar to iron meteorites for the core and the range of crustal densities corresponding to the HED meteorites, the core radius ranges from 110 to 138 km. The gravity model of Vesta has an effective resolution of 18 spherical harmonic degrees. The power of the Bouguer anomaly is lower and therefore the effective resolution of the Bouguer anomaly is lower (15 degrees). Vesta's topography is not compensated. After computing the Bouguer anomaly, we find that there are a limited number of interpretable gravity signals that can be attributed to geomorphologic, geologic or other features identified from remote sensing data. The two most characteristic features are the region of highest topography – Vestalia Terra

– with the strongest positive anomaly and the central peak of Rheasilvia, which is also associated with a positive anomaly which likely represents the deeper and denser layers excavated by the Rheasilvia impact. It is likely that the porosity field controls a substantial fraction of the remaining gravity signals.

Unlike Vesta, Ceres possesses plenty of interpretable gravity anomalies even though the gravity model of Ceres has a lower resolution (degree 9-12). Gravity/topography admittance analysis reveals that Ceres' topography is isostatically compensated. We combine the gravity/topography data and finite element modeling to constrain Ceres' rheology and density structure. We find that Ceres' crust is light and mechanically strong with the volumetric water ice content <30 vol%. Ceres has experienced limited viscous relaxation as evidenced by the deviation of its topographic power spectrum from the power law at low degrees.

The divergent geodynamic evolutions of Vesta and Ceres may be attributed to several factors. The main difference between Vesta and Ceres is their size. Being smaller, Vesta cooled more quickly than Ceres and developed an elastic lithosphere before acquiring most of its topography. Ceres, on the other hand, had a longer cooling time and has not developed an appreciable lithosphere at a 4.5 Gy timescale. Consequently, Ceres' topography is isostatically compensated. Additionally, having accreted further out in the asteroid belt Ceres accreted and subsequently retained more volatiles, unlike mostly silica-dominated Vesta. This compositional difference affects the rate viscous relaxation of topography making Ceres' near surface viscosities several orders of magnitude lower than those of Vesta.

Using the moments of inertia constrained by the Dawn gravity data we study the obliquity history of Ceres. We find that Ceres' obliquity has undergoes large oscillations with the main period of 25 ky and a maximum of 19.7°. The obliquity oscillations are driven by the periodic change of Ceres' orbit inclination and the pole precession. Interestingly, the present day obliquity is close to the minimum obliquity. Ceres passed a local obliquity minimum 1327 years ago (ε_{min}=2.4°). The most recent maximum was 13895 years ago (ε_{max}=18.5°). At such high obliquity, most of the present-day permanently shadowed regions receive direct sunlight. We

find a correlation between bright crater floor deposits (BCFD) and the most persistent PSRs. In the northern hemisphere, we find that only two PSRs remain at ϵ_{max}. Interestingly, these PSRs contain BCFDs. In the southern hemisphere, we also find that only one crater with a BCFD remains in shadow at maximum obliquity.

The GRAIL mission has provided an incredible gravity set. We have investigated the spatial and spectral characteristics of the GRAIL gravity models. The GRAIL gravity models have highly non-uniform resolution. We compute the coherence between the GRAIL gravity and gravity-from-topography models. For most of the arcs coherence drops significantly at degrees corresponding to integer multiples of the spacecraft separation. Therefore, care should taken if the characteristic scale of the feature of interest is comparable to one of the resonant scales.

8.2 Future work

8.2.1 Vesta

In our future work, we plan to localize the gravity and topography of Vesta using Slepian functions in order to constrain the lateral density variations of the crust.

8.2.2 Ceres

We plan to analyze the geophysical structure of the biggest impact basins on Ceres (Kerwan, Urvara and Yalode) using the observed isostatic gravity anomalies from the LAMO gravity model. Additionally, we plan to study the possibility of the recent or present-day geologic activity in the Occator and Ahuna Mons regions using the gravity/topography data and finite element modeling. Ongoing work also includes computation of the irradiance of individual BCFDs given the orbital and obliquity history.

8.2.3 The Moon

We plan to conduct a study on correlations between the radar data collected by the Kaguya spacecraft and GRAIL gravity data. The Lunar Radar Sounder (LRS; Ono et al. 2010) on JAXA's Kaguya spacecraft (Kato et al., 2010) investigated the geologic subsurface structure of the Moon to a depth of a few km. GRAIL gravity models are potentially sensitive to subsurface structure at such depths in some regions of the Moon. GRAIL gravity and LRS radar data are complementary since both are sensitive to density/compositional heterogeneities. Cross-correlation of GRAIL and LRS data has the potential to produce new constraints on the structure and evolution of the lunar maria.

Subsurface radar reflections have been observed primarily in the maria. Originally, subsurface reflections were detected with Lunar Sounder Experiment aboard Apollo 17 (Phillips et al., 1973). Subsurface layering was attributed to multiple episodes of volcanism (cf. Sharpton and Head 1982). Later, Kaguya's LRS produced similar measurements but with global-scale coverage (Ono et al., 2009; Oshigami et al., 2009, 2014).

Laboratory measurements (Kiefer et al., 2012) show that density variations among mare basalts can be up to ~200 kg/m^3 or ~7%. The LRS measurements have detected subsurface reflection in the upper 1 km of the crust. Combining these two estimates and using the Bouguer slab approximation, we estimate that anomalies of order 1-10 mGal are expected due to potentially varying density of surface and/or subsurface horizons. This accuracy is achievable with the latest GRAIL gravity models (Konopliv et al., 2014b; Lemoine et al., 2014).

The LRS surface backscattering power is indicative of surface and near sub-surface dielectric properties, which are sensitive to target density and roughness. We investigate the northwestern part of the Procellarium basin because it is the region with the strongest signal-to-noise ratios in gravity model within maria. To examine shallow subsurface structure, we map the surface received power by tracking the first return of radar echoes and compare it with gravity gradients (Andrews-Hanna et al., 2013),

which are particularly sensitive to small-scale structures.

C.H. Acton. Ancillary data services of NASA's Navigation and Ancillary Information Facility. *Planetary and Space Science*, 44(1):65–70, 1996.

E. Akim. Determination of the gravity field of the Moon from movement of artificial satellite of the moon Luna-10. In *Doklady Akademii Nauk USSR*, volume 170, pages 799–802, 1966.

E. Ammannito, M.C. De Sanctis, E. Palomba, A. Longobardo, D.W. Mittlefehldt, H.Y. McSween, S. Marchi, M.T. Capria, F. Capaccioni, A. Frigeri, and et al. Olivine in an unexpected location on Vesta's surface. *Nature*, 504(7478):122–125, 2013.

J.C. Andrews-Hanna, S.W. Asmar, J.W. Head, W.S. Kiefer, A.S. Konopliv, F.G. Lemoine, I. Matsuyama, E. Mazarico, P.J. McGovern, H.J. Melosh, and et al. Ancient igneous intrusions and early expansion of the Moon revealed by GRAIL gravity gradiometry. *Science*, 339(6120):675–678, 2013.

J.R. Arnold. Ice in the lunar polar regions. *Journal of Geophysical Research: Solid Earth*, 84(B10):5659–5668, 1979.

S.W. Asmar, A.S. Konopliv, R.S. Park, B.G. Bills, R.W. Gaskell, C.A. Raymond, C.T. Russell, D.E. Smith, M.J. Toplis, and M.T. Zuber. The gravity field of Vesta and implications for interior structure. In *Lunar and Planetary Science Conference*, volume 43, page 2600, 2012.

G. Balmino. Gravitational potential harmonics from the shape of an homogeneous body. *Celestial Mechanics and Dynamical Astronomy*, 60(3):331–364, 1994. ISSN 1572-9478. doi: 10.1007/BF00691901. URL `http://dx.doi.org/10.1007/BF00691901`.

E.E. Barnard. Micrometrical determinations of the diameters of the minor planets Ceres (1), Pallas (2), Juno (3), and Vesta (4), made with the filar micrometer of the 36-inch equatorial of the Lick Observatory. *Mon. Not. R. Astron. Soc.*, 55: 55–63, 1895.

A.W. Beck and H.Y. McSween Jr. Diogenites as polymict breccias composed of orthopyroxenite and harzburgite. *Meteoritics & Planetary Science*, 45(5):850–872, 2010.

A.W. Beck, T.J. McCoy, J.M. Sunshine, C.E. Viviano, C.M. Corrigan, T. Hiroi, and R.G. Mayne. Challenges in detecting olivine on the surface of 4 Vesta. *Meteoritics & Planetary Science*, 48(11):2155–2165, 2013.

B. Bertoni. Multi-dimensional ellipsoidal fitting. *Department of Physics, South Methodist University, Tech. Rep. SMU-HEP-10-14*, 2010.

J. Besserer, F. Nimmo, M.A. Wieczorek, R.C. Weber, W.S. Kiefer, P.J. McGovern, J.C. Andrews-Hanna, D.E. Smith, and M.T. Zuber. GRAIL gravity constraints on the vertical and lateral density structure of the lunar crust. *Geophysical Research Letters*, 41(16):5771–5777, 2014. ISSN 1944-8007. doi: 10.1002/2014GL060240. URL `http://dx.doi.org/10.1002/2014GL060240`.

B.G. Bills and F.G. Lemoine. Gravitational and topographic isotropy of the Earth, Moon, Mars, and Venus. *Journal of Geophysical Research: Planets*, 100(E12): 26275–26295, 1995. ISSN 2156-2202. doi: 10.1029/95JE02982. URL `http://dx.doi.org/10.1029/95JE02982`.

B.G. Bills and F. Nimmo. Forced obliquities and moments of inertia of Ceres and Vesta. *Icarus*, 213:496–509, 2011a.

B.G. Bills and F. Nimmo. Rotational dynamics and internal structure of Titan. *Icarus*, 214(1):351–355, 2011b.

B.G. Bills, S.W. Asmar, A.S. Konopliv, R.S. Park, and C.A. Raymond. Harmonic and statistical analyses of the gravity and topography of Vesta. *Icarus*, 240:161–173, 2014.

R.P. Binzel and S. Xu. Chips off of asteroid 4 Vesta evidence for the parent body of basaltic achondrite meteorites. *Science*, 260(5105):186–191, 1993.

M.T. Bland. Predicted crater morphologies on Ceres: Probing internal structure and evolution. *Icarus*, 226(1):510–521, 2013.

M.T. Bland, C.A. Raymond, P.M. Schenk, R.R. Fu, T. Kneissl, J.H. Pasckert, H. Hiesinger, F. Preusker, R.S. Park, S. Marchi, and et al. Composition and structure of the shallow subsurface of Ceres revealed by crater morphology. *Nature Geoscience*, 9(7):538–542, 2016.

N. T. Bobrovnikoff. The spectra of minor planets. *Lick Observatory Bulletin*, 14: 18–27, 1929.

T.J. Bowling, D.A. Minton, J.C. Castillo-Rogez, B.C. Johnson, and J.K. Steckloff. Eroding the hydrosphere of 1 Ceres: water mass loss due to impact induced sublimation. In *in Proc. Astrobiol. Sci. Conf.*, 2015.

D.T. Britt and Consolmagno S.J., G. Stony meteorite porosities and densities: A review of the data through 2001. *Meteoritis & Planetary Science*, 8:1161–1180, 2003a.

D.T. Britt and Consolmagno S.J., G. Stony meteorite porosities and densities: A review of the data through 2001. *Meteoritics & Planetary Science*, 38(8):1161–1180, 2003b.

D.T. Britt, R.J. Macke, W. Kiefer, and Consolmagno S.J., G. An overview of achondrite density, porosity and magnetic susceptibility. In *Lunar and Planetary Science Conference*, volume 41, page 1869, 2010.

R.H. Brown, C.M. Morrison, C.M. Tellesco, and W. E. Brunk. Calibration of the radiometric asteroid scale using occultation diameters. *Icarus*, 52:188–195, 1982.

V.F. Buchwald. *Handbook of iron meteorites*, volume 1-3. JSTOR, 1975.

D.L. Buczkowski, B.E. Schmidt, D.A. Williams, S.C. Mest, J.E.C. Scully, A.I. Ermakov, F. Preusker, P. Schenk, K.A. Otto, H. Hiesinger, and et al. The geomorphology of Ceres. *Science*, 353(6303):aaf4332, 2016.

T.H. Burbine, P.C. Buchanan, R.P. Binzel, S.J. Bus, T. Hiroi, J.L. Hinrichs, A. Meibom, and T.J. Mccoy. Vesta, Vestoids, and the howardite, eucrite, diogenite group: Relationships and the origin of spectral differences. *Meteoritics & Planetary Science*, 36(6):761–781, 2001.

A.A. Burns, V.S. Safronov, and T. Gold. Asteroid nutation angles. *Monthly Notices of the Royal Astronomical Society*, 165(4):403–411, 1973. doi: 10.1093/mnras/165.4.403. URL `http://mnras.oxfordjournals.org/content/165/4/403.abstract`.

B. Carry, C. Dumas, M. Fulchignoni, W.J. Merline, W.J. Merline, J. Berthier, D. Hestroffer, T. Fusco, and P. Tamblyn. Near-infrared mapping and physical properties of the dwarf-planet Ceres. *A&A*, 478:235–244, 2008.

J.C. Castillo-Rogez. Ceres – neither a porous nor salty ball. *Icarus*, 2015:599–602, 2011.

J.C. Castillo-Rogez and T.B. McCord. Ceres' evolution and present state constrained by shape data. *Icarus*, 205:443–459, 2010.

J.C. Castillo-Rogez, T. Bowling, R.R. Fu, H.Y. McSween, C.A. Raymond, N. Rambaux, B. Travis, S. Marchi, D.P. O'Brien, B.C. Johnson, and et al. Loss of Ceres' icy shell from impacts: Assessment and implications. In *Lunar and Planetary Science Conference*, volume 47, page 3012, 2016.

J.F. Cavanaugh, J.C. Smith, X. Sun, A.E. Bartels, L. Ramos-Izquierdo, D.J. Krebs, J.E. McGarry, R. Trunzo, A.M. Novo-Gradac, J.L. Britt, and et al. The Mercury Laser Altimeter instrument for the MESSENGER mission. In *The Messenger Mission to Mercury*, pages 451–479. Springer, 2007.

A. Cellino, V. Zappalà, M. Di Martino, P. Farinella, and P. Paolicchi. Flattening, pole, and albedo features of 4 Vesta from photometric data. *Icarus*, 70(3):546–565, 1987.

N.L. Chabot, C.M. Ernst, B.W. Denevi, J.K. Harmon, S.L. Murchie, D.T. Blewett, S.C. Solomon, and E.D. Zhong. Areas of permanent shadow in Mercury's south

polar region ascertained by MESSENGER orbital imaging. *Geophysical Research Letters*, 39(9), 2012.

N.L. Chabot, C.M. Ernst, B.W. Denevi, H. Nair, A.N. Deutsch, D.T. Blewett, S.L. Murchie, G.A. Neumann, E. Mazarico, D.A. Paige, and et al. Images of surface volatiles in Mercury's polar craters acquired by the MESSENGER spacecraft. *Geology*, 42(12):1051–1054, 2014.

S. Chandrasekhar. Ellipsoidal figures of equilibriumâĂŤan historical account. *Communications on Pure and Applied Mathematics*, 20(2):251–265, 1967.

G. Chin, S. Brylow, M. Foote, J. Garvin, J. Kasper, J. Keller, M. Litvak, I. Mitrofanov, D. Paige, K. Raney, and et al. Lunar Reconnaissance Orbiter overview: The instrument suite and mission. *Space Science Reviews*, 129(4):391–419, 2007.

G.S. Collins. Numerical simulations of complex crater formation with dilatancy: Implications for gravity anomalies of lunar and terrestrial craters. In *Lunar and Planetary Science Conference*, volume 44, page 2917, 2013.

G.J. Consolmagno S.J., D.T. Britt, and R.J. Macke. The significance of meteorite density and porosity. *Chemie der Erde-Geochemistry*, 68(1):1–29, 2008.

M. C. De Sanctis, E. Ammannito, M. T. Capria, F. Tosi, F. Capaccioni, F. Zambon, F. Carraro, S. Fonte, A. Frigeri, R. Jaumann, and et al. Spectroscopic characterization of mineralogy and its diversity across Vesta. *Science*, 336(6082):697–700, 2012.

S.F. Dermott. Shapes and gravitational moments of satellites and asteroids. *Icarus*, 37(3):575–586, 1979.

A.N. Deutsch, N.L. Chabot, E. Mazarico, C.M. Ernst, J.W. Head, G.A. Neumann, and S.C. Solomon. Comparison of areas in shadow from imaging and altimetry in the north polar region of Mercury and implications for polar ice deposits. In *Lunar and Planetary Science Conference*, volume 47, page 1134, 2016.

D. P. Dobson, W. A. Crichton, L. Vočadlo, A. P. Jones, Y. Wang, T. Uchida, M. Rivers, S. Sutton, and J. P. Brodholt. In situ measurement of viscosity of liquids in the Fe-FeS system at high pressures and temperatures. *American Mineralogist*, 85(11-12):1838–1842, 2000.

J. Drummond and J. Christou. Triaxial ellipsoid dimensions and rotational poles of seven asteroids from Lick observatory adaptive optics images, and of Ceres. *Icarus*, 197(2):480–496, 2008.

J. Drummond, A. Eckart, and E.K. Hege. Speckle interferometry of asteroids IV. reconstructed images of 4 Vesta. *Icarus*, 73(1):1–14, 1988.

J.D. Drummond and E.K. Hege. Speckle interferometry of asteroids. In *Asteroids II*, volume 1, pages 171–191, 1989.

J.D. Drummond, R.Q. Fugate, and J.C. Christou. Full adaptive optics images of asteroids Ceres and Vesta: Rotational poles and triaxial ellipsoid dimensions. *Icarus*, 132:80–99, 1998.

J.D. Drummond, B. Carry, W.J. Merline, C. Dumas, H. Hammel, S. Erard, A. Conrad, P. Tamblyn, and C.P. Chapman. Dwarf planet Ceres: Ellipsoid dimensions and rotational pole from Keck and VLT adaptive optics images. *Icarus*, 236:28 – 37, 2014. ISSN 0019-1035. doi: http://dx.doi.org/10.1016/j.icarus.2014.03.038. URL `http://www.sciencedirect.com/science/article/pii/S001910351400164X`.

D.W. Dunham, S.W. Killen, and T.L. Boone. The diameter of Ceres from a lunar occultation. *Bull. Amer. Astron. Soc.*, 6:432–433, 1974.

L.T. Elkins-Tanton, B.P. Weiss, and M.T. Zuber. Chondrites as samples of differentiated planetesimals. *Earth and Planetary Science Letters*, 305(1):1–10, 2011.

A.I. Ermakov, M.T. Zuber, D.E. Smith, C.A. Raymond, G. Balmino, R.R. Fu, and B.A. Ivanov. Constraints on VestaâĂŹs interior structure using gravity and shape models from the Dawn mission. *Icarus*, 240:146–160, 2014.

A.I. Ermakov, R.R. Fu, J.C. Castillo-Rogez, C.A. Raymond, R.S. Park, F. Preusker, C.T. Russell, D.E. Smith, and M.T. Zuber. Constraints on Ceres' internal structure and evolution from its shape and gravity measured by the Dawn spacecraft. *in prep for JGR*, 2016.

C.M. Ernst, R.W. Gaskell, E.G. Kahn, O.S. Barnouin, J.H. Roberts, and K.K. Wilcomb. Updated shape models of Phobos and Deimos from stereophotoclinometry. In *Lunar and Planetary Science Conference*, volume 46, page 2753, 2015.

F.P. Fanale and J.R. Salvail. The water regime of asteroid (1) Ceres. *Icarus*, 82(1):97 – 110, 1989. ISSN 0019-1035. doi: http://dx.doi.org/10.1016/0019-1035(89)90026-2. URL `http://www.sciencedirect.com/science/article/pii/0019103589900262`.

W.M. Folkner, J.G. Williams, D.H. Boggs, R.S. Park, and P. Kuchynka. The planetary and lunar ephemerides DE430 and DE431. *Interplanet. Netw. Prog. Rep*, 196: 1–81, 2014.

M. Formisano, C. Federico, S. De Angelis, M.C. De Sanctis, and G Magni. The stability of the crust of the dwarf planet Ceres. *Monthly Notices of the Royal Astronomical Society*, 463(1):520–528, 2016.

A.D. Fortes, I.G. Wood, and K.S. Knight. The crystal structure and thermal expansion tensor of $MgSO_4 11 D_2O$ (meridianiite) determined by neutron powder diffraction. *Physics and Chemistry of Minerals*, 35(4):207–221, 2008.

R.R. Fu, B.H. Hager, A.I. Ermakov, and M.T. Zuber. Efficient early global relaxation of asteroid Vesta. *Icarus*, 240:133–145, 2014.

R.R. Fu, A.I. Ermakov, M.T. Zuber, and B.H. Hager. The interior structure of Ceres as revealed by surface topography. *In prep.*, 2016.

M.J. Gaffey. The asteroid (4) Vesta: Rotational spectral variations, surface material heterogeneity, and implications for the origin of the basaltic achondrites. In *14th Lunar and Planetary Science Conference*, volume 497, page 14, 1983.

W. Gander, R. Strebel, and G.H. Golub. Fitting of circles and ellipses least squares solution. *SVD and Signal Processing*, 3:349–356, 1995.

R. Garmier, J.-P. Barriot, A.S. Konopliv, and D.K. Yeomans. Modeling of the Eros gravity field as an ellipsoidal harmonic expansion from the NEAR Doppler tracking data. *Geophysical Research Letters*, 29(8), 2002.

R.W. Gaskell. SPC shape and topography of Vesta from DAWN imaging data. In *AAS/Division for Planetary Sciences Meeting Abstracts*, volume 44, 2012.

R.W. Gaskell and N. Mastrodemos. Lunar topography from stereophotoclinometry. In *Lunar and Planetary Science Conference*, volume 39, page 1152, 2008.

R.W. Gaskell, O.S. Barnouin-Jha, and D.J. Scheeres. Modeling Eros with stereophotoclinometry. In *Lunar and Planetary Science Conference*, volume 38, page 1333, 2007.

R.W. Gaskell, O.S. Barnouin-Jha, D.J. Scheeres, A.S. Konopliv, T. Mukai, S. Abe, J. Saito, M. Ishiguro, T. Kubota, T. Hashimoto, and et al. Characterizing and navigating small bodies with imaging data. *Meteoritics & Planetary Science*, 43 (6):1049–1061, 2008.

A. Ghosh and H.Y. McSween. A thermal model for the differentiation of asteroid 4 Vesta, based on radiogenic heating. *Icarus*, 134(2):187–206, 1998.

S. Gong, M.A. Wieczorek, F. Nimmo, W.S. Kiefer, J.W. Head, C. Huang, D.E. Smith, and M.T. Zuber. Thicknesses of mare basalts on the Moon from gravity and topography. *Journal of Geophysical Research: Planets*, 121(5):854–870, 2016.

S. Goossens, K. Matsumoto, Q. Liu, F. Kikuchi, K. Sato, H. Hanada, Y. Ishihara, H. Noda, N. Kawano, N. Namiki, and et al. Lunar gravity field determination using SELENE same-beam differential VLBI tracking data. *Journal of Geodesy*, 85(4): 205–228, 2011.

M. Hamy. *Annales de l'Observatoire de Paris.* 1889.

S. Han. Determination and localized analysis of intersatellite line of sight gravity difference: Results from the GRAIL primary mission. *Journal of Geophysical Research: Planets*, 118(11):2323–2337, 2013.

S. Han, N. Schmerr, G. Neumann, and S. Holmes. Global characteristics of porosity and density stratification within the lunar crust from GRAIL gravity and Lunar Orbiter Laser Altimeter topography data. *Geophysical Research Letters*, 41(6): 1882–1889, 2014.

P.O. Hayne and O. Aharonson. Thermal stability of ice on Ceres with rough topography. *Journal of Geophysical Research: Planets*, 120(9):1567–1584, 2015b.

D. Hemingway, F. Nimmo, H. Zebker, and L. Iess. A rigid and weathered ice shell on Titan. *Nature*, 500:550–552, 2013.

H. Hiesinger, S. Marchi, N. Schmedemann, P. Schenk, J.H. Pasckert, A. Nessemann, D.P. O'Brien, T. Kneissl, A.I. Ermakov, M.T. Fu, R.R. Bland, A. Nathues, T. Platz, D.A. Williams, R. Jaumann, J.C. Castillo-Rogez, O. Ruesch, B. Schmidt, R.S. Park, F. Preusker, D.L. Buczkowski, C.T. Russell, and C.A. Raymond. Cratering on Ceres: Implications for its crust and evolution. *Science*, 353(6303):aaf4759, 2016.

C. Hirt and M. Kuhn. Evaluation of high-degree series expansions of the topographic potential to higher-order powers. *Journal of Geophysical Research: Solid Earth*, 117(B12), 2012. ISSN 2156-2202. doi: 10.1029/2012JB009492. URL `http://dx.doi.org/10.1029/2012JB009492`. B12407.

G. Hirth and D.L. Kohlstedt. Water in the oceanic upper mantle: implications for rheology, melt extraction and the evolution of the lithosphere. *Earth and Planetary Science Letters*, 144(1):93–108, 1996.

E.W. Hobson. *The theory of spherical and ellipsoidal harmonics*. CUP Archive, 1931.

B.A. Ivanov and H.J. Melosh. The Rheasilvia crater on Vesta: Numerical modeling. In *Lunar and Planetary Science Conference*, volume 43, page 2148, 2012.

B.A. Ivanov and H.J. Melosh. Two-dimensional numerical modeling of the Rheasilvia impact formation. *Journal of Geophysical Research: Planets*, 118(7):1545–1557, 2013.

R. Jaumann, D.A. Williams, D.L. Buczkowski, R.A. Yingst, F. Preusker, H. Hiesinger, N. Schmedemann, T. Kneissl, J.B. Vincent, D.T. Blewett, and et al. Vesta's shape and morphology. *science*, 336(6082):687–690, 2012.

T.V. Johnson and T.R. McGetchin. Topography on satellite surfaces and the shape of asteroids. *Icarus*, 18(4):612–620, 1973.

K.J. Johnston, P.K. Seidelmann, and C.W. Wade. Observations of 1 Ceres and 2 Pallas at centimeter wavelengths. *Astron. J.*, 87:1593–1599, 1982.

Frederik J.S. Mmass: Lematre, October 2014. URL `http://dx.doi.org/10.5281/zenodo.12002`.

M. Jutzi and E. Asphaug. Mega-ejecta on asteroid Vesta. *Geophysical Research Letters*, 38(1), 2011.

M. Jutzi, E. Asphaug, P. Gillet, J.-A. Barrat, and W. Benz. The structure of the asteroid 4 Vesta as revealed by models of planet-scale collisions. *Nature*, 494(7436): 207–210, 2013.

M. Kato, S. Sasaki, Y. Takizawa, and et al. The Kaguya mission overview. *Space Science Reviews*, 154(1-4):3–19, 2010.

W.M. Kaula. Determination of the Earth's gravitational field. *Reviews of Geophysics*, 1(4):507–551, 1963.

W.M. Kaula. *Theory of Satellite Geodesy.* Blaisdell, Waltham, MA., 1966.

W.S. Kiefer, R.J. Macke, B.T. Britt, A.J. Irving, and G.J. Consolmagno. Regional variability in the density of lunar mare basalts and implications for lunar gravity modeling. In *43rd Lunar and Planetary Institute Science Conference, Woodlands*, 2012.

J. Kim. *Simulation study of a low-low satellite-to-satellite tracking mission.* PhD thesis, Univ. of Texas at Austin, 2000.

M.G. Kleinhans, H. Markies, S.J. De Vet, F.N. Postema, and et al. Static and dynamic angles of repose in loose granular materials under reduced gravity. *Journal of Geophysical Research: Planets*, 116(E11), 2011.

A.S. Konopliv. Ceres gravity from the dawn mission. *In Prep.*, 2016.

A.S. Konopliv, W.L. Sjogren, R.N. Wimberly, and R. Cook. A high resolution lunar gravity field and predicted orbit behavior. *Astrodynamics 1993*, pages 1275–1294, 1994.

A.S. Konopliv, S.W. Asmar, E. Carranza, W.L. Sjogren, and D.N. Yuan. Recent gravity models as a result of the Lunar Prospector mission. *Icarus*, 150(1):1–18, 2001.

A.S. Konopliv, R.S. Park, D.-N. Yuan, S.W. Asmar, M.M. Watkins, J.G. Williams, E. Fahnestock, G. Kruizinga, M. Paik, D. Strekalov, N. Harvey, D.E. Smith, and M.T. Zuber. The JPL lunar gravity field to spherical harmonic degree 660 from the GRAIL Primary Mission. *Journal of Geophysical Research: Planets*, 118(7): 1415–1434, 2013. ISSN 2169-9100. doi: 10.1002/jgre.20097. URL `http://dx.doi.org/10.1002/jgre.20097`.

A.S. Konopliv, S.W. Asmar, R.S. Park, B.G. Bills, F. Centinello, A.B. Chamberlin, A.I. Ermakov, R.W. Gaskell, N. Rambaux, C.A. Raymond, C.T. Russell, D.E. Smith, P. Tricarico, and M.T. Zuber. The Vesta gravity field, spin pole and rotation period, landmark positions, and ephemeris from the Dawn tracking and optical data. *Icarus*, 240:103–117, 2014a.

A.S. Konopliv, R.S. Park, D.-N. Yuan, S.W. Asmar, M.M. Watkins, J.G. Williams, E. Fahnestock, G. Kruizinga, M. Paik, D. Strekalov, and et al. High-resolution lunar gravity fields from the GRAIL Primary and Extended Missions. *Geophysical Research Letters*, 41(5):1452–1458, 2014b.

A.B Kovačević. Determination of the mass of Ceres based on the most gravitationally efficient close encounters. *Monthly Notices of the Royal Astronomical Society*, 419: 2725–2736, 2012.

A.B. Kovačević and M. Kuzmanoski. A new determination of the mass of (1) Ceres. *Earth, Moon, and Planets*, 100(1-2):117–123, 2007.

K. Lambeck. Lateral density anomalies in the upper mantle. *Journal of Geophysical Research*, 81(35):6333–6340, 1976. ISSN 2156-2202. doi: 10.1029/JB081i035p06333. URL `http://dx.doi.org/10.1029/JB081i035p06333`.

J. Laskar, A.C.M. Correia, M. Gastineau, F. Joutel, Levrard B., and P. Robutel. Long term evolution and chaotic diffusion of the insolation quantities of Mars. *Icarus*, 170(2):343 – 364, 2004. ISSN 0019-1035. doi: http://dx.doi.org/10.1016/j.icarus.2004.04.005.

L.A. Lebofsky, M.V. Sykes, E.F. Tedesco, G.L. Veeder, D.L. Matson, I.G. Nott, J.V. Radostitz, P.A.R. Ade, W.K. Gear, M.J. Griffin, and E.I. Robson. Thermal properties of the regolith of asteroid 1 Ceres. *Bull. Amer. Astron. Soc.*, 16:698, 1984.

F.G. Lemoine, D.E. Smith, and M.T. Zuber. Goddard lunar gravity model-1 (GLGM-1): a 70th degree and order gravity model for the moon. *EOS, Transactions, American Geophysical Union*, 75:400, 1994.

F.G. Lemoine, S. Goossens, T.J. Sabaka, J.B. Nicholas, E. Mazarico, D.D. Rowlands, B.D. Loomis, D.S. Chinn, D.S. Caprette, G.A. Neumann, and et al. High–degree gravity models from GRAIL primary mission data. *Journal of Geophysical Research: Planets*, 118(8):1676–1698, 2013.

F.G. Lemoine, S. Goossens, T.J. Sabaka, J.B. Nicholas, E. Mazarico, D.D. Rowlands, B.D. Loomis, D.S. Chinn, G.A. Neumann, D.E. Smith, and et al. GRGM900C: A degree 900 lunar gravity model from GRAIL primary and extended mission data. *Geophysical Research Letters*, 41(10):3382–3389, 2014.

F.G.R. Lemoine, D.E. Smith, M.T. Zuber, G.A. Neumann, and D.D. Rowlands. A 70th degree lunar gravity model (GLGM-2) from Clementine and other tracking data. *Journal of Geophysical Research: Planets*, 102(E7):16339–16359, 1997.

J. Lorell and W.L. Sjogren. Lunar gravity: Preliminary estimates from Lunar Orbiter. *Science*, 159(3815):625–627, 1968.

G.W. Lugmair and A. Shukolyukov. Early solar system timescales according to 53 Mn-53 Cr systematics. *Geochimica et Cosmochimica Acta*, 62(16):2863–2886, 1998.

B.E. Mandler and L.T. Elkins-Tanton. The origin of eucrites, diogenites, and olivine diogenites: Magma ocean crystallization and shallow magma chamber processes on Vesta. *Meteoritics & Planetary Science*, 48(11):2333–2349, 2013.

M. Mao and W.B. McKinnon. Internal structures of Ceres and Enceladus: compactions and contrasts. In *47th Lunar and Planetary Science Conference, held March 21-25, 2016 at The Woodlands, Texas. LPI Contribution No. 1903, p.1637*, 2016.

S. Marchi, H.Y. McSween, D.P. OÂŠ'Brien, P. Schenk, M.C. De Sanctis, R.W. Gaskell, R. Jaumann, S. Mottola, F. Preusker, C.A. Raymond, and et al. The violent collisional history of asteroid 4 Vesta. *Science*, 336(6082):690–694, 2012.

S. Marchi, A.I. Ermakov, C.A. Raymond, R.R. Fu, D.P. O'Brien, M.T. Bland, E. Ammannito, M.C. De Sanctis, P. Schenk, J. Scully, D. L. Buczkowski, H. Hiesinger, and C.T. Russell. The missing large impact craters on Ceres. *Nature Communications*, 2016.

I. Matsuyama and F. Nimmo. Reorientation of Vesta: Gravity and tectonic predictions. *Geophysical Research Letters*, 38(14), 2011.

E. Mazarico, G.A. Neumann, D.E. Smith, M.T. Zuber, and M.H. Torrence. Illumination conditions of the lunar polar regions using LOLA topography. *Icarus*, 211 (2):1066–1081, 2011.

D.W. McCarthy, J.D. Freeman, and J.D. Drummond. High resolution images of Vesta at 1.65 μm. *Icarus*, 108(2):285–297, 1994.

T.B. McCord and C. Sotin. Ceres: Evolution and current state. *JGR*, 110:1–14, 2005.

T.B. McCord, J.B. Adams, and T.V. Johnson. Asteroid Vesta: Spectral reflectivity and compositional implications. *Science*, 168(3938):1445–1447, 1970.

T.B. McCord, J.C. Castillo-Rogez, and A.S. Rivkin. Ceres: Its origin, evolution and structure and Dawn's potential contribution. *Space Sci Rev*, 163:63–76, 2011.

D. McKenzie. The relationship between topography and gravity on Earth and Venus. *Icarus*, 112(1):55 – 88, 1994. ISSN 0019-1035. doi: http://dx.doi.org/10.1006/icar.1994.1170. URL `http://www.sciencedirect.com/science/article/pii/S0019103584711705`.

W.B. McKinnon. Could Ceres be a refugee from the Kuiper Belt? In *Asteroids, Comets, Meteors, Baltimore, MD. LPI Contribution No. 1405, p. 8389.*, 2008.

H.Y. McSween, E. Ammannito, V. Reddy, T.H. Prettyman, A.W. Beck, M.C. De Sanctis, A. Nathues, L. Le Corre, D.P. O'Brien, N. Yamashita, and et al. Composition of the Rheasilvia basin, a window into Vesta's interior. *Journal of Geophysical Research: Planets*, 118(2):335–346, 2013.

H.Y. McSween Jr and G.R. Huss. *Cosmochemistry.* Cambridge University Press, 2010.

H.Y. McSween Jr, D.W. Mittlefehldt, A.W. Beck, R.G. Mayne, and T.J. McCoy. HED meteorites and their relationship to the geology of Vesta and the Dawn mission. In *The Dawn Mission to Minor Planets 4 Vesta and 1 Ceres*, pages 141–174. Springer, 2010.

H.J. Melosh, A.M. Freed, B.C. Johnson, D.M. Blair, J.C. Andrews-Hanna, G.A. Neumann, R.J. Phillips, D.E. Smith, S.C. Solomon, M.A. Wieczorek, and et al. The origin of lunar mascon basins. *Science*, 340(6140):1552–1555, 2013.

R.E. Milliken and A.S. Rivkin. Brucite and carbonate assemblages from altered olivine-rich materials on Ceres. *Nature Geoscience*, 2:258–261, 2009.

R. L. Millis and et al. The size, shape, density, and albedo of Ceres from its occultation of BD+8 471. *Icarus*, 72:507–518, 1987.

D.L. Mitchell, R.S. Hudson, K.D. Rosema, D.B. Campbell, R. Velez, J.F. Chandler, I.I. Shapiro, J.F. Giorgini, and D.K. Yeomans. Radar observations of asteroids 1 Ceres, 2 Pallas, and 4 Vesta. *Icarus*, 124:113–133, 1996.

J.E. Moores. Lunar water migration in the interval between large impacts: Heterogeneous delivery to Permanently Shadowed Regions, fractionation, and diffusive barriers. *Journal of Geophysical Research: Planets*, 121(1):46–60, 2016.

H. Moritz. *Theoretical Geodesy and the Earth's Interior*. Wichmann, 1990.

D. Morrison and B. Zellner. Polarimetry and radiometry of the asteroids. in Asteroids (T. Gehrels, Ed). *Univ. of Arizona Press, Tucson*, pages 1090–1097, 1979.

P.M. Muller and W.L. Sjogren. Mascons: Lunar mass concentrations. *Science*, 161 (3842):680–684, 1968.

P.M. Muller and W.L. Sjogren. Consistency of Lunar Orbiter residuals with trajectory and local gravity effects. *Journal of Spacecraft and Rockets*, 6(7):849–850, 1969.

P.M. Muller, W.L. Sjogren, and W.R. Wollenhaupt. Lunar gravity: Apollo 15 doppler radio tracking. *The Moon*, 10(2):195–205, 1974.

G.A. Neumann, M.T. Zuber, D.E. Smith, and F.G. Lemoine. The lunar crust: Global structure and signature of major basins. *Journal of Geophysical Research*, 101:16–841, 1996.

G.A. Neumann, J.F. Cavanaugh, X. Sun, E.M. Mazarico, D.E. Smith, M.T. Zuber, D. Mao, D.A. Paige, S.C. Solomon, C.M. Ernst, and et al. Bright and dark polar deposits on Mercury: Evidence for surface volatiles. *Science*, 339(6117):296–300, 2013.

W. Neumann, D. Breuer, and T. Spohn. Modeling the internal structure of Ceres: Coupling of accretion with compaction by creep and implications for the water-rock differentiation. *A&A*, 584(A117):16, 2015. doi: http://dx.doi.org/10.1051/0004-6361/20152708.

M. Neveu and S.J. Desch. Geochemistry, thermal evolution, and cryovolcanism on Ceres with a muddy ice mantle. *Geophysical Research Letters*, 42, 2015. doi: 10.1002/2015GL066375.

F. Nimmo, B.G. Bills, and P.C. Thomas. Geophysical implications of the long-wavelength topography of the Saturnian satellites. *Journal of Geophysical Research: Planets*, 116(E11), 2011. ISSN 2156-2202. doi: 10.1029/2011JE003835. URL `http://dx.doi.org/10.1029/2011JE003835`.

D.P. O'Brien and M.V. Sykes. The origin and evolution of the asteroid belt–implications for Vesta and Ceres. *Space Sci Rev*, 163:41–61, 2011.

T. Ono, A. Kumamoto, H. Nakagawa, Y. Yamaguchi, S. Oshigami, A. Yamaji, T. Kobayashi, Y. Kasahara, and H. Oya. Lunar radar sounder observations of subsurface layers under the nearside maria of the Moon. *Science*, 323(5916):909–912, 2009.

T. Ono, A. Kumamoto, Y. Kasahara, Y. Yamaguchi, A. Yamaji, T. Kobayashi, S. Oshigami, H. Nakagawa, Y. Goto, K. Hashimoto, and et al. The lunar radar sounder (LRS) onboard the Kaguya (SELENE) spacecraft. *Space Science Reviews*, 154(1-4): 145–192, 2010.

S. Oshigami, Y. Yamaguchi, A. Yamaji, T. Ono, A. Kumamoto, T. Kobayashi, and H. Nakagawa. Distribution of the subsurface reflectors of the western nearside maria observed from Kaguya with Lunar Radar Sounder. *Geophysical Research Letters*, 36(18), 2009.

S. Oshigami, S. Watanabe, Y. Yamaguchi, A. Yamaji, T. Kobayashi, A. Kumamoto, K. Ishiyama, and T. Ono. Mare volcanism: Reinterpretation based on Kaguya

Lunar Radar Sounder data. *Journal of Geophysical Research: Planets*, 119(5): 1037–1045, 2014. ISSN 2169-9100. doi: 10.1002/2013JE004568. URL http://dx.doi.org/10.1002/2013JE004568.

D.A. Paige, M.A. Siegler, J.A. Zhang, P.O. Hayne, E.J. Foote, K.A. Bennett, A.R. Vasavada, B.T. Greenhagen, J.T. Schofield, D.J. McCleese, and et al. Diviner lunar radiometer observations of cold traps in the Moon's south polar region. *Science*, 330(6003):479–482, 2010.

E. Palmer and R.W. Gaskell. Error analysis of stereophotoclinometry in support of the OSIRIS-REx mission. In *AAS/Division for Planetary Sciences Meeting Abstracts*, volume 47, 2015.

R.S. Park, A.S. Konopliv, S.W. Asmar, B.G. Bills, R.W. Gaskell, C.A. Raymond, D.E. Smith, M.J. Toplis, and M.T. Zuber. Gravity field expansion in ellipsoidal harmonic and polyhedral internal representations applied to Vesta. *Icarus*, 240: 118–132, 2014b.

R.S. Park, A.S. Konopliv, B.G. Bills, N. Rambaux, J.C. Castillo-Rogez, C.A. Raymond, A.T. Vaughan, A.I. Ermakov, M.T. Zuber, R.R. Fu, and et al. A partially differentiated interior for (1) Ceres deduced from its gravity field and shape. *Nature*, 2016.

J.W. Parker, S.A. Stern, P.C. Thomas, M.C. Festou, and E.F. Merline, W.J. Young. Analysis of the first disk-resolved images of Ceres from ultraviolet observation with the Hubble Space Telescope. *Astron. J.*, 123:549–557, 2002.

M.E. Perry, G.A. Neumann, R.J. Phillips, O.S. Barnouin, C.M. Ernst, D.S. Kahan, S.C. Solomon, M.T. Zuber, D.E. Smith, S.A. Hauck, S.J. Peale, J.-L. Margot, E. Mazarico, C.L. Johnson, R.W. Gaskell, J.H. Roberts, R.L. McNutt, and J. Oberst. The low-degree shape of Mercury. *Geophysical Research Letters*, 42(17):6951–6958, 2015. ISSN 1944-8007. doi: 10.1002/2015GL065101. URL http://dx.doi.org/10.1002/2015GL065101.

M.S. Petrovskaya and A.N. Vershkov. Non-singular expressions for the gravity gradients in the local north-oriented and orbital reference frames. *Journal of Geodesy*, 80(3):117–127, 2006.

R.J. Phillips, G.F. Adams, W.E. Brown Jr, R.E. Eggleton, P. Jackson, R. Jordan, W.J. Peeples, L.J. Porcello, J. Ryu, G. Schaber, and et al. The Apollo 17 lunar sounder. In *Lunar and Planetary Science Conference Proceedings*, volume 4, page 2821, 1973.

T. Platz, A. Nathues, N. Schorghofer, F. Preusker, E. Mazarico, S.E. Schröder, T. Kneissl, N. Schmedemann, J.-P. Combe, S. Byrne, M. Schäfer, G.S. Thangjam, M. Hoffmann, P. Gutierrez-Marques, M. Landis, J. Ripken, K.-D. Matz, and C.T. Russell. Into darkness: Ice deposits in Ceres' northern permanent shadows. Submitted to Nature Astronomy, 2016.

V. Pohánka. Gravitational field of the homogeneous rotational ellipsoidal body: a simple derivation and applications. *Contrib. Geophys. Geodes.*, 41(2):117–157, 2011.

T.H. Prettyman, D.W. Mittlefehldt, N. Yamashita, A. W. Beck, W. C. Feldman, J. S. Hendricks, D. J. Lawrence, T.J. McCoy, H.Y. McSween, P.N. Peplowski, and et al. Neutron absorption constraints on the composition of 4 Vesta. *Meteoritics & Planetary Science*, 48(11):2211–2236, 2013.

T.H. Prettyman, N. Yamashita, J.C. Castillo-Rogez, W.C. Feldman, D.J. Lawrence, H.Y. McSween, N. Schorghofer, M.J. Toplis, O. Forni, S.P. Joy, and et al. Ceres' hydrogen-rich regolith. In *EGU General Assembly Conference Abstracts*, volume 18, page 10429, 2016.

F. Preusker, F. Scholten, K.-D. Matz, R. Jaumann, T. Roatsch, C.A. Raymond, and C.T. Russell. Topography of Vesta from Dawn FC stereo images. *Lunar Planet. Sci. 43. Abstract*, 2012.

F. Preusker, F. Scholten, K.-D. Matz, T. Roatsch, S. Elgner, R. Jaumann, S.P. Joy,

C.A. Polanskey, C.A. Raymond, and C.T. Russell. Shape model and rotational state of dwarf planet Ceres from Dawn FC stereo images. 2015.

F. Preusker, F. Scholten, K.-D. Matz, S. Elgner, R. Jaumann, T. Roatsch, S.P. Joy, C.A. Polanskey, C.A. Raymond, and C.T. Russell. Dawn at Ceres–shape model and rotational state. In *Lunar and Planetary Science Conference*, volume 47, page 1954, 2016.

N. Rambaux, J. Castillo-Rogez, V. Dehant, and P. Kuchynka. Constraining Ceres' interior from its rotational motion. *Astronomy & Astrophysics*, 535:A43, 2011.

N. Rambaux, F. Chambat, and J.C. Castillo-Rogez. Third-order development of shape, gravity and moment of inertia for highly flattened celestial bodies - application to Ceres. *A&A*, 584(A127):8, 2015.

M.D. Rayman, T.C. Fraschetti, C.A. Raymond, and C.T. Russell. Dawn: A mission in development for exploration of main belt asteroids Vesta and Ceres. *Acta Astronautica*, 58(11):605–616, 2006.

C.A. Raymond, R.S. Park, S.W. Asmar, A.S. Konopliv, D.L. Buczkowski, M.C. De Sanctis, H.Y. McSween, C.T. Russell, R. Jaumann, and F. Preusker. Vestalia Terra: An ancient mascon in the southern hemisphere of Vesta. In *Lunar and Planetary Science Conference*, volume 44, page 2882, 2013a.

V. Reddy, A. Nathues, and M.J. Gaffey. First fragment of asteroid 4 Vesta's mantle detected. *Icarus*, 212(1):175–179, 2011.

V. Reddy, A. Nathues, L. Le Corre, H. Sierks, J.-Y. Li, R. Gaskell, T. McCoy, A. W. Beck, S.E. Schröder, C.M. Pieters, and et al. Color and albedo heterogeneity of Vesta from Dawn. *Science*, 336(6082):700–704, 2012.

J.E. Richardson, H.J. Melosh, R.J. Greenberg, and D.P. O'Brien. The global effects of impact-induced seismic activity on fractured asteroid surface morphology. *Icarus*, 179(2):325–349, 2005.

K. Righter and M. J. Drake. A magma ocean on Vesta: Core formation and petrogenesis of eucrites and diogenites. *Meteoritics & Planetary Science*, 32(6):929–944, 1997.

O. Ruesch, H. Hiesinger, M.C. De Sanctis, E. Ammannito, E. Palomba, A. Longobardo, M.T. Capria, F. Capaccioni, A. Frigeri, F. Tosi, and et al. Distribution of the near-IR spectral signature of olivine on Vesta with VIR/Dawn data: The ultramafic side of Vesta's surface. In *Lunar and Planetary Science Conference*, volume 45, page 1715, 2014.

R. Rummel, R.H. Rapp, H. Sunkel, and C.C. Tscherning. Comparisons of globaltopographic/isostatic models to the Earth's observed gravity field,. Technical Report Rep. No. 388, Department of Geodetic Science and Surveying, The Ohio State University, Columbus, Ohio, 1988.

C.T. Russell and C.A. Raymond. The Dawn mission to Vesta and Ceres. *Space Science Reviews*, 163(1-4):3–23, 2011.

C.T. Russell, A. Coradini, U. Christensen, M.C. De Sanctis, W.C. Feldman, R. Jaumann, H.U. Keller, A.S. Konopliv, T.B. McCord, L.A. McFadden, and et al. Dawn: A journey in space and time. *Planetary and Space Science*, 52(5):465–489, 2004.

C.T. Russell, C.A. Raymond, A. Coradini, H.Y. McSween, M.T. Zuber, A. Nathues, M.C. De Sanctis, R. Jaumann, A.S. Konopliv, F. Preusker, and et al. Dawn at Vesta: Testing the protoplanetary paradigm. *Science*, 336(6082):684–686, 2012.

A. Ruzicka, G.A. Snyder, and L.A. Taylor. Vesta as the howardite, eucrite and diogenite parent body: Implications for the size of a core and for large-scale differentiation. *Meteoritics & Planetary Science*, 32(6):825–840, 1997.

O. Saint-Pe, M. Combes, and F. Rigaut. Ceres surface properties by high-resolution imaging from Earth. *Icarus*, 105:271–281, 1993.

A.B. Sanin, I.G. Mitrofanov, M.L. Litvak, A. Malakhov, W.V. Boynton, G. Chin, G. Droege, L.G. Evans, J. Garvin, D.V. Golovin, and et al. Testing lunar per-

manently shadowed regions for water ice: LEND results from LRO. *Journal of Geophysical Research: Planets*, 117(E12), 2012.

P. Schenk, S. Marchi, D.P. O'Brien, D.L. Buczkowski, R. Jaumann, A. Yingst, T. McCord, R.W. Gaskell, T. Roatsch, H.E. Keller, and et al. Mega-impacts into planetary bodies: Global effects of the giant Rheasilvia impact basin on Vesta. In *Lunar and Planetary Science Conference*, volume 43, page 2757, 2012a.

N. Schorghofer. The lifetime of ice on main belt asteroids. *The Astrophysical Journal*, 682(1):697, 2008.

N. Schorghofer, E. Mazarico, T. Platz, F. Preusker, S.E. Schroder, C.A. Raymond, and C.T. Russell. The permanently shadowed regions of dwarf planet ceres. *Geophysical Research Letters*, pages n/a–n/a, 2016. ISSN 1944-8007. doi: 10.1002/2016GL069368. URL `http://dx.doi.org/10.1002/2016GL069368`.

S.E. Schröder, T. Maue, P. Gutiérrez Marqués, S. Mottola, K.M. Aye, H. Sierks, H.U. Keller, and A. Nathues. In-flight calibration of the Dawn Framing Camera. *Icarus*, 226(2):1304–1317, 2013.

V.L. Sharpton and J.W Head. Stratigraphy and structural evolution of southern Mare Serenitatis: A reinterpretation based on Apollo Lunar Sounder Experiment data. *Journal of Geophysical Research: Solid Earth*, 87(B13):10983–10998, 1982.

M.A. Siegler, R.S. Miller, J.T. Keane, M. Laneuville, D.A. Paige, I. Matsuyama, D.J. Lawrence, A. Crotts, and M.J. Poston. Lunar true polar wander inferred from polar hydrogen. *Nature*, 531(7595):480–484, 2016.

H. Sierks, H.U. Keller, R. Jaumann, H. Michalik, T. Behnke, F. Bubenhagen, I. Büttner, U. Carsenty, U. Christensen, R. Enge, and et al. The Dawn framing camera. *Space science reviews*, 163(1-4):263–327, 2011.

F. J. Simons and F. A. Dahlen. Spatiospectral concentration on a sphere. *SIAM Review*, 48(3):504–536, 2006.

F.J. Simons. Slepian functions and their use in signal estimation and spectral analysis. In *Handbook of Geomathematics*, pages 891–923. Springer, 2010.

W.L. Sjogren, R.N. Wimberly, and W.R. Wollenhaupt. Lunar gravity via the Apollo 15 and 16 subsatellites. *The Moon*, 9(1-2):115–128, 1974.

E. Skoglöv, P. Magnusson, and M. Dahlgren. Evolution of the obliquities for ten asteroids. *Planetary and space science*, 44(10):1177–1183, 1996.

D.E. Smith, F.J. Lerch, R.S. Nerem, M.T. Zuber, G.B. Patel, S.K. Fricke, and F.G. Lemoine. An improved gravity model for Mars: Goddard Mars model 1. *Journal of Geophysical Research: Planets*, 98(E11):20871–20889, 1993.

D.E. Smith, M.T. Zuber, G.A. Neumann, and F.G. Lemoine. Topography of the Moon from the Clementine lidar. *Journal of Geophysical Research*, 102(E1):1591–1611, 1997.

D.E. Smith, M.T. Zuber, G.A. Neumann, F.G. Lemoine, E. Mazarico, M.H. Torrence, J.F. McGarry, D.D. Rowlands, J.W. Head, T.H. Duxbury, and et al. Initial observations from the lunar orbiter laser altimeter (LOLA). *Geophysical Research Letters*, 37(18), 2010.

D.E. Smith, M.T. Zuber, R.J. Phillips, S.C. Solomon, S.A. Hauck, F.G. Lemoine, E. Mazarico, G.A. Neumann, S.J. Peale, J.-L. Margot, and et al. Gravity field and internal structure of Mercury from MESSENGER. *Science*, 336(6078):214–217, 2012.

D.E. Smith, M.T. Zuber, G.A. Neumann, E. Mazarico, F.G. Lemoine, J.W. Head, P.G. Lucey, O. Aharonson, M.S. Robinson, X. Sun, and et al. Summary of the results from the Lunar Orbiter Laser Altimeter after seven years in lunar orbit. *Icarus*, 2016.

J.R. Snyder. Map projections used by the US Geological Survey. Technical report, US Government Printing Office, 1982.

J.M. Soderblom, A.J. Evans, B.C. Johnson, H.J. Melosh, K. Miljkovic, R.J. Phillips, J.C. Andrews-Hanna, C.J. Bierson, J.W. Head, C. Milbury, G.A. Neumann, F. Nimmo, D.E. Smith, S.C. Solomon, M.M. Sori, M.A. Wieczorek, and M.T. Zuber. The fractured Moon: Production and saturation of porosity in the lunar highlands from impact cratering. *Geophysical Research Letters*, 42(17):6939–6944, 2015. ISSN 1944-8007. doi: 10.1002/2015GL065022. URL `http://dx.doi.org/10.1002/2015GL065022`.

M.G. Sterenborg and J.W. Crowley. Thermal evolution of early solar system planetesimals and the possibility of sustained dynamos. *Physics of the Earth and Planetary Interiors*, 214:53–73, 2013.

T.J. Stubbs and Y. Wang. Solar illumination conditions at 4 Vesta: Predictions using the digital elevation model derived from HST images. In *Lunar and Planetary Science Conference*, volume 42, page 2506, 2011.

H. Takeda, H. Mori, J. S. Delaney, M. Prinz, and G. E. Harlow. Mineralogical comparison of Antarctic and non-Antarctic HED (howardites-eucrites-diogenites) achondrites. *National Institute Polar Research Memoirs*, 30:181–205, 1983.

B.D. Tapley, S. Bettadpur, M. Watkins, and Ch. Reigber. The gravity recovery and climate experiment: Mission overview and early results. *Geophysical Research Letters*, 31(9), 2004.

P.C. Thomas, R.P. Binzel, M.J. Gaffey, B.H. Zellner, A.D. Storrs, and E. Wells. Vesta: Spin pole, size, and shape from HST images. *Icarus*, 128(1):88–94, 1997. doi: 10.1006/icar.1997.5736. cited By 124.

P.C. Thomas, J.W. Parker, L.A. McFadden, C.T. Russell, S.A. Stern, M.V. Sykes, and E.F Young. Differentiation of the asteroid Ceres as revealed by its shape. *Nature*, 437:224–226, 2005.

T.N. Titus. Ceres: Predictions for near-surface water ice stability and implications for plume generating processes. *Geophysical Research Letters*, 42(7):2130–2136, 2015.

M.J. Toplis, H. Mizzon, M. Monnereau, O. Forni, H.Y. Mcsween, D.W. Mittlefehldt, T.J. Mccoy, T.H. Prettyman, M.C. De Sanctis, C.A. Raymond, and C.T. Russell. Chondritic models of 4 Vesta: Implications for geochemical and geophysical properties. *Meteoritics and Planetary Science*, 48(11):2300–2315, 2013. doi: 10.1111/maps.12195. cited By 18.

J. Touma and J. Wisdom. Lie-Poisson integrators for rigid body dynamics in the solar system. *Astronomical Journal*, 107:1189–1202, 1994.

B.J. Travis, P.A. Bland, W.C. Feldman, and M.V. Sykes. Unconsolidated Ceres model has a warm convecting rocky core and aconvecting mud ocean. *46th Lunar and Planetary Science Conference*, (Abstract 2360), 2015.

P. Tricarico. Geoid and terrain slope of Vesta from Dawn. *Lunar Planet. Sci*, 43, 2012. cited By 1.

P. Tricarico. Multi-layer hydrostatic equilibrium of planets and synchronous moons: Theory and application to Ceres and to solar system moons. *Astrophysical Journal*, 782(2), 2014. doi: 10.1088/0004-637X/782/2/99. cited By 5.

D.L. Turcotte. A fractal interpretation of topography and geoid spectra on the Earth, Moon, Venus, and Mars. *Journal of Geophysical Research: Solid Earth*, 92(B4), 1987.

D.L. Turcotte, R.J. Willemann, W.F. Haxby, and J. Norberry. Role of membrane stresses in the support of planetary topography. *Journal of Geophysical Research: Solid Earth*, 86(B5):3951–3959, 1981. ISSN 2156-2202. doi: 10.1029/JB086iB05p03951. URL `http://dx.doi.org/10.1029/JB086iB05p03951`.

K. Watson, B.C. Murray, and H. Brown. The behavior of volatiles on the lunar surface. *Journal of Geophysical Research*, 66(9):3033–3045, 1961.

P.D. Welch. The use of fast Fourier transform for the estimation of power spectra: A method based on time averaging over short, modified periodograms. *IEEE Trans. Audio Electroacoust.*, AU-15:70–73, 1967.

R.A. Werner. The gravitational potential of a homogeneous polyhedron or don't cut corners. *Celestial Mechanics & Dynamical Astronomy*, 59(3):253–278, 1994. doi: 10.1007/BF00692875. cited By 84.

R.A. Werner and D.J. Scheeres. Exterior gravitation of a polyhedron derived and compared with harmonic and mascon gravitation representations of asteroid 4769 Castalia. *Celestial Mechanics and Dynamical Astronomy*, 65(3):313–344, 1996.

M.A. Wieczorek. 10.05 - Gravity and topography of the terrestrial planets. In Gerald Schubert, editor, *Treatise on Geophysics*, pages 165 – 206. Elsevier, Amsterdam, 2007a. ISBN 978-0-444-52748-6. doi: http://dx.doi.org/10.1016/B978-044452748-6.00156-5. URL `http://www.sciencedirect.com/science/article/pii/B9780444527486001565`.

M.A. Wieczorek. Gravity and topography of the terrestrial planets. *Planets and Moons*, pages 165–206, 2007b.

M.A. Wieczorek. SHTOOLS - Tools for working with spherical harmonics (v2.9.1), Oct 2014. URL `http://dx.doi.org/10.5281/zenodo.12158`.

M.A. Wieczorek and R.J. Phillips. Potential anomalies on a sphere: Applications to the thickness of the lunar crust. *Journal of Geophysical Research*, 103(E1): 1715–1724, 1998.

M.A. Wieczorek and F.J. Simons. Localized spectral analysis on the sphere. *Geophysical Journal International*, 162(3):655–675, 2005.

M.A. Wieczorek, G.A. Neumann, F. Nimmo, W.S. Kiefer, G.J. Taylor, H.J. Melosh, R.J. Phillips, S.C. Solomon, J.C. Andrews-Hanna, S.W. Asmar, and et al. The crust of the Moon as seen by GRAIL. *Science Express*, 2012.

J. Wisdom. Rotational dynamics of irregularly shaped natural satellites. *ApJ*, 94: 1350–1360, 1987.

J. Wisdom and M. Holman. Symplectic maps for the n-body problem. *Astronomical Journal*, 102:1528–1538, 1991.

C.F. Yoder. *Astrometric and Geodetic Properties of Earth and the Solar System*, pages 1–31. American Geophysical Union, 2013. ISBN 9781118668078. doi: 10.1029/RF001p0001. URL `http://dx.doi.org/10.1029/RF001p0001`.

V.N. Zharkov and V.P. Trubitsyn. *Physics of Planetary Interiors*. University of Arizona, Pachart Pub House, Tucson, 1978.

M.Yu. Zolotov. On the composition and differentiation of Ceres. *Icarus*, 204:183–193, 2009.

M.T. Zuber and D.E. Smith. Topography of the lunar south polar region: Implications for the size and location of permanently shaded areas. *Geophysical Research Letters*, 24(17):2183–2186, 1997.

M.T. Zuber, D.E. Smith, A.F. Cheng, J. B. Garvin, O. Aharonson, T.D. Cole, P.J. Dunn, Y. Guo, F.G. Lemoine, G.A. Neumann, D.D. Rowlands, and M.H. Torrence. The shape of 433 Eros from the NEAR-Shoemaker Laser Rangefinder. *Science*, 289 (5487):2097–2101, 2000. doi: 10.1126/science.289.5487.2097. URL `http://www.sciencemag.org/content/289/5487/2097.abstract`.

M.T. Zuber, H.Y. McSween, R.P. Binzel, L.T. Elkins-Tanton, A.S. Konopliv, C.M. Pieters, and D.E. Smith. Origin, internal structure and evolution of 4 Vesta. *Space Science Reviews*, 163(1):77–93, 2011.

M.T. Zuber, D.E. Smith, R.J. Phillips, S.C. Solomon, G.A. Neumann, S.A. Hauck, S.J. Peale, O.S. Barnouin, J.W. Head, C.L. Johnson, and et al. Topography of the northern hemisphere of Mercury from MESSENGER laser altimetry. *Science*, 336 (6078):217–220, 2012.

M.T. Zuber, D.E. Smith, M.M. Watkins, S. W. Asmar, A. S. Konopliv, F. G. Lemoine, H. Jay Melosh, Gregory A. Neumann, R.J. Phillips, S.C. Solomon, M.A. Wieczorek, J.G. Williams, S.J. Goossens, G. Kruizinga, E. Mazarico, R.S. Park, and

D.-N. Yuan. Gravity field of the Moon from the Gravity Recovery and Interior Laboratory (GRAIL) mission. *Science*, 339(6120):668–671, 2013. ISSN 0036-8075. doi: 10.1126/science.1231507. URL http://science.sciencemag.org/content/339/6120/668.